ELECTRODE GEOMETRY EFFECTS ON THE COLLECTION EFFICIENCY OF SUBMICRON AND ULTRAFINE DUST PARTICLES IN WIRE-PLATE ELECTROSTATIC PRECIPITATORS

By

DRAZENA BROCILO, B.ENG., M.ENG.

A Thesis

Submitted to the School of Graduate Studies

in Partial Fulfilment of the Requirements

for the Degree

Doctor of Philosophy

McMaster University

ELECTRODE GEOMETRY EFFECTS

IN WIRE-PLATE ESP

DOCTOR OF PHILOSOPHY (2003) McMaster University

(Electrical and Computer Engineering) Hamilton, Ontario

TITLE: Electrode geometry effects on the collection efficiency of submicron and ultrafine dust particles in wire-plate electrostatic precipitators

AUTHOR: Drazena Brocilo, M.Eng. (McMaster University)

SUPERVISORS: Dr. J.S. Chang and Dr. R.D. Findlay

NUMBER OF PAGES: XXXII, 273

ABSTRACT

Recent interest in emission control of fine particulate matter has resulted from scientific studies on the effect of fine particulate matter on human health. Hence, many western countries introduced a new emission regulation known as PM2.5, that regulates particles less than 2.5 microns in diameter. The existing particle separation devices such as electrostatic precipitators (ESPs) are of particular interest since they can economically capture particles effectively with a low pressure drop. The present ESPs provide high collection efficiencies of around 99.99% for micron and larger particles. However, the collection efficiency of submicron particles in the range from 0.1 to 1 μm and ultrafine particles, that is with particle diameters less than 0.1 μm, can be less than 50%.

In this work, numerical and experimental studies were conducted to examine the effect of electrode geometries on the improvement of collection efficiency of submicron and ultrafine dust particles in electrostatic precipitators. The collection efficiency prediction was based on a modified Deutsche's equation after calculation of the three-dimensional electric potential and ion distribution. The particle charging models for diffusion and field charging methods were considered, based on the Knudsen number $(Kn=2\lambda_i/d_p)$, where λ_i is the mean free path of negative ions and d_p is the dust particle diameter. The constitutive relationship developed from the optical emission experiments was implemented to simulate ion distribution of corona discharge for various discharge

electrodes. Experimental validations for total and partial collection efficiencies for particle size from 10-2 to 20 mm were conducted for bench and full scale ESPs.

Results show that the collection efficiency of submicron and ultrafine particles can be predicted with good accuracy for various geometries of discharge and dust collection electrodes. The spike-type discharge electrode with the I-type collecting electrode improves collection efficiency of fine particles when compared to the wire or rod discharge electrode with I-type collecting electrode. In the case of U and C-type collecting electrodes, there is an optimum fin length for which the highest collection efficiency can be reached. Comparison of experimental and predicted results shows that the total collection efficiency predicted by the present model agrees well with experimental results for the bench-scale ESPs. For the large-scale wire-plate type ESP, the present simulation results conducted for various gas temperatures and dust resistivities agree quantitatively and qualitatively with the experimental results.

The model proved to be useful for prototype design of collecting and discharge electrodes, modification and existing ESP's and scale-up of new ESP's in order to meet new emission regulations.

ACKNOWLEDGMENTS

I would like to thank Dr. J.S. Chang and Dr. R.D. Findlay, my supervisors, for excellent guidance and support. I would also like to express my appreciation to the members of my supervisory committee, Dr. J. Dableh, and Dr. D. Corr for their comments and interest in my thesis.

A special thanks to P. Looy and Dr. Y. Uchida for help with the experimental set-up. Many thanks to Dr. V. Morgan, Dr. R. Godard, Dr. K. Urashima, Dr. Ohyama, and Y. Kawada for valuable comments and discussions. I would like to thank C. Gies for the help with administrative aspects of my studies.

I really enjoyed studying in a very comfortable environment created by A. Jovicic, N. vonStyp-Rekowski, F. Rong and C. del Perugia in the power research lab.

Finally, I am grateful to my husband for his great patience and love, as well as to my parents, in-laws and friends for their support and understanding.

TABLE OF CONTENTS

LIST OF FIGURES

LIST OF TABLES

NOMENCLATURES

α, β		Variables depending on pulse frequency and pulse width
α^*_i		Ion sink constant
α^*_{cd}		Charged dust source constant
α_g		Void fraction
ε_o	$[F/m]$	Electric permittivity of free space $\varepsilon_o = 8.85419 \times 10^{-12}$ $[F/m]$
ε_p		Relative dielectric constant of dust particle
η	$[\%]$	Collection efficiency of dust particle
κ		Effective Knudsen number $(\kappa \cong Kn)$
λ_i	$[m]$	Mean free path of ions
$\lambda_{Di}, \lambda_{Dd}$	$[m]$	Ion and dust Debye length
μ_i	$[m^2 V^{-1} s^{-1}]$	Mobility of ions
μ_d, μ_k, μ_{cd}	$[m^2 V^{-1} s^{-1}]$	Mobility of charged particles
μ_g	$[Pa\ s]$	Dynamic viscosity of the gas
ν	$[m^2/s]$	Kinematic viscosity of the gas
ρ_g	$[kg/m^3]$	Gas density
Ω	$[\Omega m]$	Dust particle resistivity
ρ_{gf}		Gas condition factor

τ_d		Characteristic diffusion charging time
τ_s	*[s]*	Characteristic field charging time in continuum regime
τ_f, τ'_f, τ_2		Dimensionless field charging time in a free molecule and transition regime
ω_{th}	*[m/s]*	Migration velocity
ω_p		Dimensionless electric field of particles
ξ		Dimensionless electric field
$\xi x, \xi y, \xi z$		Dimensionless electric field x,y, and z component
Φ, Φ_o		Dimensionless electric potential ($\Phi_o=eV_o/kT$)
Φ^*		Dimensionless electric potential ratio ($\Phi^*=\Phi/\Phi_o$)
Φ_p, Φ_{pd}, Φ_{pf}, Φ_i, Φ_s,		Dimensionless potential of the dust particle due to the diffusion charging, field charging, initial charge, saturation charge
c_o, c_1, c_2		Constant depending on the dust resistivity
c_{in}	*[m³]*	Particle concentration at the inlet of ESP
c_{out}	*[m³]*	Particle concentration at the exit of ESP
d_s	*[m]*	Length of the spike tip
d	*[m]*	Wire diameter
d_p	*[m]*	Dust particle diameter
e	*[C]*	Elementary charge ($e=1.602\times10^{-19}[C]$)
f_{EM}	*[N]*	Body force

$\boldsymbol{i}$		Field charging enhancement factor
k	$[J/K]$	Boltzmann constant ($k = 1.38062\times10^{-23}$ $[J/K]$)
m		Index
m_s, $m_{s\text{-}dc}$, $m_{s\text{-}fc}$		Number of elementary charges on the particle surface due to diffusion or field charging
m_i	$[kg]$	Ion mass
m_G		Discharge electrode factor
n_i		Dimensionless ion density
n_{nd}		Dimensionless density of neutral dust
n_{ncd}		Dimensionless density of charged dust
p	$[atm]$	Gas pressure
p_i	$[\%]$	Dust particle penetration
r_{in}	$[m]$	Inner diameter
r_{out}	$[m]$	Outer diameter
r_o, r_p	$[m]$	Radius of dust particle
t	$[s]$	Charging/exposure time
u_g	$[m/s]$	Average gas velocity
u_m	$[m/s]$	Theoretical migration velocity of charged particle
$\overline{v}_i$	$[m/s]$	Mean thermal velocity of ions ($\overline{v}_i = \sqrt{8kT/\pi m_i}$)
x, y, z	$[m]$	x, y, and z coordinates

x'		Normalized horizontal position $(x'=x/d_s;\ -0.5 \leq x' \leq 0.5)$ with respect to the length of the spike tip (d_s).
x^*, y^*, z^*		Dimensionless x, y, and z coordinates
A	$[m^2]$	Surface area
A_f		Correction function
A_o		Slip correction factor
A_{probe}	$[m^2]$	Surface area of current probe
C_m		Cunningham correction factor
C_p	$[C]$	Particle capacitance $(C_p = 4\pi\varepsilon_o r_p\,[C])$
D	$[m]$	Plate-to-plate spacing
D_{bi}, D_{bd}		Ion and particle Debye numbers
D^*_{bi}, D^*_{bd}		Ion and particle Debye ratio
D_k, D_i, D_{cd}, D_{nd}	$[m^2/s]$	Diffusion of species, ion, charged dust, neutral dust
De		Deutsches number
E, E_o	$[V/m]$	Modulus of the external electric field
E_i	$[V/m]$	On-set electric field
E_{hd}		EHD number
F	$[N]$	Forces acting on dust particles
F_E		Electric field number
I_T	$[A]$	Total discharge current
J	$[A/m^2]$	Current density

J_{probe}	$[A/m^2]$	Probe current density
K		Constant
K_G		Constant· depending on the collecting and discharge electrode geometry
K_d		Constant· depending on the dust loading
K_g		Constant· depending on the gas parameters
Kn		Knudsen number $(Kn=\lambda_i/r_p)$
K_o	$[s^{-1}]$	Characteristic diffusion charging constant
L	$[m]$	Characteristic length (wire-plate distance)
M		Mach number
N_2		Nitrogen molecule
N_3O^+, $N_2O_2^-$		Nitrogen oxide ions
N_i	$[m^{-3}]$	Ion density
N_{io}, N_{do}	$[m^{-3}]$	Initial number of ions (N_{io}) or dust (N_{do})
N_{cd}	$[m^{-3}]$	Charged dust density
N_i	$[m^{-3}]$	Ion density
N_{in}	$[m^{-3}]$	Number of dust particles at the inlet of ESP
N_{out}	$[m^{-3}]$	Number of dust particles at the outlet of ESP
O_2, O^+, O_2^-		Oxygen molecule, ions
Q_o	$[C]$	Initial charge on the surface of dust particle ($Q_o=eN_o$)
Q_{fc}	$[C]$	Particle charge due to field charging ($Q_{fc}=eN_{fc}$)

Q_g	$[m^3/s]$	Flow rate of a main gas
Q_s	$[C]$	Saturation charge due to field charging
Ra_i		Ion diffusion Reynolds number
Ra_{cd}		Charged dust diffusion Reynolds number
Re		Reynolds number
S_{io}		Ion speed ratio
Sc_i		Ion Schmidt number
T_g	$[K]$	Gas temperature
U_g	$[m/s]$	Gas velocity
U_i	$[m/s]$	Drift velocity of ions
U_{ik}	$[m/s]$	Relative drift velocity between ions and dust particles
U_o	$[m/s]$	Mean gas velocity
U_x	$[m/s]$	x-component of gas velocity
U_y	$[m/s]$	y-component of gas velocity
U_z	$[m/s]$	z-component of gas velocity
V	$[V]$	Applied voltage
V_i, $V_{on\text{-}set}$	$[V]$	Corona on-set voltage
Y	$[m]$	Collecting electrode length
W	$[m]$	Wire-to wire distance

ABBREVIATIONS

ac	Alternating Current
CE	Collecting Electrode
CNPC	Condensation Nucleation Particle Counter
CWD	Canada-Wide Standards
dc	Direct Current
DE	Discharge Electrode
ESP	ElectroStatic Precipitators
EHD	Electro-HydroDynamic
ESEM	Environmental Scanning Electron Microscopy
F_G	Gravitational Force
F_JR	Johnsen-Rahbek Force
F_QE	Electric Force
F_T	Thermophoretic Force
F_VdW_ps	Van der Waals Force between Particle and Substrate
F_VdW_pp	Van der Waals Force between two Particles
FTIR	Fourier Transform Infrared Spectroscopy
HW	Helical or spiralling Wires
NA	Not Available
NAA	Neutron Activation Analysis

NS	Navier Stokes
PN	Plate with Needles
PSSF	Particle Size Separation Filters
RDE	Rod with Emitters (rigid-type)
RNS/RNP	Rod with Needles Arranged in Staggered or Parallel way
RR	Rectangular Rods
SEM	Scanning Electron Microscopy
SS	band-type with spikes or Serrated Strip
SSR	Star Shaped Rods
SW/ SR	Smooth Wires or Rods
TEM	Transmission Electron Microscopy
TR	Threaded Rods
TS	Twisted Square
TSP	Total Suspended Particulate
XR	Rod with cross arranged needles

CHAPTER 1

INTRODUCTION

1.1 BACKGROUND

1.1.1 Particulate Matter Health Related Issues

Several scientific studies [1-5] have linked particulate matter (PM) emission with a wide range of health-related disorders resulting in daily mortality, respiratory and cardiovascular hospitalizations, adverse impaired lung function, etc. Recent investigations by the Ontario Ministry of the Environment provided a list of pollutants and their effect on human health [4]. Table 1.1 shows the effect of some pollutants on the premature death and hospital admissions in the Hamilton-Wentworth area [6].

Particles larger than $10\ \mu m$ in diameter are of little health concern since they are mostly caught by mucus in the nose and throat and can be cleared out of the body. Particles smaller than $10\ \mu m$ (PM_{10}) fall into two categories, with the threshold diameter around $2.5\ \mu m$ ($PM_{2.5}$). The coarse fraction or inhalable particles, between 2.5 and $10\ \mu m$ in diameter, settles in the bronchial tubes, and can cause various health impacts. Recently, it was observed that respiratory particles smaller than $2.5\ \mu m$ in diameter, have the greatest impact on health since they can penetrate deeply into the lungs [5]. The problem is complicated, since the PM may contain various toxic compositions and there is no known threshold concentration below which exposures represent no health risk.

Table 1.1
Human health effects of pollutants in Hamilton-Wentworth [6]

Pollutants	**Premature Death**	**Hospital Admissions**
PM_{10}	85	150
Sulphates	50	190
Ground Level Ozone	5	50
Sulphur Dioxide	40	30
Nitrogen Oxides	0	40
Carbon Monoxide	0	20

1.1.2 Canadian and Worldwide Particulate Matter Regulations and Strategies

Current scientific understanding of the health effect of particulate matter has advanced PM emission regulations based on the particulate matter size. The existing Canadian government ambient air quality standard for the total suspended particulate (TSP) was revised, too. The national TSP acceptable level was *120* $\mu g/m^3$ and *70* $\mu g/m^3$ based on *24-hour* and annual averaging, respectively. In June 2000, the Government of Canada, the provinces and territories, except Quebec, proposed new Canada-Wide Standards (CWD) for PM. The CWD standard sets the ambient air quality concentration target of *30* $\mu g/m^3$ for fine particulate matter $PM_{2.5}$ by the year 2010. $PM_{10}/PM_{2.5}$

standards and objectives worldwide are shown in Table 1.2. These recent emission standards and objectives require development of advanced new, or modifications of existing electrostatic precipitators.

Table 1.2
$PM_{10}/PM_{2.5}$ current standards, target levels and dates [1, 7, 8]

Country	PM_{10}/ $PM_{2.5}$	Limits
Ontario	PM_{10}	50 μg/m^3; 24-hour limit
Canada	$PM_{2.5}$	30 μg/m^3; 24-hour limit (98th percentile measurement 3 years average)
USA	PM_{10}	150 μg/m^3 ; 24-hour limit 50 μg/m^3; annual limit
	$PM_{2.5}$	65 μg /m^3; 24-hour limit; by 2015 15 μg /m^3; annual limit
EU	PM_{10}	50 μg/m^3; 24-hour limit; by 2005; (not to be exceeded 25 times/year) 30 μg/m^3; annual limit
	$PM_{2.5}$	50 μg /m^3; 24-hour limit; by 2010; (not to be exceeded 7 times/year) 20 μg /m^3; annual limit
Australia	PM_{10}	50 μg /m^3 ; 24-hour limit
	$PM_{2.5}$	25 μg/m^3 ; 24-hour limit
Hong Kong	PM_{10}	180 μg/m^3 ; 24-hour limit 55 μg/m^3; annual limit
Sweden	TSP	100 μg/m^3 ; 24-hour limit
UK	TSP	50 μg/m^3 ; 24-hour limit
South Africa	TSP	50 μg/m^3 ; 24-hour limit

Table 1.2 (continued)

Country	**PM_{10}/ $PM_{2.5}$**	**Limits**
Japan *	TSP	50-150 μg/m^3; (depending on size of coal fired boiler)
Korea *	TSP	50-150 μg/m^3; (depending on size of coal fired boiler)
China *	TSP	200 μg/m^3; (power industry standard)
Mexico	TSP	150 μg/m^3 ; 24-hour limit

PM_{10} and $PM_{2.5}$...particulate matter less then *10* and *2.5 μm* in diameter; TSP... total suspended particulate; *...industry dependent limits available.

1.1.3 Major Sources of Particulate Matter in Canada

In addition to strengthening the PM emission standards, the governments in North America have also prompted industry to develop strategies for reduction of particulate matter emissions. One of the first steps was development of monitoring stations in order to identify the PM emission sources. The major sources of PM in Canada are natural sources, industry, transportation and transboundary states. Natural sources such as agricultural tilling, forest fires, and dust from paved and unpaved roads are major sources of PM in some provinces. US transboundary industry is one of the major sources of PM in southern Ontario. In order to reduce emissions from US transboundary states the Canada-United States Air Quality Agreement was achieved in 1991. The particulate emission sources of Canadian industries are shown in Figure 1.1.

Roughly, they are divided into industrial processes, fuel combustion, transportation, and other processes. The industrial processes include coal mining, iron mining, grain/rock mining, aluminum smelting, steel smelting, asphalt paving, cement/concrete production, chemical production, petrochemical processes, pulp/paper processing, wood production and other processes. The major $PM_{2.5}$ industrial process source is the wood industry with *12 %* of total emissions. Pulp and paper contributes *9.3%* to total emissions, while the steel industry contributes around *3.5 %.* Fuel combustion sources which include electrical utilities, commercial and residential fuel combustion, residential sources, mainly from wood combustion, contribute *37 %* to total emissions. Transportation sources such as air flights, heavy duty vehicles, light duty vehicles, marine, rail and off-road transportation, contribute only *20 %* to the total emission with the highest contributions from heavy duty transportation of *7 %.*

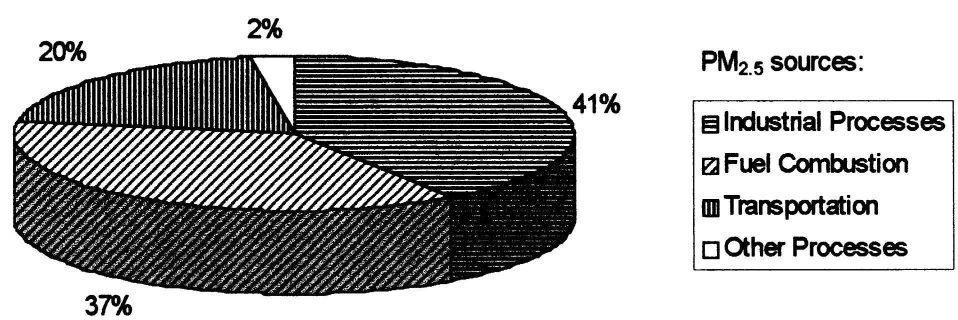

Figure 1.1 Canada particulate emissions, industry sources for $PM_{2.5}$ for 1995 [9]

The electrostatic precipitator (ESP) is one of the devices used for the removal of suspended particles from the gas. The ESPs separate dust particles from the main gas flow, based on the principle of electrostatic force acting on the charged dust particle.

Electrostatic precipitators (ESPs) have been used in various industries such as coal-fired power plants, steel, cement, and paper manufacturing, food processing, etc., and in commercial and home ventilation systems. Compared to other mechanical dust particle separation devices, ESPs are highly efficient for a wide range of particle sizes, can handle high gas flow rates with only a relatively low pressure drop, and have low operating costs. The characteristics of some typical dust collection devices are shown in Table 1.3.

Table 1.3
Comparison of dust particle separation devices [10, 11]

Dust Collection System	Effective for Dust Particle Size	Pressure Drop	Gas Flow Velocity	Operational Cost
Gravitational	> 100 μm	low	< 0.1 m/s	low
Cyclone	> 1 μm [11] > 10μm [10]	medium	1-2 m/s	medium
Impact	> 10 μm	medium	< 50 m/s	low
Bag Filter	Depending on the filter material >0.01 μm	depending on operational time	< 0.05 m/s	high
Packed Bed	> 0.1 μm	high	~0.05 m/s	high
Wet Scrubbers	0.2 μm [11] > 0.02 μm [10]	high	< 2 m/s	high
Dry ESPs	> 0.01 μm	low	0.5-2 m/s	low
Wet ESPs	> 0.01 μm	medium	0.5-2 m/s	high

1.2 TYPES OF ELECTROSTATIC PRECIPITATORS AND PRINCIPLE OF OPERATION

1.2.1 Principle of Operation

There are five fundamental steps in the operation of electrostatic precipitators, as shown in Figure 1.2. These are corona discharge, particle charging through combined diffusion and field charging, particle transport by electrical and gas flow forces, formation of the dust layer on the collecting electrode, and removal of collected dust by rapping techniques. In general, the discharge electrode is connected to the high voltage power supply, while the collecting electrode is grounded. The high electric field in the vicinity of a discharge electrode causes ionization of the gas molecules, known as a corona discharge. Ions are then moving along the electric field lines towards the collecting electrode. On their way to the collecting electrode they may attach to the surface of the suspended dust particles by diffusion or field charging mechanism. Field charging occurs due to the bombardment of the dust particle surface by ions that are moving under the influence of the electric field. Diffusion charging occurs due to the attachment of the ions to the surface of the dust particle diffusing in accordance with the laws of gas kinetic theory. After that, the charged particles will move towards the collecting electrode due to the introduced electrical force. Once the charged particles reach the collecting electrode, they will transfer their charge to collecting electrode and form a dust layer that will be further removed to the hopper by some of the dust removing techniques.

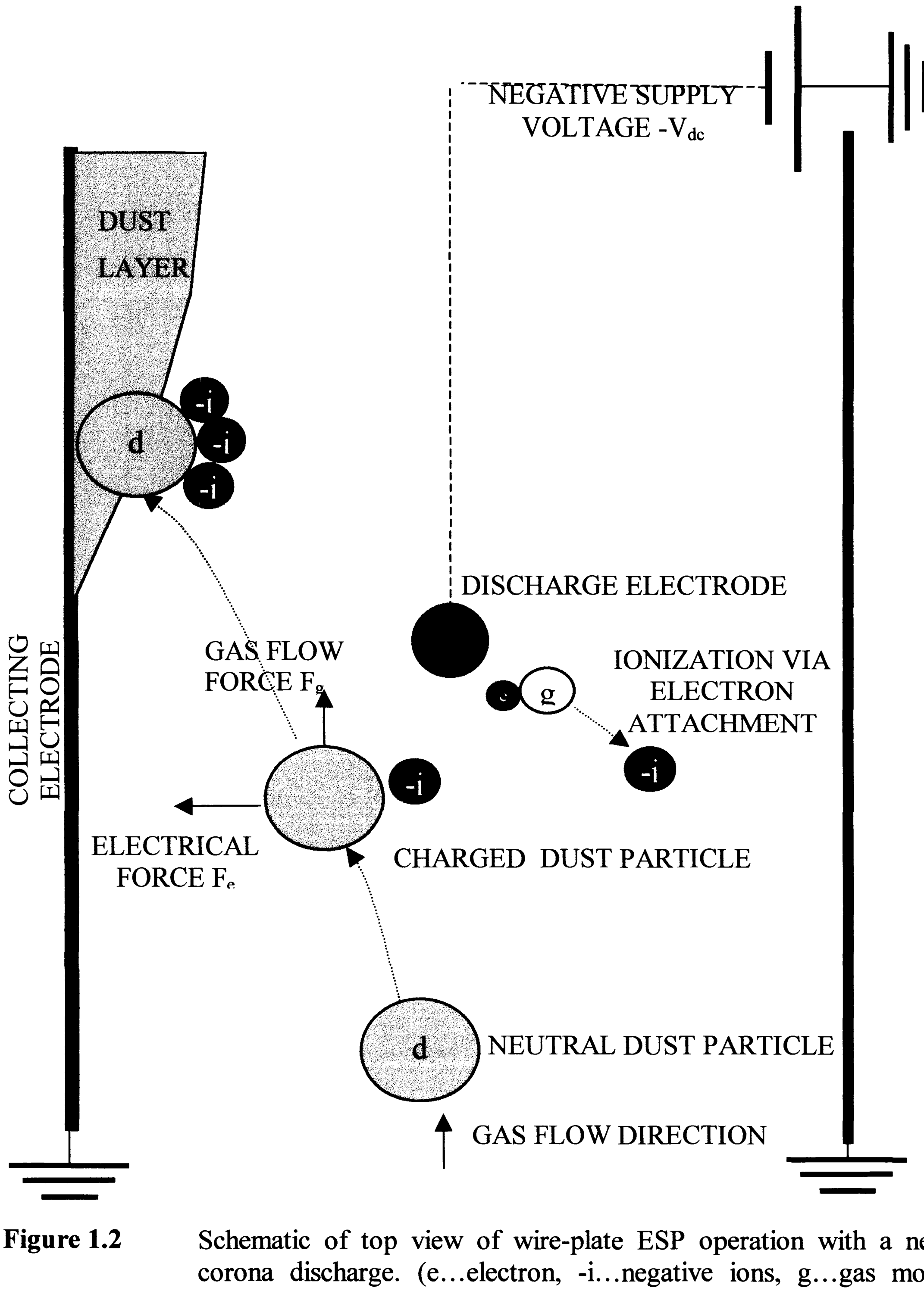

Figure 1.2 Schematic of top view of wire-plate ESP operation with a negative corona discharge. (e…electron, -i…negative ions, g…gas molecule, d…dust particle)

1.2.2 Types of ESP

The design of electrostatic precipitators (ESPs) depends on their application area and can be classified in several groups. According to the overall field geometry ESPs can be classified as wire-pipe (See Figure 1.3), wire-plate (See Figure 1.4), and wire-duct type of ESPs. Different geometries of discharge (See Figure 1.5) and collecting (See Figure 1.6) electrodes can be used. Most common discharge electrodes, are smooth wires and rigid-type. Most common collecting electrode is G-type. With respect to the electrode arrangement, ESP's can further be classified as single stage or two stage ESPs. In a single stage ESP charging and collection of particles occurs simultaneously, whereby in two stage ESPs those processes are separated. Accordingly a two-stage ESP consists of the precharger section and collection section. Common precharger geometries are wire-plate, wire-rod and quadrupole wire-rod geometries. Common collecting geometry is plate-plate geometry. Depending on the type of the applied discharge electrode voltage, ESPs can be electrically energised by negative or positive dc, short pulse, or an intermittent type of applied voltage. According to the direction of gravitational force with respect to the main gas flow, ESPs can be classified as vertical or horizontal. Sometimes gas conditioning with water may be used to enhance the dust collection efficiency of very fine or high resistivity dust particles. Accordingly, electrostatic precipitators can be classified as dry or wet ESPs.

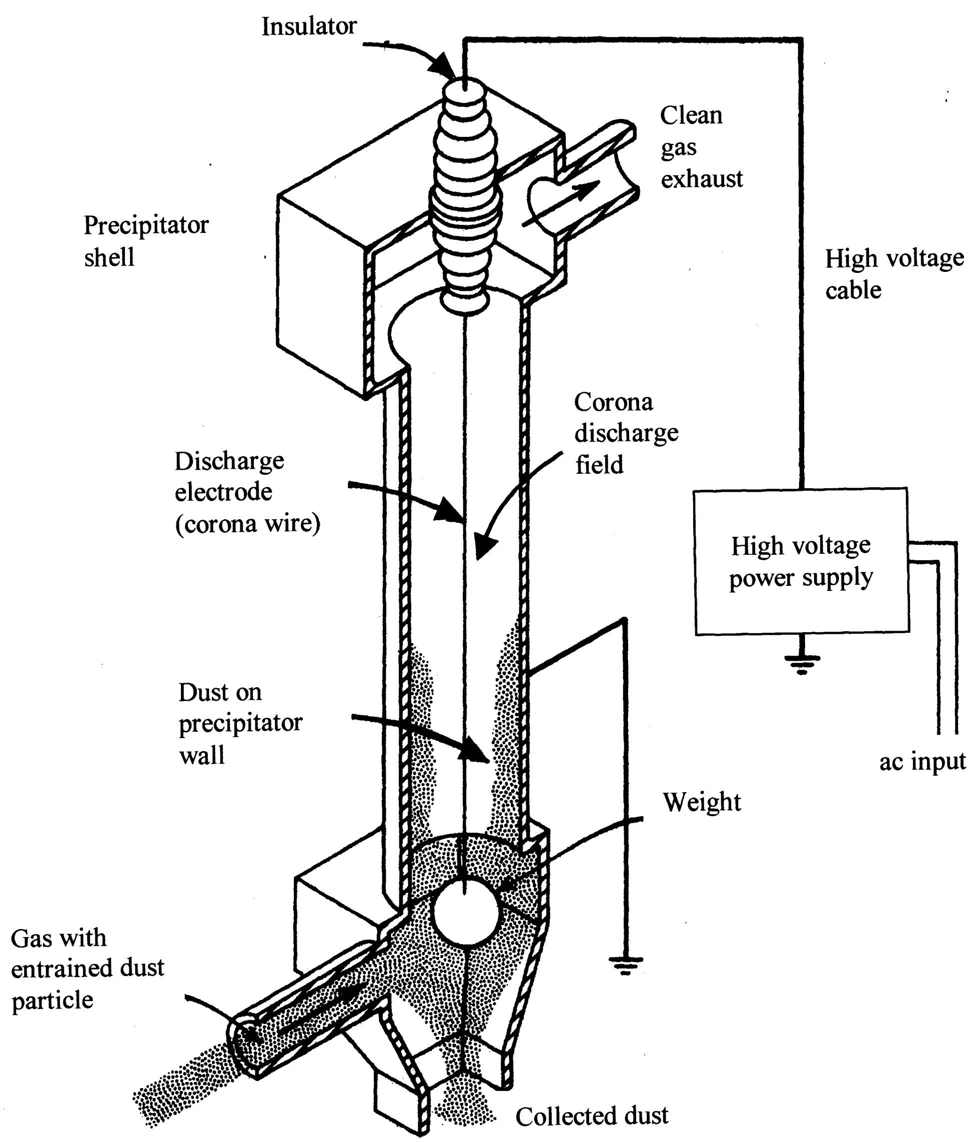

Figure 1.3 Typical cylindrical-type ESPs with vertical gas flow (modified from [12])

a)

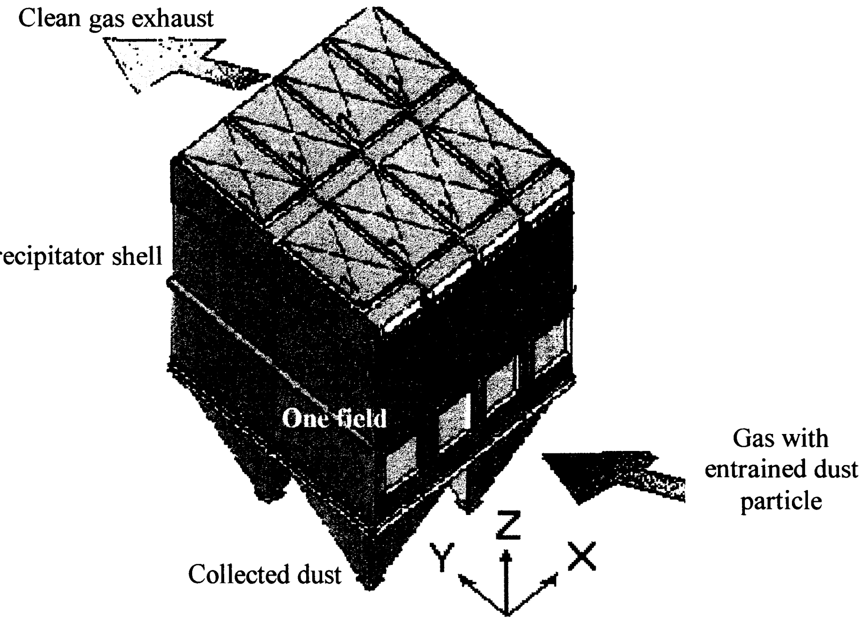

b)

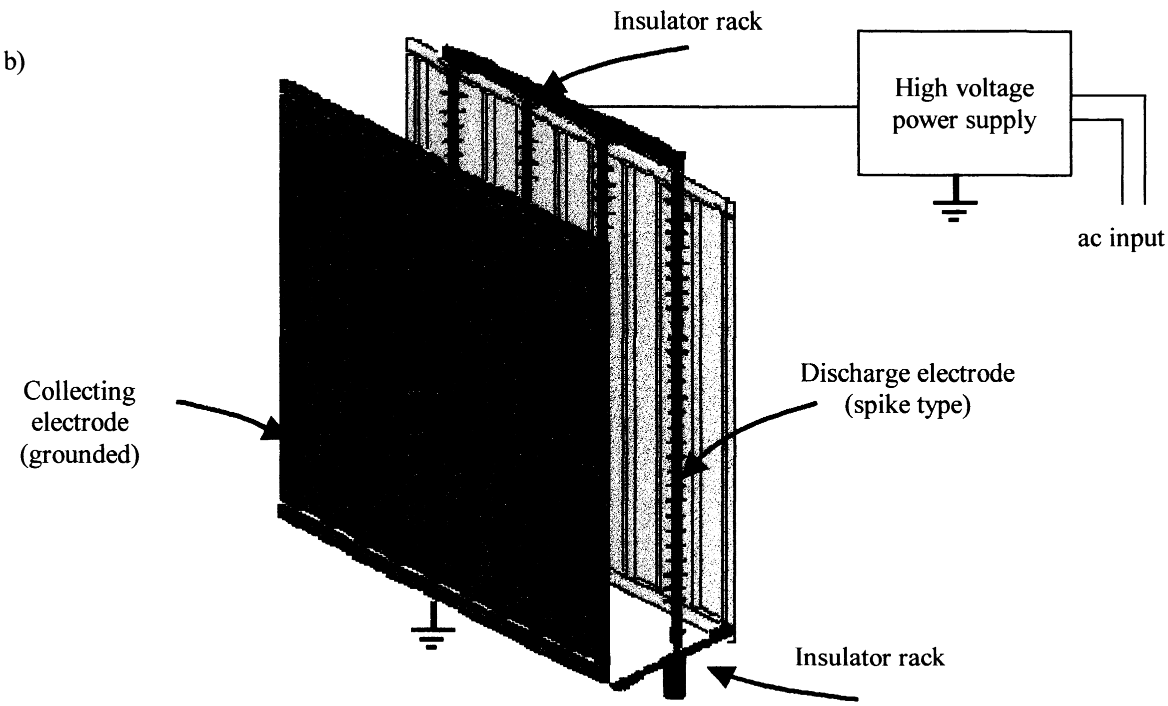

Figure 1.4 Typical wire-plate type ESPs with horizontal gas flow
(a) whole ESP structure consisting of sixteen fields, and
(b) one field structure containing four discharge electrodes.

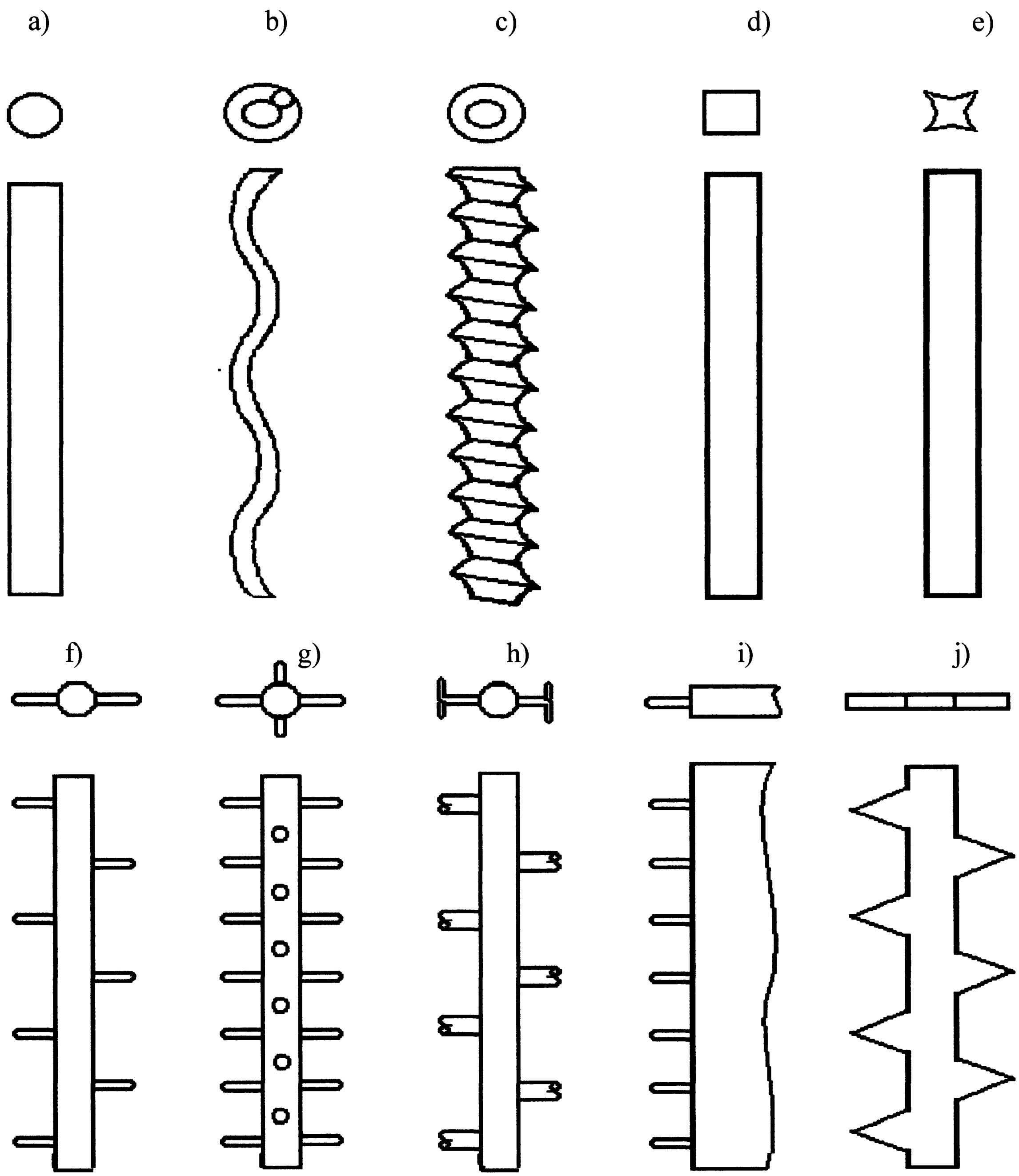

Figure 1.5. Typical discharge electrode (DE) geometries used in ESP: (a) smooth wires (SW) or rods (SR), (b) helical or spiralling wires (HW), (c) threaded wires and rods (TR), (d) rectangular rods (RR)or twisted square (TS), (e) star shaped rods (SSR), (f) rod with needles arranged in staggered (RNS) or opposing way (RNP) (shown is staggered arrangement), (g) rod with cross arranged needles (XR), (h) rod with emitters (rigid-type) (RDE), (i) plate with needles (PN), and (j) band-type with spikes (SS) (serrated strip). (Modified from [12])

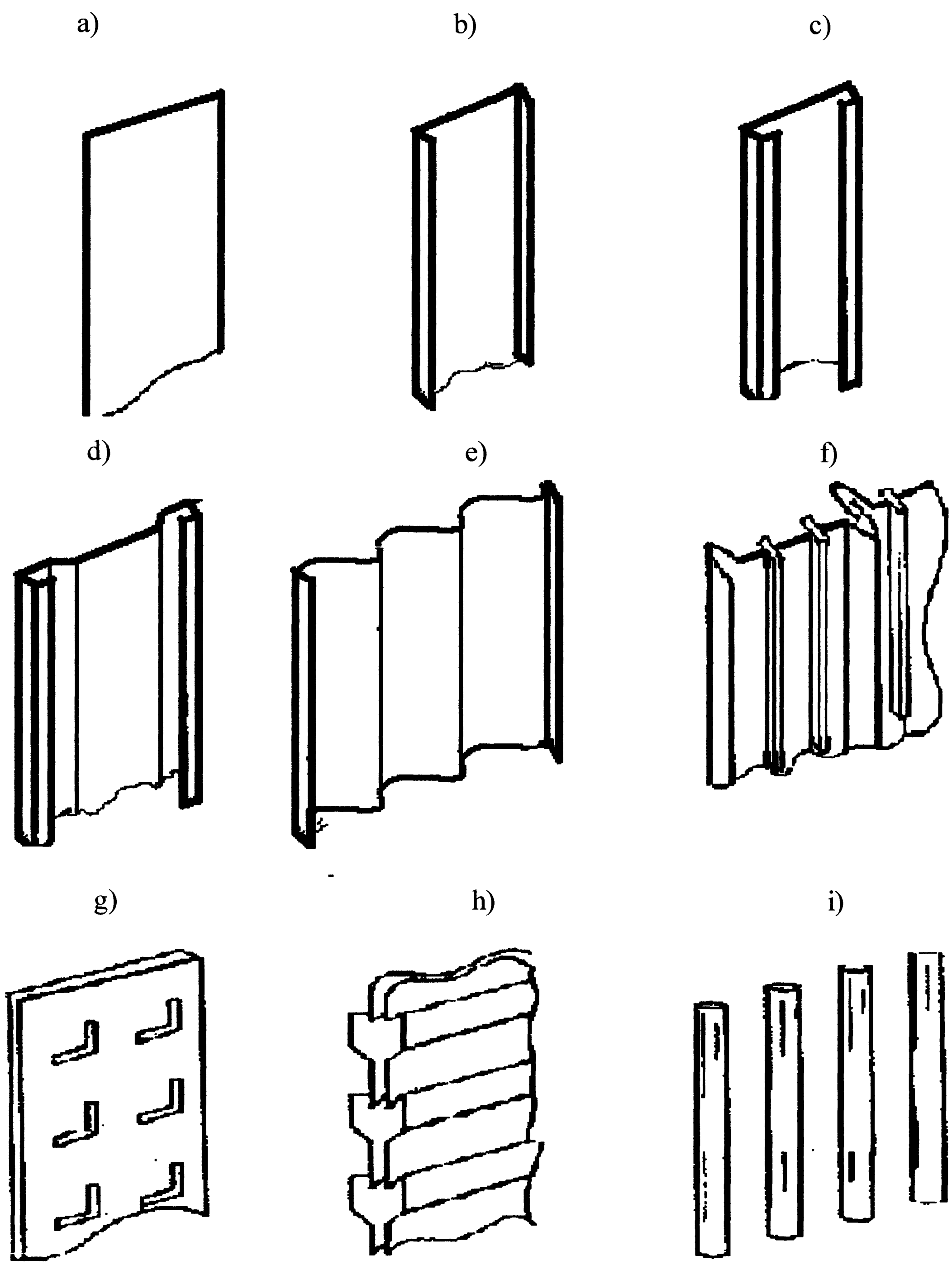

Figure 1.6. Typical collecting electrode (CE) geometries used in ESP: (a) smooth plate or I-type, (b) U-type, (c) C-type, (d) G-type or sometimes referred as Z-type, (e) sine-wave-type, (f) fence-type, (g) plate with L-pockets, (h) plate with tulip pockets, (i) rod curtain.

1.2.3 Historical Background of ESPs Development

The electrostatic precipitation of dust particles was known back in the 19^{th} century, after Sir Oliver Lodge installed the first industrial unit in 1883 [13, 14]. The discovery was almost forgotten until 1906, when Federick G. Cottrell demonstrated the collection of sulphuric acid mist with ESP powered by rotary switch rectifiers. Since that time, the objective has been to improve the collection efficiency by various techniques. The back corona discharge associated with high resistivity fly ashes represented major problem in ESP design for years. In 1970's the ESPs with wide plate spacing had been investigated experimentally by several authors [15-19], that reported improved collection efficiency, decreased steel consumption and pressure drop with installation of wide-plate spacing. Approaches such as gas temperature reduction, amines and SO_3 injection, were not very competitive with bag filter technology until the improved collection efficiency of high resistivity fly ashes with application of pulsed energization was reported by Masuda et al. [20, 21]. The results were confirmed on industrial scale ESPs by Dinelli et al. [22]. Several following years the research was oriented to investigation, development and control of various type of energization. After that, the research interest moved to the investigation of the gas and particle flow. Yamamoto and Velkoff [23] pointed out the influence of electrohydrodynamically-induced secondary flow (EHD) on fine-particle collection. These initial investigations attracted interest and other workers started to make contributions. Parker and Hughes [24], Adachi [25], and Kallio and Stock [26] studied the EHD flow by visualization techniques. Additionally, Atten et al [27], Adachi et al. [28, 29], and Watanabe [30] studied the effects of EHD flow on the motion of the fly-ash particles with the aid of computer simulations for wire-plate ESPs. Whenever a low corona on-set voltage was preferred, discharge electrode geometries with needles and sharp-edge were utilized. Imposed by new particulate matter emission regulations, today's research focus is on the collection efficiency of submicron and ultrafine dust particles.

1.3 METHODS FOR IMPROVEMENT OF COLLECTION EFFICIENCY OF SUB-MICRON AND ULTRAFINE DUST PARTICLES

Most of the present ESPs are designed based on the past emission regulations with overall mass based collection over *99 %*. However, the collection of dust particles from the submicron-size range was observed to be as low as *60-80 %* [31, 32]. Additionally, the collection of particles below *30 nm* is below *50 %* [31, 32] due to a majority of particles being uncharged [32]. With the adoption of the new $PM_{2.5}$ standard there is a new interest in the efficient capture of submicron and ultra-fine dust particles. Several approaches, briefly discussed in this section, are based on the principle of: (a) dust particles preconditioning by means of mechanical or chemical agglomeration of particles, (b) surface charge enhancement by new charging methods or improved corona charging with precharges, (c) new and hybrid devices such as a thermal precipitator, electret filters, wet-electrostatic precipitators and vortex scrubbers, and (d) new ESP designs including new geometries and optimization of existing designs.

Preconditioning of dust particles include particle agglomeration by mechanical and chemical means. Agglomeration of particles when injecting chemical conditioning agents such as amines and SO_3 was observed as a secondary effect, while trying to reduce the back-corona problem and particle resistivity. It is believed that by improving the stickiness of the particles the agglomeration of particles is enhanced. Mechanical agglomeration by injecting charged or uncharged dust particles or water droplets was investigated by several authors. Test systems employed the agglomeration agent of much larger diameter and opposite charge than treated particles. By imposing acoustic agglomeration, the average size of the particles can be increased to the point where the conventional ESP is efficient. From pilot-scale studies [33-35] it is still unclear what the optimum acoustic frequency range for particle agglomeration is. Some studies showed faster agglomeration at $44\ Hz$ [34]. On the other side, Nakane et al. [33] showed experimentally that the collection efficiency in a wire-cylinder configuration at a main gas velocity of $0.75\ m/s$ and for a diluted particle size range of $0.3\text{-}0.5\ \mu m$ can be improved from 99.14 to $99.98\ \%$ by means of a $22\ kHz$ ultrasonic vibrator. In addition to high equipment costs, one of the drawbacks of the acoustic agglomeration is the difficulty to penetrate into larger gas and particle volumes. For the electrostatic agglomeration of submicron particles, the charge and size of agglomeration agents has to be large compared to submicron particles [36]. Ohkubo et al. [37] studied agglomeration of two oppositely precharged particle plumes in an electric field of approximately $2.5\ kV/cm$. As a result, the concentration of submicron size range of dust particles has been lowered from $75\ \%$ to $18\ \%$. They showed that the rate of agglomeration was dominated significantly by the precharging voltages with the best performance for a positive charging voltage of $7\ kV$ and negative charging voltage of $-5.8\ kV$. Agglomeration of submicron particles under an ac external electric field has showed almost two times higher agglomeration compared to that under dc electric fields, as shown by Koizumi et al. [36].

The electron charging [38, 39], photo-charging including UV [40] and soft X-rays irradiation [42], and pulsed charging are proposed as a means of enhancement of particle surface charges. The photo-electric charging by using UV irradiation has limited successes [40]. It was experimentally observed that higher dust loadings lead to reduction of the mean particle charge from *9* to *5* elementary units due to the bipolar charge distribution [41]. Enhancement of collection efficiency of ultra-fine particles *(0.02-0.6 μm)* while irradiated with X-rays *(*energy level range *3.5-9.5 keV* and wave length of λ*=0.13-0.41 nm)* under positive corona showed better performance than for operating conditions including: (a) X-ray with negative corona, (b) X-rays only, and (c) negative/positive dc corona only, as reported by Kulkarni et al. [42]. Originally, a short pulsed type energization (voltage rise of microsecond order) was used to improve collection efficiency of high resistivity dust, as shown by Masuda et al [20, 21]. Based on the fractional collection efficiency of full-scale ESP, Dinelli et al. [22] observed better collection efficiency of fine particulate matter ($d_p < 5\ \mu m$) under pulsed energization than under conventional energization. This may be attributed to the fact that a pulsed discharge penetrates deeper into inter-electrode space with higher electron energy than dc discharge, thus leading to better particle charging. Zukeran et al. [43] examined fractional collection efficiency of two particle size groups (*0.01-0.1 μm* and *0.1-20 μm*) under dc and short-pulse type energization. Results showed that at low dust loadings the collection efficiency of both particle size groups is better with dc than with pulsed energization. At high dust loadings, the collection efficiency of *0.01-0.1* μm particles is much higher under short-pulsed energization than under dc energization. For *0.1* to *20* μm dust particles, during either high or low dust loading conditions, the collection efficiency was better with dc then with short-pulse energization. The reason for this selective behaviour of short pulsed-type energization with respect to the different particle sizes at different dust loadings still stays unresolved.

Electret filters [44], special type of bag filters with electrically charged fibres, provide high initial collection efficiency in the range from (*80-95 %*) for particle size range between *0.05* and *5* μm. However, the results for the long-term operations in case of charged dust particles showed a sharp decrease in collection efficiency, reaching values comparable to those for uncharged filters. Contrary to this, when collecting uncharged dust particles, the initial collection efficiency was lower, followed by a further drop in collection efficiency. A filtration time progressed however, the collection efficiency improved. The major drawbacks of that technology are increased pressure drop, small volume applications, and high operating/maintenance costs. Particles in the range from *(0.001-0.1*μm*)* are strongly influenced by thermophoresis force [45]. However, the major drawback is required high temperature gradients [45-47] that would require implementation of cold collecting electrodes. Risk of a water-pollution is still a major drawback for ionizing wet scrubbers or wet-type ESPs [48, 49].

The improvement of collection efficiency of submicron and ultra-fine particulate matter based on the ESP geometry modifications is still a very desirable solution because of its influence on the size, capital, and running cost of the ESP unit. Therefore, the review of previous experimental and theoretical work will be emphasized on the collecting and discharge electrodes and their effect on the collection efficiency. The electrical aspects such as current-voltage curve and current density distribution on the collecting electrodes and main gas flow modification due to the EHD induced secondary flow has been investigated for various electrode geometries, and will be discussed briefly in Chapters 2, 3, and 5.

1.3.1 Previous Experimental Work on Discharge and Collecting Electrode Effect

Papers summarized in Table 1.4 were categorized based on : (a) size of ESP; (b) discharge electrode type, (c) collecting electrode type, (d) dust particle size, (e) flow velocity, (f) type of applied voltage, and (g) collection efficiency estimations.

Table 1.4

Categorization of experiments with emphasis on effect of discharge and collecting electrode geometries on collection efficiency in wire-plate ESPs

Author	CE Width × Length × Height [m]	CE Shape	DE Shape/ Number of DE in a field	Particle Size [μm]	Flow Regime: Laminar/ Turbulent	Applied Voltage Type/ Range [kV]	Measured Variable and Applied Method for Collection Efficiency Calculation
Jedrusik et al. [50]	0.2× 1.5× NA	I	RDE; SS	10-100	Turbulent	dc	Estimated migration velocity from the particle trajectories.
Pajak [51]	(0.3-0.48) ×NA×NA	G	RDE (A-D)	N.A.	Turbulent	dc	Inlet and outlet mass concentration
Watanabe [30]	0.25× 1× 0.5	I	∅ 3mm SW	15	Turbulent	-dc [62.5]	Particle trajectories analysis obtained by stroboscope and camera

Table 1.4 (continued)

Author	CE Width × Length × Height [m]	CE Shape	DE Shape/ Number of DE in a field	Particle Size [μm]	Flow Regime: Laminar/ Turbulent	Applied Voltage Type/ Range [kV]	Measured Variable and Applied Method for Collection Efficiency Calculation
Miller et al. [52]	(0.2-0.4) ×2× 0.4	I	BR/13	Mean diameter ≈6	NA	-dc	Fractional collection efficiency
Self et al. [53]	0.05× 0.5× 0.25	I	∅0.1, 0.89 mm SW	4	Laminar	±dc	Particle concentration by rationing the pulses of scattered light of particles illuminated by He-Ne beam during ON and OFF ESP modes.
Howe and Houlgreave [54]	0.3× 4.5× 0.35	I	∅6 mm SW ; 6 mm TS ; 25×1.5mm SS /15	5μm (50%); 2.5μm (25%)	Turbulent	-dc [60-65]	Inlet and outlet mass concentration
Kim and Lee [31]	(0.1-0.4) ×0.75× 0.3	I	∅{1,2,3,4} mm SW /7	4	Turbulent	-dc	Inlet and outlet mass concentration
Davidson and McKinney [55]	0.15× 0.9× 0.6	I	∅1.6mm SW/6; BP (A-C)	0.5-10	Laminar	dc	Visualization of flow gas by Ar-Laser
Parker and Huges [24]	0.3× 0.9× 0.9	I	SW, TS, SS, SP	0.1-5	Turbulent	-dc [5-70]	Average transverse particle velocity by semi-empirical model derived from image analysis
Halldin et al. [56]	0.3× 2× 1	G	HW/10; RDE/4	0.18	Turbulent	IE	Particle velocity with LDV by Ar-Ion Laser
Yoo et al. [57]	0.45× 0.62×NA	I	∅0.1mm SW	0.03-0.2	Turbulent	+dc [12]	Number concentration at the outlet with power on/off modes
Present Work	0.05× (0.1-0.2)× 0.3	I	∅{0.25;1.5} mm SW, SS/1,2	0.01-20	Laminar	-dc [5-30]	Number concentration at the inlet and outlet.

DE…Discharge Electrode; CE…Collecting Electrode; dc…direct current; SW…Smooth Wire; HW… Helical Wire; SS…Serrated strip; TS…Twisted Square; RDE…Rigid-type Discharge Electrode; BR…Barbed Rod; SP…Smooth Plate; BP…Barbed Plate; IE…Intermittent Energization, LDV…Laser Doppler Velocity meter; NA…Not Available

Parker and Hughes conducted comparisons among serrated strip (spike or saw band), twisted square-wire, and flat plate based on the transverse or drift velocity of particles. The transverse velocity was obtained from a semi-empirical model based on the photographic recordings of the smoke plume induced isokinetically into the air flow. Results showed that the serrated strip electrode oriented parallel to collecting electrodes instead of their usual perpendicular orientation, imposed higher transverse or drift velocities on dust particles than the twisted square-wire.

Howe and Houlgreave [54] also obtained much higher collection efficiency within the first *1.6* metres of ESP length with serrated strip electrode compared to a smooth wire and twisted square as discharge electrodes. However, there is no discussion about the reduction of the effect in later sections of ESP after approximately *3* metres.

Miller et al [52] conducted lab-scale experimental studies with respect to the fractional collection efficiency of barbed-rod type discharge and I-type collecting electrode. The results showed that at same applied voltage, an increase in the barb length improves collection efficiency of $0,5\ \mu m$ dust particles from *86.7 %* to *94 %*, mainly due to the higher current. However, the shorter barbs showed better performance when comparing the electrodes at the same power, for which the shorter electrode has a higher electric field. The higher field seems to compensate for the smaller particle surface charge caused by the lower operating current. For the same input power, a higher electric field results from the higher operating voltage of shorter barbs compared to longer barbs. With respect to the barb spacing effect, only a small improvement of collection efficiency has been found, and the optimum distance was approximately *5 cm*. The fractional efficiencies results showed that the shorter collecting and discharge electrode spacings are favourable for submicron dust particle collection.

The full-scale plant installations of various barbed-rod type discharge electrodes placed between G-type collecting electrodes are examined by Pajak [51]. The barbs were oriented parallel to the collecting electrodes with staggered and non-staggered barb configuration, and of various barb length and barb spacing. Results showed that the barbed-rod with staggered barbs, barb length of *10 cm*, and barb spacing of *20 cm* in combination with G type collecting electrode (field length *0.5 m*, plate spacing *0.4 m*) has the highest collection efficiency.

Jadrusik et al. [50] compared rigid (barbed distance is *3 cm*) and spiked band (spike distance is *6 cm*) type discharge electrodes placed between I-type collecting electrodes. The collection efficiency was calculated over the estimated migration or drift velocity obtained from the particle trajectories. The spiked band electrode generates higher migration velocity in spite of the smaller current at same applied voltage. Additionally, very unusual particle behaviour was reported, i.e. increase of particle migration velocity with increased main gas velocity.

From the literature survey, two trends are noticed. One group evaluates ESPs based on the measured inlet and outlet dust concentration. The others, evaluates particle trajectories from the image analysis. Most experiments are conducted for the micron size particles. The exception is work by Yoo et al. [57] and Halldin et al. [56] that covers submicron and ultrafine particle range.

1.3.2 Previous Modelling Work on Discharge and Collecting Electrode Effect

Models for the prediction of the dust particle collection efficiency of electrostatic precipitators (ESPs) exist in many variations. In general, they can be divided into three major groups: lumped parameter, hybrid, and complex numerical models. The first group of models, denoted as the lumped parameter models, express the collection efficiency based on the modified Deutsch expression, whereby the quantities appearing in the expression are implicitly obtained, either from an experimental data set or by simplified theoretical expressions [58, 59]. Hybrid models [60-63] also utilize the modified Deutsch equation. However, they require complex numerical calculations for electric field, ion density profile, and particle surface-charge, in order to arrive at appropriate values for some variables in the Deutsch equation. The third group expresses the dust collection efficiency based on the dust density profile at the inlet/outlet of the ESP (Eulerian approach) or by predicting the particle trajectories (Lagrangian approach). Usually, complex numerical simulations are applied to find the electric field, gas flow, and ion and dust density distributions, with included dust charging models. The third group of models can be further subdivided according to the considered geometry, applied numerical methods, and complexity of the sub-models for the gas flow, electric field, corona discharge, dust particle charging, and dust collection. Some models are summarized in Table 1.5.

Lawless and Sparks [58] examined several ESP lumped parameter models such as Deutsch-Anderson, Matts-Ohnfeld, Cooperman, Robinsons, Southern Research, ESPVI 4.0 [63], and sectional model by Research Triangle Institute, and compared their predictions against the measured data. All those models have assumptions with respect to unmodelled effects, which appear as adjustable parameters whose values are determined implicitly or explicitly.

Table 1.5
Categorization of modelling papers
with emphasis on collection efficiency prediction

<table>
<tr><th></th><th>ESP Geometry</th><th>Electric Field</th><th>Ion Density</th><th>Particle Density</th><th>Flow Field</th><th rowspan="4">Collection Efficiency</th></tr>
<tr><th rowspan="3">Author</th><th>DxLxH</th><th>Domain</th><th>Domain</th><th>Particle Size. Charging Type</th><th>Domain</th></tr>
<tr><th>DE Type</th><th colspan="4">Type of Equation</th></tr>
<tr><th>CE Type</th><th colspan="4">Type of Applied Numerical Method</th></tr>
<tr><td rowspan="3">ESPVI 4.0 [63]</td><td>NA</td><td>2D</td><td rowspan="3">NA</td><td rowspan="3">Field Saturation Charge Q_∞</td><td rowspan="3">Average Velocity</td><td rowspan="3">Modified Deutsches</td></tr>
<tr><td>SW</td><td>Laplace</td></tr>
<tr><td>Smooth CE</td><td>Cooperman Equation</td></tr>
<tr><td rowspan="3">Lawless [64]</td><td>N.A.</td><td>1D</td><td>NA</td><td>NA</td><td rowspan="3">Average Velocity</td><td rowspan="3">Deutsches</td></tr>
<tr><td>SW</td><td>NA</td><td>NA</td><td>Field Charging</td></tr>
<tr><td>Smooth CE</td><td>Analytic Approx.</td><td>Analytic Approx.</td><td>Not Considered</td></tr>
<tr><td rowspan="3">Ohyama et al. [62]</td><td>NA</td><td>2D</td><td>2D</td><td rowspan="3">Field and Diffusion Charging</td><td rowspan="3">Average Velocity</td><td rowspan="3">Deutsches</td></tr>
<tr><td>SW</td><td>Laplace</td><td>Mobility</td></tr>
<tr><td>Smooth CE</td><td>Cooperman Equation</td><td>Finite Differences</td></tr>
<tr><td rowspan="3">Yamamoto [65]</td><td>NA</td><td>2D</td><td rowspan="3">Mobility</td><td>Saturation Charge</td><td rowspan="3">Approx. function for EHD flow</td><td rowspan="3">Outlet/Inlet Dust Concentration</td></tr>
<tr><td>SW</td><td rowspan="2">Poisson</td><td rowspan="2">Eulerian</td></tr>
<tr><td>Smooth CE</td></tr>
</table>

Table 1.5 (continued)

Author	ESP Geometry	Electric Field	Ion Density	Particle Density	Flow Field	Collection Efficiency
	DxLxH	Domain	Domain	Particle Size. Charging Type	Domain	
	DE Type	Type of Equation				
	CE Type	Type of Applied Numerical Method				
Gallimberti [66]	0.3×0.6	2D	2D	0.15-350 μm Diffusion & Field	3D turbulent κ-ε model without EHD for whole ESP and 2D simulation for one field	Outlet/Inlet Dust Concentration
	SW	Poisson	Mobility Diffusion	Eulerian. + Lagrangian. Convection Mobility and Diffusion		
	Smooth CE	Fin. Diff.	Fin. Diff	NA		
Cristina and Feliziani [67]	0.4×0.5	2D	2D	1-120 μm Saturation Charge	Analytic Approx. for main gas flow and EHD	Deutsches. It is not clear how particle density is obtained
	∅2.5mm SW	Poisson	Mobility	Not specific		
	C-type CE	Fin. Elm.	Fin. Diff.			
Soldati [68]	0.04×0.25 ×0.125	2D	2D	4-32 μm Saturation Charge	3D NS with EHD	Based on the particle trajectory simulation of 4000 particles.
	SW	P	Mobility	Lagrangian		
	Smooth CE	Fin. Diff.	Fin. Diff.	Num. Integration Explicit Method		
Canadas et al. [59] (PRELEC code)	0.4×(4×5)×1 4.5	2D	NA	0.13-80 μm Diffusion & Field	NA	Deutsches
	∅2.7mm SW	N.A		N.C.		
	Smooth CE	Mirror. Image		N.C.		
Levin [69] Levin and Hoburg [70]	0.22×0.076	2D	2D	15 μm Saturation Charge		Outlet/Inlet Dust Concentration
	3∅ 2mm SW	Poisson	Mobility	Eulerian, with Convection Mobility and Diffusion	Analytic Approx.	
	Smooth CE	NA	Don. Cell		Neglected	

Table 1.5 (continued)

Author	**ESP Geometry**	**Electric Field**	**Ion Density**	**Particle Density**	**Flow Field**	**Collection Efficiency**
	DxLxH	**Domain**	**Domain**	**Particle Size. Charging Type**	**Domain**	
	DE Type	**Type of Equation**				
	CE Type	**Type of Applied Numerical Method**				
Stock [71]	NA	1D	2D	1-10 μm Saturation Charge	Average Velocity	Deutsches
	SW	Analytic Approx.	Mobility	Eulerian		
	Smooth CE		Fin. Diff.			
Self et al. [53]	NA	2D	NC	4 μm Saturation Charge	NA	Outlet/Inlet Dust Concentration
	SW	Analytic Approx.		Eulerian		
	Smooth CE					
Choi and Fletcher [72]	0.2×0.45	2D	2D	2 μm Field Charging	Two-layer model for viscosity affected and turbulent region	Solves for particle trajectories. Then computes particle mass concentration and charge density.
	∅2mm SW	Poisson	Convection Mobility Diffusion	Lagrangian; Convection Mobility and Diffusion		
	Smooth CE	NA	Fin.Vol.			
Riehle and Loffler [73]	NA	2D	NA	0.1-10μm Saturation Charge	NA	Outlet/Inlet Dust Concentration
	SW	Poisson		Eulerian.		
	Smooth CE	NA				
Lu and Huang [74]	0.23×0.15	2D	NA	0.005-10μm Saturation Charge	Average Velocity	Dust concentration of polydisperse dust particles
	SW	Poisson	Mobility	1D, Not specific		
	Smooth CE	FD(SOR)	Finite Diff.			
Ko and Ihm [17]	0.16× 2.53×0.38	1D	NA	Poly-disperse Saturation Charge	Average Velocity	Dust concentration of polydisperse dust particles
	SW	Electric field		1D Convection Mobility and Diffusion		
	Smooth CE	Analytic Approx.		Method of lines		

Table 1.5 (continued)

	ESP Geometry	Electric Field	Ion Density	Particle Density	Flow Field	
Author	**DxLxH**	**Domain**	**Domain**	**Particle Size. Charging Type**	**Domain**	**Collection Efficiency**
	DE Type	**Type of Equation**				
	CE Type	**Type of Applied Numerical Method**				
Kogel-schatz et al. [75]		3D	3D	0.05-5μm Diffusion & Field	3D N.S. with EHD	Particle Trajectory
	HW	Poisson	Mobility	3D Lagrangian Convection Mobility and Diffusion		
	G-type	NA	NA			
Watanabe [30]	0.25×1×0.5	2D	2D	Diffusion & Field	2D Vorticity-Stream with EHD	Particle trajectory considering tuft density in particle charging
	∅3mm SW	Poisson	Mobility	Lagrangian		
	Smooth N.A CE	NA	Finite Elem			
Yoo et al. [57]	0.45×0.62	2D	NA	Diffusion & Field	NC	Particle trajectories
	SW	Poisson	Mobility	Lagrangian		
	Smooth CE	NA	NA			
Liang and M.F. Cheng [76]	0.2× (NA)	2D	2D	Diffusion & Field	2D	Based on the dust concentration
	∅1.27mm SW	Poisson	Mobility	Eulerian with Convection Mobility and Diffusion	Turbulent κ-ε model	
	Smooth CE	Finite Diff.	Finite Diff.	Finite Diff.	Control volume approach	
Present Work	0.05× (0.1-0.2) ×0.3	3D	3D	0.01-20μm Diffusion & Field	2D Analytic Approx. for laminar flow	Cumulative Deutsche's
	∅0.25 and ∅1.5mm SW, SS	Poisson	Convection Mobility Diffusion	Eulerian with Convection Mobility and Diffusion		
	Smooth, U- and C-type CE	Finite Diff.	Finite Diff.	Finite Diff.		

N.S...Navier Stokes; EHD...electrohydrodynamic; NA...Not Available ; DE...Discharge Electrode; CE...Collecting Electrode; DxLxH...ESP Width by Length by Height; SW...Smooth Wire, HW... Helical Wire; RDE...Rigid Type Discharge Electrode; SS...Serrated Strip; TS...Twisted Square; SP...Smooth Plate; BP...Barbed Plate

A model by Ohyama et al. [62] predicts the collection efficiency of a wire-plate ESP for various dust particle sizes. The electric field is obtained from the Cooperman equation [77]. The ion density distribution is obtained from the current continuity equation, taking into account only drift motion of ions. The boundary conditions at the discharge electrode and collecting electrodes are specified according to experimentally obtained results by Ohkubo et al. [61]. The particle surface charge incorporates diffusion and field charging models depending on the particle size regime.

Kogelschatz et al. [75] investigated a complex ESP geometry with a helical corona electrode and specially shaped, so-called G-collecting electrodes. The model predicts the dust particle collection efficiency by following particle trajectories through the precipitator. Accordingly, 3D models for electric field, ion density, and flow field with induced 'corona wind' were developed. Then, the differential equation describing the particle charging and the particle trajectories were simultaneously solved. They used a modular concept that required the interlinking of different program packages and the transfer of data among several parallel processing computers.

Gallimberti [66] developed a comprehensive mathematical model for the simulation of the operating conditions of wire-plate ESPs. The fluid dynamic simulation was divided into a 3D model of the entire system and a 2D model of each field. Once the 2D ion density equation, together with the Poisson equation was solved, the charging rate was calculated. The values are classified into two characteristics assigned by the particle radius and initial charge class. The last part solves the charged particle transport equation for all particle classes, whereby the local dependent drift velocity was obtained from the

Langrangian dynamic equation. The collection efficiency is calculated based on the outlet mass flux.

Soldati [68] studied the influence of electrohydrodynamic (EHD) induced secondary flow on ESP collection efficiency of by means of particle tracking in the flow field. The Lagrangian simulation was implemented by dispersing swarms of precharged particles in the flow field with and without EHD flow. Numerical results indicated that there is no significant effect of EHD flow on the collection efficiency of particles ranging from *4* to *32 μm*. Since the behaviour of already precharged dust particles was evaluated, the numerical results does not capture the effect of EHD flow on particle charging in entrance section of ESP. Additionally, the approach is computationally time costly, especially for higher numbers of particle trajectories.

Yoo et al. [57] particle charging rate equation is solved simultaneously with the particle transport equation of motion under the varying electric field and ion density. Yamamoto [65] carried out a 2D numerical simulation for the wire-plate and plate-plate ESP, based on the analytic expression of 2D-laminar EHD flow and transport equation of monodispersed already precharged dust particles.

Liang and Cheng [76] modelled collection efficiency in turbulent flow for high Reynolds number. Numerical analyses reveal that the collection efficiency prediction based on the turbulent model is *23 %* higher and *15 %* lower than the collection efficiency prediction from the conventional Deutsch equation and laminar flow model, respectively.

From the literature survey, two simulation trends are noticed. One group predicts the charged dust collection efficiency by solving the charged particle trajectory equation (Lagrangian approach). The other group predicts the charged dust collection efficiency by solving the charged particle transport equation (Eulerian approach). Most ESP simulations are confined to two dimensions, but Kogelschatz et al. used 3D simulation. Except for Gallimberti and Kogelschatz et al., most researchers considered only the mono particle size distribution. Related to the dust particles charging models, most simulations are either done with precharged dust particles or by implementing simplified particle charging models. Only Gallimberti and Ohyama et al. consider various field and diffusion particle charging models, depending on the Knudsen number. Most simulations consider smooth corona wire and smooth collection electrode plates, in spite of the new design trends to enhance the particle collection efficiency by various discharge electrode geometries. Notable exceptions to this were performed by Kogelschatz et al. and Davidson et al.

1.4 RESEARCH OUTLINE

1.4.1 Objectives of this Research

Several experimental studies [24, 54, 78] have showed that the serrated strip or spike type discharge electrodes, when oriented parallel to collecting electrodes, provide much better collection efficiency in first few metres of ESP compared to the smooth wire or rod type discharge electrodes. The experimental and numerical studies on similar electrode geometries indicated different distribution of current, electric field, and main gas flow. However, there is a lack of comprehensive study about their effect on charging of dust particles and collection efficiency. Thus, in this research the smooth wire, rod, and spike types of discharge electrodes placed between the I, U, and C type of collection electrodes were evaluated experimentally and numerically, with emphasise on the collection efficiency of ultra-fine and submicron dust particles. The experimental tests in this research, were conducted for bench-scale single-field and multi-field ESP for wire-plate, rod-plate, and spike-plate electrode arrangements by measuring the outlet and inlet dust concentration of various dust particle sizes at various negative dc applied voltages and operating flow rates. Additionally, several other experiments were performed for electrical characterisation of corona discharge. These include: (a) current-voltage characteristic, (b) optical emission of negative corona at various discharge electrodes, and (c) current density at collecting electrode. Some of the above experiments are used later to justify the model assumptions and to set the model boundary conditions on the discharge/collecting electrodes. Then, the prediction model was developed based on coupling among multidimensional models of electric field, gas flow field, ion density, neutral and charged dust density of various dust particle sizes. For ultrafine and submicron particles, the particle charge due to diffusion and field charging were considered based on the Knudsen number $(Kn=\lambda_i/r_p)$, where λ_i is the mean free path of negative ions and r_p is the dust particle radius. The total collection efficiencies were predicted based on the (a) knowledge of main gas flow, electric field, and ion density distribution, denoted as Mode 1, and (b) neutral and charged dust density distribution, denoted as Mode 2. After the validation of the model by comparing predicted and measured collection efficiency, numerical studies were conducted and used to: (a) compare the electric field distribution for various geometries and to provide evidence that the spike type discharge electrode creates higher electric fields in the inter-electrode space, (b) compare the ion density distribution for various geometries and to provide evidence that the spike type discharge electrode creates higher ionic space charge when compared to the rod-type discharge electrode, (c) provide information about the magnitude of EHD secondary flow, (d) analyse the development of the surface charge on the various dust particles, (e) determine the conditions for which an increase in electric field can compensate for the smaller particle surface charge due to the smaller ion density since the particle charge increases logarithmically with the charge concentration and the electrical forces increase linearly with the electric field, and (f) determine the limits of the model with respect to the collection efficiency of ultrafine and submicron dust particles. Finally, in order to use a model as a design and scale-up tool, the large-scale wire-plate type ESP validations were conducted for various gas temperatures and dust resistivities as well as the prototype design of spike-type discharge electrode in combination with U and C type collection electrodes.

1.4.2 Organization of Thesis

General information about the new emission regulations and their impact on the electrostatic precipitator technology, as well as the analysis of the previous work with emphasis on the discharge and collection geometries are given in Chapter 1.

Chapter 2 begins with an investigation of corona discharge. After that, it summarizes dust particle charging models used in ESP modelling and provides brief introduction into the dust collection processes.

Chapter 3 outlines the basic equations and numerical procedures used for the calculation of gas flow velocity, electric field, ions, neutral and charged dust densities, as well as the dust collection efficiency. The present numerical model is outlined and reflected to other approaches and methods.

Chapter 4 contains the parametric study for geometry effects, applied voltage, gas flow velocity.

The validation of numerical code by comparing predicted versus experimental results is presented in Chapter 5.

The research for this thesis is concluded in Chapter 6 together with some recommendations addressed in Chapter 7.

Appendix A provides the set of experiments performed for corona discharge and particulate matter characterization that are used in Chapter 3 for establishment of boundary conditions in numerical model.

CHAPTER 2

ELECTROSTATIC PRECIPITATION

This chapter: (a) summarizes corona discharge characteristics, (b) compares various particle charging models, and (c) categorises various dust particle transfer and deposition mechanisms.

2.1 CORONA DISCHARGE

Corona discharges have been studied for many years. Loeb [79] was one of the first researchers to give a clarification of the physical mechanism involved. Detailed classifications, application areas, and physical mechanism explanations are summarized by Chang et al. [80]. Corona discharges exist in several forms, depending on the polarity of the applied voltage, gas mixture characteristic and electrode geometry [80, 81]. Most industrial ESPs operate at negative voltage due to the higher permissible operating current and voltage, and higher sparking potential compared to the positive voltage operation. The corona discharge starts when the electric field in the vicinity of the discharge electrode reaches the threshold value for ionisation of the gas molecules by electron collision. The initiating electron could be produced by photoemission, positive ion impact, metastable action, or field emission from the surface of the discharge electrode. After that, an electron avalanche starts to develop away from the discharged electrode in the direction of the electric field lines. The electron avalanche is produced by electron impact ionisation of metastable or excited gas molecules, as shown in Figure 2.1. With the growth of the avalanche, more electrons and photons are produced at the avalanche head and more positive ions are left in the avalanche wake. The avalanche will continue to grow until it reaches the ionisation-zone boundary, where the photon production and absorption are same. The ionisation or corona zone extends only a few millimetres from the discharge electrode. Due to the high mobility of electrons, the electrons will be further transported by the electric field outside the ionisation zone. Outside the corona zone negative ions are formed by electron attachment [82] and further transported by the electric field. The electron attachment reactions to gas atoms or molecules are classified as: (a) radiative attachment with a small reaction rate of approximately 10^{-14} cm^3/s, (b) dissociative attachment depending on the gas temperature and humidity with the reaction rate range from 10^{-14} to 10^{-9} cm^3/s, and a (c) three-body attachment depending on the gas and electron temperature with the reaction rate range from 10^{-32} to 10^{-29} cm^6/s.

A typical current waveform of negative corona is shown in Figure 2.2, which indicates that the negative corona current is composed of small pulses. However, the time average current is steady. The current-voltage curve reflects discharge electrode shape, collection electrode dimensions, polarity of applied voltage, and all possible operational conditions in ESP [83]. Figure 2.3 shows, time average current as a function of negative and positive applied voltage. Wire-plate geometry has been studied experimentally at various operating conditions by various authors [31, 84-98]. In general the following behaviour can be summarized. An increase in wire size leads to a higher starting (corona onset) voltage and lower current for the same applied voltage. An increase in the plate-to-plate spacing slightly increases corona onset voltage and causes a large drop in the current for the same applied voltage. An increase in wire-to-wire spacing slightly decreases corona onset voltage and the slope of the curve. An increase in the gas temperature results in a stronger current at same applied voltage due to the electrical resistance and gas density reduction. Mechanical misalignment of the electrodes causes an increase in the electric field locally and further reflects in the reduction of the corona onset as well as the spark-over voltage. The dust build-up on the discharge electrode will cause an increase in the onset voltage and a general shift of I-V curve to the right. If a thick or high resistivity layer develops on the collecting electrode, the corona starts at a lower voltage and has higher currents throughout the range of voltages. High dust loading and electrical space charge requires a high applied voltage to yield the same current as in the dust free conditions. With respect to the visual characteristic, the corona generated at a negative applied voltage may form "tufts", corona discharges concentrated in small spots, or negative rapidly moving corona glow accompanied with acoustic noise. The I-V curve of discharge electrode with needles has been characterized in several studies [52, 99-105]. Study by Miller et al. [52] showed that: (a) an increase in the needle length slightly effects corona onset voltage but causes a large increase in the current for the same applied voltage, (b) an increase in a number of barbs causes a slight decrease in the onset voltage, an increase in the total discharge current, but an decrease of current per barb [52, 101].

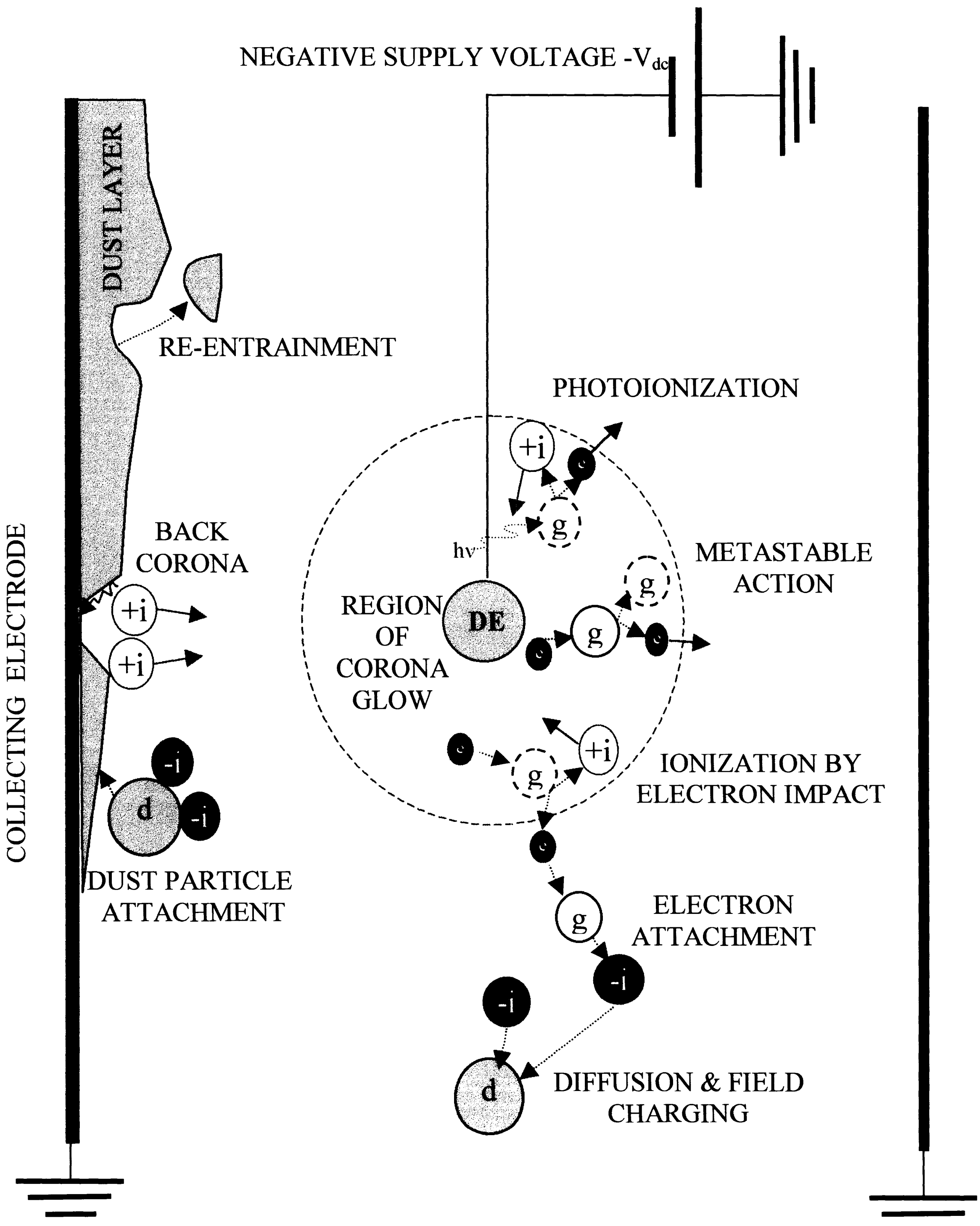

Figure 2.1 Schematic of corona discharge, particle charging and dust collection processes in ESP (top view of wire-plate ESP)

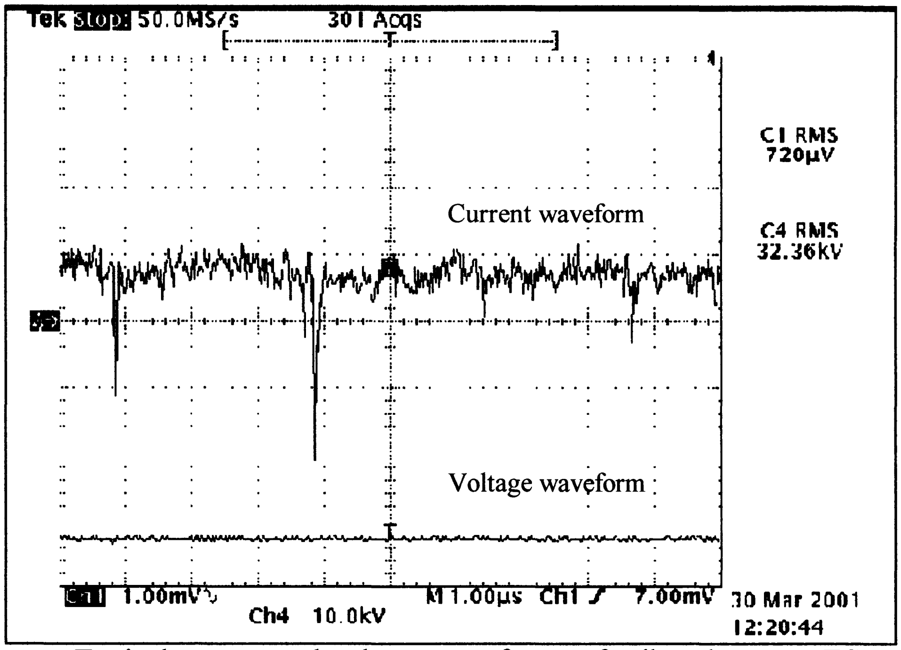

Figure 2.2 Typical current and voltage waveforms of spike-plate type ESP at –33 kV (Channel C1 is connected to the current probe of 1V=0.1A ratio)

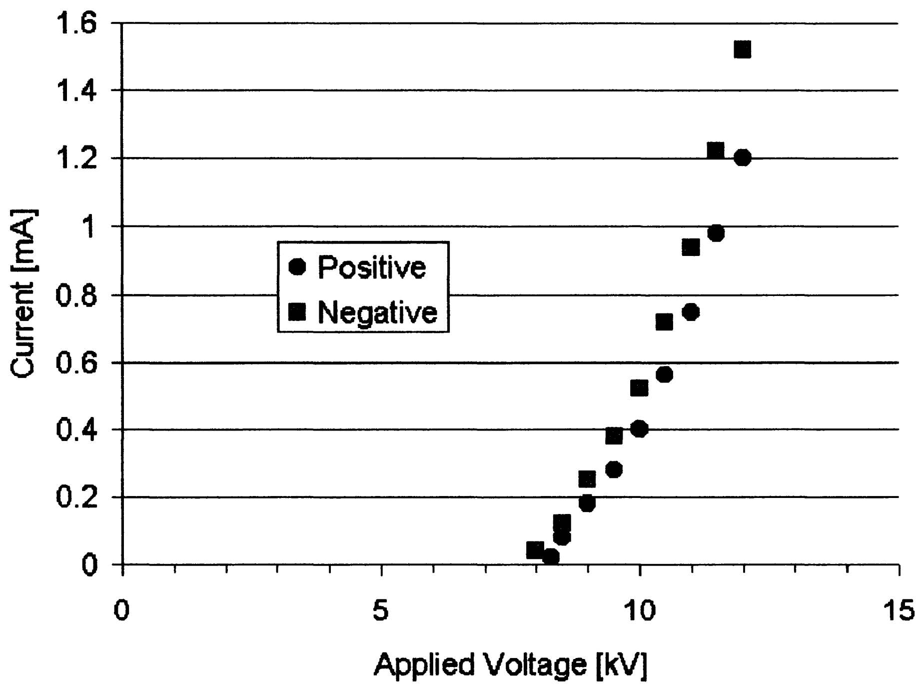

Figure 2.3 Typical time averaged current-voltage (I-V) characteristic for the negative and positive polarity of applied voltage. On-set voltages for the negative and positive corona are -8 kV and 8.3 kV, respectively.

2.2 UNIPOLAR DUST PARTICLE CHARGING

In general, the particles acquire charge by two mechanisms: field charging and diffusion charging. Field charging occurs due to the bombardment of the dust particle surface by ions that are moving under the influence of the electric field. Diffusion charging occurs due to the attachment of the ions to the surface of the dust particle diffusing in accordance with the laws of gas kinetic theory. Additionally, the particle charging can be further classified according to the size regime: in free molecule ($Kn>>10$), transition ($0.1<Kn<10$), and continuum ($Kn<<0.1$). The size regimes were determined based on the Knudsen number ($Kn=\lambda_i /r_p$), ratio of ion mean free path (λ_i) and particle radius (r_p). For air or combustion flue gases at atmospheric pressure, the ultrafine and submicron particles ($r_p<1$) are in a free-molecule and transition conditions.

Dust particle charging was studied experimentally and theoretically by many investigators. The principal models are summarized in Table 2.1. In 1923, Rohmann [106] performed an experimental study of field charging for $1<r_p[\mu m]<2.5$. In 1925, Arendt and Kallmann studied experimentally and theoretically [107] the diffusion charging mechanism of mist particles ($0.5<r_p[\mu m]<2.2$) for the case where the particles already have considerable charge. In 1932, Pauthenier and Moreau-Hanot performed a comprehensive theoretical and experimental study of field charging [108] for conducting and insulating spherical particles for diameter sizes ranging from 10 to 100 μm. In 1947, Fuchs [109] developed the theory of ultra-fine dust particles for diffusion charging. In 1951, White [110] provided solution for the diffusion charging equation of initially

Table 2.1. Unipolar charging models spherical dust particles

<table>
<tr><th>Author</th><th>Type of Analysis</th><th>Free molecule ($Kn \gg 10$)</th><th>Transition ($0.1 \le Kn \le 10$)</th><th>Continuum ($Kn \le 0.1$)</th></tr>
<tr><td>Rohmann [106]</td><td>Experiment (1-2.5μm)</td><td></td><td></td><td>Field</td></tr>
<tr><td>Pauthenier and Moreau-Hanot [108]</td><td>Experiment (10-100μm) & Theory</td><td></td><td></td><td>Field</td></tr>
<tr><td>Brock [111] and Parker [112]</td><td>Theory</td><td colspan="2">Field</td><td></td></tr>
<tr><td>Chang et al. [113]</td><td>Theory</td><td>Field</td><td></td><td></td></tr>
<tr><td>Arendt and Kallmann [107]</td><td>Experiment (0.5-2.2μm) & Theory</td><td></td><td></td><td>Diffusion</td></tr>
<tr><td>White [110]</td><td>Theory</td><td>Diffusion</td><td></td><td></td></tr>
<tr><td>Fuchs [109]</td><td>Theory</td><td></td><td></td><td>Diffusion</td></tr>
<tr><td>Laframboise [114] and Chang [114, 115]</td><td>Theory</td><td colspan="3">Diffusion</td></tr>
<tr><td>Cochet [116]</td><td>Theory (0.05-0.5μm)</td><td></td><td>Diffusion and Field</td><td></td></tr>
<tr><td>Fjeld and McFarland [117]</td><td>Theory</td><td></td><td></td><td>Diffusion and Field</td></tr>
</table>

uncharged particles. For dust particles in the submicron range, the differences between theoretical values by White and experimental values of dust particle surface charge have led to further modifications of the models. In 1956, Cochet [116] proposed semi-empirical law which takes into account both charging processes for particles ranging from *0.05* to $0.5\mu m$. In 1970, Brock [111] derived an equation describing a free molecule field charging for negligible dust particle polarisation and dust particle velocity. The effect of the reduced ion velocity due to the movement of the dust particles under electric field is not negligible in the free molecule regime for higher ion speed ratios (defined as a ratio between the dust particle velocity and the most probable velocity of thermal ions) as shown by Chang [113]. Chang and Laframboise performed a comprehensive study of diffusion charging of arbitrary shaped dust particles [114, 115]. Parker [112] and Chang et. al. [115, 118] approximated the number of charges on the surface of the dust particles in free molecular and transition regime due to the field charging by a product of ion speed ratio and the number of charges on the surface of the dust particle due to the diffusion charging. In 1983, Fjeld and McFarland proposed combination of field and diffusion charging mechanisms together with polynomial curves describing particle charge acquisition in continuum region for various particle charges and electric field values. Davison and Gentry [119] investigated the slow down of the diffusion charging process due to the increase of ion mass in the case of mono-polar charging.

2.2.1 Some Diffusion Charging Models

Based on the gas kinetic theory, the thermal motions of ions and image forces can be considered as a basis of the ion deposition on the surface of the dust particle in diffusion charging mechanism. This charging mechanism depends mainly on the thermal energy of ions, particle and ion size, and exposure time. Therefore, the higher the thermal energy of ions, the particle radius and the ion density, the faster and the higher the particle becomes charged.

Chang and Laframboise [114, 115] expressed diffusion charging rate in all three dust particle size regions by a single expression (2.1a) .

$$\frac{d\Phi_p}{d\tau_d} = \frac{(1+\kappa)\Phi_p}{(1+\kappa\Phi_p)e^{\Phi_p} - 1} \tag{2.1a}$$

The proposed solution of (2.1a) is shown in (2.1b)

$$\tau_d = \frac{4\pi r_p e^2 N_i D_i t}{C_p kT(1+\kappa)} = \frac{1}{1+\kappa}\sum_{m=1}^{\infty}\{\frac{\Phi_p{}^m}{m \cdot m!} + \frac{\kappa\Phi_p{}^{m+1}}{(m+1)\cdot m!}\} + \frac{\kappa\Phi_p}{\kappa+1} \tag{2.1b}$$

$$\Phi_p = \frac{eV_p}{kT_g} = \frac{e\dfrac{em_{s-dc}}{4\pi\varepsilon_o r_p}}{kT_g} = \frac{e^2 m_{s-dc}}{4\pi\varepsilon_o kT_g r_p} = 1.669\times10^{-5}\frac{m_{s-dc}}{r_p T_g} \tag{2.1c}$$

where Φ_p is the dimensionless surface potential of the charged dust particle (2.1c), $m_{s\text{-}dc}$ is the number of elementary charges on the surface of the dust particle, τ_d is the charging characteristic time, t is the exposure time, κ is the effective Knudsen number $(\kappa=Kn)$, r_p is the radius of the dust particle, N_i is the ion density, D_i is the ion diffusion, λ_i is the mean free path of ions, T_g is the gas temperature, $C_p = 4\pi\varepsilon_o r_p$ is the capacitance of spherical particles, e is the elementary charge, and k is the Boltzmann constant. Figure 2.4 shows the solution of (2.1b) in dimensionless coordinates Φ_p and τ_d for various dust particle sizes. The same solution in form of the number of surface charges versus residence time is shown in Figure 2.5.

For the free-molecule regime, as Kn approaches infinity (2.1b) reduces to (2.2b) which agrees with solution of well known White's [110] diffusion charging rate equation (2.2a), essentially derived as a simplification of diffusion charging equation proposed by Arendt and Kalmann [107],

$$\frac{d\Phi_p}{d\tau} = \frac{er_p\bar{v}_i}{4\mu_i kT} e^{-\Phi_p} \tag{2.2a}$$

$$\Phi_p = \ln(1 + \frac{e^2 r_p \bar{v}_i N_i}{4\varepsilon_o kT} t) \tag{2.2b}$$

where $\tau = e^2 N_i D_i t/(\varepsilon_o kT)$ is the characteristic charging time, $\bar{v}_i = \sqrt{8kT/\pi m_i}$ is the mean thermal velocity of ions at temperature T_g and ion mass m_i.

For the continuum regime, as Kn approaches zero, (2.1a) and (2.1b) reduce to (2.3a) and (2.3b), respectively.

$$\frac{d\Phi_p}{d\tau} = \frac{\Phi_p}{e^{\Phi_p} - 1}; \tag{2.3a}$$

$$\sum_{m=1}^{\infty} \frac{\Phi_p{}^m}{m!m} = \frac{e^2 N_i D t}{\varepsilon_o k T_g} \tag{2.3b}$$

The solutions of (2.2b) and (2.3b) compared to the corresponding numerical solutions of (2.1b) are shown in Figure 2.6.

2.2.2 Some Field Charging Models

If a spherical uncharged particle is placed in an external electric field, the electric field lines will be modified due to the relative dielectric constant of the dust particle, as shown in Figure 2.7a. An ion will follow the electric field lines and therefore attach to the surface of the dust particle. As the particle charging proceeds, the particle surface charge will modify the surrounding electric field as shown in Figure 2.7b and

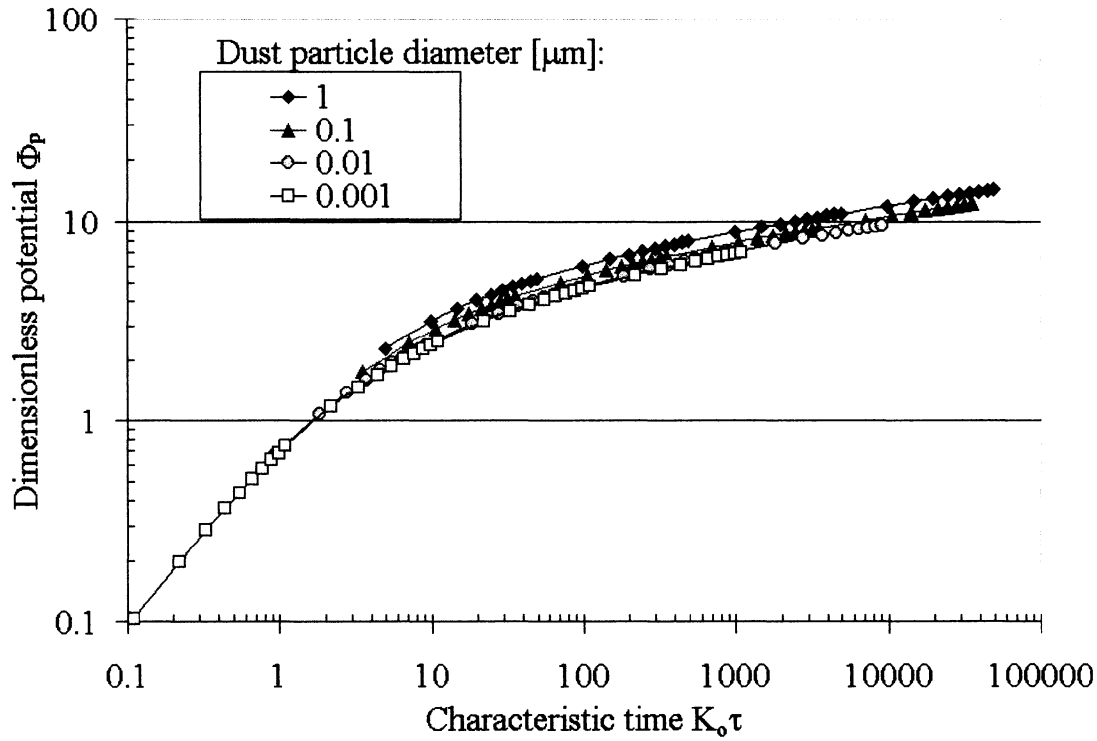

Figure 2.4 Dimensionless potential Φ_p of a dust particle as a function of dimensionless characteristic time $\tau_d = K_o \tau$ for diffusion charging.
(Results are obtained numerically from Equation 2.1b)

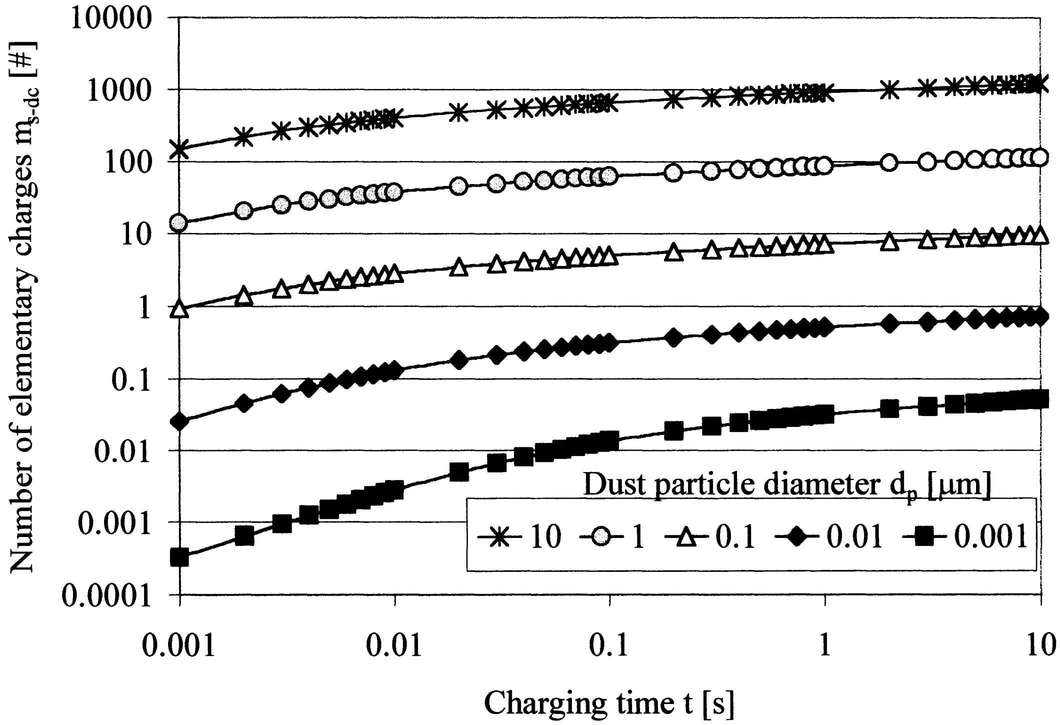

Figure 2.5 Typical number of elementary charges $m_{s\text{-}dc}$ on the particle surface due to the diffusion charging mechanism.

(Results are obtained from Equation 2.1b for the following conditions: gas temperature T_g=20 [^oC], ion density N_i =1×10^{15} [m^{-3}], mean free path of ions λ_i=3.72×10^{-8} [m].

Considering above conditions in addition to the mean gas flow velocity of 1 m/s and ESP length of 10 m, it can be concluded that particles smaller than 0.01μm will not even accumulate one charge on the surface due to diffusion charging.)

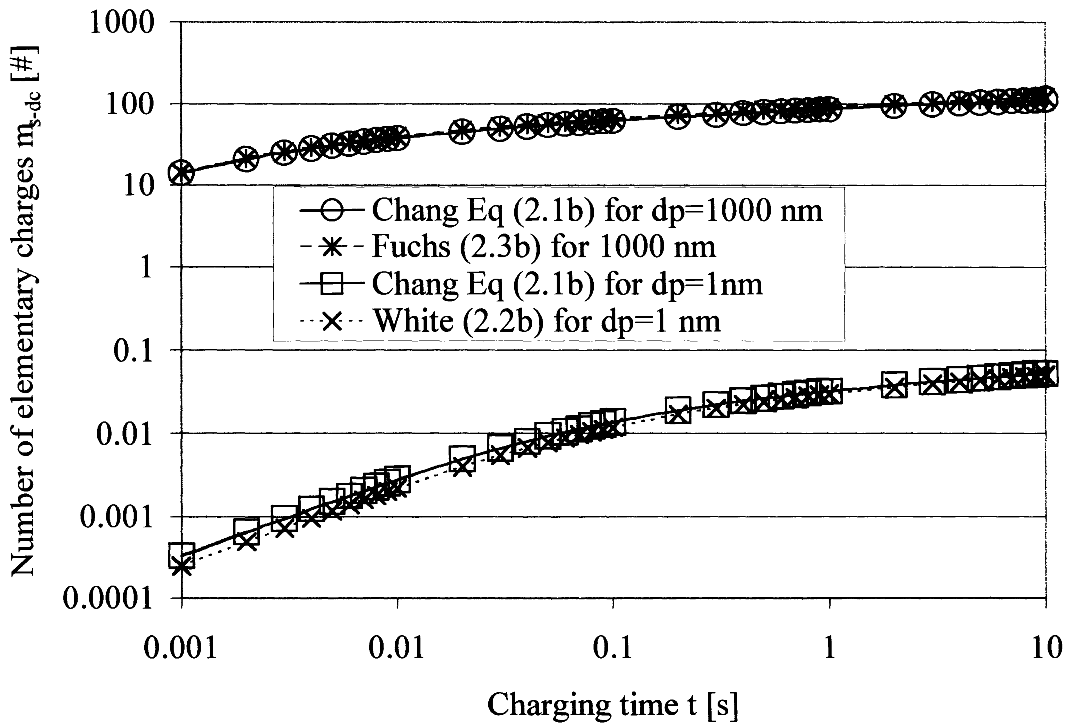

Figure 2.6 Comparison among numerical and approximate solutions for the diffusion charging models in the free and continuum regime.
(Results are obtained from Equations 2.1-2.3 at the following conditions: ion density $N_i = 1\times10^{15} [m^{-3}]$, mean free path of ions $\lambda_i=3.72\times10^{-8} [m]$ and gas temperature $T_g=20$ [°C]. There is a quite good agreement in the continuum regime and some discrepancies for the free molecule regime at shorter exposure times.)

thus reduce the rate of charging. The particle charging will continue until the dust particle reaches the saturation charge. Based on the field charging theory, the higher the ion concentration and the higher the ion mobility, the faster the particle becomes charged. The higher the electric field and the particle size, the higher the saturation or limiting charge on the dust particles.

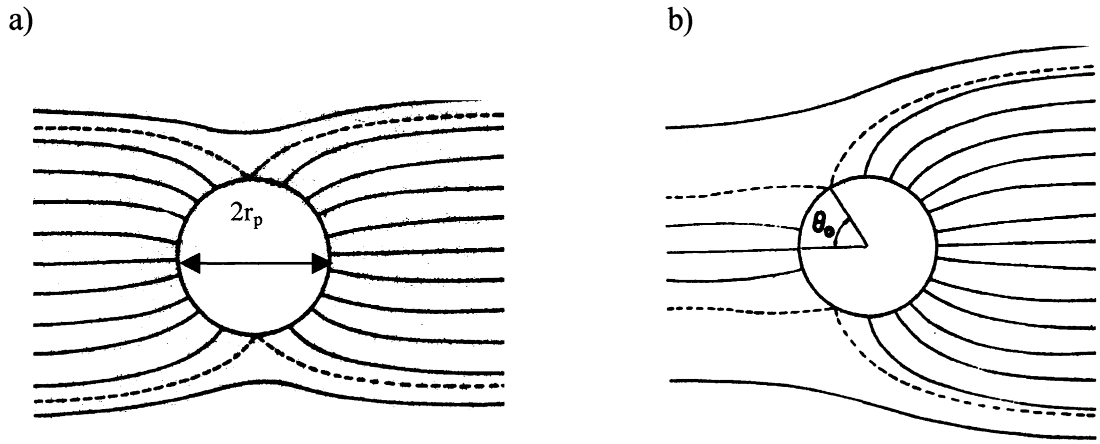

Figure 2.7 Sketch of the electric field near (a) an uncharged and (b) a charged spherical dust particle (modified from [110])

Considering the free molecular and transition size regime [111, 113], constant ion density and electric field, the rate of field charging can be expressed as

$$\frac{d\Phi_p}{d\tau_f} = \left(\frac{r_p}{2\lambda_{Di}}\right)^2 \mathbf{i}(\Phi_p, S_{io}) \tag{2.4a}$$

where Φ_p is the dimensionless potential of the dust particle at temperature T, $\tau_f = \bar{v}_i t / r_p$ is the dimensionless time, $\bar{v}_i = \sqrt{8kT/\pi m_i}$ is the mean thermal velocity of ions, t is the charging/exposure time, r_p is the radius of the dust particle, N_i is the ion density,

$\lambda_{Di} = \sqrt{\varepsilon_o kT / e^2 N_i} = 68.99\sqrt{T/N_i}$ is the Debye length, and ***i*** is the charging enhancement factor defined by Brock [111] and Parker [112] as follows:

$$i = e^{-\Phi_p^2}\{\frac{e^{-S_{io}^2}}{4S_{io}}[(\Phi_p + S_{io})e^{2S_{io}\Phi_p} - (\Phi_p - S_{io})e^{-2S_{io}\Phi_p}] + \frac{\sqrt{\pi}e^{\Phi_p^2}}{4S_{io}}(\frac{1}{2} + S_{io}^2 - \Phi_p^2)[erf(\Phi_p + S_{io}) - erf(\Phi_p - S_{io})]$$
(2.4 b)

where $S_{io} = \frac{U_{ik}}{\sqrt{2kT/m_i}}$ is the ion speed ratio taking into account charged dust particle motion as revised by Chang et al. [113], $U_{ik}=(\mu_i-\mu_{cd})E$ is the relative drift velocity of ions, E is the electric field, μ_i is the mobility of ions, μ_{cd} is the mobility of charged particles defined as

$$\mu_{cd} = \frac{em_{s-fc}}{6\pi r_p \mu_g}(1 + A_o\frac{\lambda_i}{r_p}) \;; \quad A_o = 1.25 + 0.42e^{-0.87r_p/\lambda_i} \tag{2.4c}$$

where e is the elementary charge , $m_{s\text{-}fc}$ is the number of surface charges due to the field charging method, r_p is the radius of dust particle, μ_g is the viscosity of the gas, A_o is the slip correction factor, and λ_i is the mean free path of ions. Dimensionless dust particle surface potential versus dimensionless charging time at various ion speed ratios is shown in Figure 2.8.

In the continuum region where dust particle is very large compared to the mean free path of ions, the field charging can be described by Pauthenier and Moreau-Hanot equation [108] as follows.

$$\frac{\partial \Phi_p}{\partial \tau} = \frac{\Phi_S}{4}(1 - \frac{\Phi_p}{\Phi_S})^2 \tag{2.5a}$$

An elementary integration for initially uncharged $(\Phi_{(t=0)}=0)$ and charged particle $(\Phi_{(t=0)}=\Phi_i)$ gives (2.5b) and (2.5c), respectively.

$$\Phi_p = \Phi_s \frac{\tau}{\tau + 4} \tag{2.5b}$$

$$\Phi_p = \Phi_s \frac{k_o \tau + 4(1 - k_o)}{4 + k_o \tau} \tag{2.5c}$$

Φ_s is the saturation level of the dimensionless surface potential as shown in (2.5d), τ is the characteristic field charging time (2.5e), $m_{saturation}$ is the number of saturation charges, and $k_o = (1 - \frac{m_{initial}}{m_{saturation}})$ is correction constant in case of initially charged particles ($m_{initial}$).

$$\Phi_s = \frac{m_{saturation} e^2}{4\pi\varepsilon_o r_p kT} = \frac{er_p E_o}{kT} \frac{3\varepsilon_p}{\varepsilon_p + 2} \tag{2.5d}$$

$$\tau = \frac{e^2 N_i D_i}{\varepsilon_o kT} t = \frac{eN_i \mu_i}{\varepsilon_o} t \tag{2.5e}$$

where ε_o is the electric permittivity of free space, ε_p the relative dielectric constant of dust particle, r_p is the radius of dust particle, E_o is the external electric field, N_i is the ion density, and μ_i is the mobility of ions.

Another approach for continuum region is that proposed by Fjeld and McFarland based on dimensionless electric field $\omega_p = \frac{er_p E}{kT}$ and particle potential $\phi_p = \frac{m_s e^2}{4\pi\varepsilon_o r_p kT}$. They proposed to use only (2.3a) for $0 \le \omega_p \le 0.1$ condition, (2.5a) for $\omega_p \ge 10$ condition, and a sum of (2.3a) and (2.5a) for $0.1 \le \omega_p \le 10$ and $\Phi_p \ge 20$ conditions. For

$0.1 \le \omega_p \le 10$ and $0 \le \Phi_p \le 20$ conditions, they proposed polynomial curve fit (2.6) with coefficients a_{kl}, as shown in Table 2.2.

$$\ln \frac{d\Phi_p}{d\tau} = \sum_{kl} a_{kl} \phi_p^{\,k} (\ln \omega_p)^l \tag{2.6}$$

Table 2.2

Polynomial curve fit coefficients a_{kl}

l \ k	0	1	2	3
0	0.448	-0.3236	-0.01571	0
1	0.4457	0.1453	0.0077	-0.00021
2	0.1085	0.0067	0	0.000064
3	0	-0.00961	0	0

Cochet proposed simplified solution, taking into account both field and diffusion charging in the transition region, based on the modification of Pauthenier and Moreau-Hanot model by coefficient α expressed in terms of λ_i/r_p ratio

$$m_{Cochet} = \{(1 + \frac{\lambda_i}{r_p})^2 + \frac{2}{1 + \frac{\lambda_i}{r_p}} \frac{\varepsilon_p - 1}{\varepsilon_p + 2}\} 4\pi\varepsilon_o r_p E / e \tag{2.7}$$

The number of surface charges due to field charging for various particle sizes and charging models is shown in Figure 2.9.

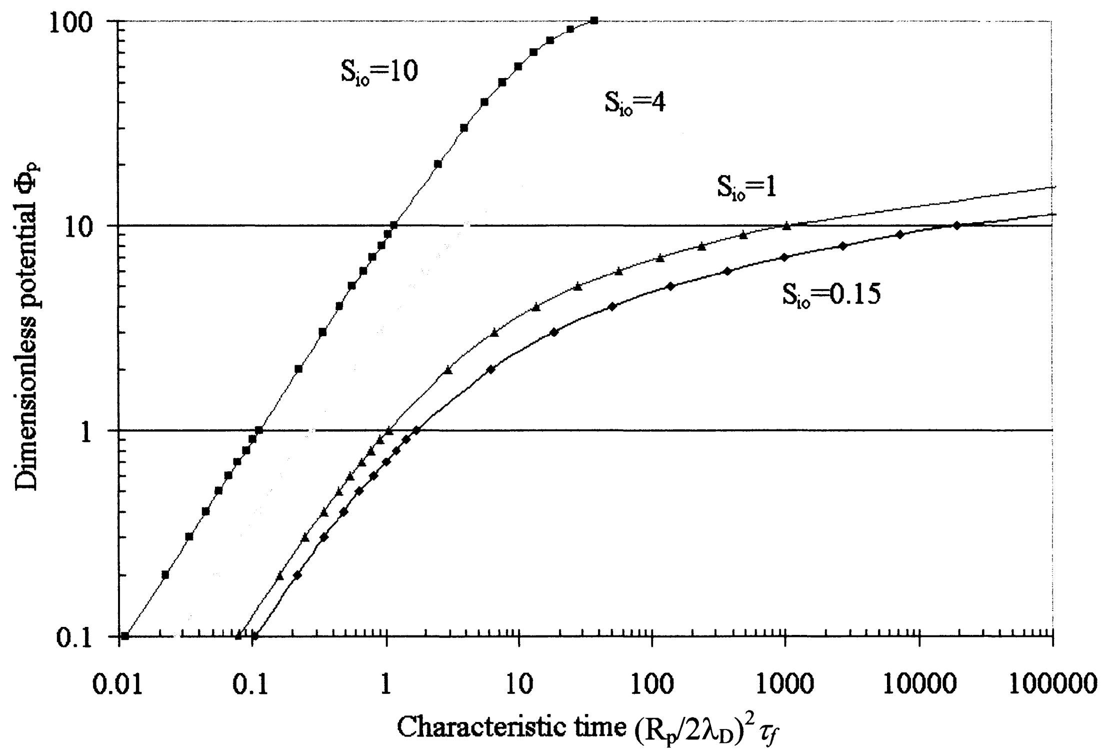

Figure 2.8 Dimensionless potential Φ_p of a dust particle as a function of characteristic time $(R_p/2\lambda_D)^2\tau_f$ for the various ion speed ratios.
(Results are obtained from Equations 2.4.
Corrections of the ion speed ratio due to the mobility of the particles have an noticeable effect on the dimensionless potential Φ_p for the smaller particle sizes and ion speed ratio greater than $S_{io}=4$. For the present ESPs configurations ion speed ratio is less than $S_{io}=1$.)

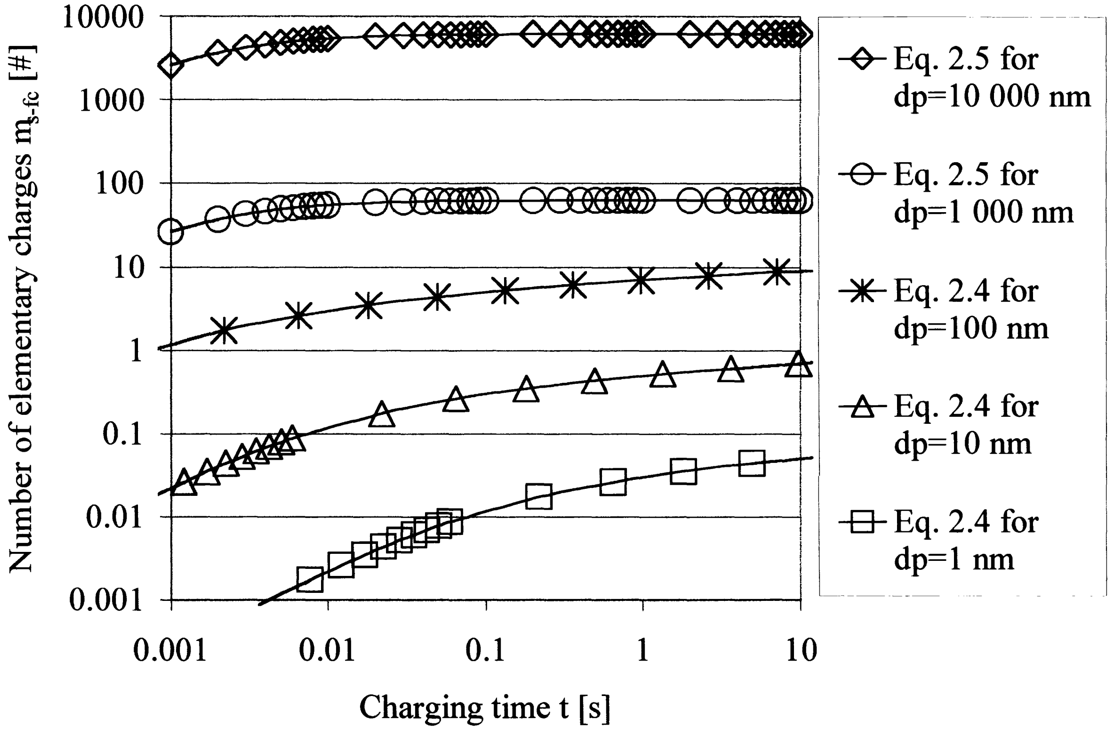

Figure 2.9 Number of elementary charges ($m_{s\text{-}fc}$) on the surface of dust particles due to the field charging.

(Results are obtained from Equations 2.4 and 2.5 for the following conditions: gas temperature T_g=20 [^oC], ion density N_i =1×10^{15}[# of ions/m^3], electric field strength E=2 [kV/cm], ion speed ratio of S_{io}=0.11, mean free path of ions λ_i=3.72×10^{-8}[m].)

2.2.3 Charging Models Used in ESP Modeling

Dust particle charging in ESP is a very complex process. The particles of various size regimes ranging from free-molecule to continuum are exposed simultaneously to field and diffusion charging mechanisms. Additionally, the particle charging in ESP is highly location dependant. The module of electric field may vary from a few *kV/m* to several *MV/m*, depending on the applied voltage and ESP geometry. The ion density is also highly dependant on the discharge and collecting electrode geometries, applied voltage, and gas velocity. As shown by Atten et al. [120] in numerical analysis of charging of submicron particles for a complex barbed-type discharge electrode, particles of the same size do not have the same charge due to the complex electric field, ion density, and gas velocity distribution.

Since the standard charging theories assume quasi-static conditions and independent charging mechanism, several approaches, summarized in Table 2.3, have been adopted in calculation of surface charges on particles within an ESP. Most authors neglect diffusion charging and assume that the particles reach field saturation charge according to (2.5d). For standard ESP geometries it is very likely that the particle may reach field saturation charge within the first few centimetres of the field. After that, the particle will be subjected only to diffusion charging [54], and therefore it should be taken into account even for the larger dust particles. For example, a $10\ \mu m$ dust particle has approximately four times higher surface charge due to field charging, compared to that due to the diffusion charging. For sub-micron $(0.1<d_p[\mu m]<1)$ dust particles, the number of elementary charges due to the diffusion charging is larger than the number of surface charges due to field charging. However, they are of the same order of magnitude. Therefore the field charging of sub-micron dust particles should be considered, especially in the vicinity of discharge electrodes, where high electric fields can enhance the surface charge.

Table 2.3
Charging models in ESP modelling

<table>
<tr><th>Author</th><th>Particle Size [μm]</th><th>Charging Methods;
Equations;
Comments</th></tr>
<tr><td>Levin [69]</td><td>15</td><td rowspan="9">• Field charging.
• Pauthenier-Moreau-Hanot equation 2.5d for continuum regime.
• It was assumed that all particles entering the modelled section are precharged up to the saturation level. Diffusion charging was neglected.</td></tr>
<tr><td>Riehle and Loffler [73]</td><td>0.1-10</td></tr>
<tr><td>Self et al. [53]</td><td>4</td></tr>
<tr><td>Stock [71]</td><td>1-10</td></tr>
<tr><td>Cristina and Feliziani [67]</td><td>1-120</td></tr>
<tr><td>Kim et al. [121]</td><td></td></tr>
<tr><td>ESPVI 4.0 [63]</td><td></td></tr>
<tr><td>Levin and Hoburg [70]</td><td>7.5</td></tr>
<tr><td>Soldati [68]</td><td>4-32</td></tr>
<tr><td>Watanabe [30]
Sum of diffusion and field charges $R_i = \frac{NT_t}{NT}$
NT is the total number of tufts;
NT_t is the number of tufts in particle trajectory</td><td>15</td><td>• Diffusion and Field charging.
• White’s diffusion model with reduction of charging time due to the tuft density $\tau_D' = \tau_D / R_i$
• Pauthenier-Moreau-Hanot field charging model with reduction of charging time due to the tuft density $\tau_F' = \tau_F / R_i$</td></tr>
</table>

Table 2.3 (continued)

Author	Particle Size [μm]	Charging Methods; Equations; Comments
Lu and Huang [74]	13.7	• Field charging. • Cochet's equation for transition regime. • This approach applies equation developed for the transition regime in continuum regime.
PRELEC,Canadas et al. [59]	0.13-80	• Diffusion and Field charging. • The type of the equation is not available.
Lawles [64]	0.1- 32	• Diffusion and Field charging. • Fuchs (2.3a) equation for Diffusion charging and Pauthenie-M.Hanot (2.5a) equation for field charging. • Sum of Field and Diffusion charging rates.
Kogel-schatz et al. [75]	0.05-5	• Diffusion and Field charging. • The type of the equation is not available.
Gallimberti [66]	0.15-350	• Sum of diffusion and field charging rates. • For diffusion charging: $\frac{\partial q}{\partial t}=eN_i r_p^{\,2}\sqrt{\frac{8kT\pi}{m_i}}(1+\frac{q}{q_s})e^{-\frac{eq}{4\pi\varepsilon_o rkT}};\ q=em_s$ • For charging Pauthenie-M.-Hanot equation (2.5a)
Yamamoto et al. [122]	0.5-5	• Diffusion and Field charging. • For Diffusion charging: • $\Phi_d=\frac{\tau}{1+\tau}B\ln(0.1+\tau);\ B=1.059+0.238\omega$ and for Field charging: $\Phi_f=\frac{\tau}{1+\tau}A;\ A=4.642+1.77\omega$

Table 2.3 (continued)

Author	**Particle Size [μm]**	**Charging Methods; Equations; Comments**
Ohyama et al. [62]	0.01-10	• Diffusion and Field charging models. • Equations 2.1, 2.4, 2.5. • Applies various charging models depending on the Knudsen number and polynomial curve fit approximations for field charging in transition region.
Yoo et al. [57]	0.03-2	• Diffusion and Field charging • Applies various Diffusion and Field charging models for continuum regime based on Fjeld & McFarland model. • However, the particle size range indicates some non-continuum regime
Adachi	0.02-0.05	• Used probability approach with different classes of charge
Present Model	10^{-3}-10^{2}	• Diffusion and Field charging • Equations 2.1, 2.4 and 2.5 based on Knudsen number.

For ultrafine dust particles $(d_p[\mu m]<0.1)$, the charging theory predicts that the residence time of the order of one second can give only a fraction of one elementary charge. Since, the particles can only acquire an integral number of elementary charges, the discrete distribution should be used to describe the number of particle charges [32]. The sum of the charges due to diffusion and field charging acting independently, is usually used as a combination of White's, and Pauthenier and Moreau-Hanot expressions. Notable exceptions to this were shown by Ohyama et al. [62], Yamamoto et al. [122], Watanabe [30], and Yoo et al. [57], who consider various field and diffusion charging models depending on the Knudsen number.

In the present work, the charging model implements diffusion and field charging in free molecule, transition, and continuum size regimes, assuming a constant ion density and electric field within the small charging time sections between grid points. The assumption that the particles acquire charge by diffusion and field charging process simultaneously seems to be reasonable. For diffusion charging, Equations 2.1 are used rather than the commonly used Equation 2.2, since it covers all size regimes. In the case of the initial surface potential (Φ_i) on the particle, the solution of equation 2.1b for ($\Phi_p=\Phi_i$) determines the initial position (τ_{di}) on the curve shown in Figure 2.4. Depending on the residence time of particle from one grid to another grid location, the characteristic charging time (τ_{dc}) was calculated. After that, Equation 2.1b was numerically solved for a given total charging time ($\tau_d=\tau_{di}+\tau_{dc}$), where the result ($\Phi_d=\Phi_p$) represents the dimensionless potential of charged particle as a result of the initial charge and charge contribution due to the diffusion charging. After that, the field charging theory was applied. For particles in the continuum regime, Equation 2.5b or 2.5c was solved, depending on the initial surface charge. For particles in a free molecule and transition size regime the field charging Equation 2.4a was used. The solution of 2.4a was obtained by numerical integration within (Φ_i *to* Φ_f) limits. The obtained Φ_f represents the total surface charge on the particles as a result of the initial surface charge and contributions due to the field charging. The total number of elementary charges due to the field and diffusion charging mechanisms on the surface of dust particles of three models is shown in Figure 2.10. The particles are exposed for $t=1\ s$ to the average ion density of $1x10^{15}$ *[#ions/m³]* and average electric field of *2 kV/cm.* Total surface charges, by the present model, are very similar to those obtained as the sum of White and Pauthenier-Moreau-Hanot models. Cochet's model seams to produce almost one order of magnitude smaller surface charge in free-molecule and transition regime compared to the other two models.

The total surface charge of various dust particle sizes at different ion densities and external electric fields are given in Figures 2.11 to 2.14. These calculations are for negative ions and a mean free path of 3.72×10^{-8} *m*. Several important aspects of particle surface charge behaviour are illustrated in these figures. The electric field has significant impact on the surface charge of particles in continuum size regime as shown in Figure 2.11. Submicron and ultrafine particles exhibit significant improvement of surface charge at electric fields higher than *10 kV/cm*. Some small improvements are observed by raising the electric field from *1* to *10 kV/cm*. The electric field affects only the field charging process, shown in Figure 2.12. Submicron and ultrafine particles are more sensitive to the ion density change, especially when they have short exposure or charging time as shown in Figures 2.13 and 2.14. The field charging rate of *1* μm and larger reduces to zero for ion densities larger than 1×10^{15} ion/m^3, indicating that particles reached saturation charge, and that there is no further surface charge improvement by an ion density increase. Conversely, the diffusion-charging rate for ion densities greater than 1×10^{15} ion/m^3 reached a constant value, indicating same rate of surface charge improvement with ion density increase.

In general, from the point of view of particle charging it is desired to have a high electric field and ion density. However, the request can be contradictory from the point of view of dust particle collection, since impaired collection efficiencies were observed in some experiments performed at high ion density and high electric field conditions. Therefore, the optimum should be found with respect to the surface charge of dust particles, their mobility towards the collecting plate, attachment to the dust layer, and re-entrainment from dust layer due to mechanical or electrical reasons.

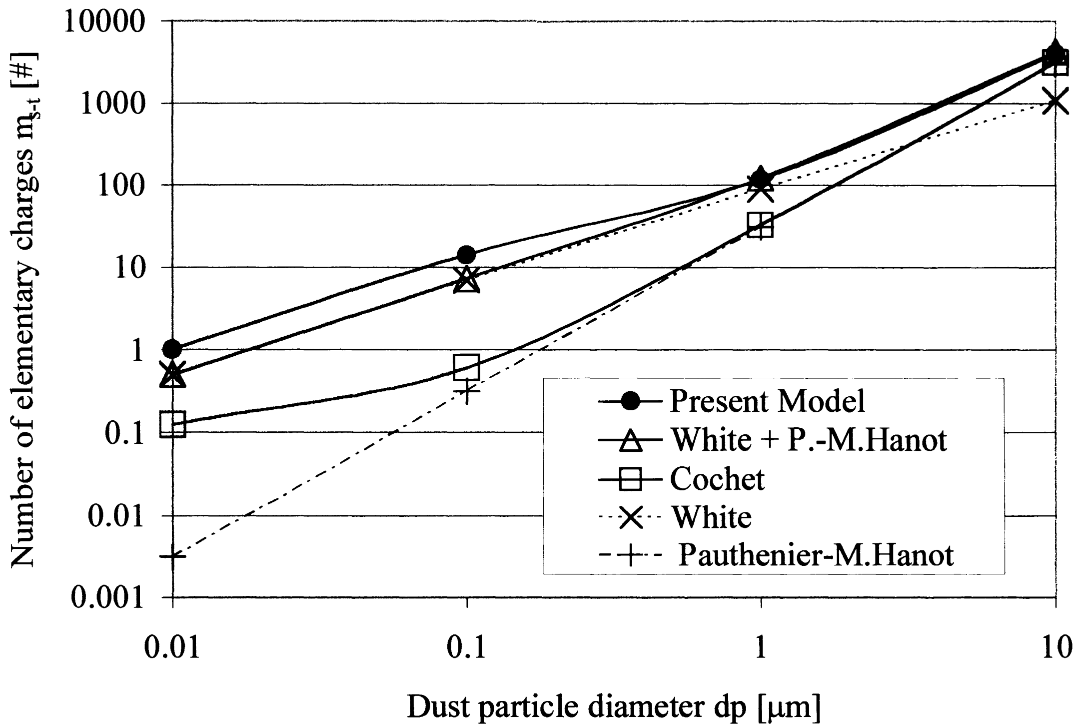

Figure 2.10 Number of elementary charges on the surface of various dust particles as a combination of various diffusion and field charging models ($m_{s\text{-}t}$). *(Results are obtained for the following conditions: gas temperature T_g=20 [^oC], ion density N_i =1×10^{15}[# of ions/m^3], electric field strength E=1 [kV/cm], ion speed ratio of S_{io}=0.11, mean free path of ions λ_i=3.72×10^{-8}[m].)*

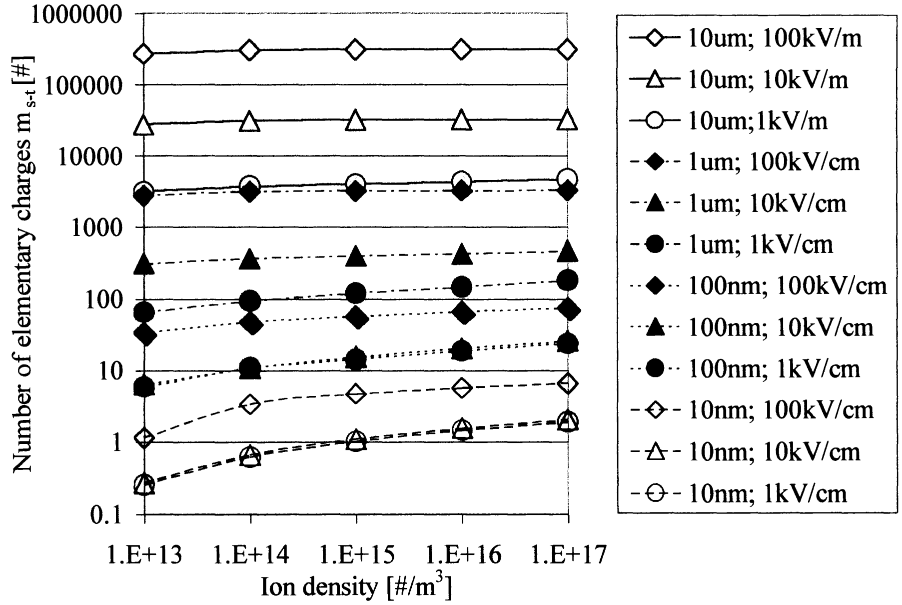

Figure 2.11 Number of elementary charges on the surface of various dust particle exposed one second to various ion densities and electric fields.

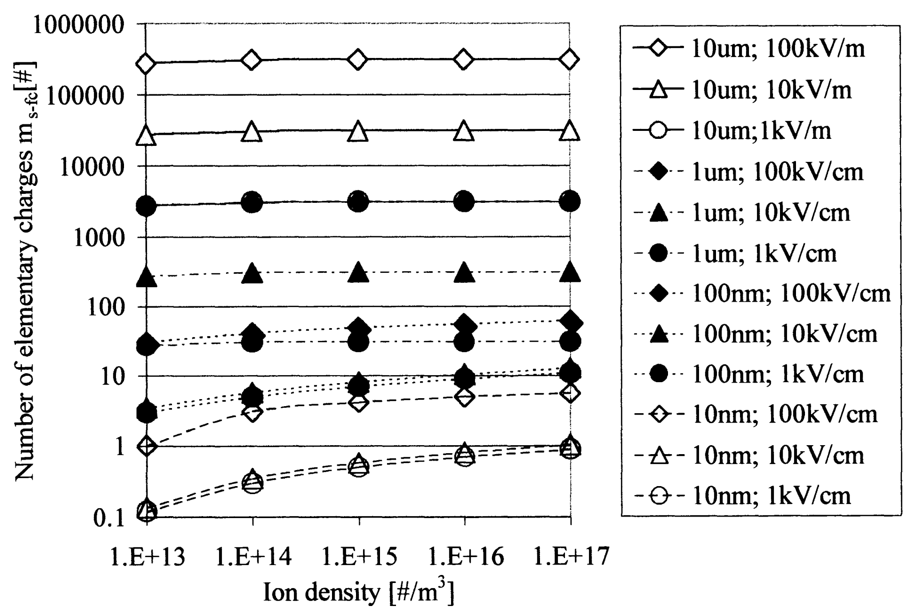

Figure 2.12 Number of elementary charges due to the field charging mechanism for various dust particle sizes exposed one second to various ion densities and electric fields.

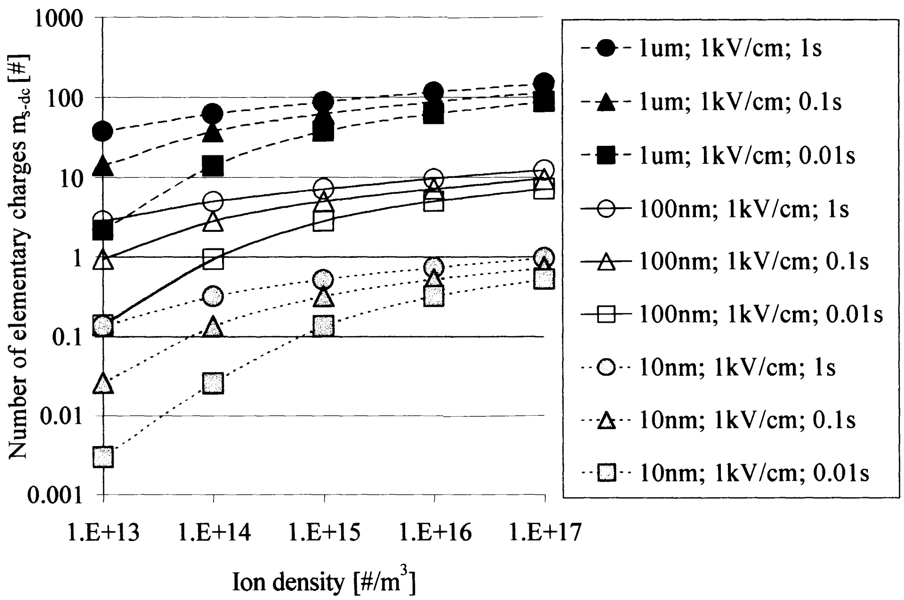

Figure 2.13 Number of elementary charges due to the diffusion charging mechanism on the surface of various dust particle sizes at electric field of *1 kV/cm* and various ion densities.

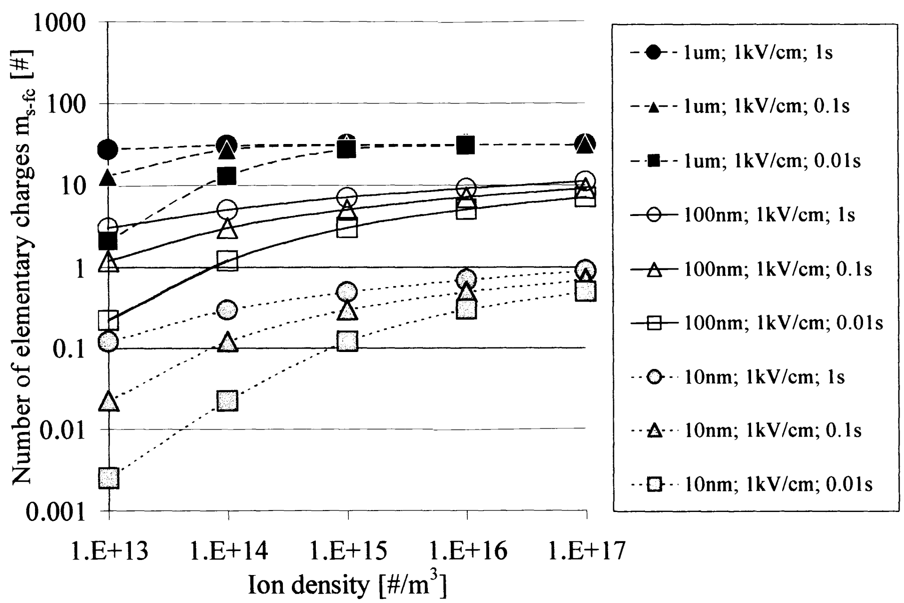

Figure 2.14 Number of elementary charges due to the field charging mechanism on the surface of various dust particle sizes at electric field of *1kV/cm* and various ion densities.

2.3 DUST PARTICLE TRANSPORT AND DEPOSITION

Dust particle collection is determined by: (a) the net deposition (or mass transfer) of neutral and charged dust particles in a direction normal to the surface of the collecting electrode, (b) the adhesion of dust particles to the surface of the collecting electrode, and (c) the removal of the dust particle layer from the collecting electrode into the hoppers, known as rapping.

2.3.1 Dust Particle Transport

The major three types of dust particle transport mechanisms considered are as follows: (a) convection, (b) electrical migration, and (c) diffusion. Convective mass transport usually coincides with the direction of the gas flow streamlines and depends on the gas flow regime and the particle size. The larger dust particles have a tendency to continue to move tangentially to the gas flow streamlines due to the inertia phenomena. Additionally, the larger particles are subject to the larger drag forces. Smaller dust particles follow the gas flow streamlines more closely than the larger particles due to the smaller inertial forces. However, the smaller the dust particles, the larger reduction of the drag force due to the increased particle slip. The mass transport due to the electrical migration coincides with the direction of the electric field lines. This type of mass transport is predominantly perpendicular to the gas flow direction, therefore leading to the deflection of the charged dust particles towards the collecting electrode. It is proportional to the surface charge of dust particles and electric field strength. The mass transport due to the diffusion of dust particles results in a net flow in a direction of matter from a region of high concentration to a region of low concentration. In some sections of ESP diffusion transport coincides with convection transport and may oppose to electrical migration transport.

2.3.2 Role of the Gas Turbulence

Very extensive experimental and theoretical investigations of the effect of a gas turbulence on collection efficiency in plate-to-plate, and wire-plate with and without corona discharge were conducted by Self et al. [53]. They showed that the collection efficiency in wire-plate configuration with corona discharge, and initially uncharged dust particles, depends very little on the inlet turbulence level of gas. The results were quite surprising, since the findings obtained under similar conditions but with precharged dust particles showed that collection efficiency degrades with increasing turbulence level. The effect was attributed to the particle charging in non homogeneous field, where the turbulence, on the average, enhances particle charging by deflecting particles towards the area of higher electric field and ion density. Moreover, they stated that the beneficial effect of the high turbulence on the particle charging is mainly near the entrance section, in few first fields, whereas the beneficial effect of low turbulence on particle transport is operative throughout ESP. Kim and Lee [31], also experimentally investigated, the effect of turbulent gas flow on particle transport and collection efficiency in wire-pate ESP geometry by inserting the mesh of various grid sizes in front of the ESP. They showed that at high applied voltages, and consequently high electric fields, the collection efficiency was not affected significantly by gas flow turbulence.

2.3.3 Dust Particle Collection Efficiency

Dust particle collection efficiency is usually based on the Deutsche model [123] that assumes complete turbulent mixing of dust particles. The model considers an invariant particle profile transverse to the gas flow and a thin boundary layer near the collecting electrode walls, where the dust particle migration velocity is assumed to be invariant along the ESP length. By equating the dust particle flux across the laminar flow boundary and the dust particle flux onto the collecting plate, an exponential function describing the change of the dust concentration along the ESP length can be obtained. Accordingly, the particle collection efficiency η can be obtained from the ratio of the outlet (c_{out}) versus the inlet (c_{in}) particle concentration as described in (2.8).

$$\eta = 100(1-\frac{c_{out}}{c_{in}}) = 100(1-e^{-(De)^k})\ [\%] \tag{2.8a}$$

$$De = \omega_{th}\frac{A}{Q_g} = \frac{\omega_{th}W}{U_o L};\quad \omega_{th} = \mu_{cd}E\ ;\quad \mu_{cd} = \frac{Q_p C_m}{6\pi\mu_g r_d} \tag{2.8b}$$

$$C_m = 1 + A_o\frac{\lambda}{r_d};\quad A_o = 1.257 + 0.42e^{-0.87\frac{r_d}{\lambda}} \tag{2.8c}$$

Where, De is Deutsche's number, ω_{th} *[m/s]* is the local theoretical migration velocity of the charged particles of radius r_d *[m]*, *W [m]* is the length of the ESP, *L [m]* is the wire-to plate spacing, *A* $[m^2]$ is the dust collection surface area, U_o *[m/s]* is the mean gas velocity, Q_g $[m^3/s]$ is the gas flow rate, μ_{cd} $[m^2/Vs]$ is the mobility of the charged particles, Q_p *[C]* is the dust particle surface charge, *E [V/m]* is the volume averaged electric field, μ_g *[Pa s]* is the gas viscosity, λ_i *[m]* is the mean free path of ions, C_m is the Cunningham slip factor, and k is the dust property correction coefficient $(0.5 \leq k \leq 1)$.

On the other hand, for laminar flow the collection efficiency is given by (2.9)

$$\eta = De \tag{2.9}$$

Those two equations, (2.8) and (2.9), represent limiting cases. Equation (2.8) corresponds to an infinite particle diffusion and (2.9) corresponds to zero particle diffusion. In the case of a finite turbulent level in ESP, it was observed that the measured collection efficiency is higher than that predicted by Deutche's model. Cooperman [124] proposed a model that takes into account a diffusion, and re-entrainment (R) of particles (2.10). He expressed the collection efficiency as a function of Peclet number $(Pe=\omega_{th}L/D_p)$ and re-entrainment factor $(R=1/Pe)$. Here, ω_{th} is the particle migration velocity, L is the characteristic length (wire-to-plate spacing) and D_p is the particle diffusion.

$$\eta = 1 - e^{Co} \tag{2.10a}$$

$$Co = \frac{U_o W}{2D_p} - \sqrt{\left(\frac{U_o W}{2D_p}\right)^2 + (1-R)Pe\left(\frac{W}{L}\right)^2} \tag{2.10b}$$

Many other researches tried to develop analytic models based on the convection-diffusion equations subject to certain approximations. Leonard et al. [124] proposed the model based on the finite eddy diffusivity according to (2.11).

$$\eta = 1 - \sum_{m=1}^{\infty} C e^{-\Omega \frac{W}{L} F} \frac{\sin\theta}{\theta} e^{\frac{Pe}{2}} \tag{2.11a}$$

$$C = \frac{A}{B}; \quad Pe = \frac{\omega_{th} L}{D_p}; \quad \Omega = \frac{\omega_{th}}{U_o} \tag{2.11b}$$

$$A = \frac{e^{-\frac{Pe}{2}} U_0}{\theta^2 + (\frac{Pe}{2})^2} \{ -Pe\cos\theta + (\theta - \frac{Pe^2}{4\theta}) \sin\theta + \frac{Pe}{e^{-\frac{Pe}{2}}} \} \tag{2.11c}$$

$$B = \frac{1}{2} + \frac{Pe}{4\theta^2} + \frac{Pe^2}{8\theta^2} + \frac{1}{4\theta}(1 - \frac{Pe^2}{4\theta^2}) \sin 2\theta - \frac{Pe}{4\theta^2} \cos 2\theta \tag{2.11d}$$

$$F = \frac{1}{\Omega^2} \frac{Pe}{2} \{ \sqrt{1 + \Omega^2 [1 + (\frac{2\theta}{Pe})^2]} - 1 \} \tag{2.11e}$$

$$\tan\theta = \frac{-2(\frac{2\theta}{Pe})}{1 - (\frac{2\theta}{Pe})^2} \tag{2.11f}$$

Xiangrong et al. [92] used the method of separation of variables to solve the particle transport equation with two diffusion coefficients.

$$\eta = 1 - e^{F \cdot De} \tag{2.12a}$$

$$F = \frac{U_0}{\omega_m} \frac{Pe_x}{2} \{ \sqrt{1 + \frac{\omega_{th}}{U_0} \frac{Pe_x}{Pe_y} [1 + (\frac{2\theta}{Pe_y})^2} - 1 \} \tag{2.12b}$$

$$Pe_x = \frac{\omega_{th} L}{D_y};\ Pe_x = \frac{U_0 L}{D_x};\ tg\theta = \frac{4(\theta / Pe_y)(F-1)}{(2\theta / Pe_y)^2 + 2F - 1}; A = \frac{2\theta}{Pe_x} B \tag{2.12c}$$

$$B = \frac{(4\theta^2 + Pe_y^{\ 2}) C_o}{(4\theta^2 + Pe_y^{\ 2})(2\sin\theta / Pe_y) e^{Pe_y/2} + 8\theta(1 - \cos\theta e^{Pe_y/2}) - (16\theta^2 / Pe_y) \sin\theta e^{Pe_y/2}} \tag{2.12d}$$

2.3.4 Dust Particle Adhesion/Re-entrainment to/from the Dust Layer

Once the particle approaches the collecting electrode, its deposition is determined by the combination of the mechanical and electrical forces. Dust particle re-entrainment occurs in two forms: (a) rapping and (b) non-rapping. Rapping of collecting electrodes results in the re-entrainment of dislodged particulate matter in a gas stream. The further capture of re-entrained particulate matter depends on the rapping location. The ESP emission can increase significantly when re-entrainment occurs in the last electrical section. Non-rapping forces include: (a) gravity force, (b) electrostatically induced force on the dust layer due to the charge acquired by induction, (c) erosion due to the gas flow and corona wind, and (d) back corona discharge. Blanchard et al. [58] conducted experiments for dust particle sizes smaller than $5 \mu m$ in diameter, indicating two major modes of dust layer growth and dust particle packing, and correlated different dust particle packing with the current density across the dust layer. The reported re-entrainment occurred from the dust layer zone with dendric structure, where the current density is much smaller than $0.01\ mA/m^2$.

Krinke et al. [125] and Mochizuki et al. [126] identified the forces and classified them according to their effect on the adhesion and re-entrainment of particles already deposited on the collecting electrode. Van der Waals force, an intermolecular force depending on the dust particle diameters, increases with decreasing dust particle diameter. Van der Waals force is higher for the dust-to-CE contact than for the dust-to-particle contact. A capillary force is generated by the condensation of the moisture between the particles with a noticeable effect when the relative humidity exceeds approximately *60 %*. The Coulomb force generated by the charge-up between the dust particles in contact is usually negligible for dust particle sizes smaller than $100\ \mu m$. The Johnsen-Rahbek force generated by the contact-surface capacitance is proportional to the dust particle resistivity, contact surface area, and current density. In general the Van der Waals force is approximately two orders of magnitude higher than the electrostaticly induced force for the particle size diameters less than *10 μm*. Johnsen-Rahbek force is higher than Van der Waals force for dust particle resistivities larger than $10^7\ \Omega m$ at current density of $0.1\ mA/m^2$. The cut-off current density for the dust particle resistivity of $10^{10}\ \Omega m$, at which the Johnsen-Rahbek force is higher than Van der Waals force, is $1\ \mu A/m^2$. Table 2.4 and Figure 2.15 summarize the forces acting on the particles near and at collecting plate.

Table 2.4
Forces acting on the dust particles

Force	Equation	Comment
Gravitational force (2.13a)	$\vec{F}_G = \frac{1}{6}\pi(2r_p)^3 \rho_p \vec{g}$	Usually, neglected for particle smaller than *100 μm.*
Therm-ophoretic force (2.13b)	$\vec{F}_T = 12\pi\mu C_{tm} r_p{}^2 \{1.42\frac{\lambda}{r_p} - 0.06\}\nabla T;$ $C_{tm} = \frac{3}{4}\sqrt{\frac{2R}{\pi T}}$	Requires high temperature gradients
Van der Waals force$_{ps}$ (2.13c)	$F_{vdW-PS} = \frac{2A_H}{3}\frac{r_p{}^3}{x^2(x+2r_p)^2}\vec{r}$	Acting between particle and substrate.
Van der Waals force$_{pp}$ (2.13d)	$F_{vdW-PP} = \frac{32A_H}{3}\frac{r_p{}^6}{x^2(x+4r_p)^2(x+2r_p)^3}\vec{r}$ Hamaker constant $A_H=4\times10^{-19}$	Acting between two particles.

Table 2.4 (continued)

Force	Equation	Comment
Johnsen-Rahbek force (2.13e)	$F_{JR} = \frac{1}{2}\varepsilon_c \rho_c^2 J_c^2 S_c$ $\rho_p = R_c \frac{S_c}{\alpha}$; $R_c = \frac{1}{2}\rho_p \sqrt[3]{\frac{E_{Young}}{F_{JR} r_c}}$; $\alpha = (\frac{F_{JR}}{n_z})^{2/3}$ $n_z = \sqrt{(\frac{16}{9\pi^2} \frac{r_{p1} r_{p2}}{(k_1 + k_2)^2 (r_{p1} + r_{p2})})}$ $k_1 = k_2 = \frac{1 - 0.14^2}{\pi E_{Young}}$	S_c.. contact surface J_c.. contact current density ρ_c...electrical resistivity of contact surface R_c... contact resistance α...displacement
Electric force (2.13f)	$F_E = Q\vec{E}$	Due to the external electric field (E)
Coulomb force (2.13g)	$Fc = \frac{Q_1 Q_2}{4\pi\varepsilon_o x^2}\vec{n}$	Acting between two particles of charge Q_1 and Q_2 spaced by x.
Electrostatic induced force (2.13h)	$F_{EI} = 0.832(\frac{2\pi^3}{12}\varepsilon_o \varepsilon_p d_{p2}^2 E^2)\vec{n}$	Induced charge on the collecting electrode due to the charge on the discharge electrode
Image force between particles and substrate (2.13i)	$F_{I-PS} = \frac{Q^2}{4\pi\varepsilon_o (2x)^2} \frac{\varepsilon_s - 1}{\varepsilon_s + 1}\vec{n}$	Force between charged particles at distance x from the neutral dust layer surface.
Image force between two particles (2.13j)	$F_{I-PP} = (\frac{d_{p2}^2 Q_1^2}{8\pi\varepsilon_o x^3} - \frac{2 d_{p2}^2 x Q_1^2}{\pi\varepsilon_o (4x^2 - d_{p2}^2)^2})\vec{n} -$ $(\frac{d_{p1}^2 Q_2^2}{8\pi\varepsilon_o x^3} - \frac{2 d_{p1}^2 x Q_2^2}{\pi\varepsilon_o (4x^2 - d_{p1}^2)^2})\vec{n}$	Between incoming particle of diameter d_{p1}, surface charge Q_1 and deposited particle (d_{p2}, Q_2) at distance x.

In this work, the re-entrainment of dust particles was neglected since the sum of the attractive forces (Van der Wals and Johnsen-Rahbek force) is greater than the sum of repulsive forces (induced and particle-particle image force) for dust particles in 0.01 to 1 μm size range.

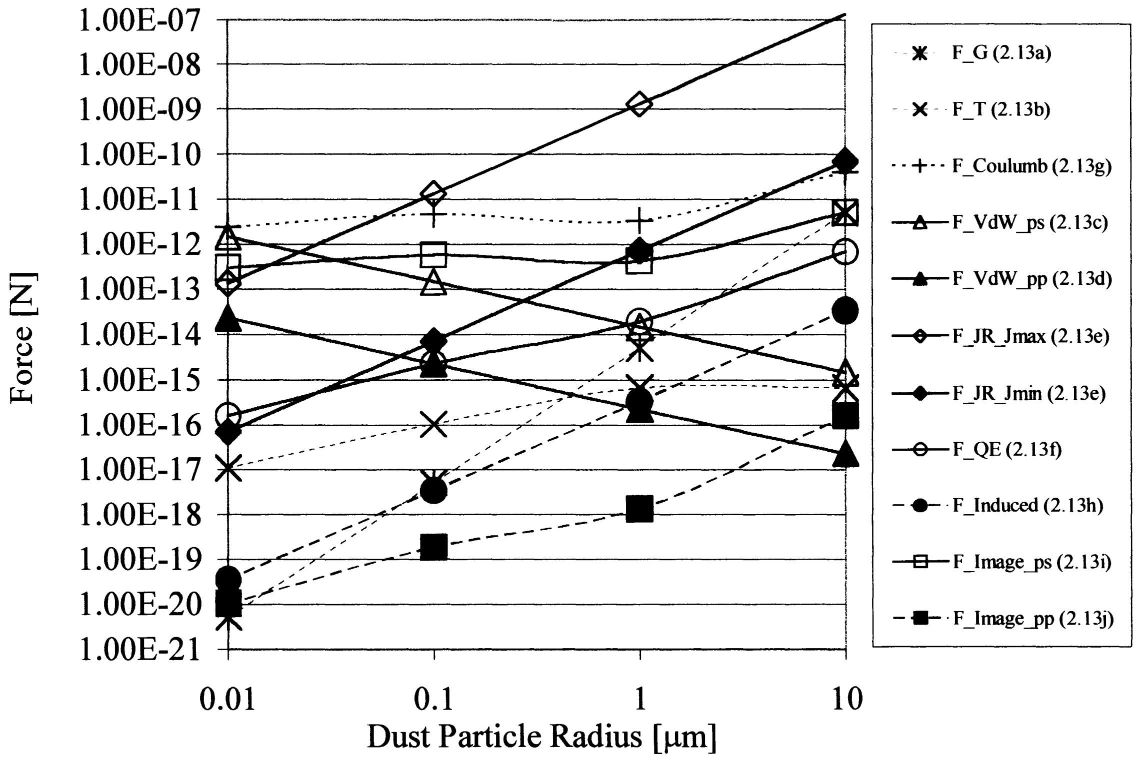

Figure 2.15 Forces acting on dust particles (F_JR_Jmax is evaluated at current density of *0.1 mA/m²* and dust resistivity of 1×10^{10} *Ωm*; F_JR_Jmin is evaluated at current density of *1 μA/m²* and dust resistivity of 1×10^{10} Ωm. Electrical forces depending on the particle surface charge are evaluated based on the values of particle surface charge from Figure 2.10. In the area of zero current density dust particles larger than 1*μm* may be re-entrained from the collecting electrode.)

2.3.5 Back Corona Discharge

Back-corona discharge is triggered by the electrical breakdown of the dust layer that occurs due to the high dust resistivity and high ionic current across the dust layer. Back-corona discharge creates positive ions that tend to neutralize incoming negatively polarized particles, and reduces the electric field near the collecting electrode, thus impairing dramatically dust collection. Masuda and Mizuno [127] observed three modes of back-corona discharge in needle-plate geometry: (a) space streamers, (b) surface streamers, and (c) a combination of space and surface streamers occurring together. Masuda et al. [128] proposed a bias-controlled pulse charging system for reducing back-discharge purely by an electrical approach. The Hofer and Schwab [129] experiments, with a barbed-type discharge electrode, show a correlation between location of the back corona discharge, porosity of dust layer, and dust resistivity. In the case of a low resistivity dust, back corona discharge was initiated outside the highly-packed dust-layer regions of ellipsoid shape. The back-corona discharge within ellipsoid regions was observed in the case of high resistivity dust. Masuda and Mizuno [127] and Chang and Bai [130] conducted experimental investigations on laboratory wire-plate type ESP for submicron dust particles. These measurements showed that in the presence of back corona discharge, the collection efficiency of submicron dust particles can be reduced significantly due to the reduction in both, particle surface charge and migration velocity.

2.3.6 Role of the EHD Flow

Electrohydrodynamically (EHD) introduced secondary flow results from the corona generated ionic flow that in collision with neutral gas molecules may transfer momentum on to the main gas flow resulting in the modification of the main gas flow streamlines. It is very unlikely that the body force of charged particles will impact the main gas flow as it has been confirmed in experimental study by Peterson and Davidson [131]. Therefore, the coupling between the body force due to the charged dust particles and main gas flow is negligible. At present, there is a strong disagreement among researchers whether the presence of EHD induced secondary flow enhances or degrades precipitator efficiency due to the interconnections between EHD flow and: (a) the main gas flow streamlines and gas turbulence level, (b) the particle transport, particle turbulence, and particle charging, and (c) the re-entraiment of already collected dust particles.

The effect of EHD flow on the main gas flow streamlines is studied experimentally and numerically by various authors for various geometries [22, 23, 55, 132-134]. For wire-plate geometries, experimental studies indicate strong dependence on the polarity of the applied voltage [25]. Positive corona in wire-plate geometry tends to produce a recirculation vortex near the collecting plates, more or less opposite to discharge electrodes. For negative corona, irregular location of discharge tufts on the time scale of a few seconds introduces quasi-steady EHD flows that contributes to redistribution of pre-existing turbulence, and opposes formation of large scale secondary flows [124, 53]. Yamamoto and Velkoff [22], and Adachi et al. [27] conducted experimental and numerical studies of flow modifications near the collecting electrode in a wire–plate configuration. Based on their numerical 2D vorticity-stream and experimental studies of main gas flow, the modification of the main gas flow streamlines by the EHD induced secondary flow at positive corona were first observed when the $N_{EHD} \approx 2$, which in the standard notification means that the E_{hd} is 2^2 times greater than the Reynolds number squared *(Re^2)* . The EHD number *(E_{hd})* and Reynolds number *(Re^2)* are defined as follows:

$$E_{hd} >> Re^2 \tag{2.14a}$$

$$Re = \frac{U_0 L}{\nu_g}; \qquad E_{hd} = \frac{I_T L^3}{A \rho_g {\nu_g}^2 \mu_i} \tag{2.14b}$$

where U_0 *[m/s]* is the mean gas velocity, L *[m]* is the characteristic length, ν_g *[m²/s]* is the gas kinematic viscosity, I_T *[A]* is the total discharge current, A *[m²]*is the surface area of the collecting electrode, ρ_g *[kg/m³]* is the gas density, and μ_i *[m²/Vs]* is the ion mobility. Recent numerical studies by Yamamoto et al. [134] for negative tuft corona showed complex Goertler-vorticity-type structure of the gas flow resembling spiral ring structure.

In the case of rods with pins or spikes where the negative tuft location can be controlled, the ion flow patterns, shown in Figure 2.16, may induce transverse recirculation vortices between electrodes and discharge barbs, that together may form the doughnut-shape vorticity associated with each discharge point. The overall effect on the orientation and intensity of vortices depends on the main gas velocity, current density, and discharge electrode geometries.

The effect of EHD flow on the transverse (normal to collecting plate) component of the particle velocity for helical- and rigid-type discharge electrodes has been conducted by Halldin et al. [56]. The results showed that the ion flow at the corona locations enhanced locally the transverse particle velocity for mean particle diameters of

0.18μm, especially in the case of rigid-type discharge electrodes. The experimental study by Atten et al. [26] indicated also that good control of EHD induced vorticieties may improve the collection efficiency of sub-micron particles. Namely, small particles may be caught in vortex regions, thus increasing the residence time, particle surface charge, and collection efficiency. Mitchner et al. [135], Self et al. [53] and Leonard et al. [124] concentrated on the investigation of the particle turbulence caused by the positive and negative corona. They conducted extensive studies for plate-to-plate, wire-plate geometry with low and high gas turbulence, precharged and not-precharged dust particles at low ionic space charge conditions. The results for precharged particles showed that the turbulence is detrimental to collection efficiency that agrees with some other experimental and theoretical work indicating that by lowering the turbulence, the collection efficiency will increase. The results for not precharged particles are completely reversed showing higher collection efficiency for high turbulence case. It seams that the mixing properties of high turbulence can be beneficial to the particle charging process within the inlet section of ESP, whereas the beneficial effect of the low turbulence on particle transport is active throughout the whole ESP.

With respect to the correlation between EHD flow and particle reentrainment, the study of the packing of the dust layer [136, 137] indicates that the EHD induced secondary flow may be the reason for re-entrainment of already collected dust particles from the dust layer with a dendric packing structure, thus detrimental for the particle collection efficiency.

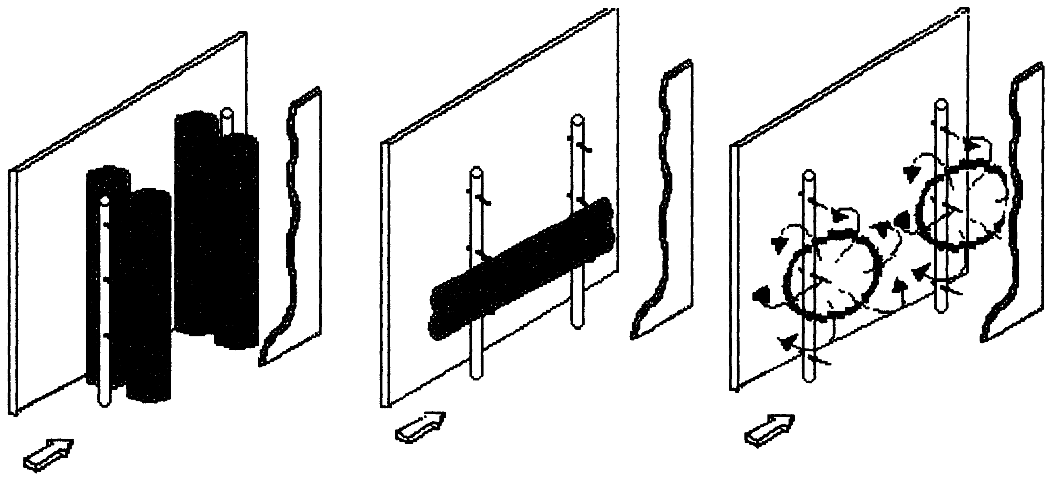

a) b) c)

Figure 2.16. EHD flow patterns for a rod with spikes discharge electrode with spikes oriented normal to the collecting plate. Shown is EHD flow:
(a) between two electrodes, (b) between two needles, (c) associated with each needle point.

CHAPTER 3

GOVERNING EQUATIONS AND NUMERICAL PROCEDURES

3.1 GENERAL GOVERNING EQUATIONS

The corona discharge, particle charging, and particle collection, extremely complex and interdependent processes, are described by a set of general governing equations that require knowledge of several engineering disciplines. For example, governing equations for gas flow are derived from the mass and momentum conservation equations. Ion, neutral dust and charged dust density profiles are obtained from the transport equations, and the electric field is obtained from Poisson's equation.

3.1.1 Gas-phase Governing Equations

The mass and momentum conservation equations of a gas-particulate mixture can be separated into gas and particle phase equations for non-reactive disperse flows [47, 138] when particle density is at diluted conditions. In general, the two-phase flow may be classified as a disperse flow when void fraction is greater than *95 %*. In general, dust loading in electrostatic precipitators is in the range from *1* to *50* g/m^3. With assumption of mean dust particle size of *0.5* μm and particle density of *1* g/cm^3 [139], the void-fraction $(\alpha_g = 1 - \alpha_p)$ would be approximately *99.99 %* and density-fraction ratio $(\alpha_p \rho_p / \alpha_g \rho_g)$ would be approximately *0.038*. In this work the particle density is well below

76.4×10[13] thus the particle phase can be separated from the gas phase. The mass conservation equation of a gas phase [138] can be described by Equation (3.1a):

$$\frac{\partial(\alpha_g \rho_g)}{\partial t} + \nabla\cdot(\alpha_g \rho_g \vec{U}_g) = 0 \tag{3.1a}$$

where α_g is the gas molecule fraction or (void fraction), ρ_g is the gas density and $\vec{U}_g$ is the gas velocity vector. For the steady-state $(\frac{\partial(\alpha_{gf}\rho_g)}{\partial t} = 0)$, incompressible $(\nabla\cdot\rho_g=0)$, and disperse flow $(\alpha_{gf}\approx 1)$ case, the Equation 3.1a reduces to Equation 3.1b.

$$\nabla\cdot(\vec{U}_g) = 0 \tag{3.1b}$$

The momentum equation for gas phase [69] is as follows:

$$\frac{\partial(\alpha_g \rho_g \vec{U}_g)}{\partial t} + \nabla\cdot(\alpha_g \vec{U}_g \rho_g \vec{U}_g) = -\nabla(\alpha_g P_g) + \nabla(\alpha_g \mu_g \nabla \vec{U}_g) + \rho_p f_d(\vec{U}_p - \vec{U}_g) - \alpha_g \rho_g \vec{g} + \vec{f}_{EM} \tag{3.2a}$$

where P_g is the pressure, μ_g is the dynamic viscosity, f_d is the interfacial drag between particle and gas phase given by Stokes as $f_d = 3\pi\mu_g d_p$, d_p is the particle diameter, $\vec{g}$ is the gravitational force vector, $\vec{U}_p$ is the particle velocity vector, and $\vec{f}_{EM}$ is the momentum change due to the electromagnetic field known as a body force. The driving forces of electromagnetic body forces [140] are as follows:

$$\vec{f}_{EM} = q\vec{E} - \frac{E^2}{2}\nabla\varepsilon + \frac{1}{2}\nabla\left(E^2 \rho\left(\frac{\partial\varepsilon}{\partial\rho}\right)_T\right) \tag{3.2b}$$

where the first term is the momentum change due to the space charge of ions and charged particles, the second term is the momentum change due to the dielectric property change, and the third term is the momentum change due to the electromagnetostriction. Under assumptions of a steady state, incompressible, disperse flow, with neglected gravitational effect, particle and gas velocity equilibrium, and ionic space charge body force, Equations 3.2a and 3.2b combined give:

$$(\vec{U}_g \rho_g \cdot \nabla)\vec{U}_g = -\nabla(P_g) + \mu_g \nabla^2 \vec{U}_g + q\vec{E} \tag{3.2c}$$

3.1.2 Governing Equations of Ions and Particles

Basically, the transport of ions, particles, or any other chemical species must satisfy the general conservation principle, described by Equation 3.3a.

$$\frac{\partial N_k}{\partial t} + \nabla \cdot (\vec{J}_k) = S_k - R_k \tag{3.3a}$$

Here, $\partial N/\partial t$ represents the rate of change or accumulation of species within the control volume, $\nabla \cdot (\vec{J})$ represents the divergence of net species flux across the control volume, subscript *k={e; ni; pi; nd; pcd; ncd}* refers to the type of species e.g. electrons (*e*), negative ions (*ni*), positive ions (*pi*), neutral dust particles (*nd*), negatively (*ncd*) and positively (*pcd*) charged dust particles, and *S* and *R* represent the source and the sink of species by chemical, mechanical or electrical reactions. Some experimental and theoretical analysis of the behaviour of dust particles in the dust layer indicates that some mechanical source terms due to back-corona discharge and re-entrainment of the dust layer should be considered [129, 130, 141]. In this work they are neglected due to the: (a) frequent cleaning of collecting electrodes, (b) sticky nature of the dust layer created by combustion of an incense stick, and (c) the relatively low resistivity $(\rho \sim 5.3\times10^{10}\ [\Omega m])$

of dust particles. Only the electrical reaction such as attachment of ions to the particle surface is considered.

The flux of the species is governed by convection, diffusion or mobility as shown in Eq. 3.3b.

$$\vec{J}_k = (\vec{U}N_k \pm \mu_k \vec{E}N_k - D_k \nabla N_k) \tag{3.3b}$$

The convection transport, first term, represents the transport due to the general gas flow ($\vec{U}$). The drift transport, second term, represents the transport due to the mobility of species (μ_k) in the electric field ($\vec{E}$). The sign of the mobility term is positive for positive ions and positively charged particles. Accordingly electrons, negative ions, and negatively charged dust particles have negative mobility term. The diffusion transport, the third term, is the transport of the species with diffusion coefficient (D_k) due to the gradient of species concentration N_k. Minus sign indicates that the species are diffusing from the region of high towards the region of low species concentration. For steady state, and substituting Eq. 3.3b in Eq. 3.3a yields

$$\nabla \cdot (\vec{U}N_k) + \nabla \cdot (\pm \mu_k \vec{E}N_k) - \nabla \cdot (D_k \nabla N_k) = S_k - R_k \tag{3.3c}$$

Further expansion of the first and second terms for incompressible flow ($\nabla \cdot \vec{U}$=0) yields,

$$\vec{U} \cdot \nabla N_k \pm N_k \vec{E} \cdot \nabla \mu_k \pm \mu_k N_k \nabla \cdot \vec{E} \pm \mu_k \vec{E} \cdot \nabla N_k - D_k \nabla^2 N_k - \nabla N_k \cdot \nabla D_k = S_k - R_k \tag{3.3d}$$

The first term is the divergence of flux due to convection by the main gas flow. The magnitude of the term depends on the species considered. It is usually neglected for ions, however, in evaluation of any new ESP geometries should be taken into account as it will be shown in Chapter 4. The second, the third, and the fourth terms combine the divergence of flux due to species migration. The second term contributes to compressibility of species and can be neglected in case of the negative/positive ions due to the constant mobility term $(\nabla\mu_k=0)$. The mobility of electrons is the function of the electric field, thus location dependent, and therefore should be taken into account. For particles charged through a non uniform electric field and ion density, the mobility is a function of both space and time. In some cases for which the particles are fully charged, the second term can be neglected due to the small mobility gradient $(\nabla\mu_k\approx 0)$. However, for submicron dust particles, that encounter high surface change in the region close to discharge electrode, the second term should be considered at least in first few fields of ESP. In later sections of ESP, where the acquired charge is not changing significantly, the second term can be neglected. The third term that contains the $(\nabla \cdot \vec{E})$ is usually substituted by Poisson's equation. The last two terms depend on the diffusion constant of the species, whereby (∇D_k) can be neglected assuming uniform diffusivity such as in the case of ions and neutral dust particles. The equation 3.3d belongs to a general convection-diffusion type equations. The well-known upwind scheme is usual procedure used for the treatment of convection part.

In this work, it was assumed that processes occurring in that zone are ion production processes, and that from the border of ionization region only ionic current consisting of negative ions is injected in an inter-electrode space [95]. The assumption is supported by the fact that the ionization region is normally very thin. Thus, positive ions and electrons, found in a corona-glow zone near a discharge electrode, are not considered. Accordingly, negatively charged dust particles and neutral dust particles are considered.

3.1.3 Governing Equations of Electric Field

Since magnetic effects are neglected, the electrostatic equations are:

$$\nabla \times \vec{E} = 0 \tag{3.4a}$$

and therefore:

$$\vec{E} = -\nabla V \tag{3.4b}$$

Gauss's law relates the electric field vector $\vec{E}$ to volume charge density q_v.

$$\nabla \cdot (\varepsilon \vec{E}) = q_v \tag{3.4c}$$

In the case of constant permittivity ε, equations (3.4b) and (3.4c) combined give Poisson's equation as follows:

$$\nabla^2 V = -\frac{e}{\varepsilon}(N_+ - N_-) \tag{3.5a}$$

Assuming that only negative ions (N_i) and negatively charged particles (N_{cd}) exist in drift space, equation (3.5a) becomes:

$$\nabla^2 V = \frac{e}{\varepsilon}(N_i + m_s N_{cd}) \tag{3.5b}$$

where m_s is the number of elementary charges on the surface of the charged dust. With respect to the dust particle charging, the total number of elementary charges on the surface of the particle ($m_s = m_{s\text{-}dc} + m_{s\text{-}fc} + m_{initial}$ is assumed to be the sum of the diffusion ($m_{s\text{-}dc}$), field ($m_{s\text{-}fc}$) and initial surface charge ($m_{initial}$).

3.1.4 Dimensionless Form of Governing Equations

The momentum, electric field, ion and charge transport equations are transformed into dimensionless form in equations (3.6)-(3.10) to establish the significance of each term.

$$(\vec{u}_g \cdot \tilde{\nabla})\vec{u}_g = -\tilde{\nabla}(p_g) + \frac{1}{\mathrm{Re}}\tilde{\nabla}^2\vec{u}_g + \frac{E_{HD}}{\mathrm{Re}^2} n_i\vec{\xi} \tag{3.6}$$

$$\tilde{\nabla}^2\Phi^* = (-D^*{}_{bi} n_{i\_} - D^*{}_{bd} c n_{cd}) \tag{3.7}$$

$$\mathrm{Ra}_i \vec{u}^*{}_g \cdot \tilde{\nabla} n_i + \mathrm{F}_E \tilde{\nabla}\cdot(n_i\vec{\xi}) - \tilde{\nabla}^2 n_i = -\alpha_i^* n_i n_{nd} \tag{3.8}$$

$$\mathrm{Ra}_{nd} \vec{u}^*{}_g \cdot \tilde{\nabla} n_{nd} - \tilde{\nabla}^2 n_{nd} = -\alpha_{nd}^* n_i n_{nd} \tag{3.9}$$

$$Ra_{cd} \vec{u}^*{}_g \cdot \tilde{\nabla} n_{cd} - F_E \tilde{\nabla}\cdot(n_{cd}\vec{\xi}) - \tilde{\nabla}^2 n_{cd} = \alpha_{cd}^* n_i n_{nd} \tag{3.10}$$

The dimensionless variables are defined as follows:

$$\tilde{\nabla} = L\nabla; \qquad \vec{u}_g = \vec{U}_g / \overline{U}; \quad p_g = P_g / \rho\overline{U}^2; \tag{3.11a}$$

$$n_i = \mathrm{N_i/N_{io}}; \quad n_{nd} = \mathrm{N_{nd}/N_{do}}; \; n_{cd} = \mathrm{N_{cd}/N_{do}}; \tag{3.11b}$$

$$\Phi^* = \Phi / F_E; \quad \Phi = eV / kT; \quad F_E = eV_o / kT; \tag{3.11c}$$

$$\vec{\xi} = \vec{E} / E_o; \qquad E_o = V_o / L; \tag{3.11d}$$

$$E_{HD} = JL^3 / \mu_i \rho_g v_g^{\,2}; \quad Re = L\overline{U} / v_g \;\; ; \tag{3.11e}$$

$$Db_i^* = Db_i^2 / F_E; \; Db_d^* = Db_d^2 / F_E; \; Db_i = L / \lambda_{Di}; \; Db_d = L / \lambda_{Dd}; \tag{3.11f}$$

$$\lambda_{Di} = \sqrt{\varepsilon kT / e^2 N_{io}}; \; \lambda_{Dd} = \sqrt{\varepsilon kT / e^2 N_{do}}; \tag{3.11g}$$

$$Ra_i = Re\,Sc_i; \; Ra_{nd} = Re\,Sc_{nd}; \; Ra_{cd} = Re\; Sc_{cd}; \tag{3.11h}$$

$$Sc_i = v_g / D_i; \;\; Sc_{nd} = v_g / D_{nd}; \; Sc_i = v_g / D_{cd}; \tag{3.11i}$$

$$\alpha_i^* n_i n_{nd} = R_i^*;\ \alpha_i^* = (L^2/D_i)(\partial m_s/\partial t)(N_{do}/N_{io}); \tag{3.11j}$$

$$\alpha_{nd}^* n_i n_{nd} = R_{nd}^*;\ \alpha_{nd}^* = (L^2/D_{nd})(\partial m_s/\partial t); \tag{3.11k}$$

$$\alpha_{cd}^* n_i n_{nd} = S_{cd}^*;\ \alpha_{cd}^* = (L^2/D_{cd})(\partial m_s/\partial t); \tag{3.11l}$$

where L is the characteristic length, $\vec{u}_g$ is the dimensionless gas velocity vector, p is the dimensionless pressure, Re is the Reynolds number, $\Phi*$ is the dimensionless electric potential ratio, F_E is the electric field number, E_{hd} is the Electrohydrodynamic (EHD) number, D^*_{bi} and D^*_{bd} are Debye versus electric field number of ions and dust, λ_{Di} and λ_{Dd} are Debye length of ions and charged dust, n_i , n_{nd} and n_{cd} are dimensionless numbers densities of negative ions, neutral and negative charged dust respectively, N_{io} is the initial number of ions, N_{do} is the initial number of dust, R_i^* is the dimensionless sink of negative ions, R_{nd}^* is the dimensionless sink of neutral dust, S_{cd}^* is the dimensionless source of negatively charged particles, $\partial m_s/\partial t$ is the rate of the charging of dust particles.

The importance of certain effects is evaluated based on dimensionless number analysis. For example, the Diffusion Reynolds number (Ra_i) versus Electric field number (F_E) ratio is used as a measure of general and diffusion ion transfer, versus ion transfer due to the electric field.

$$\frac{Ra_i}{F_E} = \frac{\mathrm{Re} \cdot Sc_i}{F_E} = \frac{\dfrac{U_0 L}{D_i}}{\dfrac{eV_0}{kT}} \tag{3.12}$$

Where, $U_0\ [ms^{-1}]$ is the mean gas velocity, $L\ [m]$ is the characteristic length, $D_i\ [m^2s^{-1}]$ is the ion diffusion, $e=1.602\times10^{-19}[C]$ is the charge of one electron, $V_o\ [V]$ is the applied voltage, $k=1.381\times10^{-23}$ $[JK^{-1}]$ is the Boltzmann constant, and $T[K]$ is the gas temperature.

The EHD number (E_{hd}) versus Reynolds number squared (Re^2) is used as a indicator of Electrohydrodynamically (EHD) induced secondary flow.

$$\frac{\mathrm{E}_{hd}}{\mathrm{Re}^2}=\frac{\dfrac{I_T\cdot L^3}{\mathrm{A}\varphi_g \upsilon_g{}^2\mu_i}}{(\dfrac{\mathrm{U}_0 L}{\upsilon_g})^2}=\frac{I_T\cdot L}{\mathrm{A}\varphi_g \mathrm{U}_0{}^2\mu_i} \tag{3.13}$$

Where, $I_T\,[A]$ is the total current, $L\ [m]$ is the characteristic length, $A\ [m^2]$ is the collector plate area, $\rho_g\ [kgm^{-3}]$ is the gas density, $U_0\ [m/s]$ is the mean gas velocity, $\mu_I\ [m^2V^{-1}s^{-1}]$ is the ion mobility, $v_g\ [m^2s^{-1}]$ is the kinematic viscosity. The modification of the main gas flow due to the EHD induced secondary flow may be observed for $E_{hd}>Re^2$.

The $(D_b{}^2/F_E)$ ratio is used as a measure of space charge effect due to ions or charged particles. Ion and charged dust Debye numbers $(D_{bi}=L/\lambda_{Di};\ D_{bd}=L/\lambda_{Dd})$ are a ratio between characteristic length (L) and Debye length (λ_D).

$$\frac{\mathrm{D_b}^2}{\mathrm{F_E}}=\frac{(\dfrac{L}{\lambda_D})^2}{\dfrac{e\mathrm{V}}{kT}}=\frac{\left(\dfrac{L}{\sqrt{\varepsilon_o kT/N_0 e^2}}\right)^2}{\dfrac{e\mathrm{V}}{kT}} \tag{3.14}$$

Where, $L\ [m]$ is the characteristic length, $\mu_i\ [m^2V^{-1}s^{-1}]$ is the ion mobility, N_0 is the initial number of ions or dust in the case of evaluation of ion or dust charge effect, $\varepsilon_o=8.854\times10^{-12}\ [Fm^{-1}]$ is the electrical permittivity, $e=1.602\times10^{-19}[C]$ is the charge of one electron, $V_0\ [V]$ is the applied voltage, $k=1.381\times10^{-23}\ [JK^{-1}]$ is the Boltzmann constant, and T_g *[K]* is the gas temperature. The ion or charged-dust space charge effect can be observed for $D_b^2/F_E > 0.001$.

3.2 DUST PARTICLE COLLECTION EFFICIENCY MODELS

Figure 3.1a shows the simplified block diagram of the Multi-dimension ESP code (MESP) [143] used in this study. The MESP code consists of three main sections.

The first section, the ESP geometry and operating parameters, involves the selection of (a) I, U, and C type of collecting electrode; (b) wire, threaded-rod, rectangular, and spike type of discharge electrodes; (c) dc, pulsed, and intermittent type of applied voltages; (d) operating flow rate of a main gas, gas composition, and temperature; (e) dust particle loading, dust size, and shape. For a known ESP system, the average current is required as an input parameter, otherwise the subroutine I-V curve is called for prediction of the operating current, that will be used in the calculation of initial ion density. After that, the program proceeds with initial calculations, that include analytic approximations for the main gas flow, Laplace's electric field, and initial number of ions on the surface of discharge electrode based on electric field on the surface of discharge electrode, and initial averaged current.

The second section starts with establishment of coupling paths based on dimensionless numbers. At first the ions' density is obtained based on the Laplacian electric field and the initial number of ions (N_{io}), estimated from the total current and electric field on the surface of the discharge electrode. After that, the search algorithm is called that searches for the N_{io} for which the critical electric field (approx. *2 MV/m)* on discharge electrode surface is satisfied by coupling ion transport and Poisson's electric field equation. The example of the search algorithm is shown in figure 3.1b. The space charge effect, due to ions and charged dust, was evaluated based on the ion and dust Debye number. Corresponding ions/charged dust and Poisson's electric sub-routines were coupled in iterative way until the volume average value of electric field and corresponding ions/charged dust density between iteration steps did not become less than *0.001*. The last coupling subroutine corresponds to the estimation of the EHD flow. In the case of the EHD flow, the ion density and electric field are passed to the gas velocity calculation. This was in general, a one-way coupling in case of negligible space charge effect due to the dust particles. Otherwise, the neutral and charged dust transport equations together with Poisson's equation and gas flow, are coupled until the iteration stop criteria was reached.

The last section of MESP code calculates the total collection efficiency of dust particles based either on the modified Deutsche's equation (Mode 1), or neutral and charged dust density at an inlet and outlet section of ESP (Mode 2).

In the case of a multi-field ESP, there is one additional loop for the numerical analysis of each field, and for the adjustment of boundary conditions between two adjacent fields in which the ion-density/initial-surface-charge at the front plane of the i^{th} field equals the value at the back plane of preceding the $(i-1)^{th}$ field.

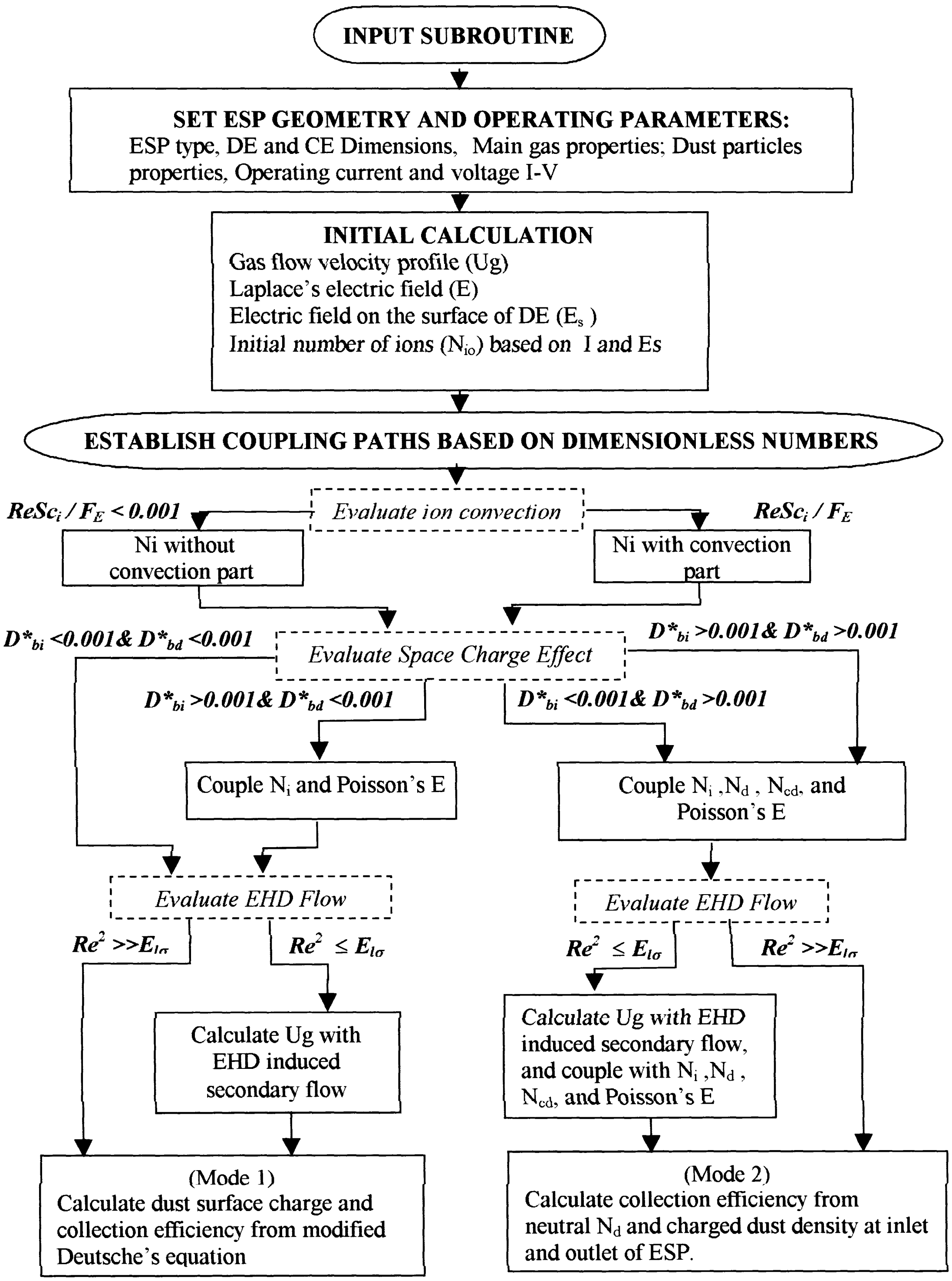

Figure 3.1a Simplified block diagram of MESP code

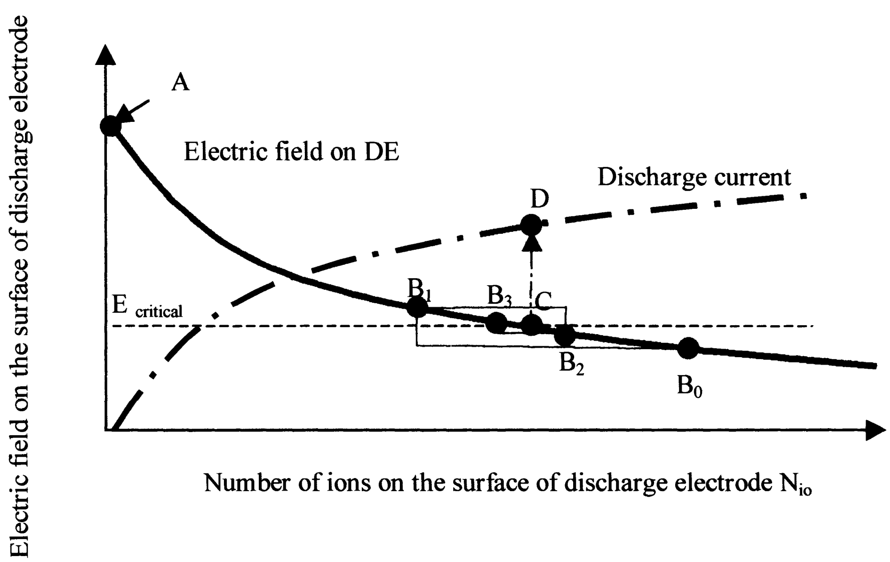

Figure 3.1b Example of determination of the initial number of ions on the surface of the discharge electrode based on the electric field at the surface of the discharge electrode. (A… solution of the Laplace equation for given applied voltage, B… solution of Poisson's equation with ion density N_{io} for various iteration steps; C… solution after convergence for which the electric field on the wire equals critical electric field; D... corresponding discharge current.

3.2.1 Three-dimensional Hybrid Model (Mode 1)

Main gas velocity, electric field, and ion density profiles are passed to the cross-sectional averaging model for i=M sections, based on which the cross-sectional surface charge on particles and cross-sectional collection efficiency η_i were obtained. Finally, the total collection efficiency was predicted based on the cumulative expression of Deutsche's equation,

$$\eta[\%] = 100(1-\sum_{i=1}^{i=M} p_i); \qquad p_i = e^{-(\frac{\omega_{th,i}A}{Q_g})^k} \tag{3.15}$$

where, p_i is the cross-sectional dust particles penetration, $\omega_{th,i}$ *[m/s]* is the local theoretical migration velocity of the charged particles, A_i *[m^2]* is the local dust collection surface area, Q_g *[m^3/s]* is the gas flow rate, and k is the dust property correction coefficient $(0.5 \leq k \leq 1)$. The present study was based on $k=1$.

In order to capture the effect of high resistivity dust on the collection efficiency, the following constitutive relationship between migration velocity (ω_p) and dust resistivity (Ω_d) is proposed based on the experiment [67]:

$$\text{for } (\Omega_d/\Omega_o) \leq c_o \qquad \omega_p = \omega_o[1-c_1(\Omega_d/\Omega_o)^{\alpha}] \tag{3.16}$$

$$\text{for } (\Omega_d/\Omega_o) \geq c_o \qquad \omega_p = \omega_o c_2(\Omega/\Omega_o)^{-\beta} \tag{3.17}$$

where ω_o is the migration velocity predicted by MESP code for the reference low dust resistivity value $\Omega_o \leq 10^{10}$ Ωm, Ω_d is the dust resistivity, and α, β, c_o, c_1, c_2 are variables dependent on the pulse frequency (P_f) and width (P_w). Here, $\alpha=0.72$, $\beta=0.73$, $c_o=250$, $c_1=0.0136$ and $c_2=33.5$ for DC ESPs are obtained from the experiments [144].

3.2.2 Three-dimensional Multi-field Model (Mode 2)

Mode 2 requires a neutral and charged dust density distribution. Hence, the total collection efficiency was obtained from equation (3.18),

$$\eta = 100(1-\frac{\sum N_{out}}{\sum N_{in}})[\%] \tag{3.18}$$

where N_{in} represents the sum of neutral and charged dust particles at the inlet plane of ESP, and N_{out} represent the sum of neutral and charged dust particles at the exit plane of ESP.

3.3. CURRENT-VOLTAGE MODELS

A current-voltage (I-V) model was developed for prediction of the operating current and initial value for the number of ions on the surface of the discharge electrode. In general, the current-voltage curve is affected by discharge and collecting electrode shape, polarity of applied voltage, and all possible operational conditions in ESP. Many other conditions, such as back-corona, the surface condition of the discharge electrode, non-uniform dust loading, etc. can affect the I-V characteristic. Therefore, it is very difficult to determine the I-V curve theoretically.

3.3.1 The Numerical Approach for Current-Voltage Characteristic

One of the approaches to obtain the I-V characteristic is to solve simultaneously the Poisson's (3.7) and current continuity equations (3.8). However, their exact solutions can only be obtained for parallel plates, coaxial cylinders, and concentric spheres. Most numerical studies of wire-plate I-V characteristic are obtained for dust-free conditions [84, 86, 87, 91, 93, 94, 97] except [88 and 67]. The standard solution process involves an initial estimate of ion density at discharge electrode and coupling of Poison's and current continuity equations until the solutions are self-consistent. After that a new initial number of ions was calculated until the critical electric field on the surface of the discharge electrode was reached. The inner iteration loop that couples Poison's and current continuity equations until the solutions are self-consistent usually requires 3 to 4 iterations. The outer loop for initial ion calculation requires 5 to 7 iterations before conversion. This, however, can be time consuming, especially for three dimensional studies. Therefore, in order to reduce the number of outer iteration loop the constitutive relationships for I-V characteristics were developed and used for the first estimate of the initial ion density. Experimental validations of I-V model were conducted for various scale-up sizes in dust free conditions, too.

3.3.2 The Constitutive Relationship for Current-Voltage Equations for Various Collecting and Discharge Electrode Geometries

Therefore, for the electrode geometry used in the experiment we used an simplified analytic expression (3.19) that gives a reasonable model for various discharge electrodes [96, 102, 145],

$$I_L = KV(V - V_i) \tag{3.19}$$

where I_L is the time-averaged current per unit length, K $(K = K_G \cdot K_d \cdot K_g)$ is constant depending on the collecting and discharge electrode geometry (K_G), dust loading (K_d), and gas parameters (K_g), V is the applied voltage, and V_i is the corona onset voltage.

The corona onset voltage V_i can be obtained from Peek's empirical expression [146] for coaxial wire-pipe electrode geometries with the discharge onset electric field (E_i) on the surface of the corona wire (3.20b),

$$V_i = E_i r_{in} \ln \frac{n}{r_{in}} \tag{3.20a}$$

$$E_i = m_G(32.15\times10^5\rho_{gf} + 9.902\times10^4\sqrt{\frac{\rho_{gf}}{r_{in}}}) \tag{3.20b}$$

$$\rho_{gf} = 0.386\frac{p[Torr]}{273+T_g[^oC]} \tag{3.20c}$$

where r_{in} is the wire diameter, r_{out} is the equivalent pipe diameter, ρ_{gf} is the gas condition factor, p is the pressure, T_g is the gas temperature, and m_G ($m_G \leq 1$) is the discharge electrode factor that takes into account the geometry and the surface condition of the electrode.

The *I-V* model for a wire-plate ESP geometry is based on the model for the cylindrical ESP, assuming that the outer radius r_{out} equals the wire-plate spacing *(D/2=L)*. However, the *I-V* characteristic does not only depend on the wire-plate spacing, but also on the wire-to-wire spacing *(2W)*. Various ESP width-over-length ratios *(D/2W=L/W)* were contained in a variable *n,* whose values are tabulated in the Table 3.1 according to Moore [145].

$$I_L = \mathrm{K_G K_d K_g} V(V-V_i) = k_G{}' \frac{4\pi\varepsilon_o}{(\frac{D}{2})^2 \ln\frac{n}{r_i}} K_d \mu_i V(V-V_i) \tag{3.21}$$

Table 3.1.

Modification of variable n according to *L/W* ratio

L/W	**n**
L/W ≤ 0.6	$4\frac{L}{\pi}$
0.6 < L/W < 2	$0.5\cdot W\cdot 0.3457e^{(1.5003\frac{L}{W})}$
L/W ≥ 2	$\frac{W}{\pi}e^{(\frac{\pi L}{2W})}$

The present work examines a plate-type collecting electrode in combination with round, rectangular, threaded, and rigid discharge electrode geometries, as shown in Figure 3.2. Discharge electrode geometries not only affect the slope of the I-V characteristic, but also the corona onset voltage (V_i). Therefore, the discharge geometry effect is incorporated into the K_G and m_G coefficients. The discharge electrode geometries are modelled by an equivalent radius r_{in} of the round discharge electrode. The equivalent diameter of the threaded wire was approximated by the mean diameter of the inside and outside thread. The equivalent diameter of the rectangular wire was approximated by the length of each side. The rigid discharge electrode requires special consideration. The value of r_{in} from equation (3.20b) was set arbitrarily to 0.15 mm. The value of r_{in} from equation (3.21) was set to half of the electrode width (B/2). Furthermore, values of m_G for round, threaded, rectangular, and rigid type discharge electrode were obtained empirically from measured corona onset voltages. In the case of a large discrepancy between the measured and calculated I-V characteristic, the geometry correction coefficient k_G' was introduced, as shown in the Table 3.2.

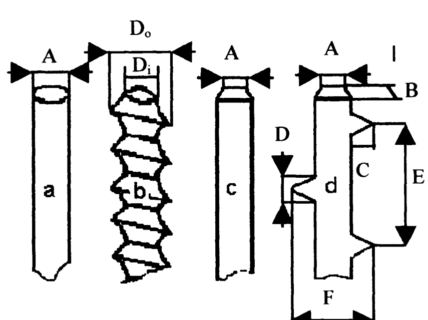

Figure 3.2. Sketch of discharge electrodes: (a) round A={0.25,1.5, 3} mm (b) threaded {Do; Di}={2.5, 2} mm, (c) rectangular A=2.7 mm, (d) spike A=10 mm, B=2 mm, C=D=9 mm, E=80 mm, F=28 mm.

Table 3.2
Values of r_i , m_G and k_G' according to DEs from Figure 3.2

DE /CE types	r_{in} [mm]	m_{DE}	k_G'
Round	0.23	0.9	4
	3		
Threaded	1.125	0.55	1.5
Rectangular #90	1.5	0.9	7
Rectangular #45			9
Rigid &short CE	1	0.9	1.3
Rigid &long CE			1.5

Rectangular #90… Discharge and collecting electrode sides are aligned.
Rectangular #45… Discharge electrode sides are rotated 45° relative to the collecting electrode orientation.

3.3.3 The Gas Composition and Temperature Effect

Gas composition and temperature effects are incorporated in the mobility of the ions [31, 85, 90] and the relative gas density. The mobility of the ions is a function of the mixture of gases, the gas temperature, the gas pressure, and the polarity of the applied voltage. A fairly substantial amount of data is available on the dependence of the ionic mobility in pure gases with gas temperature, and electric field versus pressure ratio [147-150]. However there is not enough experimental data for various gas mixtures. Therefore, the corona chemistry simulation of Chang and Kwan [151] is used to determine the dominant ion species, depending on the voltage polarity. For negative corona the dominant ion in air is $N_2O_2^-$, and for positive corona the dominant ion in air is N_3O^+.

The mobility of ions can be estimated from the reference mobility of O_2^- and O^+ ions [147-150], and the molar mass ratio [151] as follows:

$$\frac{\mu_{N_2O_2^-}}{\mu_{O_2^-}} = \sqrt{\frac{m_{O_2^-}}{m_{N_2O_2^-}}} \quad and \quad \frac{\mu_{N_3O^+}}{\mu_{O^+}} = \sqrt{\frac{m_{O^+}}{m_{N_3O^+}}} \tag{3.22}$$

The effect of the gas temperature T_g and pressure p on the mobility of the ions [147] can be approximated by:

$$\mu^i{}_T = \mu^i{}_{To} \frac{T_g[K]}{293} \frac{760}{p[Torr]} \tag{3.23}$$

3.4 GAS FLOW VELOCITY MODEL

The gas flow velocity profile is required by density distribution models of ions, neutral dust, and charged dust and by the charging rate model. Ions, neutral dust, and charged dust density distribution is governed by the convection term which depends on the gas flow velocity distribution. In order to determine the charging rate coefficient at a specific location, the charging time, which is inversely proportional to the velocity, is required.

The flow field is assumed to be fully developed laminar with constant properties (Reynolds number $Re \leq 2500$, Mach number $M<0.2$) in a bench-scale ESP, as in the most ESPs in normal operating conditions. At present the analytic solution of the flow field between two plates is implemented as follows:

$$U_y = U_o[1-(\frac{x}{x_o})^2];\ U_x = 0;\ U_z = 0 \tag{3.24}$$

Since the velocity at the surface of the discharge electrode is zero, a correction for the presence of the discharge electrode in the center of the field was implemented. Furthermore, modifications are conducted in the regions of the flow recirculation which occurs in the case of U and C-type collection electrodes. In that area the velocity was arbitrary set to zero, thus the charging time becomes the infinity value. The charging time in the flow recirculation area was set to be at least equal to the residence time of the particles.

3.5 ELECTRIC FIELD MODEL

The electric field model is required by: (a) transport models of ions, neutral dust, and charged dust, (b) particle charging model, and (c) particle collection efficiency model. The ions and charged dust transport is governed by the drift term, which is directly proportional to the electric field. The sink and source terms in the transport equation of ions, neutral dust, and charged dust are indirectly dependant on the electric field.

3.5.1 Electric Field Equations

The electric potential is obtained from the dimensionless Poisson's equation (3.25) that reduces to the Laplace equation $\tilde{\nabla}^2\Phi^* = 0$ for ion and dust Debye numbers $D^*_{bi} << 1$ *and* $D^*_{bd} << 1$,

$$\tilde{\nabla}^2\Phi^* = -(D^*_{bi} n_{i\_} + D^*_{bd} m n_{cd}) \tag{3.25}$$

where the $\Phi^*=\Phi/\Phi_o$ is the dimensionless electric potential ratio, $\Phi_o=F_E=eV_o/kT$ is the electric field number, L is the characteristic length, $D^*_{bi}=D_{bi}^2/F_E$ and $D^*_{bd}=D_{bdi}^2/F_E$ are Debye (D_b) versus electric field number (F_E) of ions and dust, $n_i=N_i/N_{io}$ is the dimensionless number of negative ions, $n_{cd}=N_{cd}/N_{do}$ is the dimensionless number of negatively charged dust particles, m is the number of elementary charges on the surface of the charged dust, N_{io} is the initial number of ions, N_{do} is the initial number of dust. In general, Equation 3.25 can be classified as a quasilinear second-order partial differential equation of elliptic type, whose solution for wire-plate geometry even in the case of the zero space charge requires numerical methods such as finite difference, finite element, donor cell methods, etc. From the analytic approximation methods, the best known is Cooperman's method based on a method of image superposition of a component without space charge, expressed in terms of series in equation (3.26a) and a component due to the space charge alone as shown in equation (3.26b),

$$\begin{aligned} V_s(x,y) = V_o[\sum_{m=-\infty}^{\infty} \ln(\frac{\cosh \pi(y-2mS_y)/2S_x - \cos(\pi x/2S_x)}{\cosh \pi(y-2mS_y)/2S_x + \cos(\pi x/2S_x)})]\times \\ [\sum_{m=-\infty}^{\infty} \ln(\frac{\cosh(\pi m S_y/S_x) - \cos(\pi a/2S_x)}{\cosh(\pi m S_y/S_x) + \cos(\pi a/2S_x)})]^{-1} \end{aligned} \tag{3.26a}$$

$$V(x,y) = V_s(x,y) + \frac{j_m S_y \ln(d/a)}{\pi \varepsilon_o \mu V_o}(S_x^{\,2} - x^2) \tag{3.26b}$$

where S_x is the wire-plate and S_y is the wire-wire spacing. In this work, the finite difference method was used to solve equation (3.25) and the Cooperman equation was used for the initial values, before iteration for faster convergence of numerical results.

3.5.2 Boundary Conditions for Electric Potential

Since the boundary conditions for the electric potential are $V=0$ at the collecting electrodes and $V=-V_o$ at the corona electrode, the dimensionless electric potential becomes $\Phi^*=0$ at the collecting electrode and $\Phi^*=1$ at the discharge electrode. The voltage gradient was set to zero in the direction normal to the boundary at the inlet, outlet, bottom, and top plane of the ESP.

3.6 ION DENSITY MODEL

The ion density profile is required by: (a) the sink term in the neutral dust transport equation, (b) the source term in the charged dust transport equation, (c) the particle charging model, and (d) the particle collection efficiency model.

3.6.1 Ion Transport Equation

The general species conservation equation (3.3d) written for the case of negative ions, constant ion mobility ($N_k \vec{E} \cdot \nabla \mu_k = 0$) and ion diffusion ($\nabla N_k \cdot \nabla D_k = 0$) simplifies to (3.27).

$$\vec{U} \cdot \nabla N_{ni} - \mu_{ni} N_{ni} \nabla \cdot \vec{E} - \mu_{ni} \vec{E} \cdot \nabla N_{ni} - D_{ni} \nabla^2 N_{ni} = -k N_{ni} N_{nd} \tag{3.27a}$$

The production of negative ions due to the electron attachment is considered zero ($S_{ni}=0$) as a consequence of bypassing the corona discharge chemistry, and using experimental data to set the boundary conditions. The ion sink (R_{ni}) due to the electron detachment or ion inter-conversion process is not considered. The ion sink due to the attachment of ions to the surface of dust particles was obtained from the particle charging rate (k).

For wire-plate ESP geometry, the standard approach for the calculation of ion density is to use the steady-state current continuity equation with mobility term only applied to two dimensional domain with constant boundary conditions on discharge electrode. For more accuracy, the convection term was considered in [66, 72] and the tuft discharge induced 3D model EHD in [134, 152]. In this work we considered the diffusion, convection and mobility terms in the 3D domain.

At first the equation was transferred into dimensionless form.

$$Ra_i \vec{u}_g \cdot \widetilde{\nabla} n_{ni} - F_E n_{ni} \widetilde{\nabla} \cdot \vec{\xi} - F_E \vec{\xi} \cdot \widetilde{\nabla} n_{ni} - \widetilde{\nabla}^2 n_{ni} = -\alpha^* n_{ni} n_{nd} \tag{3.27b}$$

where $Ra_i = U_o L / D_{ni}$ is the dimensionless diffusion Reynolds number, $\vec{u}^*{}_g = \vec{U}_g / U_o$ is the dimensionless gas velocity, $n_i = N_{ni}/N_{io}$ is the ion number density ratio, N_{io} and N_{do} are the initial number density of ions and dust particles, $F_E = eV_o / kT$ is the dimensionless electric field number, L is the characteristic length, α^* is the dimensionless ion attachment coefficient. The ion mobility is considered to be invariant to the electric field and is correlated with ion diffusion D_{ni} over Einstein's relation $D_i = \mu_i \dfrac{kT}{e}$.

The equation 3.27b is of the steady convection-diffusion type. The nature of the solution of the equation 3.27b can be understood from the Figure 3.3 that shows the solution for one-dimensional domain $0<x^*<1$ subjected to the following arbitrary boundary conditions: (a) $n^*(0)=0$, and (b) $n^*(1)=1$. When Ra_i and F_E numbers are zero, the problem is pure diffusion controlled. When the flow is in the positive x-direction ($Ra_i>0$) and F_E negligible, the value of n^* is influenced by the upstream value $n^*(0)$. For very large Ra_i values, the value of n^* remains very close to the upstream value over much of the domain. For very large $|-F_E| >> Ra_i$ values the picture is reversed, and the value of n^* remains very close to the other boundary condition (n*(1)=1).

The upwind differencing method is the well-known approach used for the formulation of the convection term for which the value at the interface is equal to the value at the grid point on the upwind side of the face.

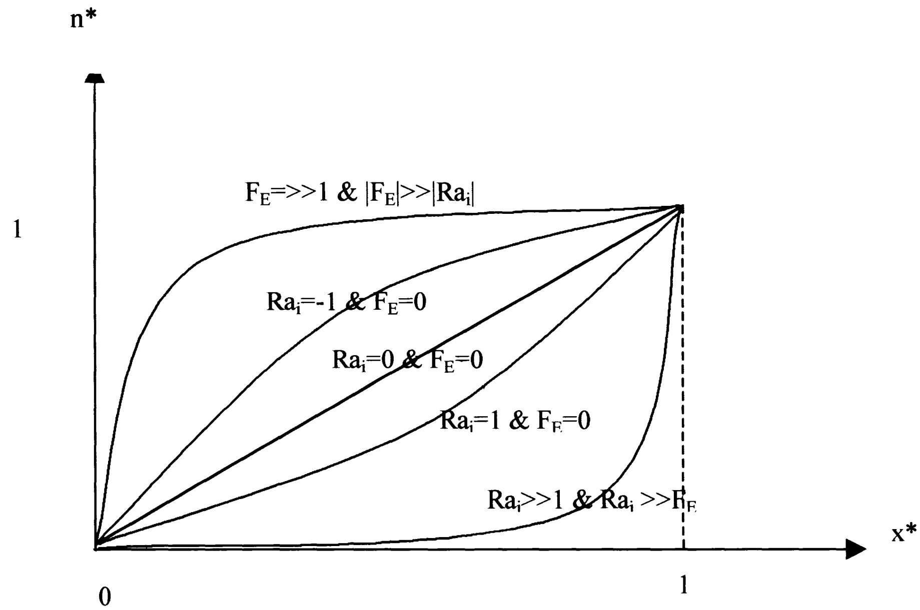

Figure 3.3 Solution for one-dimensional convection diffusion problem depending on Ra_i and F_E values

3.6.2 Boundary Conditions on the Discharge Electrode Surface

For smooth wires, most models assume constant ion density along the discharge electrode surface. Lawless et al. [85] conducted comprehensive experimental studies of individual tuft-corona discharges on wires of various diameters: *3.18*, *6.35* and *9.53 mm.* Since the characteristic of individual tuft discharges was very difficult to measure, Lawless et al. [85] studied tufts from micro-points. The total current from each tuft was restricted to approximately *30 μA* and typical minimum value of about *2 μA* at corona onset for which very unstable tufts were observed. Tufts locations were random both along the wire and around its circumference. Some tufts moved continuously along the wire, and some appeared to be switched off, as other appeared elsewhere. As the voltage was raised, tufts become uniformly distributed along the full length of the wire. They showed that in the case of tuft location pointing normal to the collecting plate, the current distribution on the collecting plate has a larger component in the transverse direction than in the longitudinal direction. The current density in the transverse direction obeys Warburg's law. As the tuft location on the circumference of the wire was moved away from the location pointing normal to the collecting plate, the deviation from Warburg's current distribution was more noticeable.

For discharge electrodes with spikes or needles, the standard approach is to set zero ion density at the non emitting portion of the discharge electrode, and a fixed constant value at the emitting portion. More detailed work with respect to constant boundary conditions on the emitting portion of discharge electrode was done by Houlgreave et al. [103] and Corbin [78]. Houlgreave et al. [103] provided the approximate expressions for the curvature dependent space charge density at a complex discharge electrode surface by introducing a new parameter called the characteristic mean radius of curvature at which the corona field is twice the breakdown strength of air and a new empirical law for the electric field at the corona discharge surface. They claim good fit to data for standard electrode designs, however, the evidence was not provided. Corbin

[78] showed that the solution of ion transport is very sensitive to the boundary condition at serrated strip-type discharge electrode. Since the standard current measuring methods at discharge electrode could not be used to determine the boundary conditions, Corbin adjusted boundary conditions empirically, until the calculated current density near the collecting electrode matched measured values to a given degree of accuracy. The best fit for the serrated strip oriented parallel to collecting electrode has come from quadratic ion distribution. For a serrated strip oriented normal to the collecting electrode, the best fit was for the uniform distribution of current density at discharge electrode.

In this work, the optical emission of the 2nd positive band of N_2 molecules that is directly proportional to the electron density and indirectly proportional to the negative ion distribution [97], was used to set the boundary condition on the discharge electrode surface in a radial direction. A detailed description of performed experiments can be found in appendix A5.

The boundary conditions on the surface of the spike type discharge electrode are determined according to equation (3.28) and shown in dimensionless form as follows,

$$n_{i^{th}\,spike}^{\ *} = \frac{n_{i^{th}\,spike}}{N_{io}} = \frac{\dfrac{\mathrm{J}_{\mathrm{i^{th}\,spike}}}{e\mu_i \overline{E_{i^{th}spike}}}}{\dfrac{\mathrm{J}_{\mathrm{total}}}{e\mu_i \overline{E_{all\,spikes}}}} = \frac{\overline{E_{all\,spikes}}}{\overline{E_{i^{th}spike}}} A_f(x') \tag{3.28a}$$

$$A_f(x') = -0.4366(x')^2 + 1; \qquad x' = x/d_s \tag{3.28b}$$

where A_f is the correction function obtained from the experiment, x' is the normalized horizontal position $(x'=x/d_s;\ -0.5\leq x'\leq 0.5)$ with respect to the length of the spike tip (d_s),

N_{io} is the ion initial value in equation (3.28c), obtained from the current density at discharge electrode, ion mobility and electric field on the surface of the electrode, usually set to the critical value.

$$N_{io} = \frac{J_{wire}}{e\mu_i E_{critical}} \tag{3.28c}$$

The location of discharges in the axial direction is determined by the spike position.

The boundary condition on the surface of the rod type discharge electrode in dimensionless form is as follows:

$$n_i^* = B_f(x') = 1.114 - \frac{0.5706}{1+(4x')^2} \tag{3.29}$$

Here, B_f is the correction function obtained from the experiment, x' is the normalized horizontal position *($x'=x/d$; $-0.5 \leq x' \leq 0.5$)*, and d is the diameter of the rod-type discharge electrode. Correction functions A_f and B_f are approximation functions of the emission profile of the 340 nm wavelength as shown in Figures 3.4 and 3.5.

In the case of a thin wire, the uniform current density profile was set as a boundary condition in a radial direction.

Digital image analysis was used to determine the boundary conditions in the axial direction. For a rod type discharge electrode, a non-linear relationship between the number of tuft discharges and the applied voltage was observed. It appears as if there is some interaction between tuft points [85, 98]. At first, by increasing the voltage, the light intensity increases, up to the point where new spots are formed. After that, the relocation of discharge spots occurs, whereby the light intensity of each spot is smaller than for the lower voltage. At voltages closer to the spark-over value, a fusion of discharge spots occurs. Results are also compared to the experimental work of McLean et al. [98] and Salasoo and Nelson [153] as shown in Figure 3.6. Salasoo and Nelson [153] performed experiments for a wire-cylinder configuration, where the wire diameter was *0.635 mm*, the wire length was *1.83 m*, and the cylinder diameter was *0.102 m*. The other curve shows result obtained by McLean et al. [98] for a wire-plate geometry. McLean et al. [98] used wire of *3.18 mm* in diameter, contaminated with smoke dust, and placed between two plates with the plate spacing of *230 mm*. Data collected in [98] and [153] are obtained visually by counting the number of tuft locations. However, present results, based on the threshold of light intensity, are more than one order of magnitude higher. Results based on the threshold of pixel-intensity derivative are approximately five times greater. The difference might be due to the different geometries, the wire diameter and the method used for the selection of tuft locations.

The ion density gradient in the direction normal to the inlet/outlet plane of the ESP is set to zero for one-field ESPs. In the case of multi-field, the ion-density/initial-surface-charge at the front plane of the i^{th}-field equals the values at the back plane of preceding the $(i-1)^{th}$-field.

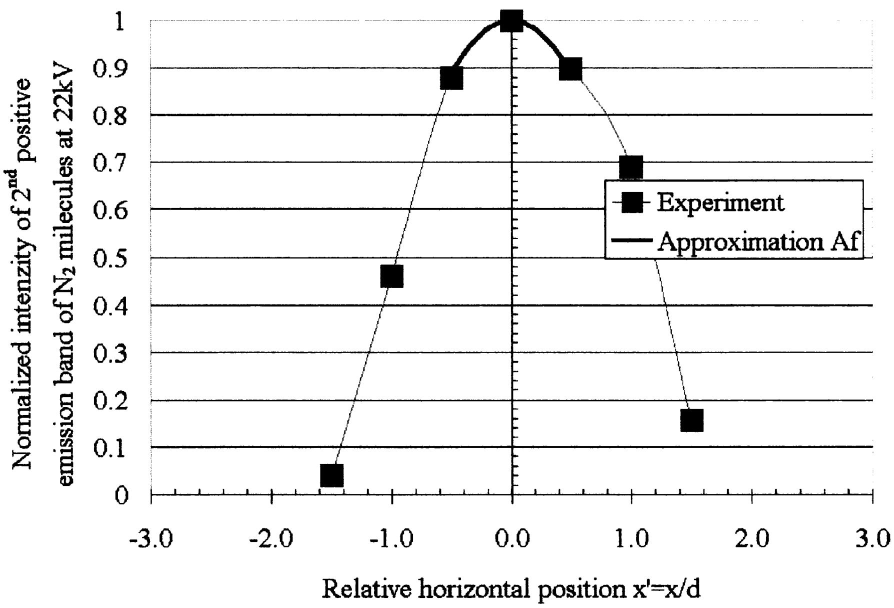

Figure 3.4 Emission profiles of the 2^{nd} positive band of N_2 molecules (*340 nm* wavelength) and approximation function A_f for a spike- type discharge electrode.

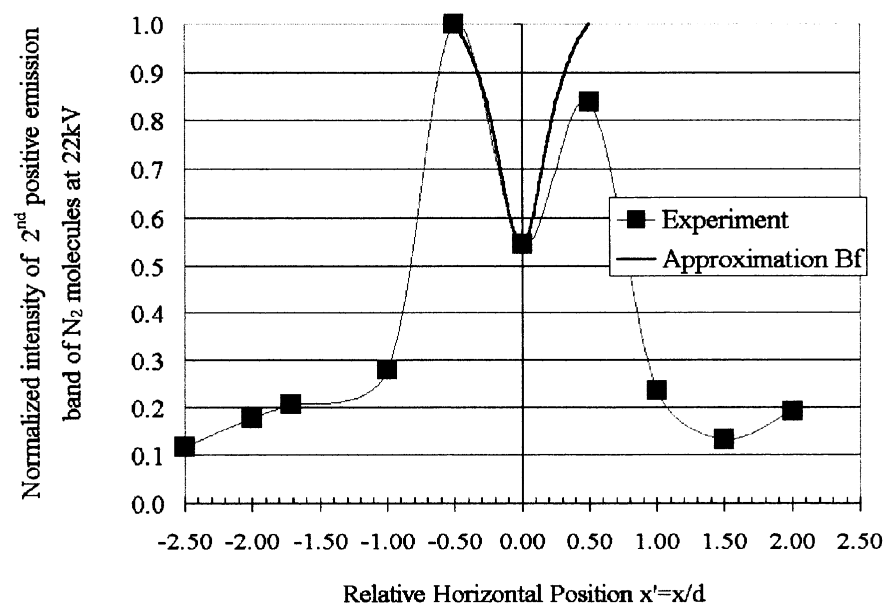

Figure 3.5 Emission profiles of the 2^{nd} positive band of N_2 molecules (*340 nm* wavelength) and approximation function B_f for a rod type discharge electrode.

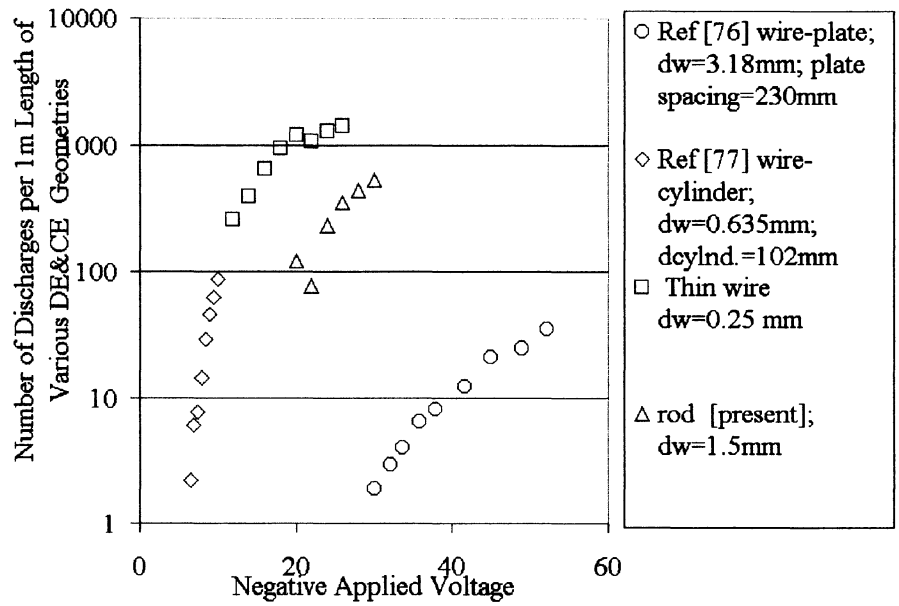

Figure 3.6 Number of discharge spots for various ESP geometries and discharge electrode types

3.6.3 Boundary Conditions on the Collecting Electrode Surface

Corbin [78] has already showed that the current density at the collecting electrode is a consequence of the boundary condition at discharge electrode, and that the boundary condition at collecting electrode does not affect significantly the solution of ion density transport in case where back-corona can be neglected. Most models that neglect the ion diffusion term do not specify the boundary condition at the collecting electrode. An exception, shown by Ohyama et al. [62] determines the boundary condition near collecting electrode, based on the analytic expression based in Warburg's current distribution law, and the electric field calculations at collecting electrode.

$$N = \frac{J_{plate}}{\mu E_{plate}} \tag{3.30}$$

Usually, the measured current density at collecting electrode is used to verify the boundary conditions at discharge electrode [78]. Another, problem with boundary conditions based on the measured current density near collecting electrode is that any new geometry or operating condition evaluations would not be possible without experiments.

In this work both boundary conditions are evaluated: (a) for zero ion density, and (b) for the case when the current density is based on experiments close to the surface of the collecting electrode. The second approach for boundary conditions produced some problems for small electric fields at conditions different than the conditions at which the current density was measured. Therefore, in this work we set the boundary condition to zero at C and U- type collecting electrodes, and for I-type collecting electrodes use the current density experiments to justify the boundary conditions at the discharge electrode. In the case of spike type discharge electrode, the calculated ion density was compared to that based on the measured current density (n_{im}^*) as shown in (3.30)

$$n_{im}^*(y^*, z^*) = \frac{n_i}{N_{io}} = \frac{\dfrac{J_{probe}}{e\mu_i E(y^*, z^*)}}{N_{io}} \tag{3.30a}$$

$$J_{probe} = I_{probe} / A_{probe} \tag{3.30b}$$

$$I_{probe}(z^*, y^*) = I_{max} A(z^*)(66e^{-3.79y^*} - 1.85e^{-5.59(y^*-0.83)}) \tag{3.30c}$$

$$A(z^*) = \cos(\tan^{-1}(z^{rs} / L))^{20} \tag{3.30d}$$

A detailed description of performed current density experiments can be found in appendix A.4

3.7 NEUTRAL DUST DENSITY MODEL

The neutral dust density distribution is required by: (a) the sink term in the ions transport model, (b) the source term in the charged dust transport model, and (c) the particle collection efficiency based on the dust density profile at inlet and outlet section of ESP.

3.7.1 Neutral Dust Density Equation

The neutral dust density distribution was obtained from the transport equation as follows:

$$\vec{U}_g \cdot \nabla N_{nd} - D_{nd}\nabla^2 N_{nd} = -kN_i N_{nd} \tag{3.31}$$

where the first term is the convection flux, flux carried by the gas flow; the second term is the neutral dust diffusion flux due to the gradient of the neutral dust density; and the right hand side is the charged particles formation by ion attachment to the surface of the neutral dust particles, known as a sink term. The diffusion of neutral dust particles is set to [31] of Brownian diffusion *(D_B)*

$$D_B = \frac{kTCc}{6\pi\mu_g r_p} \tag{3.32}$$

The dimensionless form of the neutral dust transport equation becomes:

$$\mathrm{Ra}_{\mathrm{nd}}\, \vec{u}^*{}_g \cdot \widetilde{\nabla} n_{nd} - \widetilde{\nabla}^2 n_{nd} = -\alpha_{nd}{}^* n_i n_{nd} \tag{3.33}$$

where $Ra_{nd}= U_gL/D_{nd}$ is the dimensionless diffusion Reynolds number of neutral dust, $u_g{*}=U_g/U_o$ is the dimensionless gas velocity, L is the characteristic length, D_{nd} is the neutral dust diffusion, $n_{nd}=N_{nd}/N_{do}$ is the dust number ratio, N_{do} is the initial number of dust particles, and α_{nd}^* is the dimensionless dust attachment coefficient.

3.7.2 Boundary Conditions for Neutral Dust Density

The boundary conditions for neutral dust are: (a) $n_{nd}=0$ at the collecting and discharge electrodes, (b) $n_{nd}=1$ in the direction normal to the inlet boundary plane, and (c) the neutral dust gradient in the direction normal to the boundary at the outlet, bottom, and top plane of the ESP is zero. In the case of a multi-field, the neutral dust at the front plane of the i^{th}-field equals to the values at the back plane of preceding the $(i-1)^{th}$-field.

3.8 CHARGED DUST DENSITY MODEL

The charged dust density profile is required by a particle collection efficiency model based on the dust density profile at inlet and outlet section of ESP.

3.8.1 Charged Dust Density Equations

The charged dust density distribution (n_{cd}) was obtained by solving the charged dust transport equation as follows:

$$\vec{U}_g \cdot \nabla N_{cd} - \nabla \cdot (\mu_{cd} N_{cd} \nabla V) - D_{cd} \nabla^2 N_{cd} = kN_i N_{nd} \tag{3.33a}$$

Further expansion of the second and third terms yields,

$$\vec{U}_g \cdot \nabla N_{cd} - N_{cd}\vec{E} \cdot \nabla(\mu_{cd}) - \mu_{cd} N_{cd} \nabla \cdot \vec{E} - \mu_{cd}\vec{E} \cdot \nabla N_{cd} - D_{cd} \nabla^2 N_{cd} - \nabla D_{cd} \cdot \nabla N_{cd} = kN_i N_{nd} \tag{3.33b}$$

The first term, charged dust convection, represents the transport due to the general gas flow. The second term *($\nabla\mu_{cd}$)* contributes to compressibility of charged dust particles and can be neglected in case of already precharged dust particles. However, for submicron dust particles, that encounter high surface charge in the region close to discharge electrode, the second term should be considered at least in first few fields of ESP. In later sections of ESP, where the acquired charge is not changing significantly, the second term can be neglected. The third term that contains the $(\nabla \cdot \vec{E})$ is usually substituted by Poisson's equation. The fourth term represents the drift due to the electric field. The fifth and sixth terms depend on the diffusion constant of the charged species which defer from the neutral dust particle diffusion. The charged particle diffusion is commonly obtained from the mobility of charged species using the Einstein relation. The right hand side, known as a source term, is the rate of the ion attachment to the surface of the neutral dust particle.

The main difficulty in solving equation 3.33b is a mobility term, that for particles charged through a non uniform electric field and ion density is a function of both space and time. Additionally, each particle size may have a different number of charges. Therefore, it would require to couple several equations for each surface charge. Many investigators lumped all charged dust particle in one group. Additionally, most models considered constant mobility term [16, 53, 65, 67-71, 73, 74, 76] by assuming that all charged dust particles have a surface charge equal to the saturation value of field charging. Exceptions are done by Gallimberti [66], who used a mixed Eulerian-Lagrangian method for ten particulate classes which are divided based on the particle diameter and percent of the saturation charge class. The Lagrangian approach calculates the particle velocity for each class and then uses an Eulerian approach that solves the conservation equation for each size class by using the average mobility of all charge classes from Lagrangian approach.

In this work, we simplified the equation (3.33b) assuming all dust particles are charged up to the saturation value by field charging thus neglecting second and sixth term. For non-uniform charged dust particle case, the mobility term was obtained semi-empirically by determining the particle surface charge based on the particle charging equation, which was solved for the average value of electric field and ion density between two grid points taking into account the surface charge in proceeding grid location and setting the charging time equal to the particle residence time between the two grid points. A dimensionless form of the charged dust transport equation is as follows:

$$\mathrm{Ra}_{\mathrm{cd}}\,\vec{u}^{*}{}_{g}\cdot\widetilde{\nabla}n_{cd}-\mathrm{F}_{E}\widetilde{\nabla}\cdot(n_{cd}\vec{\xi})-\widetilde{\nabla}^{2}n_{cd}=\alpha_{cd}{}^{*}n_{i}n_{nd} \qquad (3.34)$$

where $Ra_{cd}=U_gL/D_{cd}$ is the dimensionless diffusion Reynolds number of charged dust, $u_g{}^*=U_g/U_o$ is the dimensionless gas velocity, F_E is the dimensionless electric field number, ξ is the dimensionless electric field, L is the characteristic length, D_{cd} is the charged dust diffusion, $n_{cd}=N_{cd}/N_{do}$ is the charged dust number ratio, N_{do} is the initial number of dust particles, and $\alpha_{cd}{}^*$ is the dimensionless charged dust attachment coefficient.

3.8.2 Boundary Conditions for Charged Dust Density

For fully adhesive wall without particle re-entrainment the usual boundary condition is taken as $n_{cd}=0$. However in the presence of migration normal to the collecting electrode, the zero-gradient condition can be used [16, 53,71, 92, 124]. For the non-collecting surfaces, the zero-flux condition was used [92]. In the direction normal to the inlet boundary plane $n_{cd}=0$, assuming no initially precharged dust particles. Only in the case of multi-field, the charged dust at the front plane of the i^{th}-field equals to the values at the back plane of the preceding $(i-1)^{th}$-field. The charged dust gradient in the direction normal to the boundary at the outlet, bottom, and top plane of the ESP is set to zero-slope condition.

3.9 GRID SIZE AND NUMERICAL PROCEDURES

The solution domain covers one section of the ESP with one discharge electrode placed in the center of the field. The normalization of the domain space was conducted with regard to the half of the field width, leading to the dimensionless domain geometry of $2\times8\times12$, for the domain of $0.05\times0.2\times0.3$ metres used in the experiments. Before applying the numerical calculation, a test calculation was conducted in order to examine the validity size of a grid. The numerical solution of the Laplace electric potential by finite differences was compared to the Cooperman's solution and finite element solution. Accordingly, a grid size of $41\times159\times159$ (in $x \times y \times z$ directions) was adopted for spike-plate ESP. Poisson's equation was solved by standard Gauss-Seidel method, and the transport equations are solved by a first order upwind differencing method [154].

CHAPTER 4

NUMERICAL STUDIES OF ELECTRODE GEOMETRY EFFECTS ON DUST PARTICLE COLLECTION EFFICIENCY

In this chapter the numerical simulations were conducted for wire and spike type discharge electrodes in combination with the I, U and C-type collecting electrodes of various lengths and spacings. The main gas flow rate was changed in the range from 0.5 to 2 *m/s*. The collection efficiency of dust particles with diameters of $0.01\mu m$, $0.1\mu m$, $0.5\mu m$, $2\mu m$ and $10\mu m$ were evaluated using the Mode1. The coupling between charged dust transport equation and Poisson's equation was not required since dust Debye number was less than 0.001, due to the small dust loading. The EHD number was below the value at which significant main gas flow modifications were observed therefore, the coupling between ion density and gas flow was disconnected.

4.1. DISCHARGE ELECTRODE GEOMETRY EFFECTS

Several aspects of discharge electrode geometry were analysed. First the wire and spike type discharge electrode were compared at various operating voltages and mean gas velocities. Then the dimensions of spike type electrode such as the number of spikes and spike length were evaluated at applied voltage of -25kV and mean gas velocity of 1m/s.

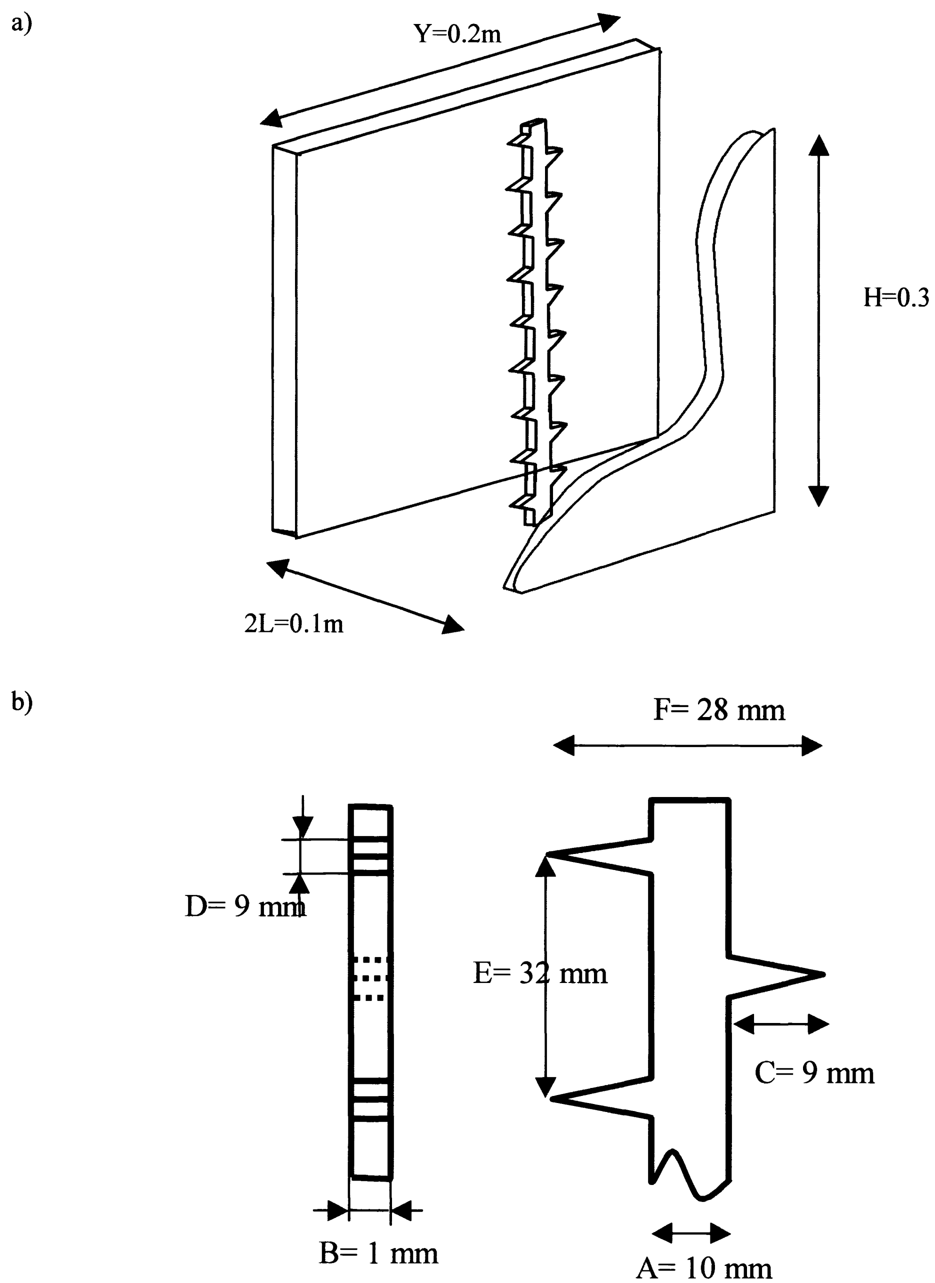

Figure 4.1 Sketch of: (a) spike-type DE and I-type CE in a single field ESP, and (b) front and side view of spike-type DE.

4.1.1. Spike Versus Wire Discharge Electrode

Electric field and ion density distributions, as well as the collection efficiency of spike-type discharge electrode (DE) with *17* spikes arranged in alternating directions (See Figure 4.1b for ESP and spike-electrode dimensions) were compared to those of the wire-type discharge electrode of $\varnothing 1$ *mm* in diameter.

Figures 4.2a and 4.2b show contour lines of electric potential without ionic space charge effect for spike-type and wire-type discharge electrodes placed between I-type collecting electrodes (CEs). Based on the analysis of Laplace electric field, the spike-type discharge electrode has approximately *24.8 %* higher electric field component in x-direction (ξ_x) and *17.8 %* higher electric field component in y-direction (ξ_y), compared to values of the wire-type DE. However, this ratio is significantly changed when the ionic space charge is considered. The contour lines of Poisson's electric potential are shown in Figures 4.3-4.5a,b for spike type DE, and *-20, -25* and *-30 kV*, respectively. The corresponding contour lines of electric field at *-20* and *-30 kV* are shown in Figure 4.6. For wire-type discharge electrodes, corresponding figures are: Figure 4.7a-b, for electric potential, Figure 4.7c-d, for ion density, and Figure 4.8a-d for electric field. In general, the average value of $|\xi_x|$ and $|\xi_y|$ increases with increased absolute value of applied voltage. However, the electric field near the discharge electrode surface slightly decreases. $|\xi_x|$ component of electric field for wire-type DE increases significantly at *–30 kV* when compared to values at *–20* and *–25 kV*. At *–20*, *-25* and *–30 kV,* the spike-type discharge electrode has *103*, *120*, and *35* % higher $|\xi_x|$ component of electric field and *36.3, 41,* and *4 %* higher $|\xi_y|$ component of electric field when compared to values of the wire-type DE..

The ion density distribution is highly affected by the discharge electrode type, corona discharge location, and applied voltage. Contour lines of ion densities at various applied voltages at x-y and y-z plane are shown in Figures 4.3-4.5b,c for spike-type and in Figures 4.7c-d for wire-type DEs, respectively. When the absolute value of applied voltage is increased, it has been observed that the contour lines of ion density close to DE surface are enclosing smaller area. This may be attributed to reduced ion mobility term due to decreased $|\xi_y|$ component of electric field near the DE surface, as shown in Figures 4.9 and 4.10. For the wire-type DEs of larger diameters, and voltages close to the corona on-set voltage, discharge tufts are located at different positions around the electrode circumference. Since the ion density distribution greatly depends on the boundary conditions on DE surface, the different ion density distributions are expected as shown in Figures 4.11a-d. At the same applied voltage, the volume averaged ion density of spike DE is one order of magnitude larger than that of the rod type, due to the higher discharge current.

Predicted particle collection efficiencies are plotted in Figures 4.12a and 4.12b as a function of particle diameter for the spike and wire type DEs in combination with I-type CE, at various main gas velocities and applied voltages. In general, the particle collection efficiency curves have a similar shape, with minimum efficiency for particles ranging from *0.1* to *0.5* μm. By comparing the predicted collection efficiencies, the spike DE improved collection efficiency of *0.5 μm* dust size particles from *2.17 %* to *6.47 %,* because of the higher electric field and ion density. Figure 4.13a shows cross-sectional averaged values of ion density $<N_i>$ and electric field $<E>$ along the ESP length. The total surface charge *Ns* of *0.5* and *2 μm* dust particles along the ESP length are shown in Figure 4.13b. For spike and wire DEs, the field charging of *2 μm* particles reaches saturation after $y^*=0.35$ and $y^*=0.49$, respectively. After that location the surface charge is increasing mainly due to the diffusion charging, however at very small rate.

4.1.2 Effect of Number of Spikes

Originally, the spike-type DE with nine spikes was designed and manufactured. The dimensions were based on the scaled down version of industrial SEI/ELEX rigid type discharge electrodes by Southern Environmental Inc. Later, the new electrode was obtained with reduced spacing between spikes based on the measured current density at CE (Appendix A4) and numerical simulations shown in Figure 4.14. Based on numerical results, the spike electrode with *9* spikes has *167 %* higher discharge current per spike. However, the volume averaged value of ion density is approximately *11 %* smaller compared to the value of DE with *17* spikes. The volume averaged value of the modulus of the electric field is approximately *3 %* smaller than the value of 17-spike electrode. All particle sizes experienced around *3 %* reduction of collection efficiency. The cross sectional averaged values of ion density, electric field, particle surface charge and collection efficiency are shown in Figure 4.15.

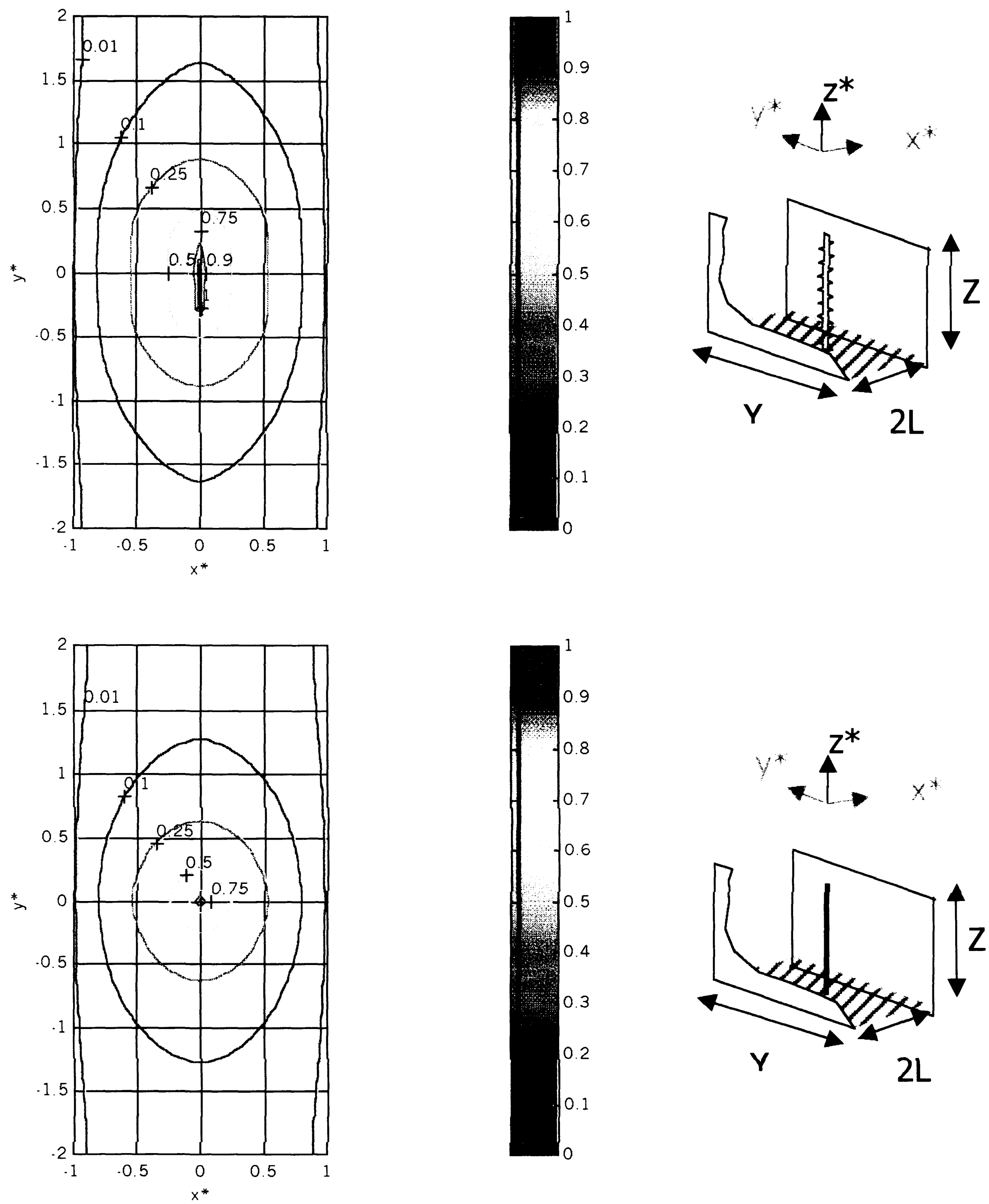

Figure 4.2 Contours of dimensionless Laplace's potential $\Phi^*(x^*, y^*)$, for: (a) spike, and (b) wire type DE. $(F_E=7.92\times10^{5})$

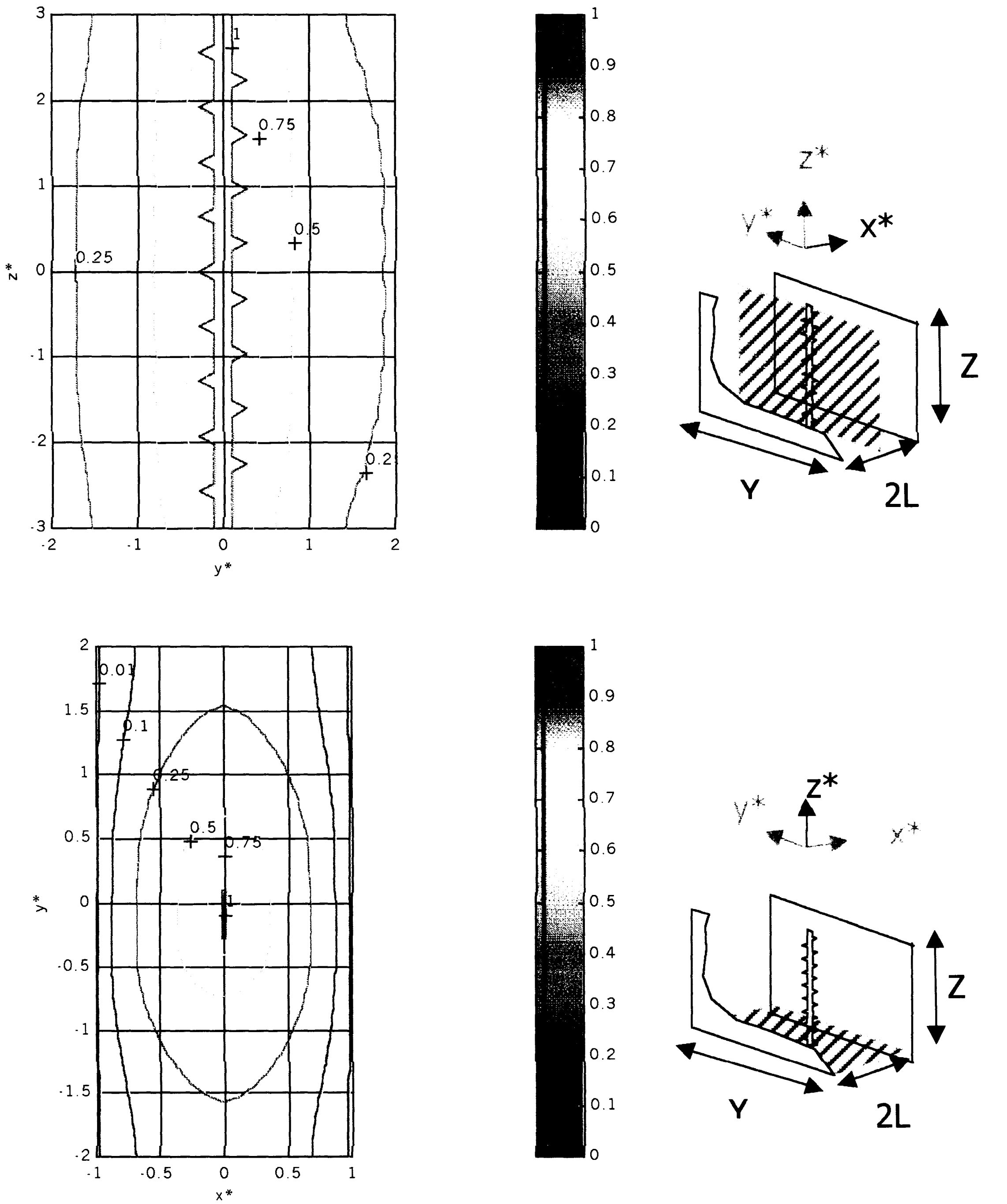

Figure 4.3 Contour of dimensionless electric potential for the spike-type DE and the I-type CE at: (a) $\Phi^*(y^*,z^*)$ at x*=0 plane, and (b) $\Phi^*(x^*,y^*)$ at z*=-2.65 plane. *(V=-20kV, U_g=1m/s, F_E=7.92×10^5, N_{io}=1.69×10^{15}, Db_i^*=3.82, Ra_i/F_{Ei}=0.016^2, E_{hd}/Re^2=0.669)*

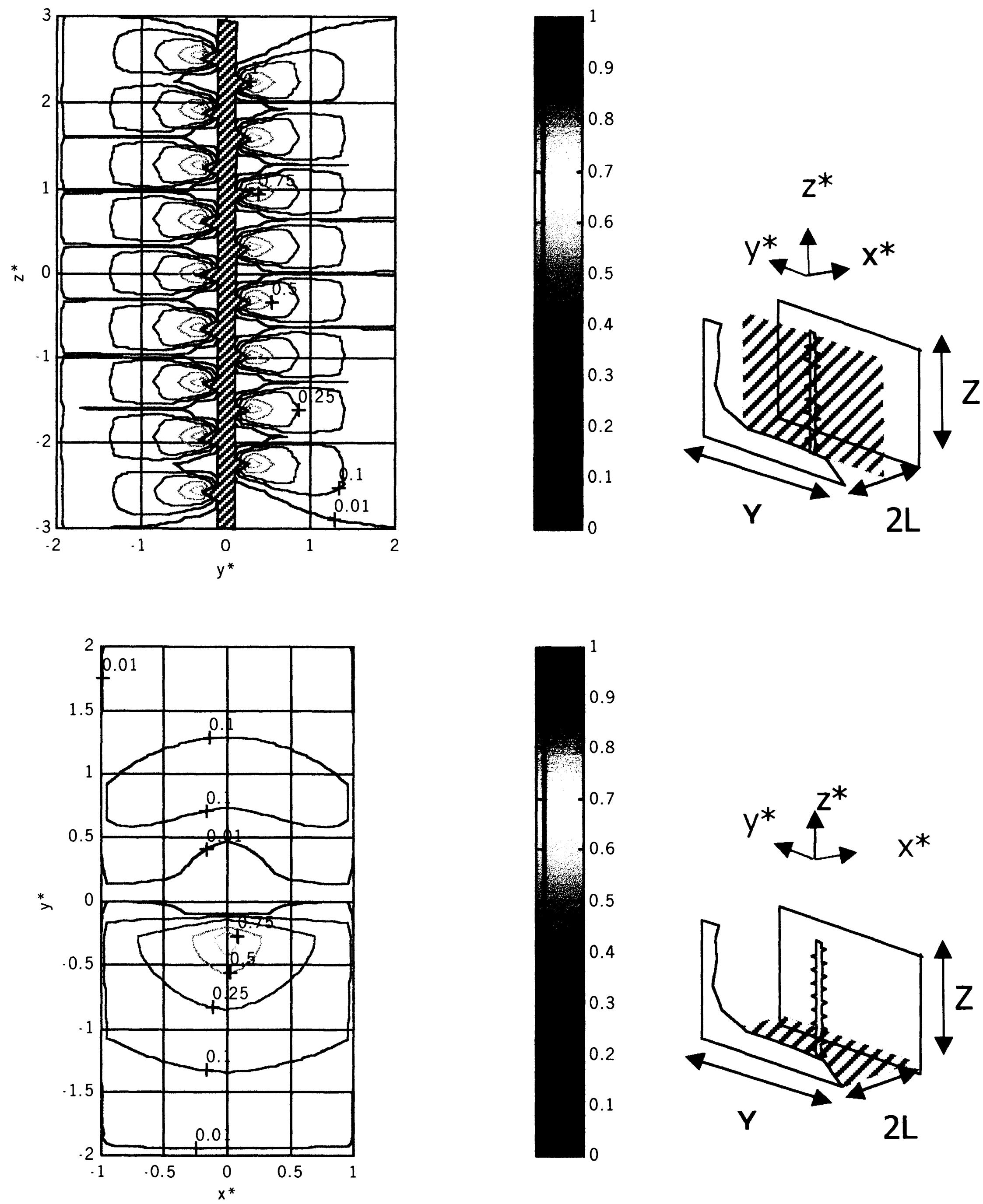

Figure 4.3 Contour of dimensionless ion density for the spike-type DE and the I-type CE for: (c) n_{ni} (y^*,z^*) at $x^*=0$ plane, and (d) n_{ni} (x^*,y^*) at $z^*=-2.65$ plane or first spike from the bottom. ($V=-20kV$, $U_g=1m/s$, $F_E=7.92\times10^5$, $N_{io}=1.69\times10^{15}$, $Db_i^*=3.82$, $Ra_i/F_{Ei}=1.58\times10^{-2}$, $E_{hd}/Re^2=0.669$)

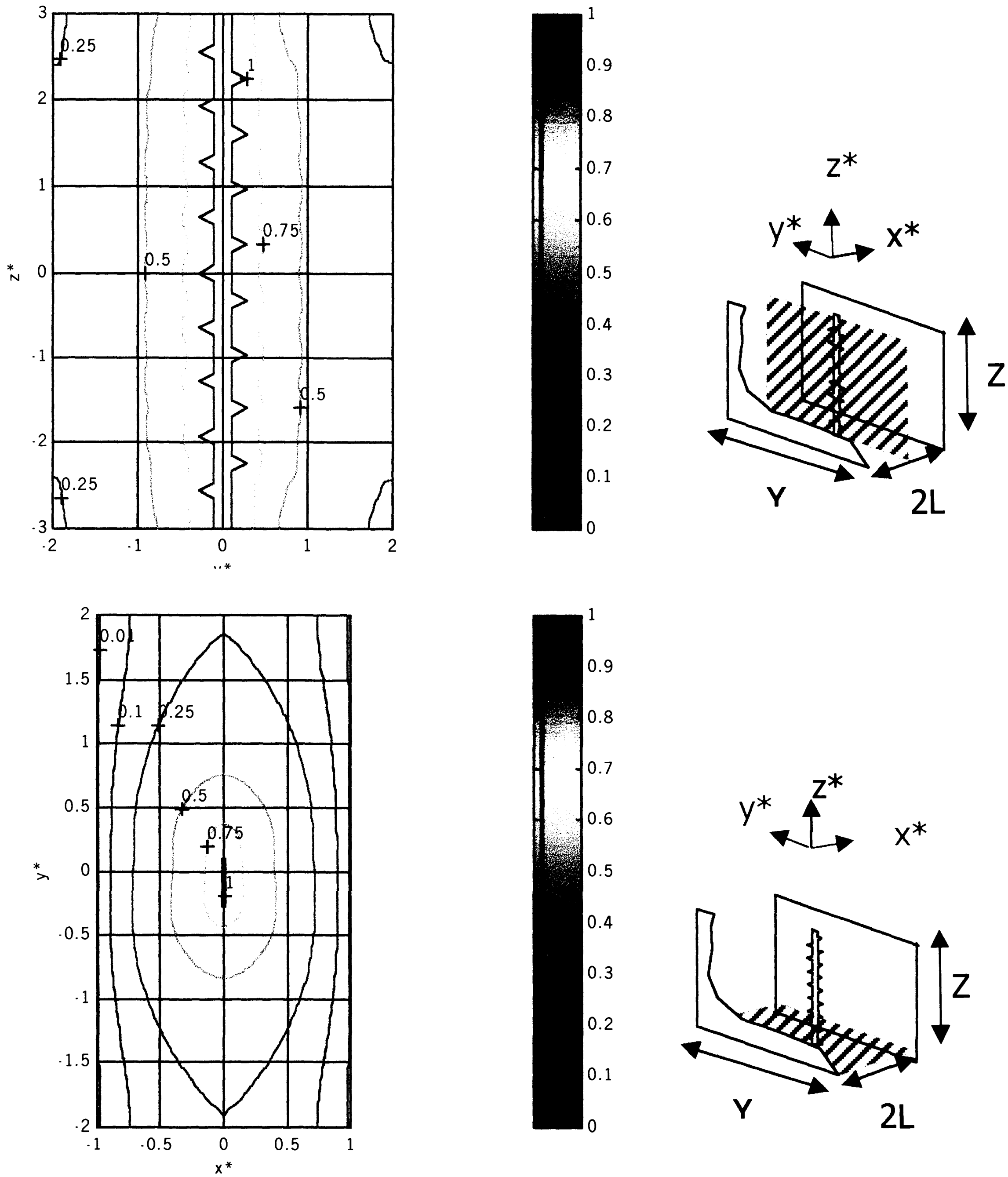

Figure 4.4 Contour of dimensionless electric potential for the spike-type DEand the I-type CE for: (a) $\Phi^*(y^*,z^*)$ at x*=0 plane, and (b) $\Phi^*(x^*,y^*)$ at z*=-2.65 plane or first spike from the bottom. *(V=-25kV, U_g=1m/s, $F_E=9.9\times10^5$, $N_{io}=4.08\times10^{15}$, $Db_i^*=7.37$, $Ra_i/F_{Ei}=0.013$, $E_{hd}/Re^2=1.19$)*

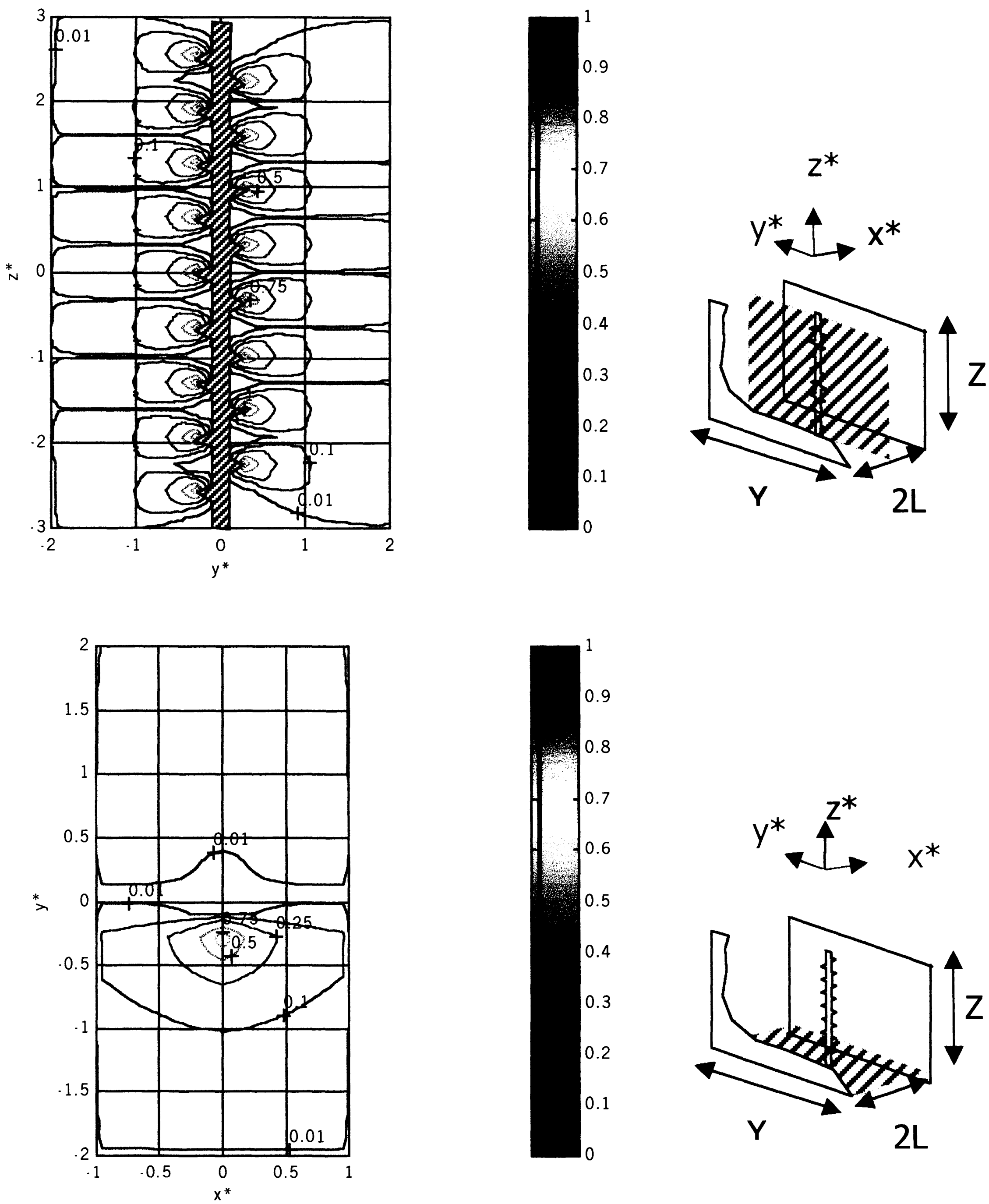

Figure 4.4 Contour of dimensionless ion density for the spike-type DE and the I-type CE for: (c) n_{ni} (y^*,z^*) at $x^*=0$ plane, and (d) n_{ni} (x^*,y^*) at $z^*=-2.65$ plane or first spike from the bottom. *($V=-25kV$, $U_g=1m/s$, $F_E=9.9\times10^5$, $N_{io}=4.08\times10^{15}$, $Db_i^*=7.37$, $Ra_i/F_{Ei}=1.27\times10^{-2}$, $E_{hd}/Re^2=1.19$)*

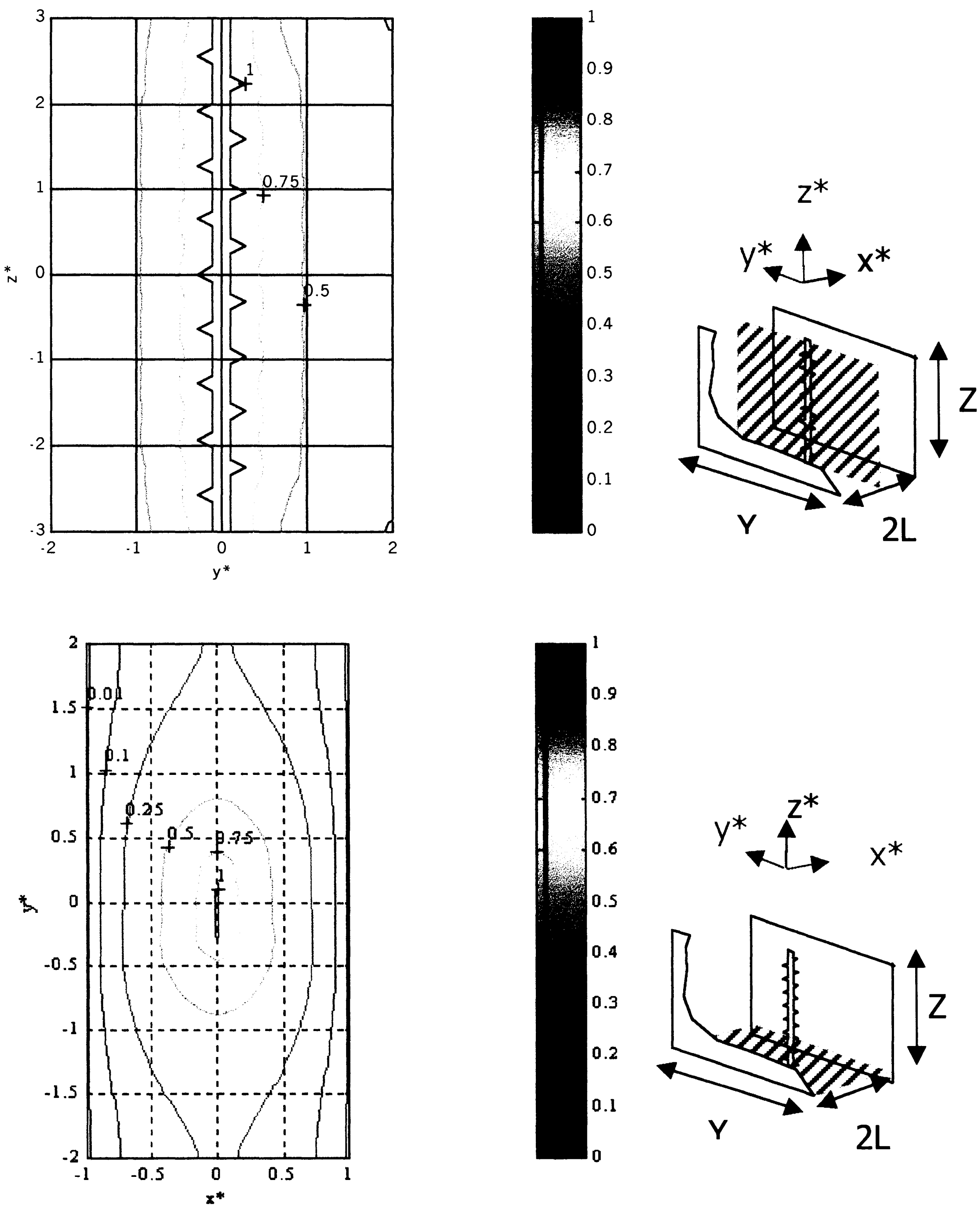

Figure 4.5 Contour of dimensionless electric potential for the spike-type DE and the I-type CE at: (a) $\Phi^*(y^*,z^*)$ at $x^*=0$ plane, and (b) $\Phi^*(x^*,y^*)$ at $z^*=-2.65$ plane or first spike from the bottom. *($V=-30kV$, $U_g=1m/s$, $F_E=1.19\times10^6$, $N_{io}=6.51\times10^{15}$, $Db_i^*=9.82$, $Ra_i/F_{Ei}=1.06\times10^{-2}$, $E_{hd}/Re^2=1.86$)*

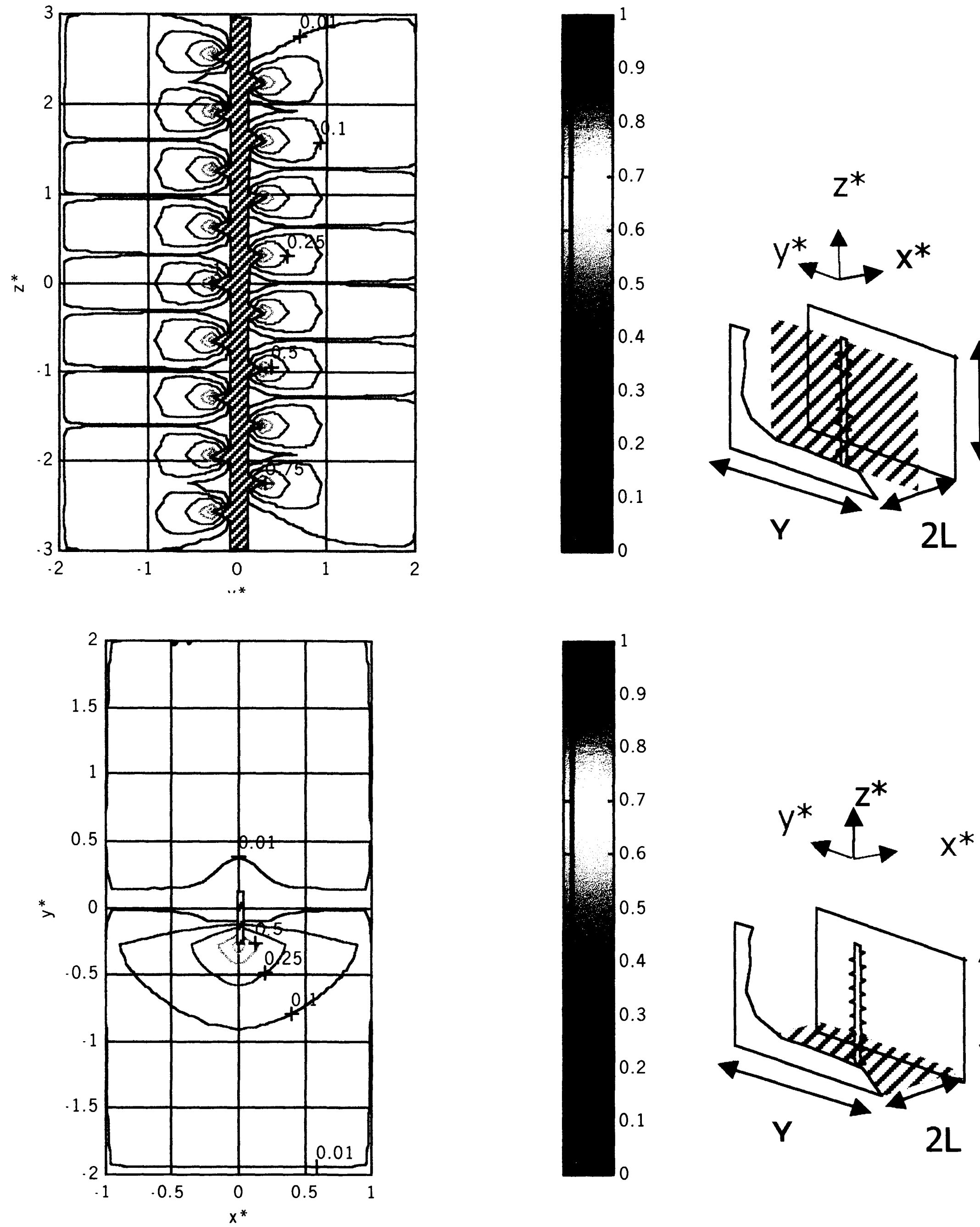

Figure 4.5 Contour of dimensionless ion density for the spike-type DE and the I-type CE at: (c) n_{ni} (y^*,z^*) at x*=0 plane, and (d) n_{ni} (x^*,y^*) at z*=-2.65 plane or first spike from the bottom. *(V=-30kV, U_g=1m/s, F_E=1.19×10^6, N_{io}=6.51×10^{15}, Db_i^*=9.82, Ra_i/F_{Ei}=1.06×10^{-2}, E_{hd}/Re^2=1.86)*

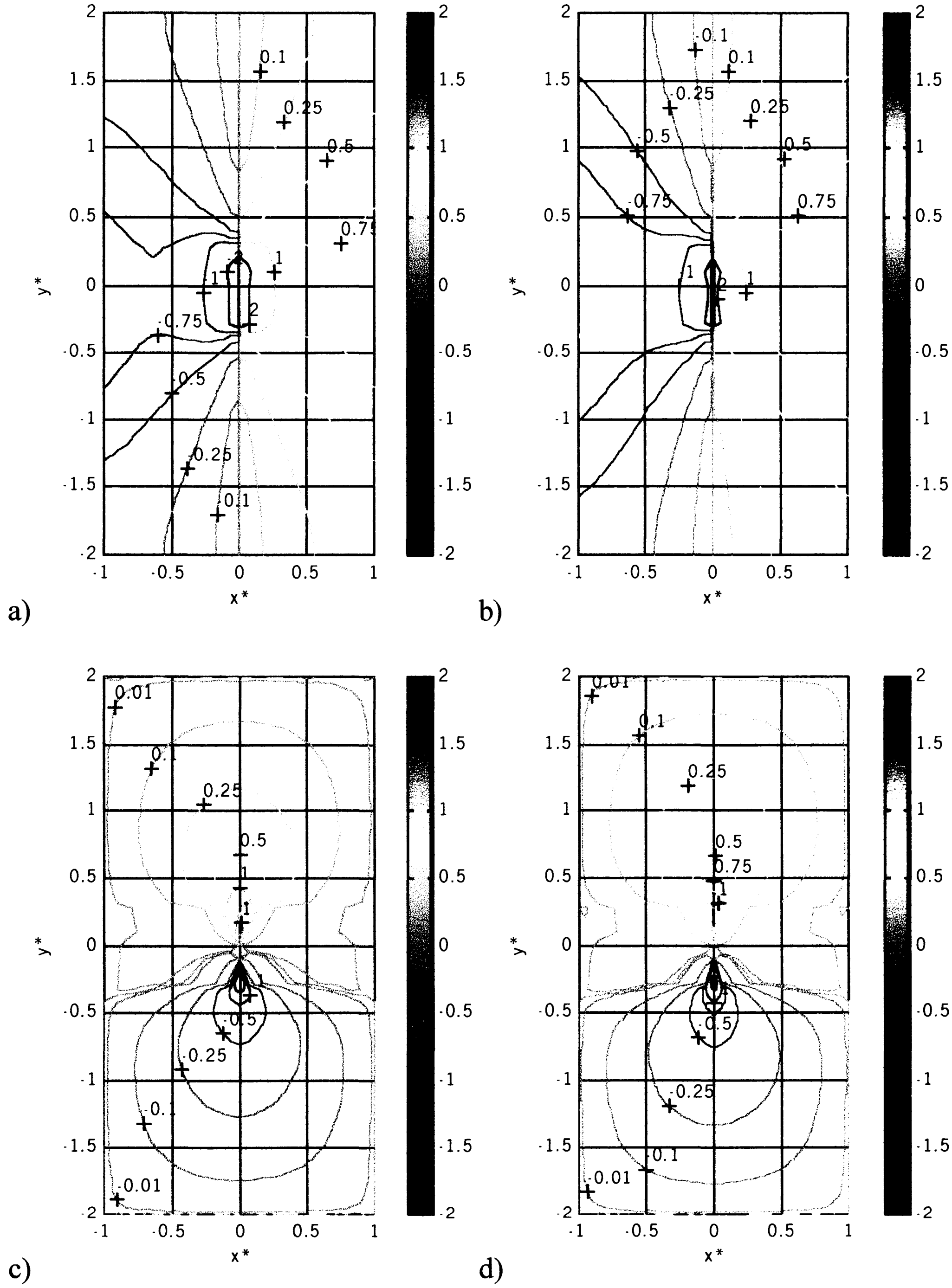

Figure 4.6 Contour of dimensionless electric field for spike-type DE and I-type CE at $z^*=-2.65$ plane for: (a) $\xi_x(x^*,y^*)$ at *20 kV*, (b) $\xi_x(x^*,y^*)$ at *30 kV*, (c) $\xi_y(x^*,y^*)$ at *20 kV*, (d) $\xi_y(x^*,y^*)$ at *30 kV*.(Mean gas velocity of *1 m/s)*

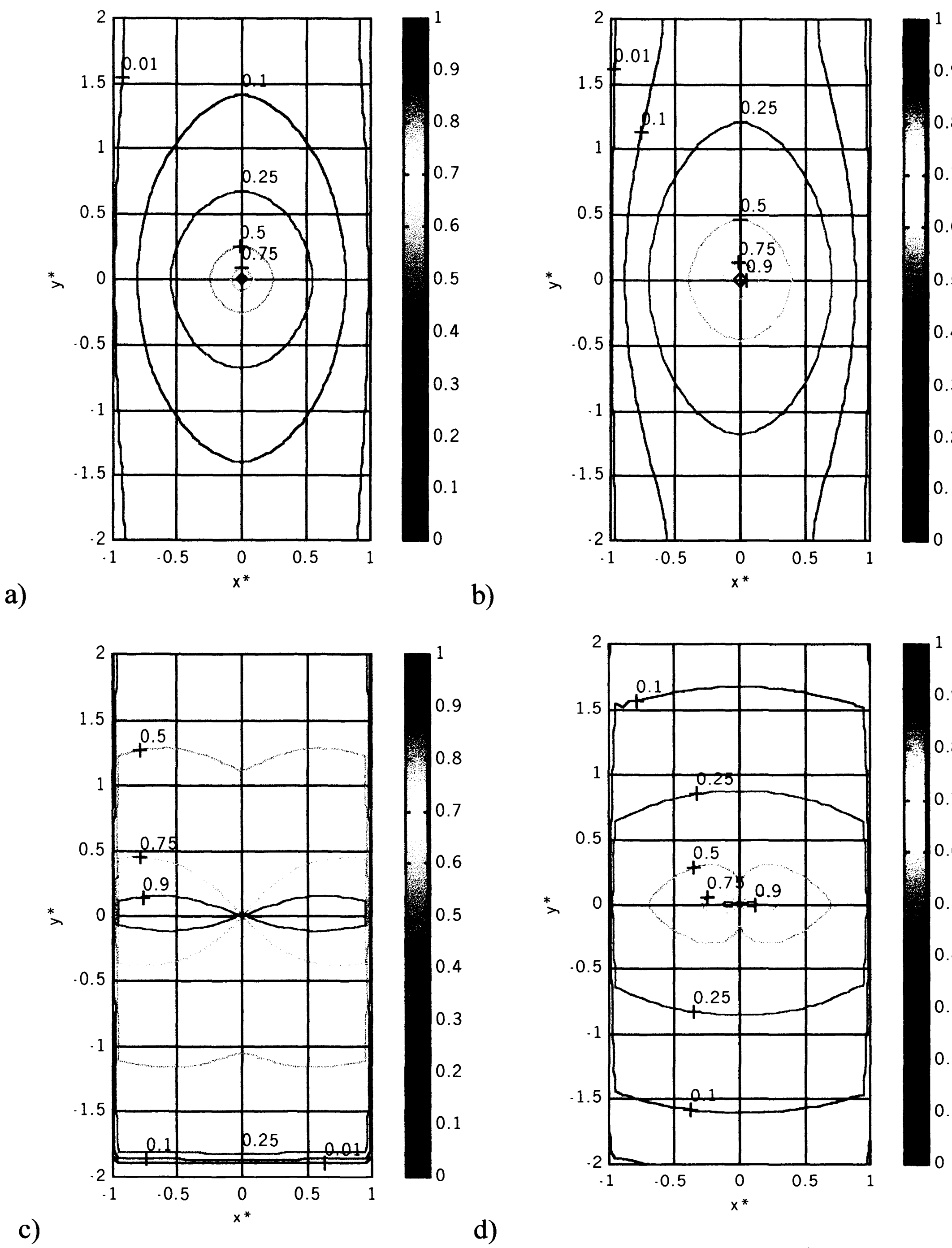

Figure 4.7 Contour of dimensionless (a, b) electric potential $\Phi^*(x^*,y^*)$ at $z^*=0$ at *-20* and *-30 kV*, and (c, d) ion density n_{ni} (x^*,y^*) at $z^*=0$ at *-20* and *-30 kV* for wire-DE and I-CE. (at *-20 kV*: $F_E=7.9\times10^5$, $N_{io}=2.7\times10^{13}$, $Db_i^*=0.06$, $Ra_i/F_{Ei}=0.016$, $E_{hd}/Re^2=0.5$); (at *-30 kV*: $F_E=1.2\times10^6$, $N_{io}=9.7\times10^{14}$, $Db_i^*=1.5$, $Ra_i/F_{Ei}=0.011$, $E_{hd}/Re^2=3.04$)

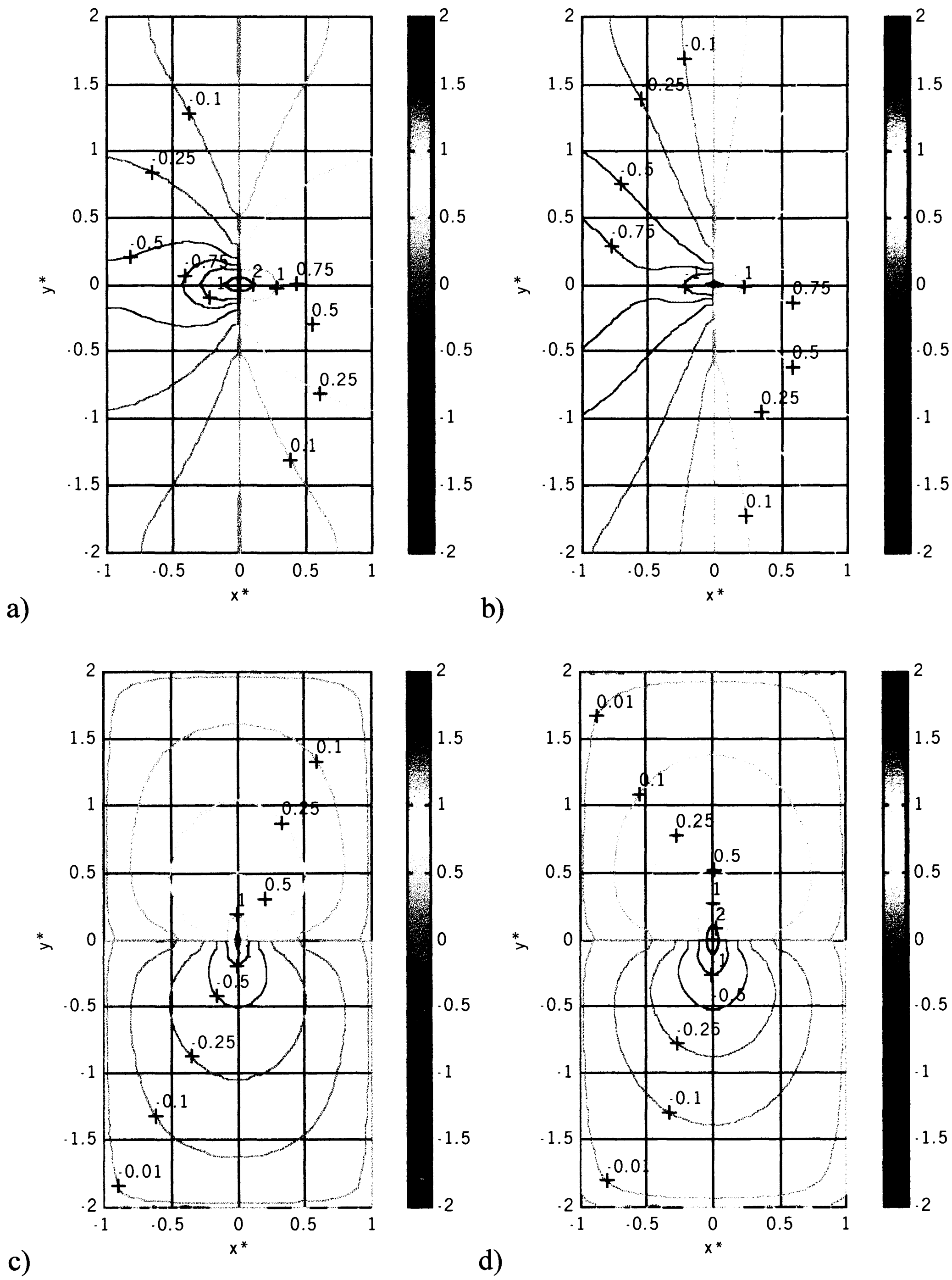

Figure 4.8 Contour of dimensionless electric field for wire-type DE and I-type CE for: (a) $\xi_x(x^*,y^*)$ at $z^*=0$ plane and $20\ kV$, (b) $\xi_x(x^*,y^*)$ at $z^*=0$ plane and $30\ kV$, (c) $\xi_y(x^*,y^*)$ at $z^*=0$ plane and $20\ kV$, (d) $\xi_y(x^*,y^*)$ at $z^*=0$ plane and $30\ kV$.

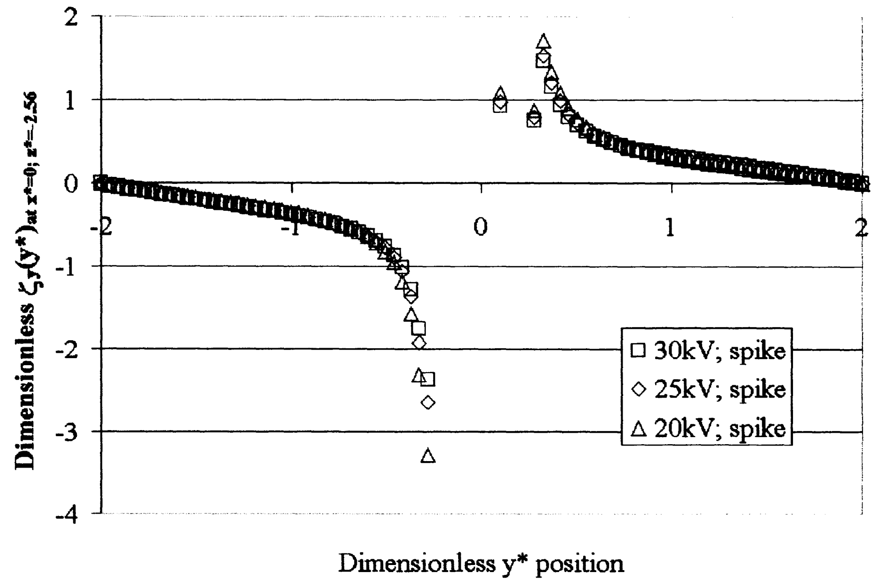

a)

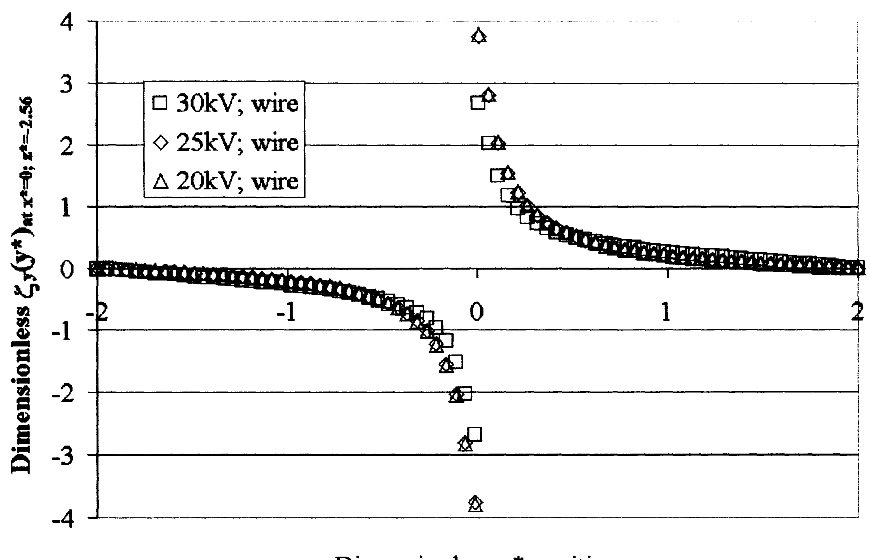

b)

Figure 4.9 Dimensionless electric field ξ_y component at various applied voltages along the line determined by the crossing of planes x*=0 and z*=-2.56 for (a) spike-type DE, and (b) wire-type DE.

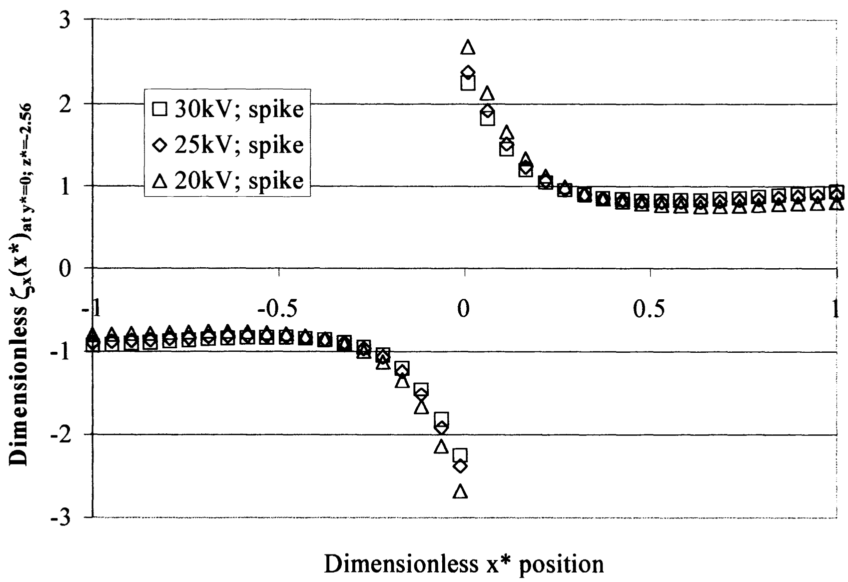

a)

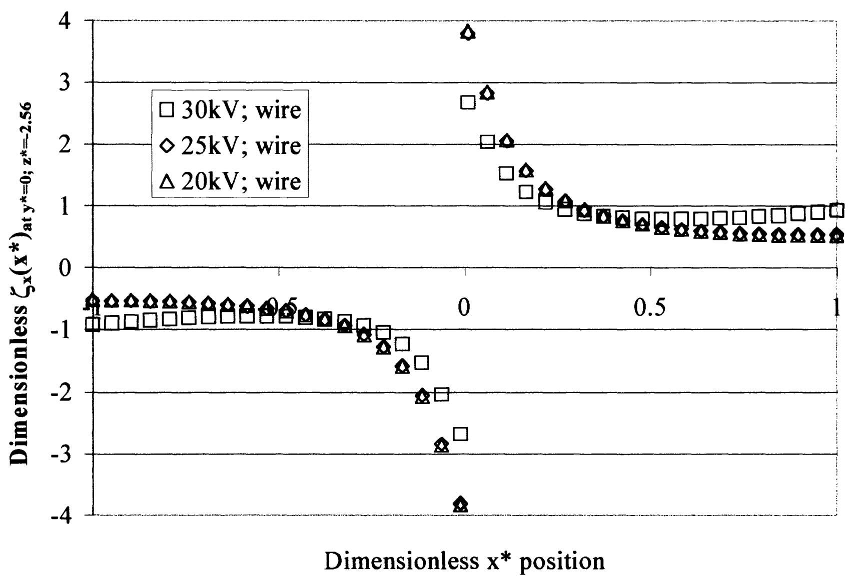

b)

Figure 4.10 Dimensionless electric field ξ_x component at various applied voltages along the line determined by the crossing of planes y*=0 and z*=-2.56 for (a) spike-type DE, and (b) wire-type DE.

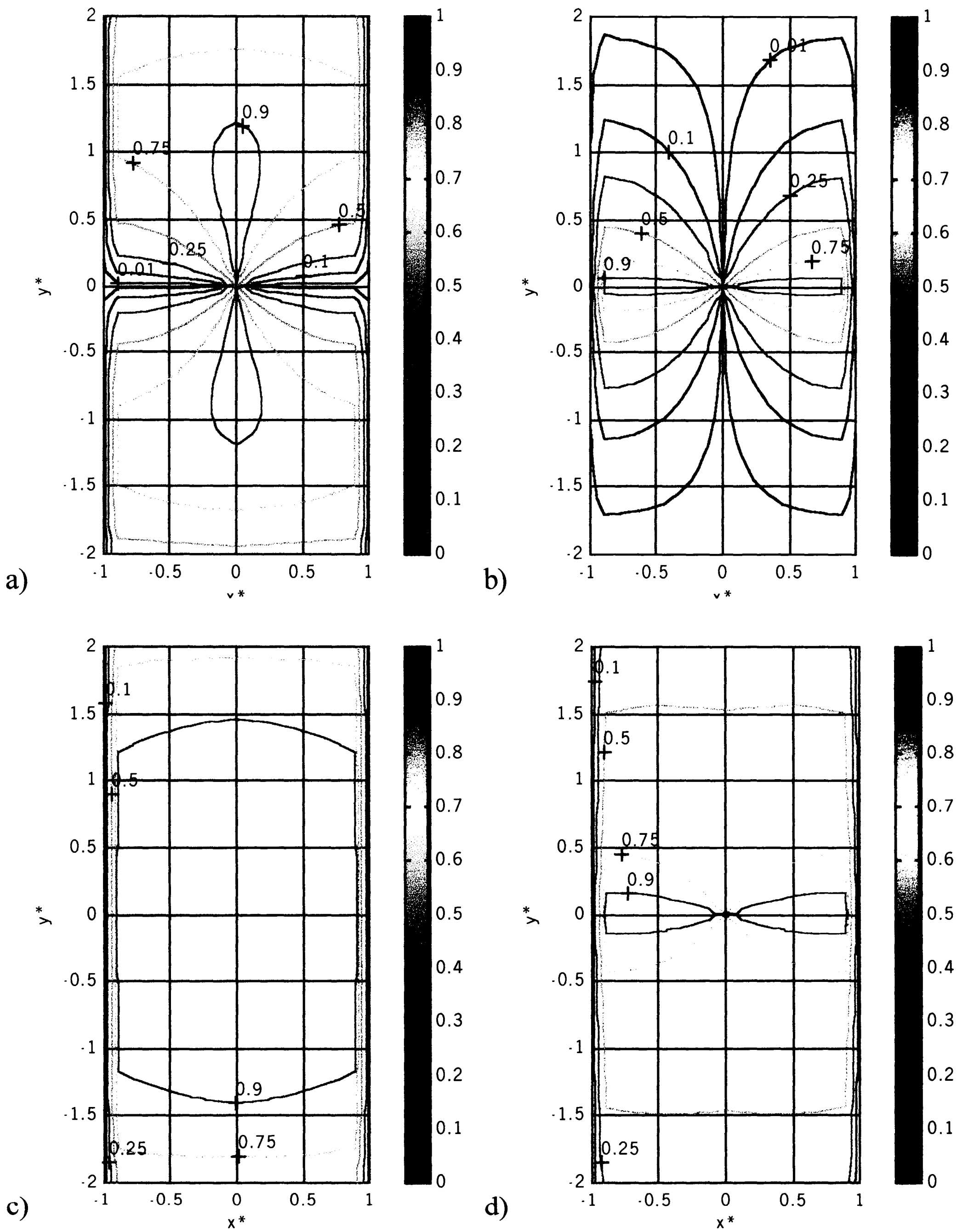

Figure 4.11 Contour of dimensionless ion density for the wire DE and the I CE at - *20 kV* and *0.5 m/s* with discharge positions: (a) at surface facing inlet and outlet of ESP; (b) at surface facing collecting electrodes; (c) uniformly distributed at DE surface, and (d) according to optical spectrometry analysis.

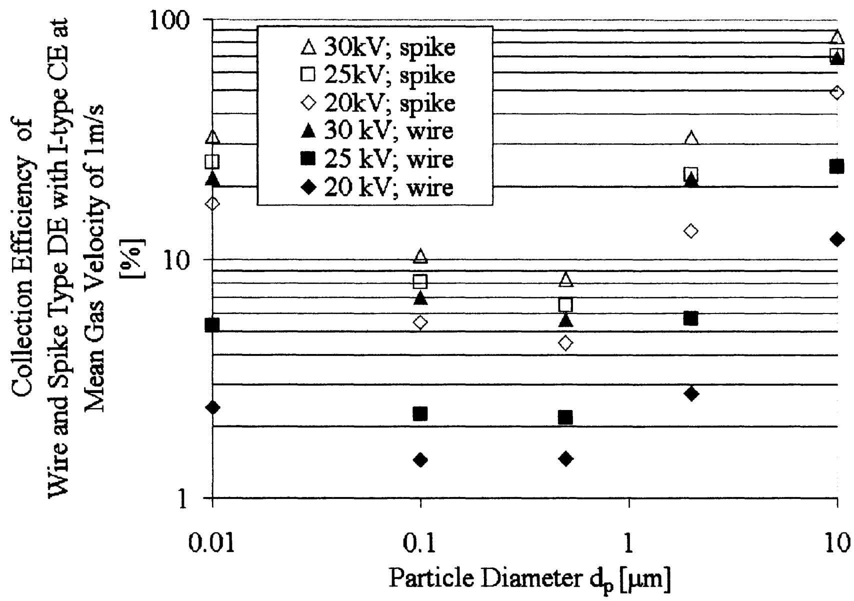

a)

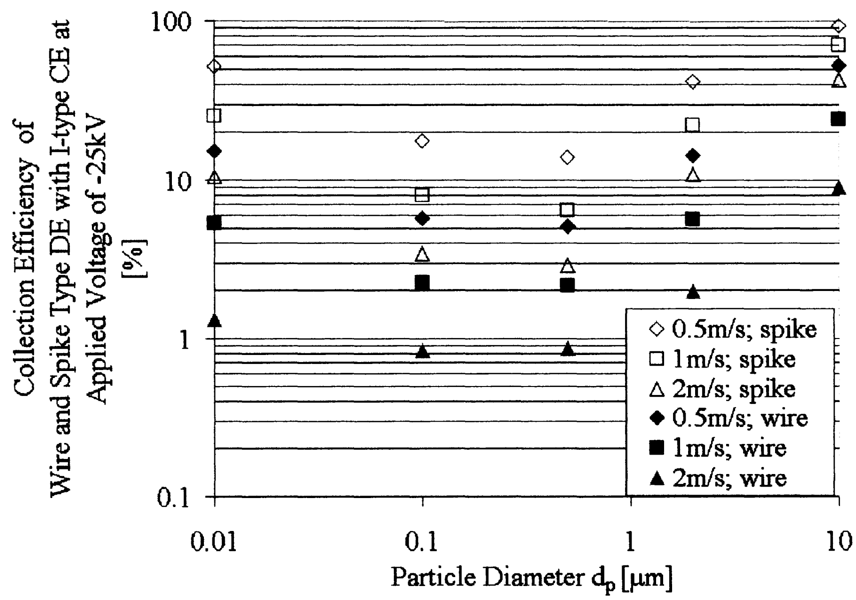

b)

Figure 4.12 Particle collection efficiencies for spike-type and wire-type DEs placed between I-type CEs at: (a) various applied voltages and mean gas flow velocity of 1m/s , and (b) various mean gas velocities and applied voltage of 25 kV.

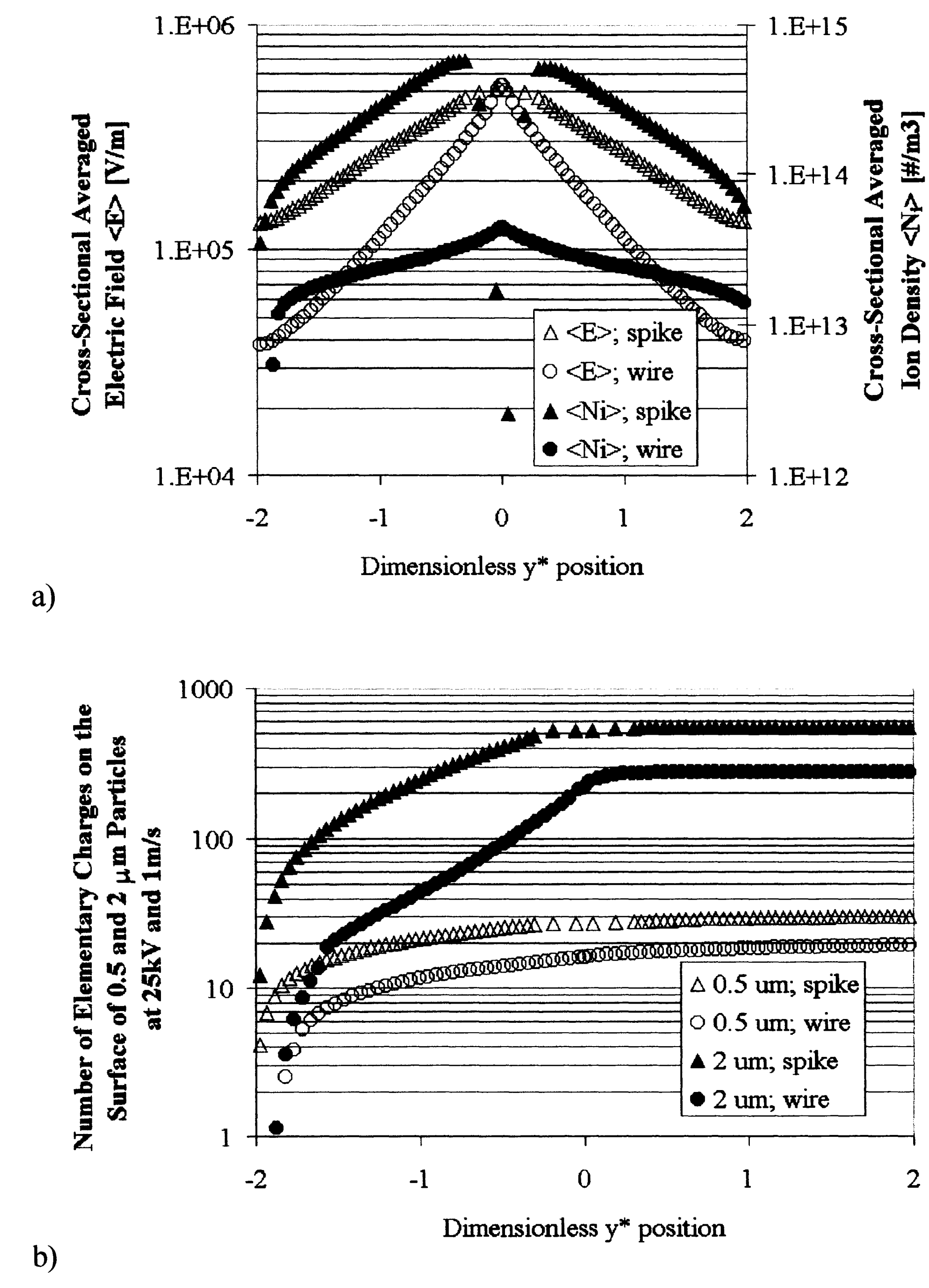

Figure 4.13 (a) Cross sectional averaged electric field and ion density for spike and wire type DE, and (b) number of elementary charges on the surface of *0.5* and *2μm* particles.

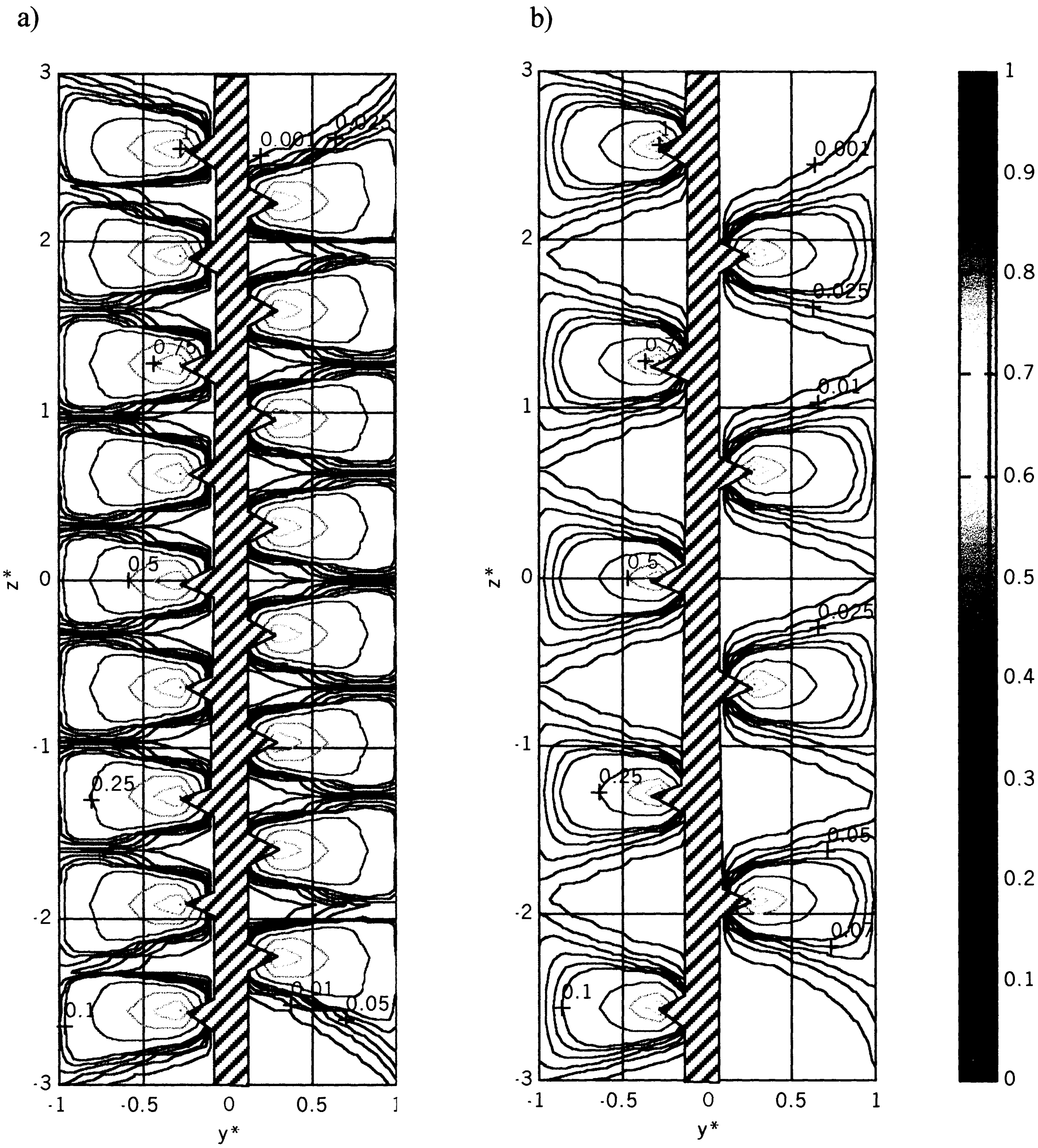

Figure 4.14 Contour of dimensionless ion density n_{ni} (y^*,z^*) at x*=0 plane for the spike-type DE and the I-type CE at *-25 kV* and *1m/s* with (a) 17 spikes and (b) 9 spikes.

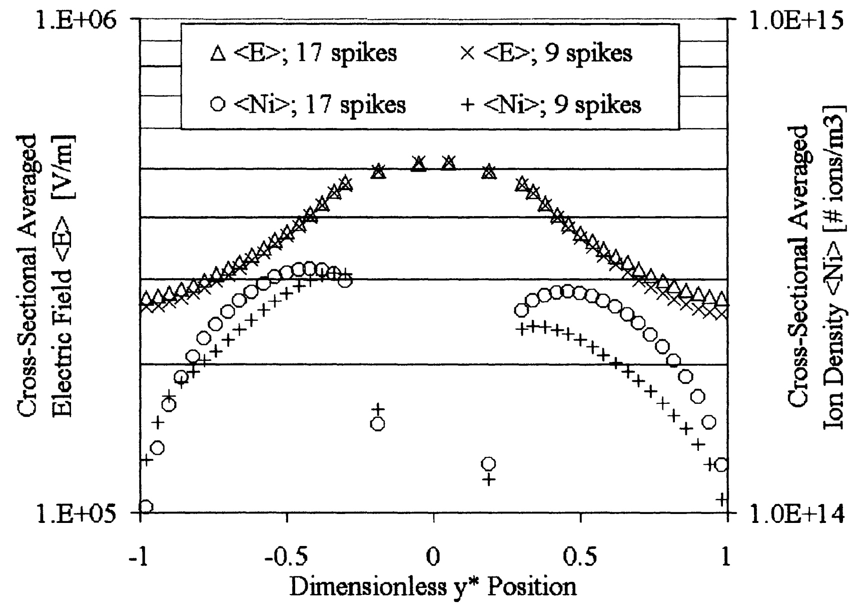

a)

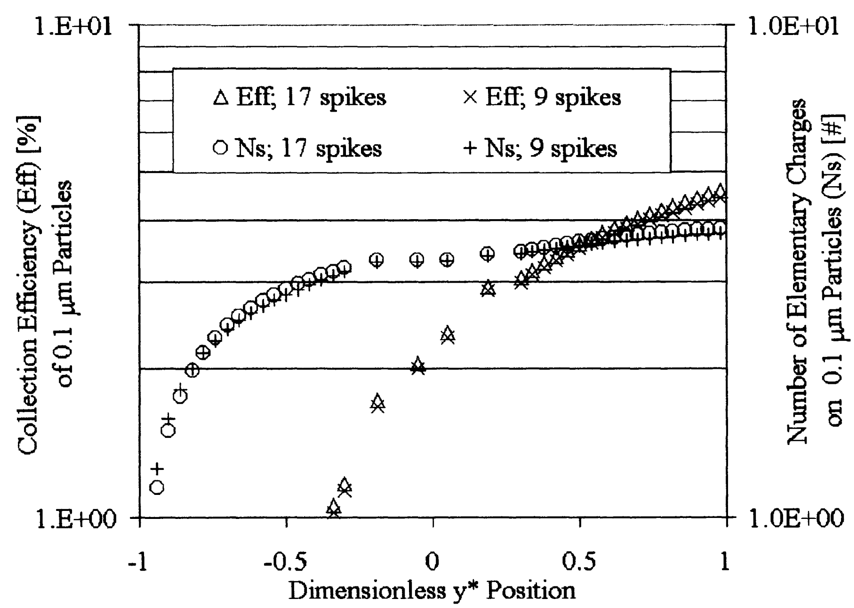

b)

Figure 4.15 (a) Cross sectional averaged electric field <E> and ion density <Ni>, and (b) Number of elementary charges (Ns) and collection efficiency (Eff) of *0.1 μm* particles for I-type CE and spike-type DE with *17* and *9* spikes.

4.2 COLLECTING ELECTRODE GEOMETRY EFFECTS

Several aspects of collecting electrode dimensions and geometry were analysed. These include: (a) the collecting electrode length and spacing were evaluated for I-type CE and spike-type DE arrangement, (b) the U and C geometries of collecting electrodes (see Figure 4.16) were compared to the I-type, and (c) the various fin lengths in the case of C-type collecting electrode. The analysis was based on the evaluation of electric field, ion density distribution, and their impact on the particle surface charge and collection efficiency of submicron and ultrafine dust particles. All numerical simulations were conducted with spike type discharge electrode connected to a dc supply voltage of *–25 kV*. The main gas velocity and temperature were set to *1 m/s* and 20^oC, respectively.

4.2.1 Effect of Collecting Electrode Length and Spacing

A decrease in collecting electrode length and collecting electrode spacing affects the particle surface charge and collection efficiency of submicron and ultrafine dust particles differently, as shown in Figure 4.17. A decrease in collecting electrode length (Y) from *20* to *10 cm* decreases the particle surface charge in the range from *-24 %* to *-7 %* and the collection efficiency in the range from *-45 %* to *-23 %* for particles ranging from *0.01* to *10* μm. The major reason for reduced collection efficiency is smaller charging time due to the shorter section. A decrease in plate-to-plate spacing (D) from *10* to *5 cm* increases the particle surface charge in the range from *28 %* to *113 %* and the collection efficiency in the range from *141 %* to *42 %*. Some of the reasons for improved collection efficiency are a *239 %* higher volume averaged ion density, and *138 %* larger volume averaged electric field.

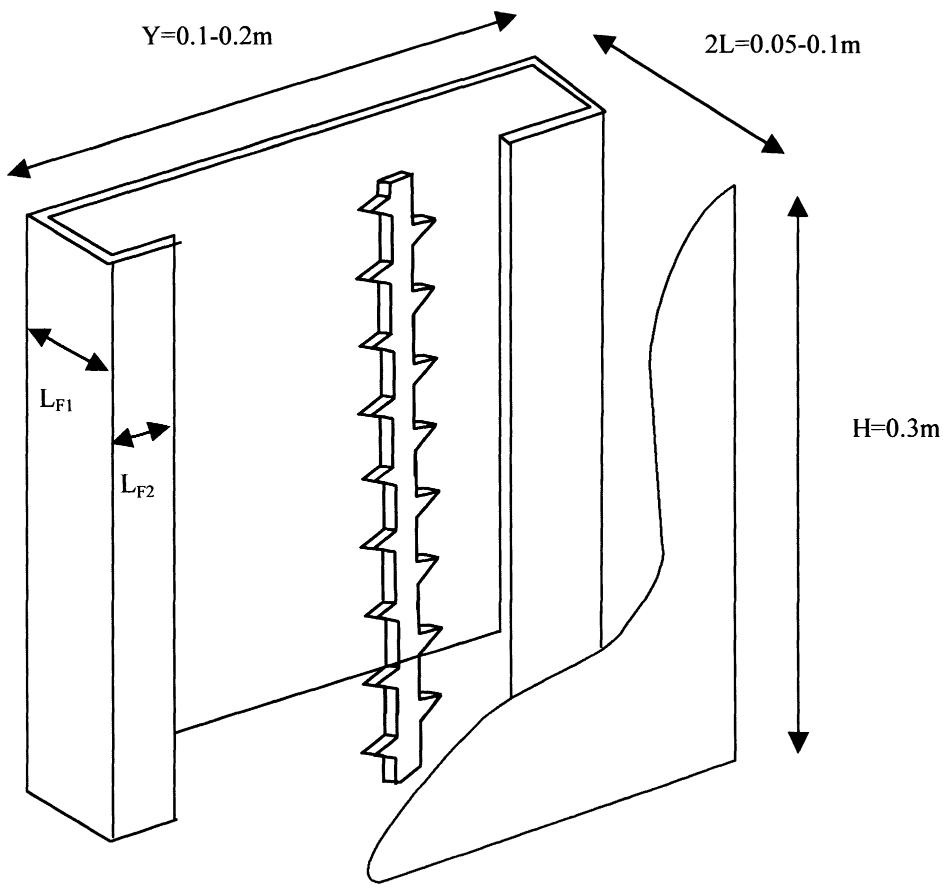

Figure 4.16 Sketch of a C-type collecting electrode. The U-type collecting electrode has only fin denoted as L_{F1}. The I-type collecting electrode does not have any fins (L_{F1}=L_{F2}=*0*).

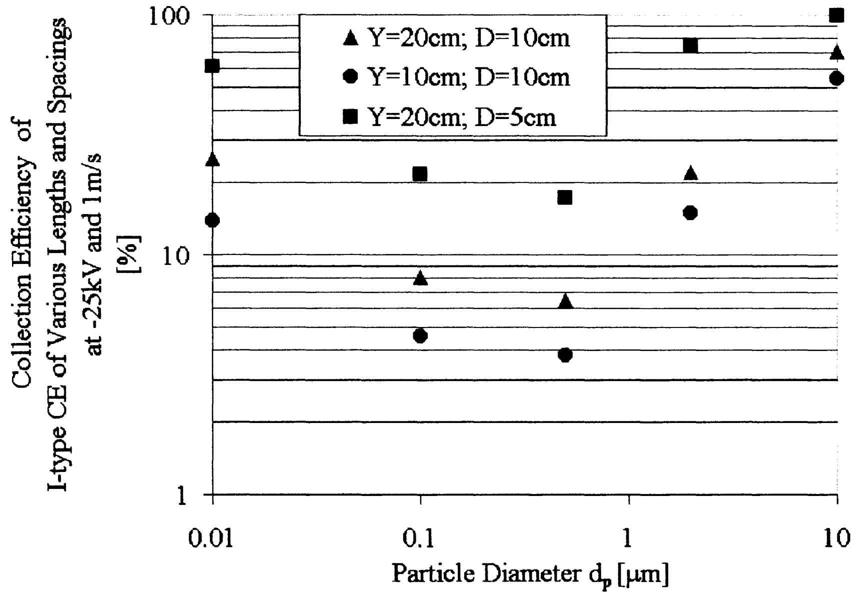

a)

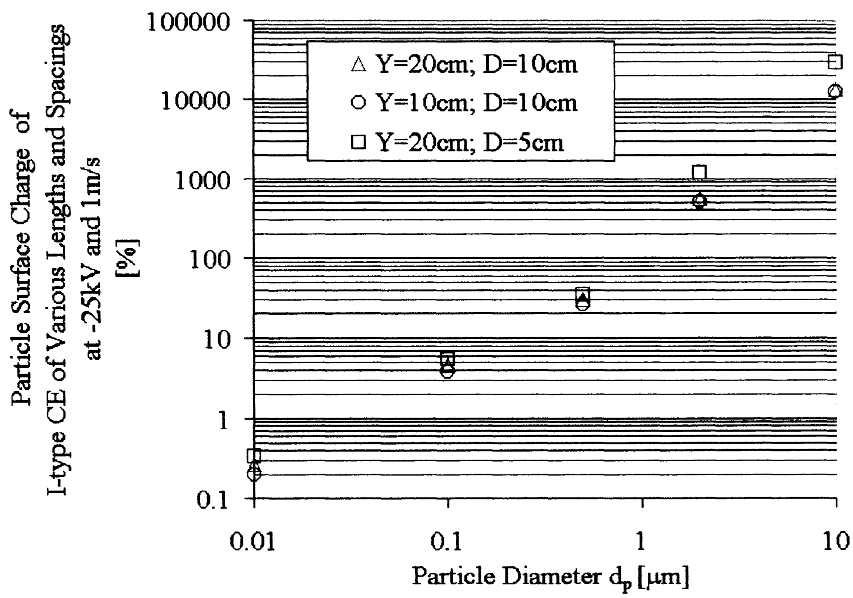

b)

Figure 4.17 (a) Collection efficiency, and (b) number of elementary charges as a function of particle diameter for various Y and D dimensions of I CE with spike DE. (Operating voltage is *-25 kV* and mean gas velocity is *1 m/s.*)

4.2.2 Effect of Collecting Electrode Geometry

The effect of the collecting electrode geometry is studied on $Y{\times}D=10{\times}10\ cm$ field at an applied voltage of $-25\ kV$ and mean gas velocity of $1\ m/s$. The contour lines of electric potential, $|\xi_x|$ and $|\xi_y|$ components of electric field, and ion density for I, U and C-type collecting electrodes are shown in Figures 4.18-4.20. The U-type collecting electrode, with dimensionless fin length of $L_{F1}^{*}=L_{F1}/L=0.36$, affects more $|\xi y|$ than $|\xi x|$ component of the electric field. The volume-averaged value of $|\xi x|$ increased by *10 %,* and $|\xi y|$ by *163 %,* compared to the value with I-type collecting electrode. With L-shaped fins, $L_{F1}^{*}= 0.36$ and $L_{F2}^{*}= 0.4$, as in the case of the C-type collecting electrode, the $|\xi_x|$ component of the electric field decreased by *–35%,* and $|\xi_y|$ components increased by *145 %*, compared to the I-type CE. In spite of the smaller $<N>/N_{io}$ ratio with U and C–type CEs, the volume averaged value of ion densities are *69.3 %* and *76 %* higher, compared to the I-type CE due to the higher initial number of ions N_{io}. The initial number of ions are 2.6 and 3 times higher for U and C-type CEs than for the I-type CE. Whereas, the $<N>/N_{io}$ ratios are *8.6 %* and *7.8 %* for U and C-type CEs, and *13.4 %* for I-type CE. The U and C-type CEs increase particle collection efficiency in the range from *7* to *27 %* depending on the particle size. The U type CE provide better collection efficiency than C-type due to the larger ξ_x component of electric field. Smaller dust particles experienced higher improvement in the collection efficiency than larger particles due to the higher increase of the ion density compared to the increase of the modulus of electric field $|\xi|$.

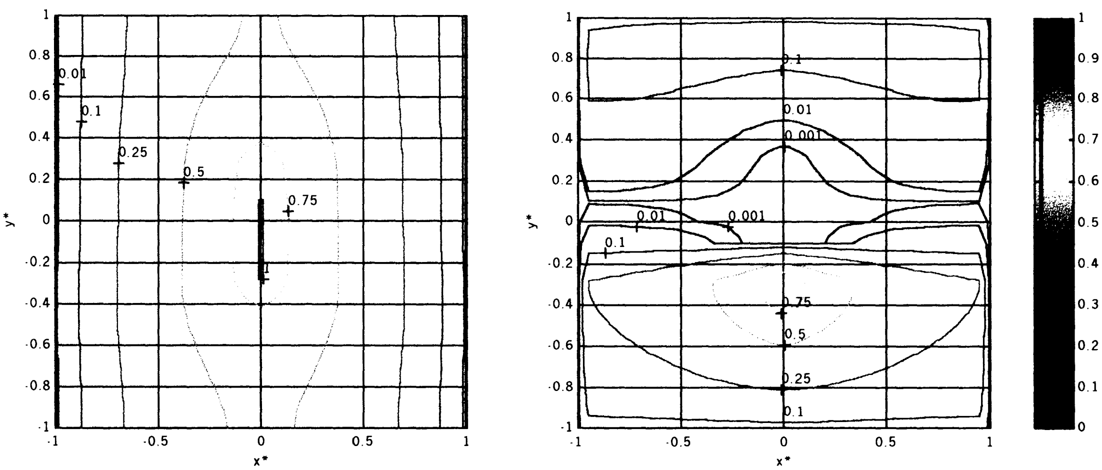

Figure 4.18a,b Contour lines of dimensionless (a) electric potential $\Phi^*(x^*, y^*)$, and (b) ion density $n_{ni}^*(x^*, y^*)$ at z*=-2.65 plane for I-type CE with spike-type DE (*Y=10 cm, L=10 cm, V=-25kV*)

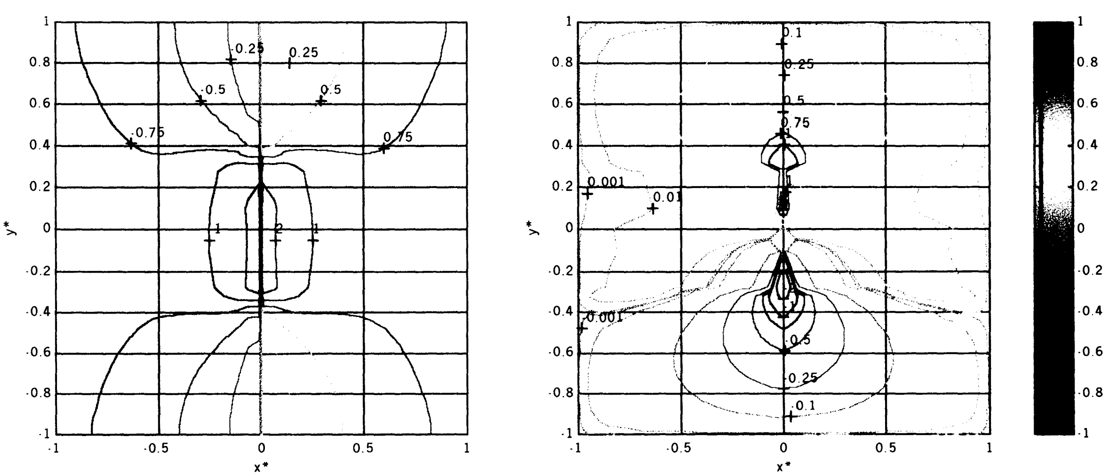

Figure 4.18c,d Contour lines of dimensionless components of electric field: (c) $\xi_x(x^*,y^*)$ and (d) $\xi_y(x^*,y^*)$ at z*=-2.65 plane for I-type CE with spike-type DE (*Y=10 cm, L=10 cm, V=-25kV*)

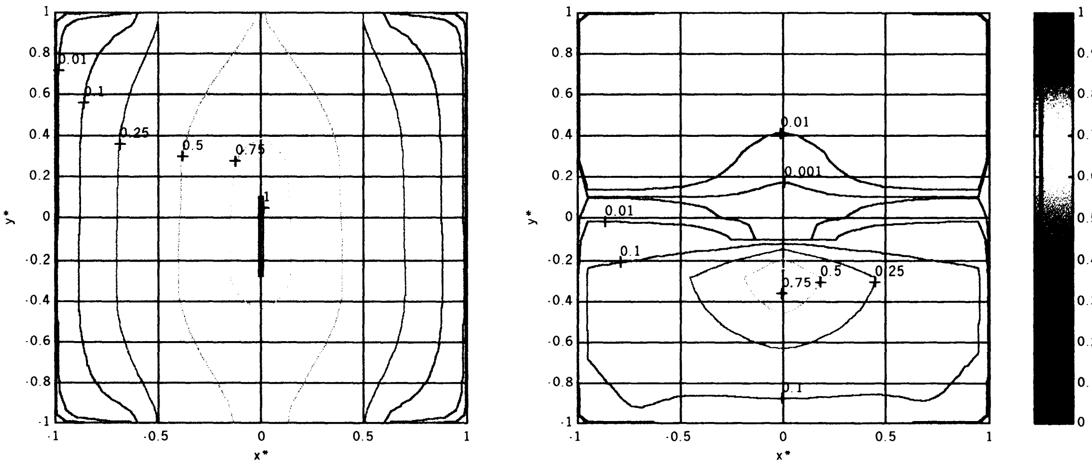

Figure 4.19a,b Contour lines of dimensionless (a) electric potential $\Phi^*(x^*, y^*)$, (b) ion density $n_{ni}^*(x^*, y^*)$ at z*=-2.65 plane for U-type CE with $L_{FI}^* = 0.36$ and spike-type DE (*Y=10 cm, L=10 cm, V=-25kV)*

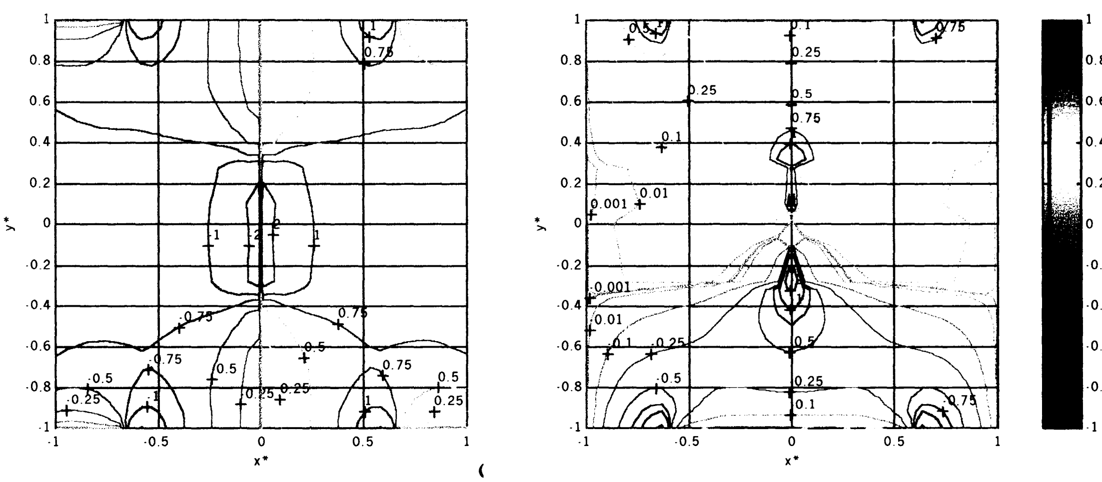

Figure 4.19c,d Contour lines of dimensionless components of electric field:
(c) $\xi_x(x^*,y^*)$ and (d) $\xi_y(x^*,y^*)$ at z*=-2.65 plane for U-type CE with $L_{FI}^* = 0.36$ and spike-type DE (*Y=10 cm, L=10 cm, V=-25kV)*

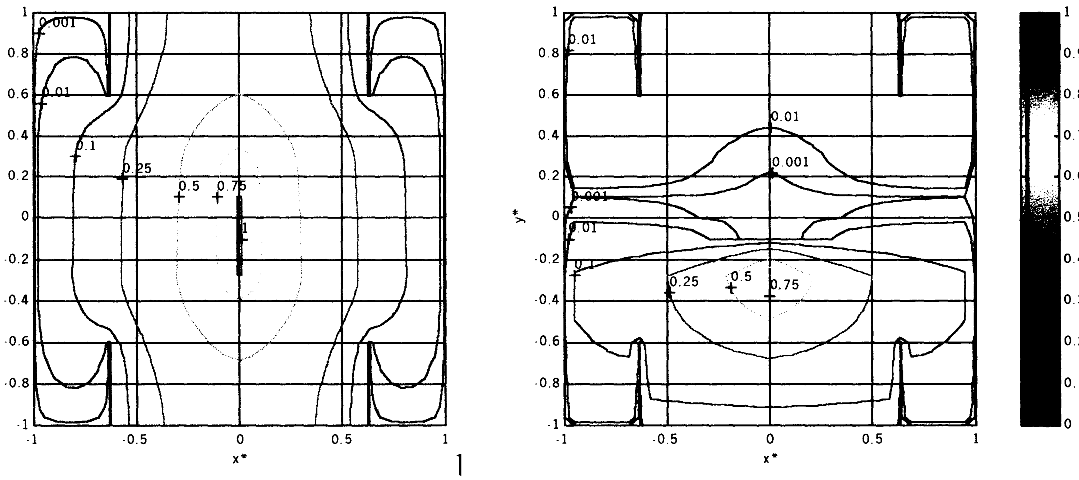

Figure 4.20a,b Contour lines of dimensionless (a) electric potential $\Phi^*(x^*, y^*)$, (b) ion density $n_{ni}^*(x^*, y^*)$ at $z^*=-2.65$ plane for C-type CE with $L_{F1}^* \times L_{F2}^* = 0.36 \times 0.4$ and spike-type DE (*Y=10 cm, L=10 cm, V=-25kV*)

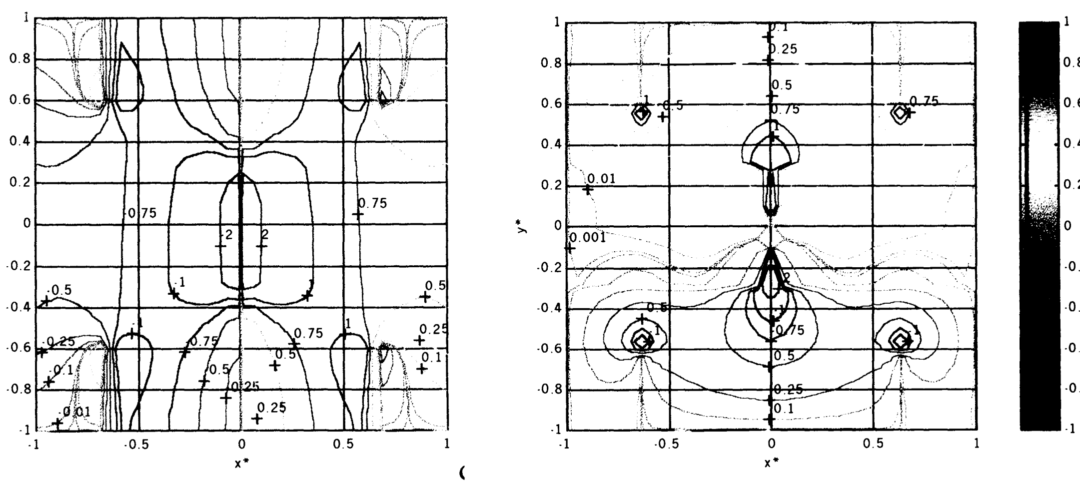

Figure 4.20c,d Contour lines of dimensionless components of electric field:
(c) $\xi_x(x^*,y^*)$ and (d) $\xi_y(x^*,y^*)$ at $z^*=-2.65$ plane for C-type CE with $L_{F1}^* \times L_{F2}^* = 0.36 \times 0.4$ and spike-type DE (*Y=10 cm, L=10 cm, V=-25kV*)

4.2.3 Effect of Fin Length in C-type CE

In the previous section it has been shown that the fins may increase the $|\xi_y|$ component of electric field, decrease the $|\xi_x|$ component, and increase the initial number of ions or discharge current. In order to see the effect of L_{F1}^* and L_{F2}^* lengths, the *10 cm* long C-type CE was evaluated with four different fin lengths combinations denoted as 1×1, 2×2, 3×2, and 3×3. The corresponding $(L_{F1}^* \times L_{F2}^*)$ lengths are 0.16×0.2, 0.36×0.4, 0.57×0.4, and 0.57×0.6. The applied voltage and gas flow velocities were *–25 kV* and *1 m/s*. The contour lines of electric potential and ion density are shown in Figures 4.21 and 4.22. The results show considerable effect of fin lengths. The longer the L_{F1}^* and L_{F2}^* lengths, the higher the discharge current or initial number of ions (N_{io}), and average ion density (See Figure 4.23). Fins have adverse effect on the electric field. They reduce ξ_x component of electric field near collecting electrode in the middle section of the ESP field, and increase both components close to the L_{F2} tip. When cross sectional averaged moduli of electric field were compared to I type CE (denoted as fin 0×0), the modulus of electric field of any four combinations was higher in the $-0.84<y^*<0.84$ section than with I-type CE. When the particles' surface charges were compared, the highest value was achieved for 3×3 combination. However, the best collection efficiencies were achieved with 3×2 combination, for which the collection efficiency of *10 μm* particles was increased by *12 %*, and of *0.01 μm* particles by *42 %*.

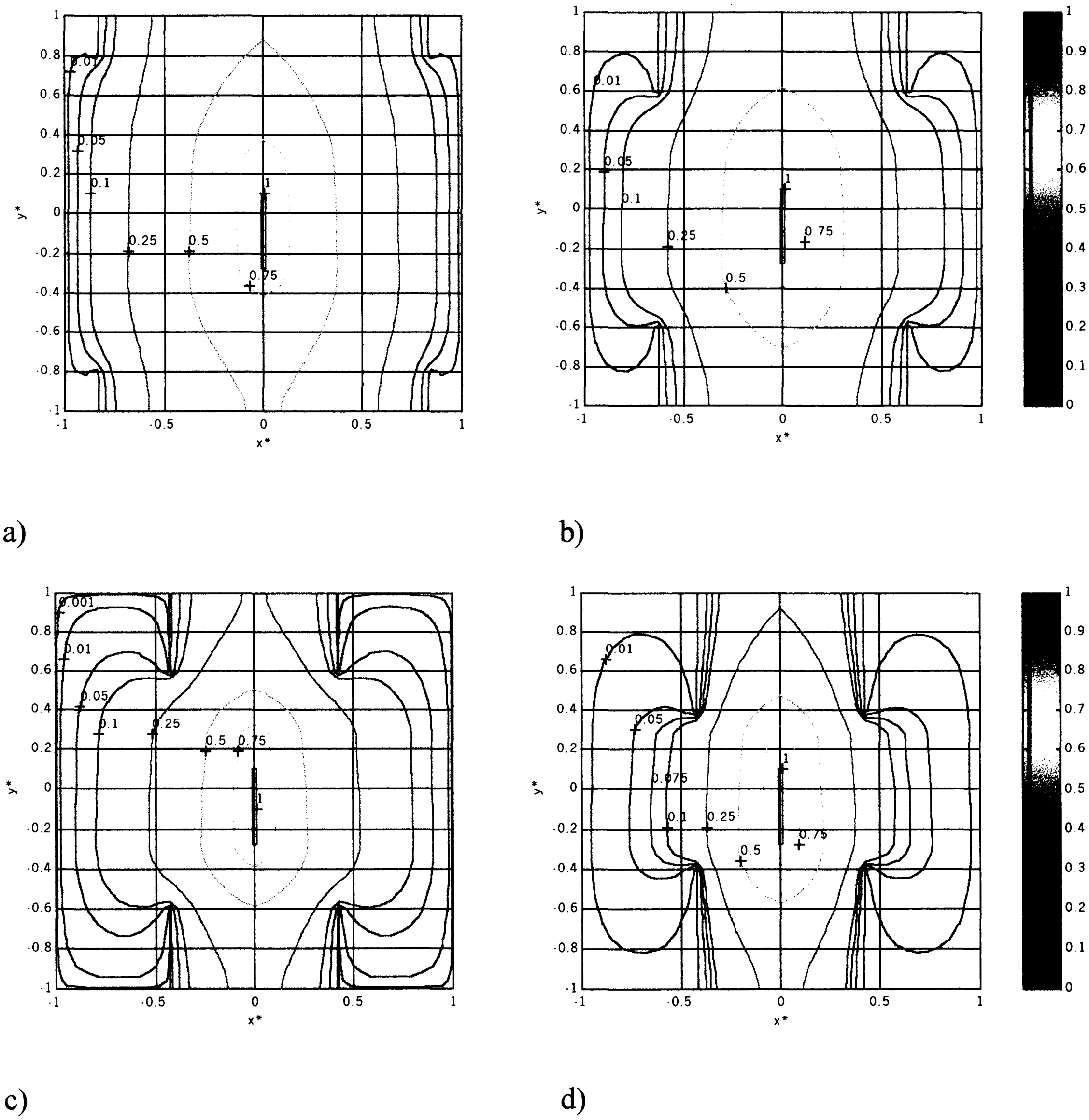

Figure 4.21 Contour lines of dimensionless electric potential $\Phi^*(x^*, y^*)$ at $z^*=-2.65$ plane for C-type CE and spike-type DE for fin lengths $L_{F1}^* \times L_{F2}^*$ of: (a) *0.16x0.2,* (b) *0.36x0.4* , (c) *0.57x0.4,* (d) *0.57x0.6.* *(Y=10 cm, L=10 cm, V=-25kV)*

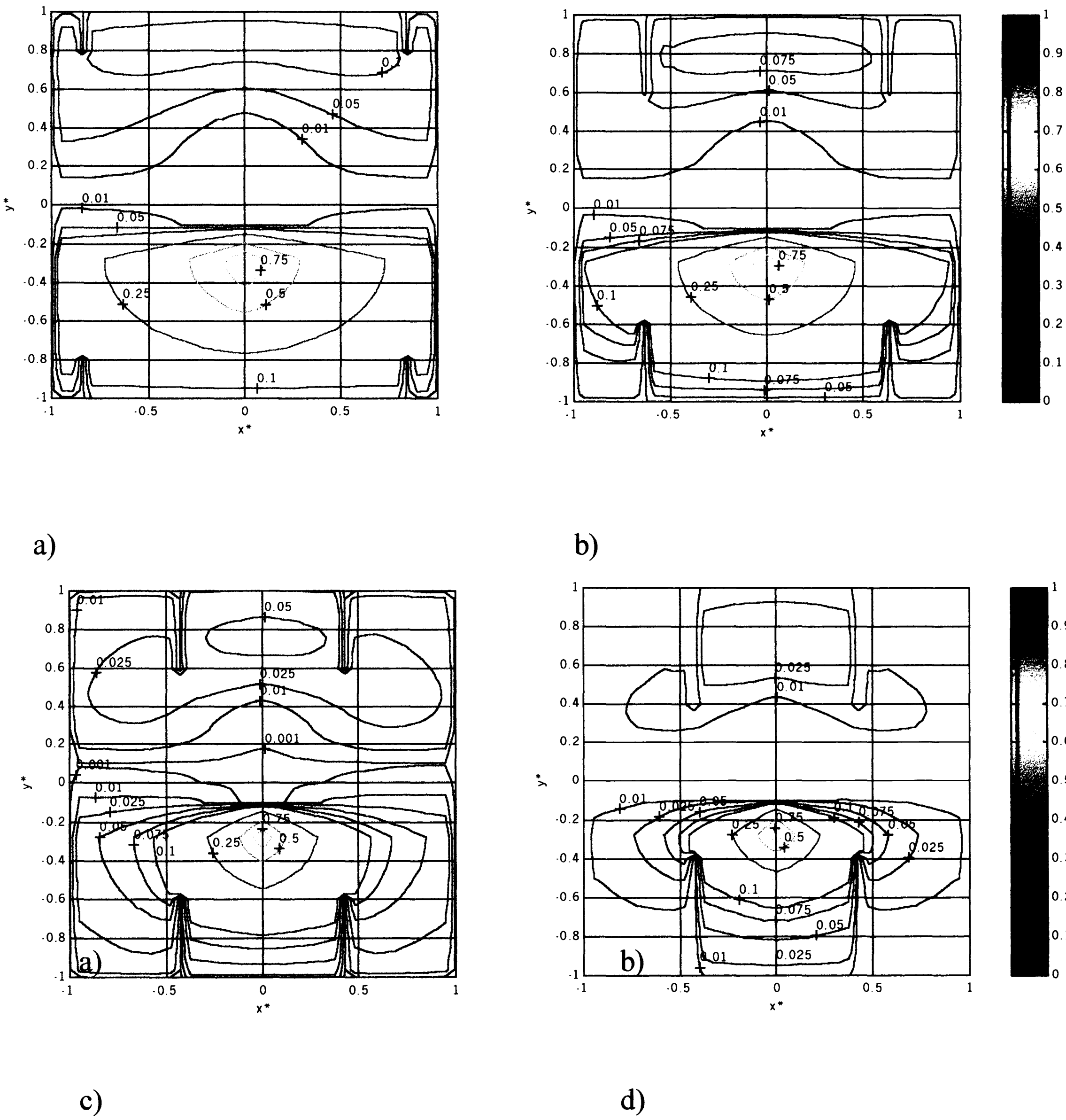

Figure 4.22 Contour lines of dimensionless ion density $n_i^*(x^*, y^*)$ at z^*=-2.65 plane for C-type CE and spike-type DE for fin lengths $L_{F1}^* \times L_{F2}^*$ of: (a) *0.16x0.2,* (b) *0.36x0.4* , (c) *0.57x0.4,* (d) *0.57x0.6.* *(Y=10 cm, L=10 cm, V=-25kV)*

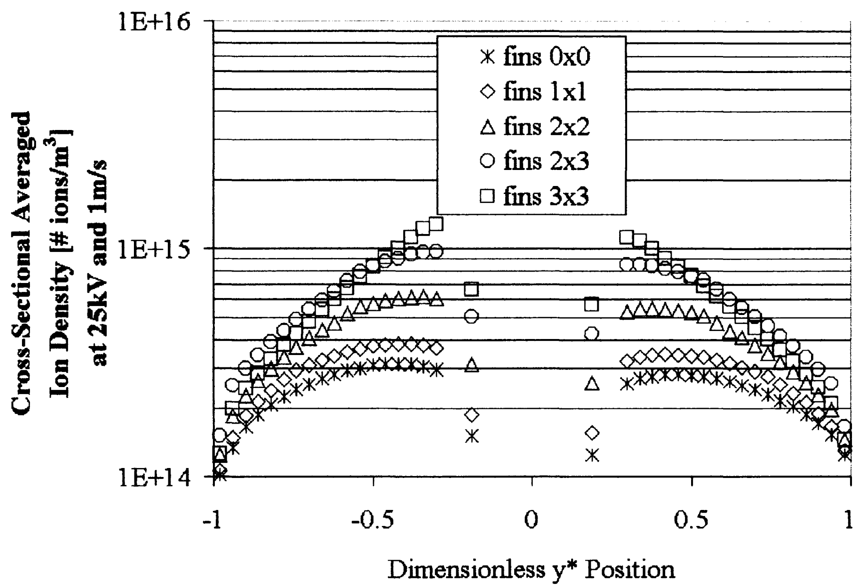

a)

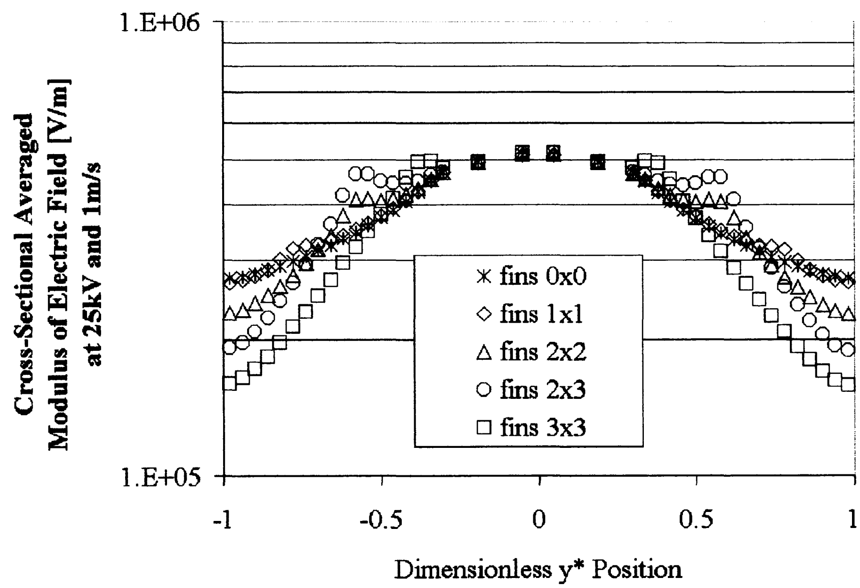

b)

Figure 4.23 Cross-sectional averaged ion density and modulus of electric field along the ESP length for C-type CEs of various fin lengths and spike-type DE. (*Y=10 cm, L=10 cm, V=-25kV*)

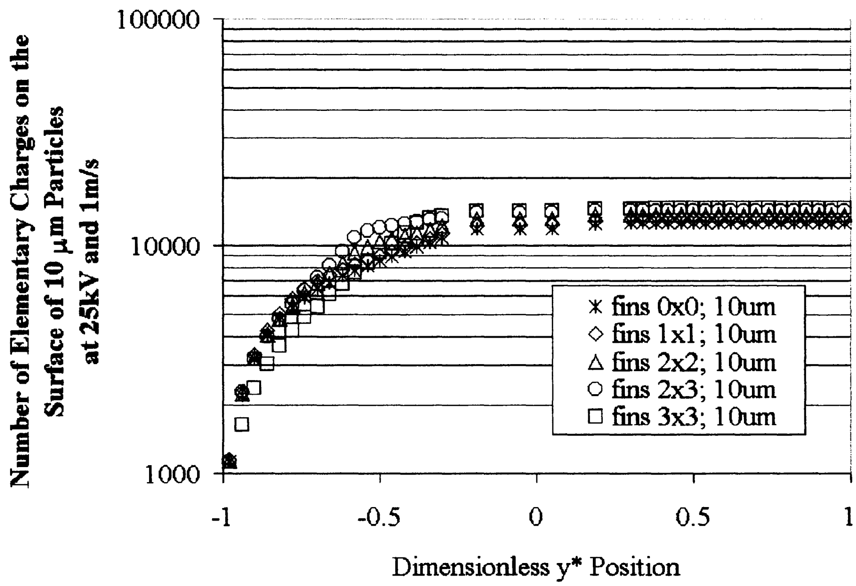

a)

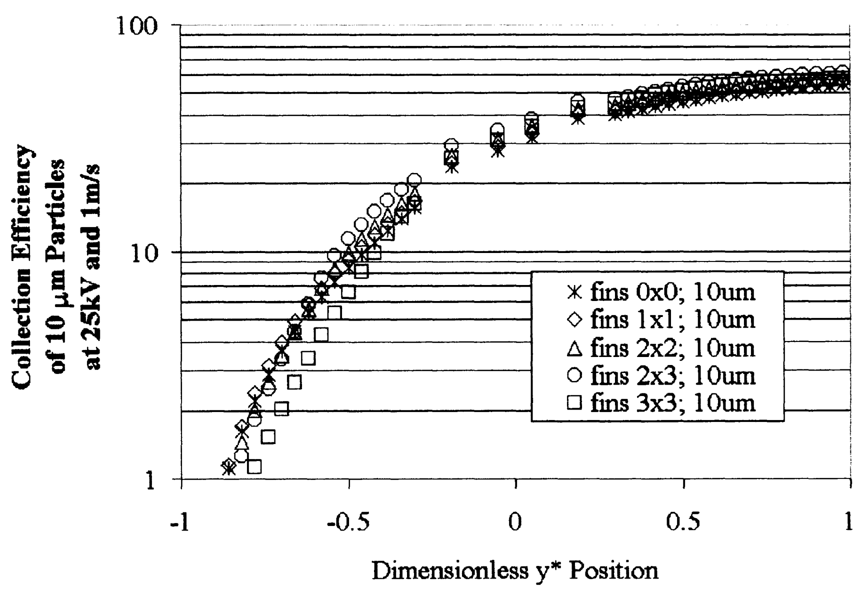

b)

Figure 4.24 Development of a) particle surface charge, and (b) cumulative collection efficiency of *10 μm* dust particles along the ESP length for C-type CEs of various fin lengths and spike-type DE. (*Y=10 cm, L=10 cm, V=-25kV*)

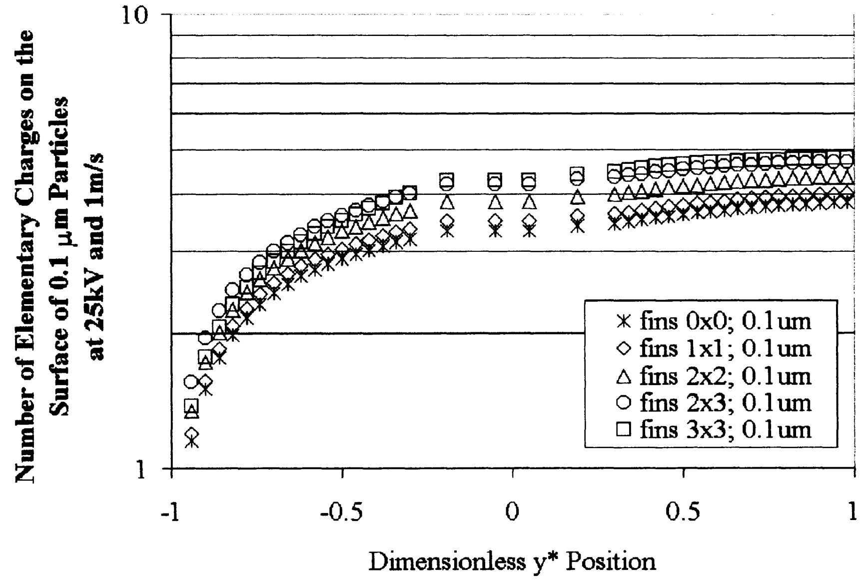

a)

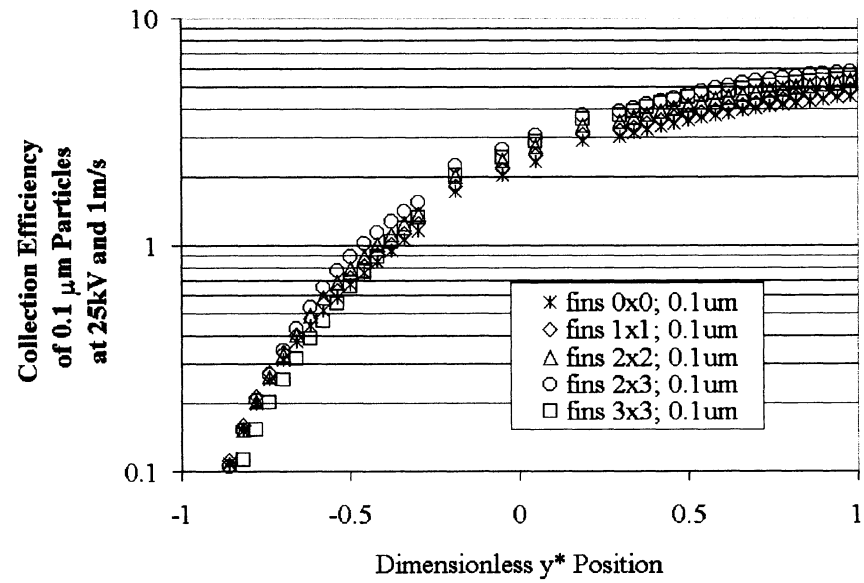

b)

Figure 4.25 Development of a) particle surface charge, and (b) cumulative collection efficiency of *0.1 μm* dust particles along the ESP length for C-type CEs of various fin lengths and spike-type DE. (*Y=10 cm, L=10 cm, V=-25kV*)

4.3 DISCUSSION ON NEW ELECRODE DESIGN

Based on the literature review with respect to the spike and barbed type DEs, it was observed that the DEs with spikes or barbs provide better collection efficiency in the first few fields of multi-field ESPs. On the other side in sections where complex dust layers were formed, the re-entrainment effects associated with the barbs oriented towards the collecting electrode may cause collection efficiency reduction. Additionally, in order to enhance submicron and ultrafine dust particles, the ion densities of 10^{16} order of magnitude, or higher and electric fields higher than *10 kV/cm* are required. Therefore, the following set of rules was established as guideline in selection of discharge and collecting electrode dimensions: (a) spike structure provides better control of discharge location then smooth wire, (b) spikes oriented parallel to the collecting electrode may be better than those oriented towards the collecting electrode due to the larger ion penetration, (c) it is desirable to have few narrow parallel channels then one wide, (d) spike length can be used as one of the parameters to improve collection efficiency by increasing the ion density and electric field in addition to the fin lengths. The numerical simulations with respect to the fin length have showed the best collection efficiency for the $(L_{F1}^* \times L_{F2}^*)$ combination of 0.57×0.4. However, it was observed that further increase of the L_{F2}^* length from 0.4 to 0.6 reduces collection efficiency due to the reduction of volume averaged electric field, in spite of some local improvements. Therefore, the length of the spike was increased from *0.9 cm* to *1.8 cm*. The results presented in Figure 4.26 show further improvement of collection efficiency.

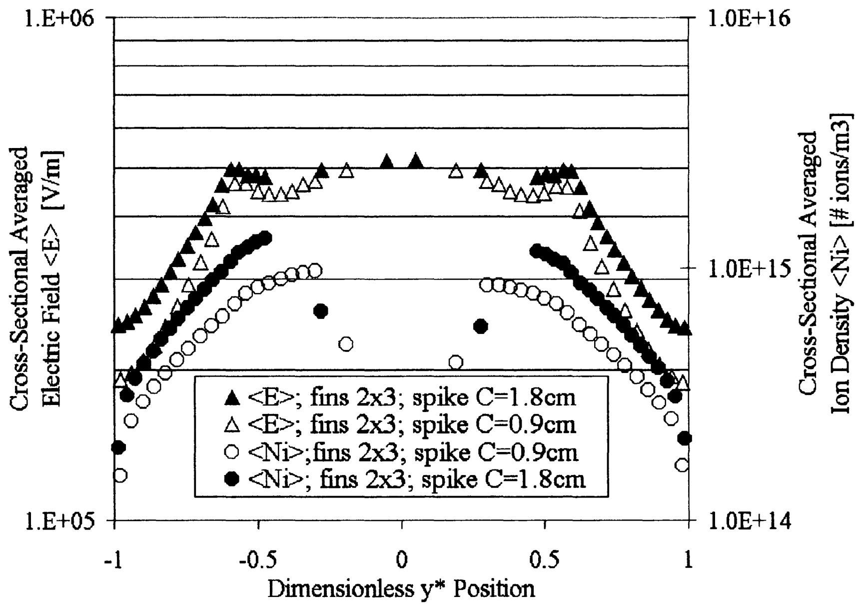

a)

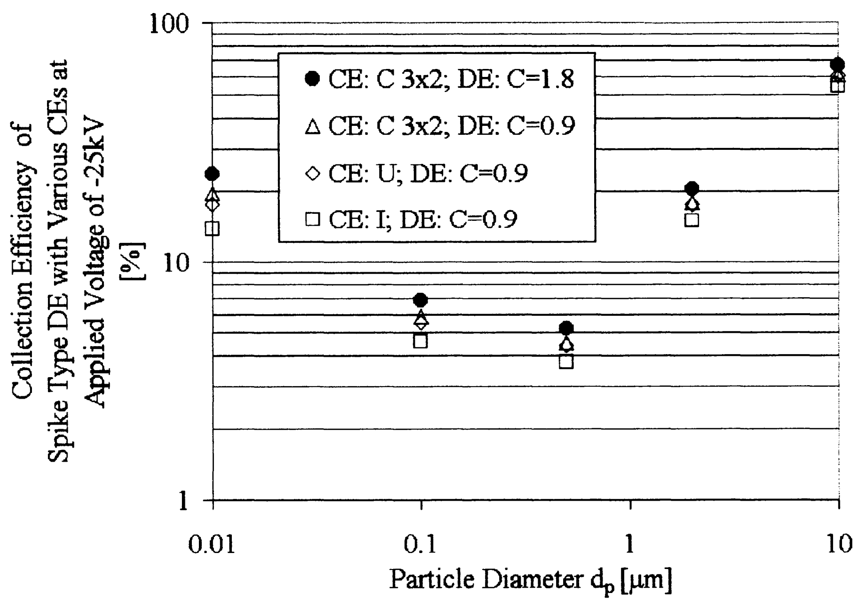

b)

Figure 4.26 (a) Cross-sectional averaged ion density and modulus of electric field along the ESP length for C-type CEs of various fin lengths and spike-type DEs with *C=0.9* and *1.8cm*, and (b) total collection efficiency of various dust particles. (*Y=10 cm, L=10 cm, V=-25kV*)

The new design resembles two-stage ESP design. However, the usually separated precharger and collector sections are here combined in one design. Fins and long spikes have a role of precharger, and provide high ion density and electric field. The body of the spike, together with CEs, has a collector role and provides high electric field. Since the collection efficiency is predicted mainly based on the evaluation of electric field and ion density, further analyses based on Mode2 would be required. It would enable the study of particle transport in details, especially the effect of fins on the flow separation and EHD flow. At present, the EHD flow was decoupled based on the evaluation of EHD number. However, C-type CE structure would require numerical confirmations and probably redefinition of EHD number based on the current density at fin structure. Additionally, studies of the dust layer behaviour at main CE section are required due to the reduced Johnsen-Rahbek force, since the most of the current is deflected to the fin section.

CHAPTER 5

EXPERIMENTAL AND NUMERICAL RESULTS FOR DUST PARTICLE COLLECTION EFFICIENCY

5.1 PROCEDURE FOR MEASUREMENT OF DUST PARTICLE CONCENTRATION

Figure 5.1 shows a schematic diagram of the experimental set-up used in this study, showing the arrangement of discharge and collecting electrodes within the ESP housing and equipment used for the measurement of dust particle concentration. The particulate matter was created by burning incense sticks upstream of ESP. The dust particle concentration, in terms of the number of particles per volume, was measured by the condensation nucleation particle counter (TSI-CNPC). TSI-CNPC was connected to two sampling probes over a directional valve and a particle size separation chamber (PSSC). The total collection efficiency of particulate matter, was obtained from measured data without PSSC. After that, the semi-partial and partial collection efficiencies were obtained by inserting particle size separation filters (PSSFs) in the particle separation chamber. Desired particle size cut was achieved by inserting a various number of PSSFs as shown in Table 5.1.

Based on some preliminary tests the following sampling limits were established: (a) delay time due to the directional valve operation was approximately four seconds, (b) minimum time of outlet sampling was half a minute, and (c) burning velocity of fragrant sticks was approximately *0.46 cm/min.* Figure 5.2 shows time dependant inlet and outlet particle concentrations of spike-plate ESP at mean gas flow rate of *21* m^3/h and various applied voltages.

Table 5.1 Number of PSSF for the desired particle size cut

Number of Screens	Particle Size Cut (50%) [μm]
1	0.017
3	0.041
5	0.062
8	0.092
10	0.112
11	0.122
15	0.162
21	0.225

At first, incense sticks were lit and inserted in a combustion chamber. After the stabilization of the inlet particle concentration, high voltage was applied to a discharge electrode and the directional valve was switched to an outlet sampling port. After approximately two minutes of outlet sampling, the directional valve was again set to sample from the inlet measuring port. The high voltage was turned off and the inlet sampling was continued for a minimum of one minute. The procedure was repeated for other voltage levels. As shown in the Figure 5.12, the inlet concentration of particulate matter is not constant during the experiment. Therefore, the outlet concentration at corresponding voltage level was corrected by the ratio between the base and the inlet concentration. The base concentration of dust particles was obtained from the averaged data points when sampled from the inlet port at the beginning of the experiment. The inlet concentration of dust particles was obtained from the averaged data points when sampled from the inlet port shortly before and after the outlet sampling at a specified voltage.

5.1.1 Total and Semi-Partial Collection Efficiency

The total and semi-partial collection efficiencies of dust particles was obtained from (5.1),

$$\eta_k = \frac{N_{in,k} - N_{out,k}}{N_{in,k}} [\%] \tag{5.1}$$

where η is the dust collection efficiency, N_{in} is the base inlet concentration of dust particles, N_{out} is the corrected outlet concentration of dust particles, subscript k refers to a number of particle size separation filters in a particle size separation chamber.

5.1.2 Partial Collection Efficiency

The partial collection efficiency of dust particles can be obtained from (5.2),

$$\eta_d = \frac{\Delta N_{in} - \Delta N_{out}}{\Delta N_{in}} [\%] \tag{5.2}$$

where subscript d refers to a dust particle size range, $\Delta N_{in} = N_{in,k2} - N_{in,k1}$ is the difference between base inlet concentrations of dust particles, $\Delta N_{out,} = N_{out,\mathrm{k}2} - N_{out,\mathrm{k}1}$ is the difference between corrected outlet concentration of dust particles when sampled with k_1 and k_2 number of particle separation filters.

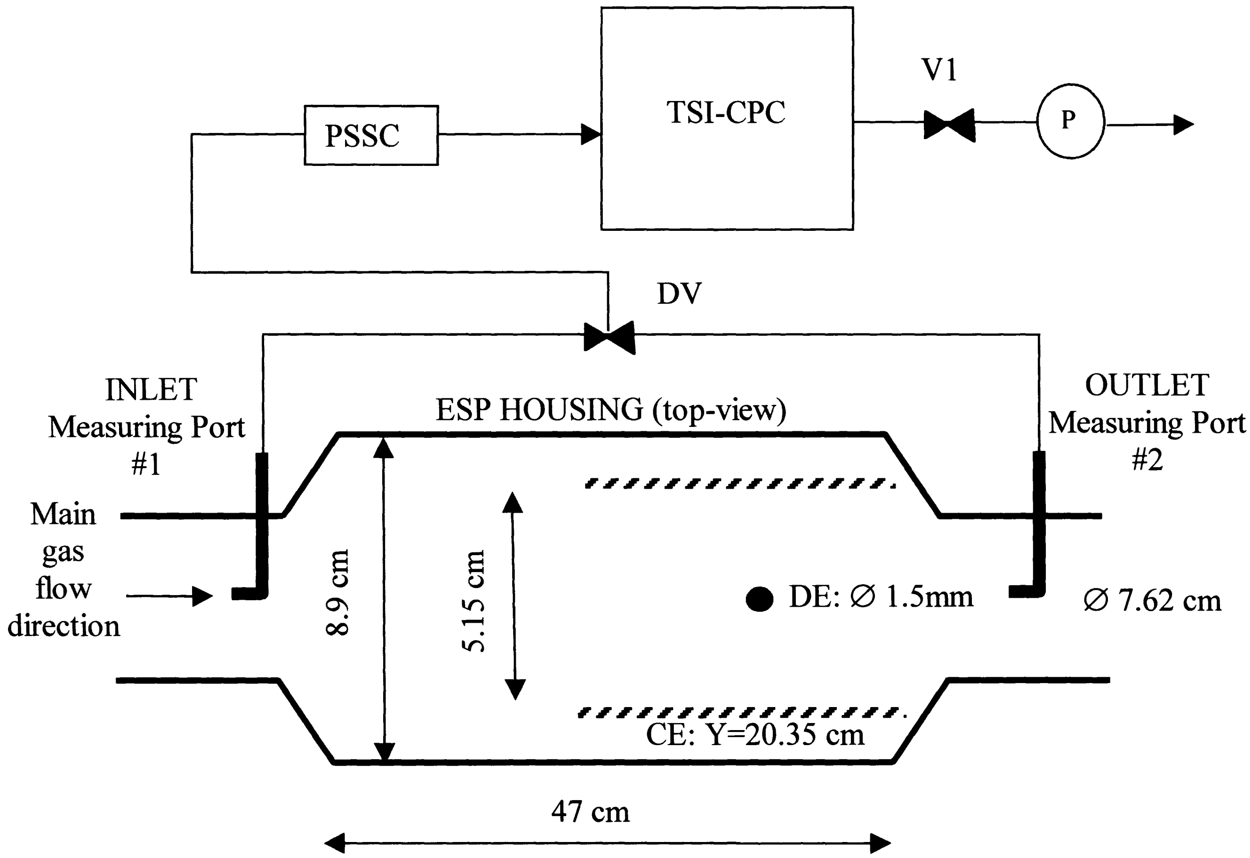

Figure 5.1 Schematic diagram of the dust particle monitoring system and electrode arrangement within the bench-scale ESP.
(TSI-CPC is the Condensation Particle Counter, PSSC is the Particle Size Separation Chamber, DV is the Directional Valve, V1 is the On-Off Valve, P is the Pump, DE is the Discharge Electrode, CE is the Collecting Electrode, Y is the length of the collecting electrode)

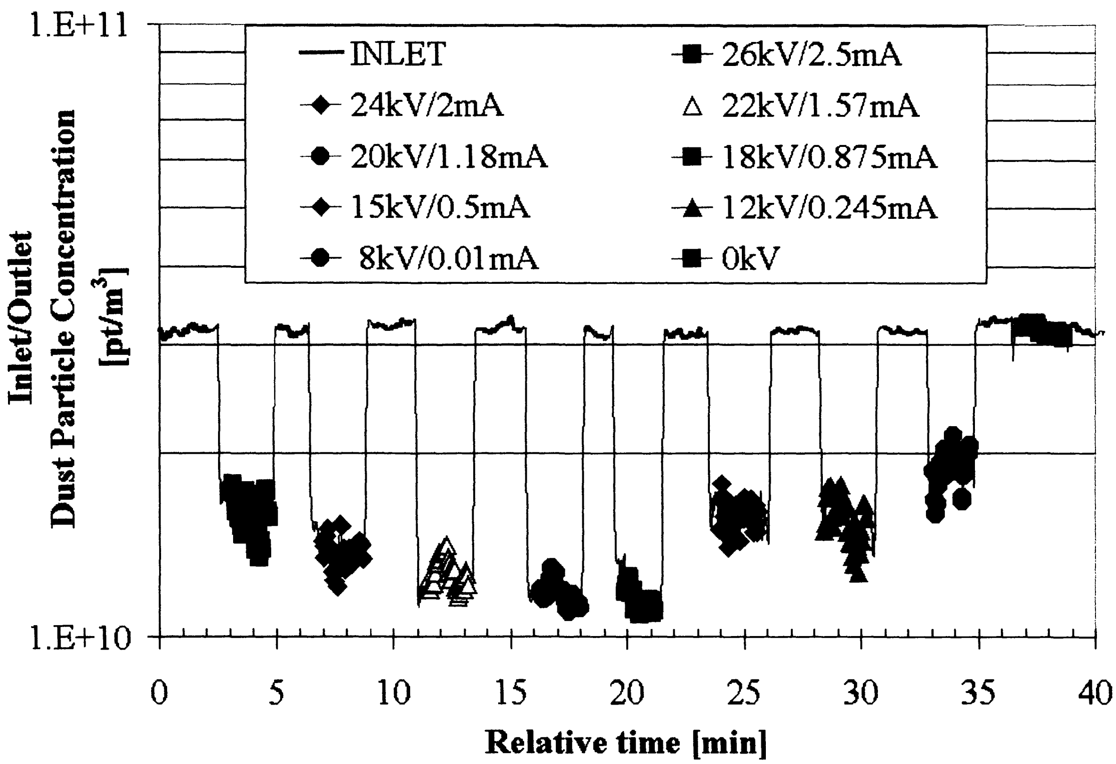

Figure 5.2 Time-dependent inlet/outlet dust particle concentration at various applied voltages and a gas flow rate of *21* m^3/h. (Usually, one set of data required replacement of incense sticks. In this particulate case, the time slot of replacement was cut out.)

5.2 EXPERIMENTAL VALIDATION OF BENCH-SCALE WIRE-PLATE TYPE ESP

5.2.1 Single-field ESP with *0.25 mm* Corona Wire

The single-field ESP, consisting of *20 cm* long collecting electrodes and *0.25 mm* corona wire, is placed in the existing bench-scale ESP housing as shown in Figure 5.3. The main gas flow rate was $16.92\ m^3/h$, the gas temperature was $20\,°C$, and the dust loading was

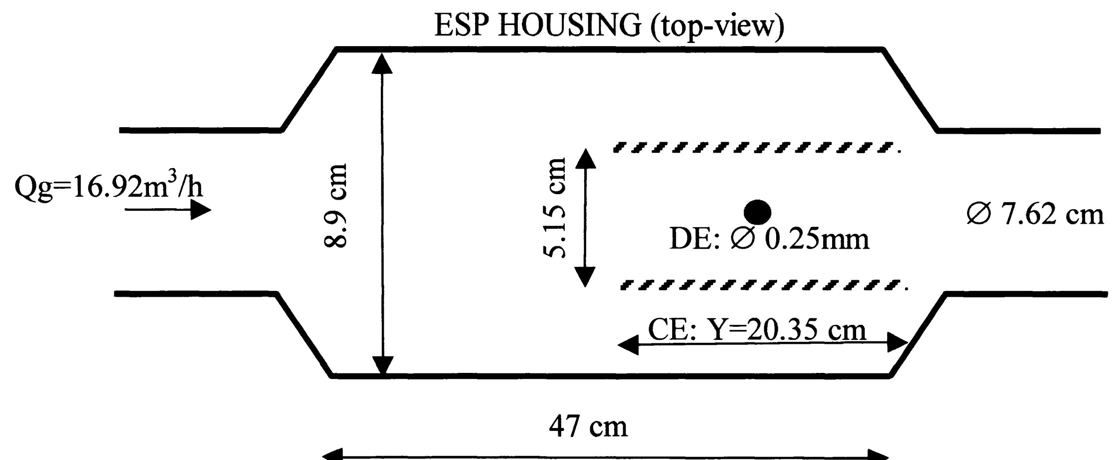

Figure 5.3 Schematic diagram of the wire-plate ESP.

approximately $3{\times}10^{10}\ \#/m^3$. Measured collection efficiency and current are shown in Figure 5.5 as functions of negatively applied voltage. The collection efficiency, obtained by averaging among five data sets, has a local maximum between *-12* and *-14 kV*. The shape of the measured current-voltage curve indicates that there may be some problems with non uniform corona discharge in the axial direction. The digital image of the dust layer from the collecting plate indicates a strong discharge at the bottom of the ESP, as shown in Figure 5.4. After that, the collection efficiency increases with increasing voltage. The comparison between experimental and numerical results is shown in Figure

5.6. There is a very good agreement between predicted measured collection efficiency for voltages higher than *-20 kV*. However, for voltages less than *-20 kV*, there is a high difference between experimental and numerical results. The difference is believed to be due to the non-uniform corona discharge in axial direction, caused by the corona wire misalignment. By simulating the corona discharge at *-10* and *12 kV* only at the bottom section of the corona wire, the predicted value falls between experimental results as marked with a triangle legend in Figure 5.6.

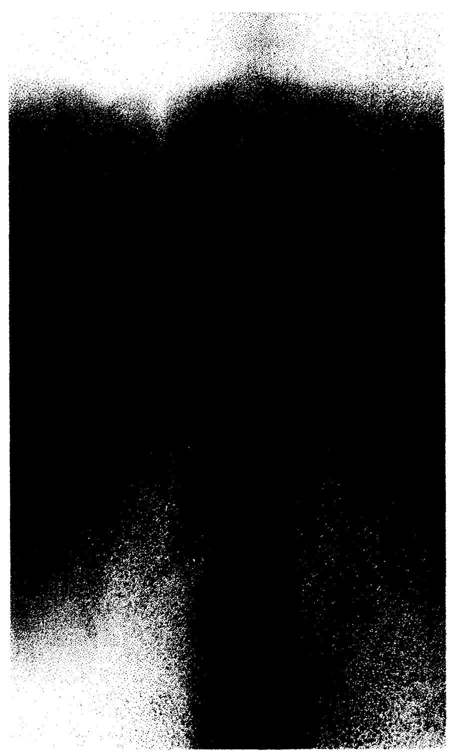

Figure 5.4 Digital image of collecting plate of ESP with *0.25 mm* corona wire.

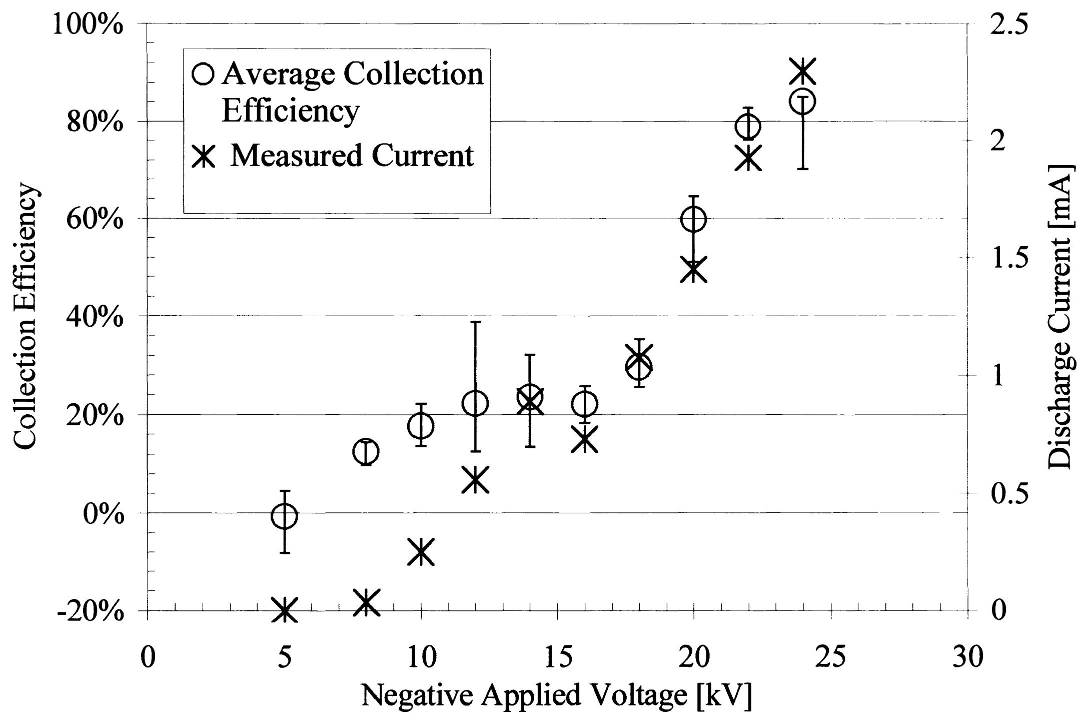

Figure 5.5 Measured current and total dust collection efficiency of single-field ESP with *0.25 mm* corona wire. (Discharge electrode diameter is *0.25 mm*. Collecting electrode length is *20 cm*. Gas flow rate is $Q_g=16.9$ m^3/h.)

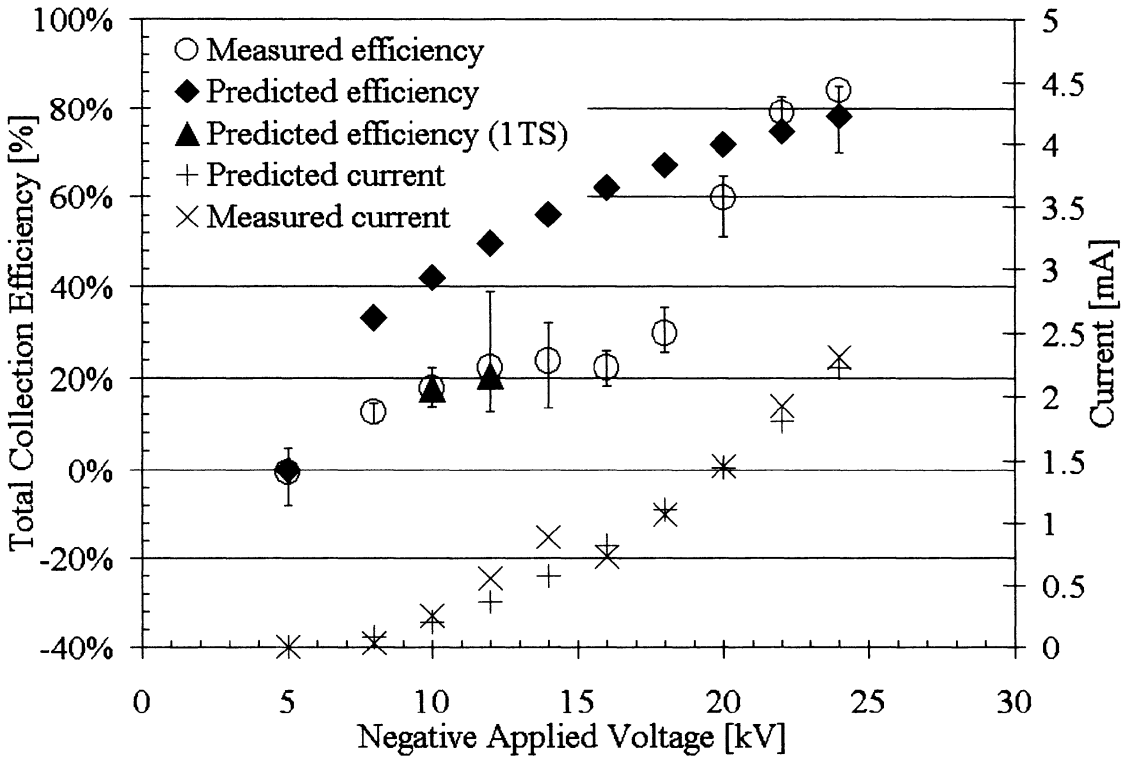

Figure 5.6 Measured and predicted total dust collection efficiency of 0.25 mm corona wire.

5.2.2 Single-Field ESP with 1.5 mm Corona Wire

In this section experimental results on single-field wire-plate ESP will be compared to numerical results. The collecting electrodes, *20* cm in length, are placed in the bench-scale ESP housing as shown in Figure 5.3. The diameter of the discharge electrode was *1.5 mm*. The main gas flow rate was set to *3.5*, *7.8*, and *16.9* m^3/h, the gas temperature was *20℃*, and the dust loading was approximately 3×10^{10} *# of particles/*m^3. The measured collection efficiency and current-voltage curves are shown in Figure 5.7. The collection efficiency has a local maximum around *-22 kV*, followed by a local minimum around *-25 kV*. The shape of the measured current-voltage curve, fairly smooth, indicates uniform corona discharge in the axial direction. However, from digital image analysis, it was observed that at *-22 kV*, approximately *85 %* of discharge spots are facing the inlet and outlet of the ESP and approximately *15 %* are facing collecting electrodes. At *-24 kV* approximately *35 %* of discharge spots are from the corona wire surface facing the inlet and outlet of the ESP. As the applied voltage is increasing, the contribution of discharge spots facing the inlet and outlet of the ESP is increasing approximately up to *65 %* at *-30 kV*. Consequently, the non-uniformity of corona discharge in radial direction may be one of the reasons for the very unusual shape of the collection efficiency versus applied voltage curve. At higher voltages the predicted and experimental results agree within *6 %* of error, as shown in Figure 5.8. However, at voltages close to the corona on-set voltage, the numerical model overestimates collection efficiency. Additionally, the dimensionless number shown in Figure 5.9 indicates strong EHD induced secondary flow or corona wind $((E_{hd}/Re^2)^{0.5}>1)$ and a presence of the ion space charge effect $(Db_i{*}>1)$. Yamamoto and Velkoff [23] showed various modifications of main gas flow in dependence with the $(E_{HD}/Re^2)^{0.5}$ number for wire-plate ESP with uniform corona discharge. They observed no circulatory cell at $(E_{HD}/Re^2)^{0.5}\approx 2$, however the fluid was slightly deflected and accelerated towards the central line of the channel. A small circulatory cell shifted towards collecting electrode appears at $(E_{HD}/Re^2)^{0.5}\approx 9$. One large counterclockwise circulatory cell near the discharge electrode was observed at $(E_{HD}/Re^2)^{0.5}\approx 35$ and the pair of downstream shifted circulatory cells at $(E_{HD}/Re^2)^{0.5}\approx 140$. Based on $(E_{HD}/Re^2)^{0.5}$ number, different modes of main gas flow modifications exist at *-22 kV* and *-25 kV*. Their effect on $0.5\ \mu m$ and $2\ \mu m$ dust particles which are affected by gas convection $(Ra_d/F_E>1)$ may be one of the additional reasons for non-uniform behaviour at *-22 kV* and *-25 kV*.

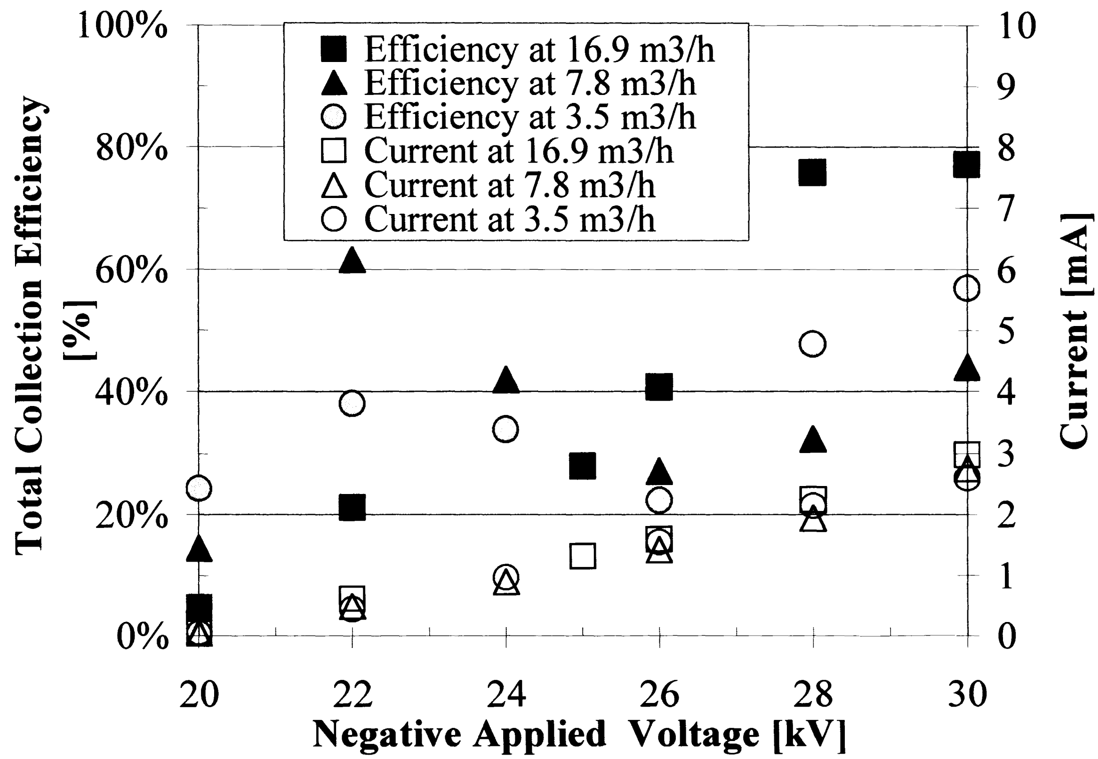

Figure 5.7 Measured dust collection efficiency and discharge current of single-field ESP with 1.5 mm corona wire at various gas flow rates and applied voltages. (Discharge electrode diameter is 1.5 mm. Collecting electrode length is 20 cm.)

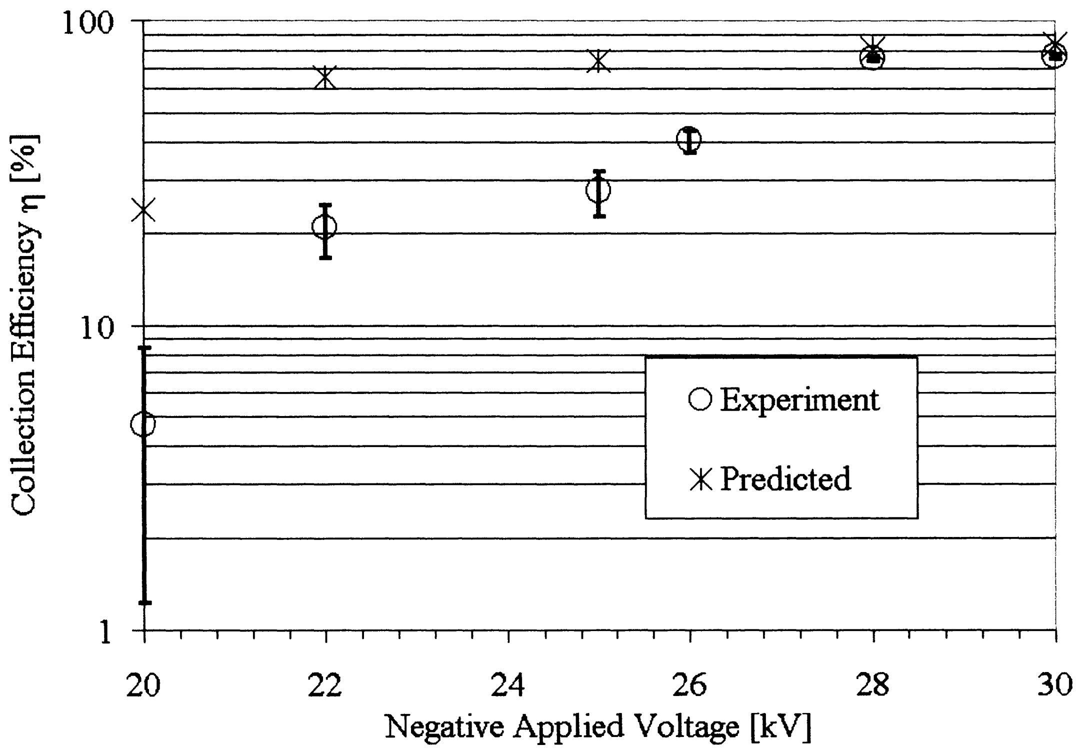

Figure 5.8 Measured and predicted total dust collection efficiency of 1.5 mm discharge electrode at gas flow rate of 16.9 m^3/h.

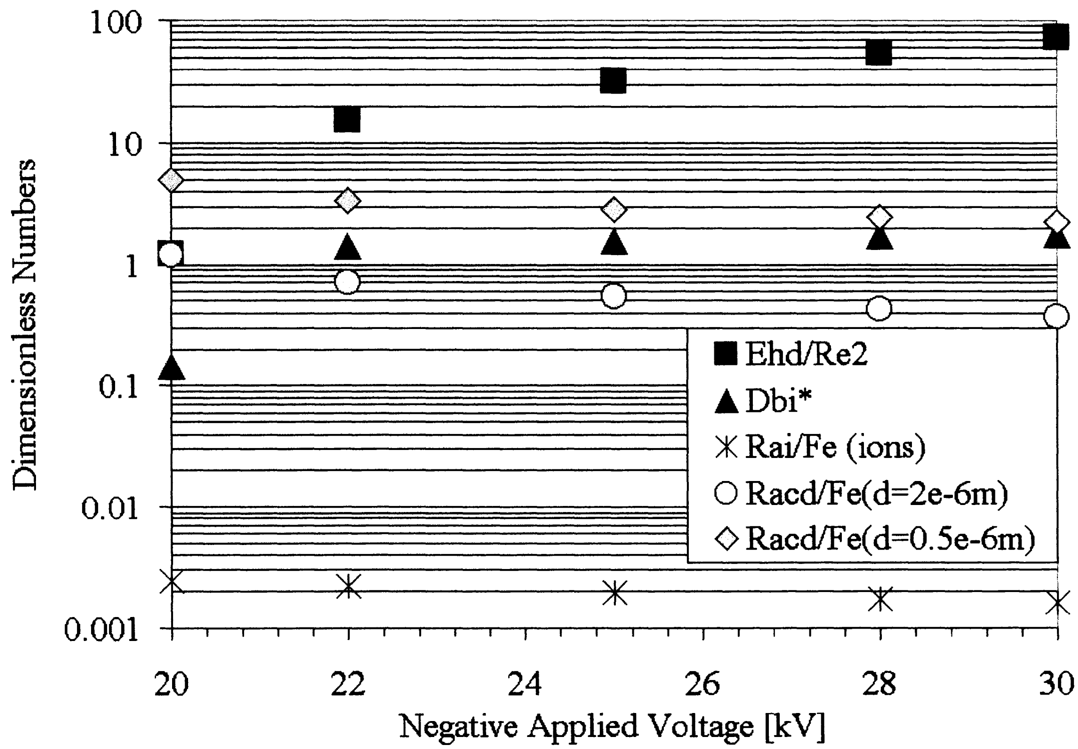

Figure 5.9 Dimensionless EHD Number ($N_{EHD}=E_{EHD}/Re^2$), Ion Debye Number (Db_i^*), and diffusion Reynolds number of ions and charged dust (Ra_i, Ra_{cd}) versus Electric Field Numbers (F_E) of 1.5 mm discharge electrode at gas flow rate of 16.9 m^3/h.

5.2.3 Multi-field ESP with 1.5 mm Corona Wire

An extensive study on collection efficiency of ultra-fine particles under dc and pulse operating mode for a wire-type discharge electrode, has been conducted by Zukeran et. al. [43]. In this section his experimental results on multi-field wire-plate ESP will be compared to numerical results. He used the same bench-scale ESP containing two wire-plate sections of *10* and *20 cm* in length. The shorter section containing one-corona wire was placed at the entrance of the ESP housing as indicated in Figure 5.10. The longer section, containing two discharge electrodes, was placed close to the exit of the ESP housing. The short and long field were approximately *10 cm* apart. The diameter of the discharge electrode was *1.5 mm*. The main gas flow rate was $11.9\ Nm^3/h$, the gas temperature was $20\,°C$, and the dust loading was approximately 5×10^{10} *# of particles* $/m^3$.

Comparison between Zukeran et al. experimental results, performed simultaneously on short and long field electrode arrangements, and numerical results of three-field electrode arrangements are shown in Figure 5.11. The numerical model considers a three-field electrode arrangement with total plate length of *30 cm*, the main gas flow rate of $11.9\ m^3/h$, the gas temperature of $20\,°C$, mean dust particle diameter of $0.5\ \mu m$, and uniform corona discharge distribution along the wire length for all voltage levels. In spite of the difference in the input geometry, there is less than *1%* difference between predicted and experimental results at higher voltage levels. At voltages close to the corona on-set voltage, the numerical model overestimates the collection efficiency approximately *15%*. One of the reasons may be the non-uniform corona discharge in the axial and radial directions.

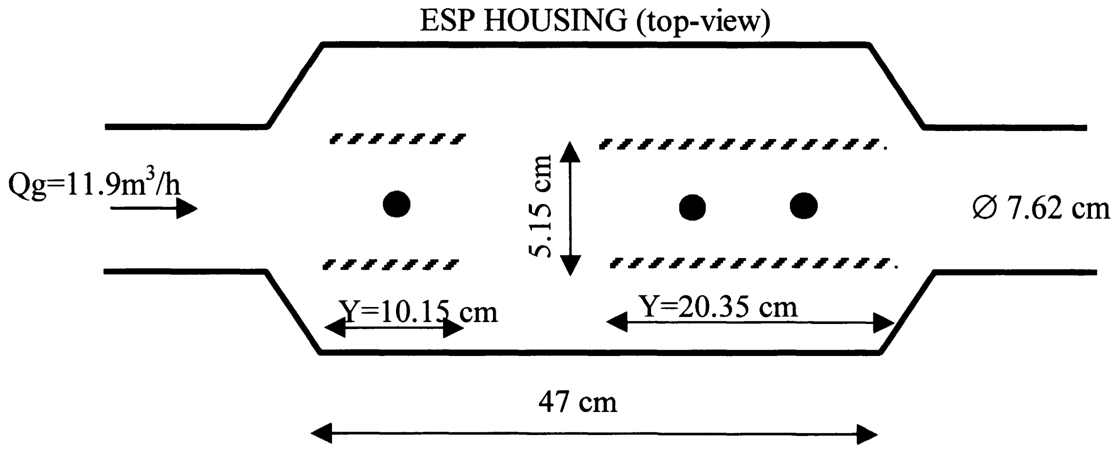

Figure 5.10 Schematic diagram of the three-field wire-plate ESP. (Discharge electrode diameter is *1.5 mm*. Gas flow rate is *11.9 Nm^3/h*)

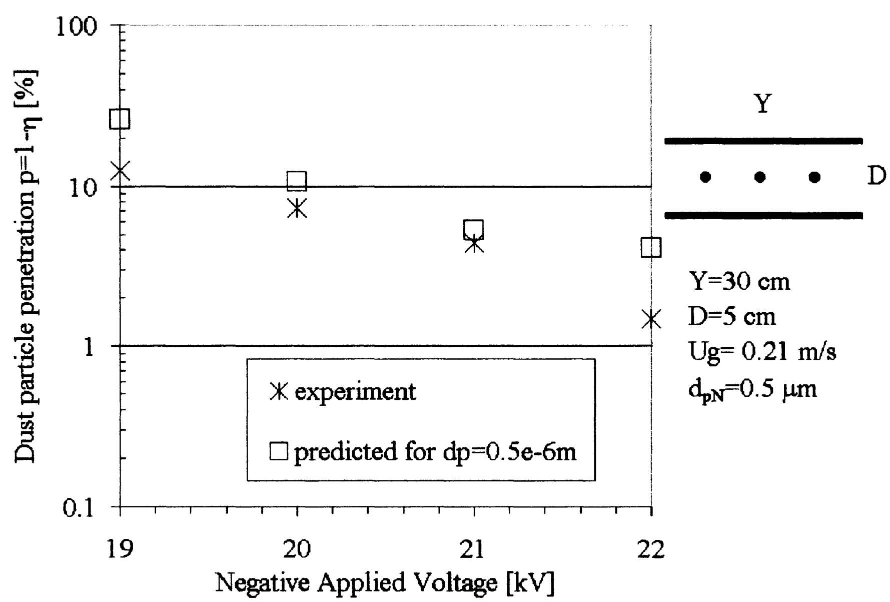

Figure 5.11 Measured and predicted dust penetration of three-field ESP with *1.5 mm* discharge electrode. (Input parameters to numerical model are as follows: total field length is *30 cm*, wire to plate spacing is *2.5 cm*, mean gas flow velocity is *0.21 m/s*, mean dust particle diameter is $d_p=0.5\ \mu m$.)

5.3 EXPERIMENTAL VALIDATION OF LARGE SCALE WIRE-PLATE TYPE ESP

Pulse energizations and moving electrodes have been used as a means of improving dust particle collection of high resistivity in wire-plate electrostatic precipitators. However, the optimization of pulse energized or hybrid ESP with moving electrodes are not well established for various resistivity dusts, since no comprehensive modelling code and well characterized experiments for wire-plate ESP exist at this moment [144]. A constitutive relationship developed for the effective migration velocity for the wide range of dust resistivity of wire-pipe pilot scale ESP for the flue gas temperature from *80* to *130 °C*, the flue gas flow rate from *0* to *2000 Nm3/h*, the resistivity of ashes from 5×10^{10} to 10^{14} Ω *cm* and the inlet dust loading from *2* to *15* g/m^3, energized by a short pulse and dc, was integrated to the MESP design and analyses codes based on Misaka et al's experiments [144].

Then, the pilot and full scale ESP operations in actual plants were simulated and compared. The tested ESP by Misaka et al. [144] consists of two fields, as shown in Figure 5.12. At the first field, a pulse power supply was added to an existing dc power supply. The first field was a fixed electrode section, and can be operated by applying the pulse, intermittent or continuous energization. The second field was a moving electrode section, applying continuous energization only. The boiler used several kinds of pulverized coals mixed together of various resistivity, as shown in Table 5.2 [144]. Measurements were performed with and without charging on the first and the second fields. Thus, the migration velocity and collection efficiency were obtained for each of the first and the second field by measuring the dust concentration at inlet and outlet ducts of the ESP. Figure 5.13 shows that the simulation results agree well, both quantitatively and qualitatively, with the experimental results. The collection efficiency is increased by reducing gas temperature from *130* to *80 °C*. High collection efficiency was maintained even with gas temperatures of *130* or *90 °C* for lower resistivity ashes from coal A and B. However, with coal C, at a conventional operating temperature of *130 °C*, the dust concentration at the outlet of ESP was increased due to high resistivity dust problem. The collection efficiency was increased sharply by reducing gas temperature to *80 °C*.

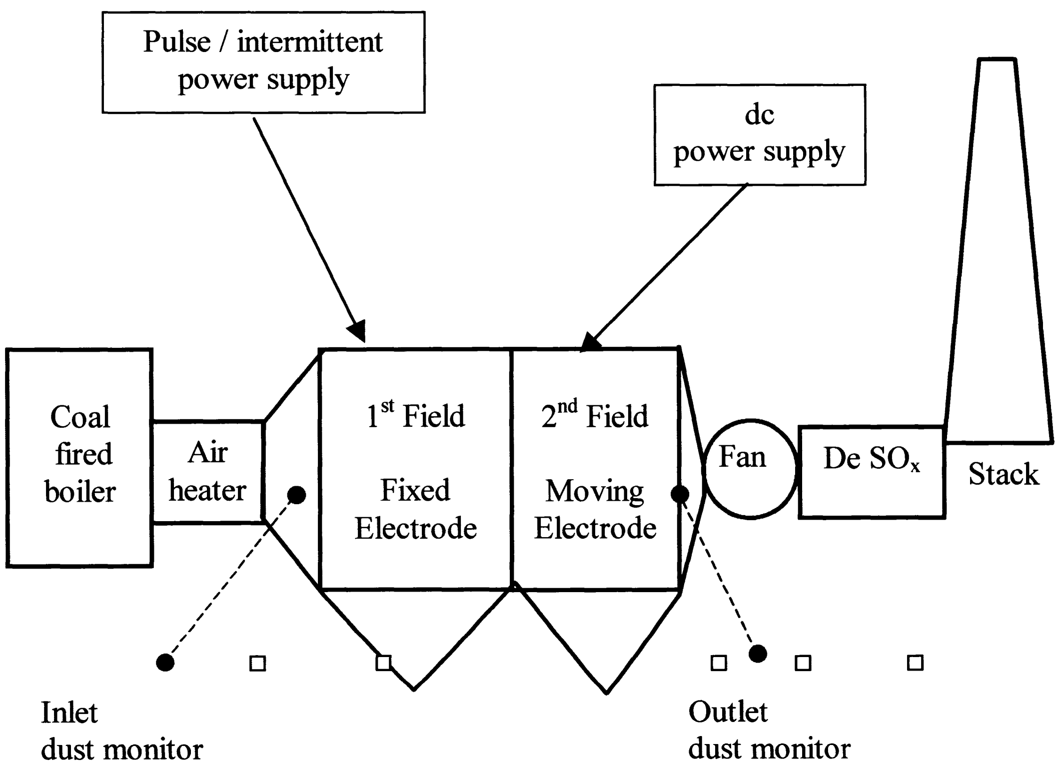

Figure 5.12 Schematics of hybrid experimental test loop of Misaka et al. [144]

Table 5.2
Fly ash particle characteristics.

Dust	Density [g/m^3]	Mean Diameter [μm]	Geometric standard deviation	Electric Resistivity [Ωcm]
Fly ash A	2.12	16.0	2.09	3.8×10^{10}~1.2×10^{11}
Fly ash B	2.33	16.0	2.32	9.5×10^{11}~7.0×10^{13}
Fly ash C	2.25	12.3	2.60	9.8×10^{12}~1.1×10^{14}

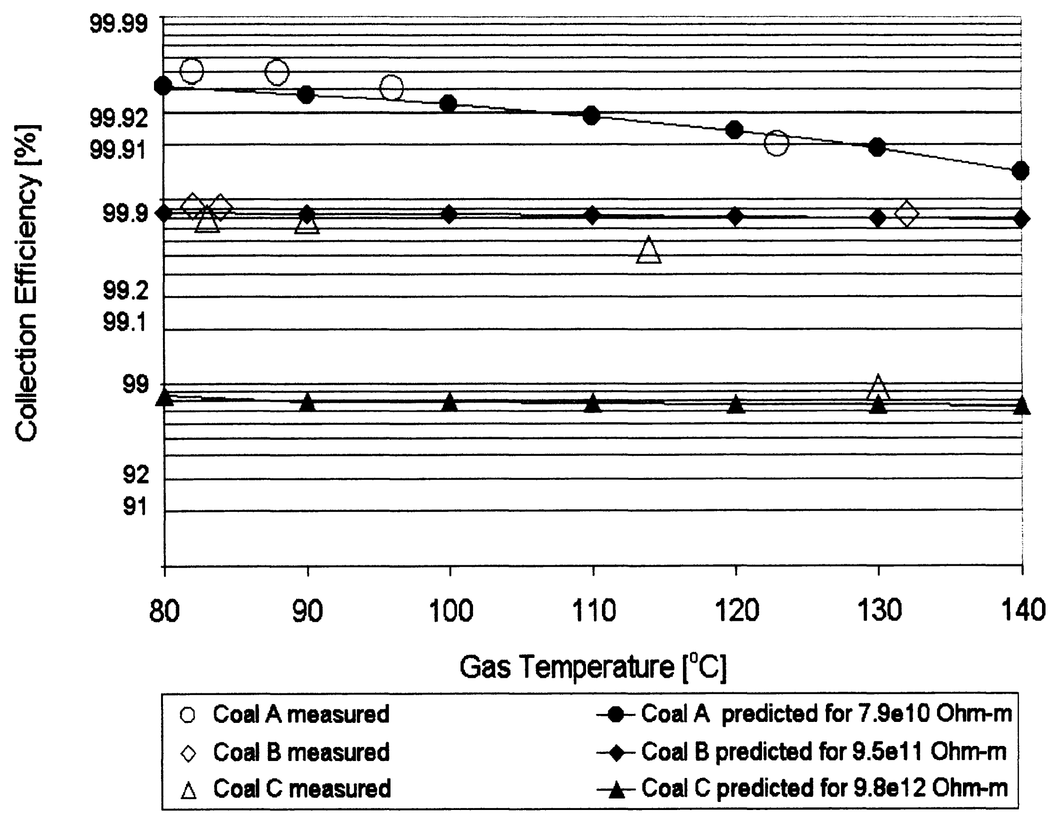

Figure 5.13 Experimental [144] and numerical predicted dc MEESP collection efficiency as a function of flue gas temperature for various coals.

5.4 EXPERIMENTAL VALIDATION OF BENCH-SCALE SPIKE-PLATE TYPE ESP

In this section experimental results of collection efficiency of single and two-field ESP with a spike electrode as a discharge electrode will be compared to numerical results. At first the total collection efficiency at main gas flow rates of *3.5* and *16.9* m^3/h was obtained without any particle size separation filters. After that, the partial collection efficiency at *16.9* m^3/h was obtained by inserting various numbers of particle size separation filters. The total length of collecting electrodes in single field as well as in the two-field ESP was *20 cm*. Dimensions of the spike discharge electrode are shown in Figure 5.14.

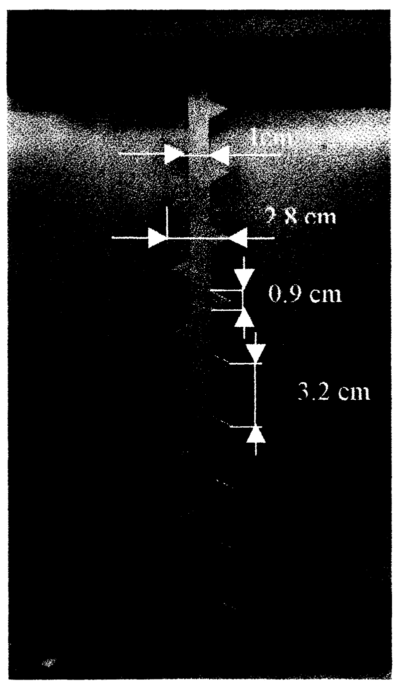

Figure 5.14 Dimensions of spike type discharge electrode.

5.4.1 Single Field ESP with Spike Type DE

Figure 5.15 shows experimental results of total collection efficiency as a function of applied voltage and current-voltage curve for various main gas flow rates. The total collection efficiency at main gas flow of *3.4* m^3/h increases with increased applied voltage up to *20 kV* and then decreases with further increasing applied voltage. At *16.9* m^3/h the maximum collection efficiency is reached at *22 kV*. One of the reasons for reduced collection efficiency after *22 kV* may be the EHD induced secondary flow. At a flow rate of *25.6* m^3/h the reduction of collection efficiency at high voltages was not observed.

In order to obtain partial collection efficiency for specific dust size range, different numbers of PSSFs were introduced. It was observed that at certain voltages the outlet dust concentration increases instead of decreases with increasing number of PSSFs. This may be attributed to either higher back pressure or the charge accumulation on the PSSFs screens that could lead to release of already captured particles from screens. Therefore, the partial collection efficiency was restricted to analysis of three groups of particle size ranges. The first group contains dust particles ranging from *0.017* μm to *0.041* μm in diameter. The second group takes into account dust particles with diameters greater than *0.041* μm and smaller than *0.062* μm. The last group consists of dust particles with diameter greater than *0.062* μm and less than *20* μm. Partial collection efficiency is shown on Figure 5.16. The outlet dust particle concentrations of the first particle size group is higher then the inlet concentrations, indicating re-entrainment from collecting plates. The second particle size group is re-entrained from collecting plates at voltages equal to or smaller than *12 kV*. At *15 kV* and higher, the outlet dust concentration is smaller than the inlet dust concentration, indicating that particles acquired certain electrical charge and are collected by ESP. Dust particles belonging to the third dust size group, are collected by ESP even at voltages as low as *10 kV*. The collection efficiency of the third group is increasing with applied voltages up to *15 kV* and than decreasing with increasing voltage. At higher applied voltages dust particles collection may be reduced due to the EHD induced flow.

Numerical simulation of total collection efficiency conducted for $16.9\ m^3/h$ and various applied voltages is shown in Figure 5.17. At lower voltages, the model underestimates collection efficiency at *–18 kV* by *14 %*. For a voltage range from *20 kV* to *22 kV*, the model agrees from *4 %* to *1.5 %*, respectively. At *26 kV* the model overestimates collection efficiency by *60 %*. The shape of the measured current-voltage curve indicates that there are no significant problems with corona discharge therefore it is believed that one of the reasons for impaired collection efficiency at higher voltages may be the EHD induced secondary flow since $(E_{hd}/Re^2 >> 1)$. Additionally, there is present ionic space charge effect $(Db_i^* > 1)$ and convection of dust particle $(Ra_d/F_E > 1)$.

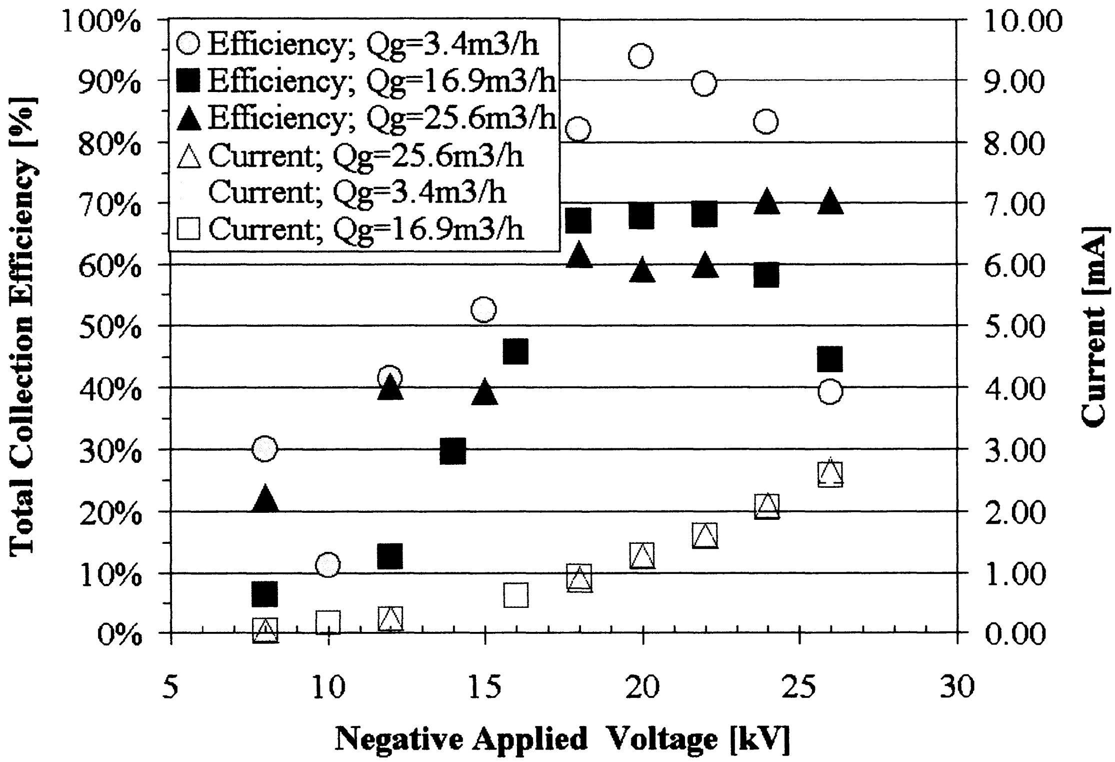

Figure 5.15 Measured collection efficiency of dust particles as a function of applied voltage and current-voltage curves at various main gas flow rates.

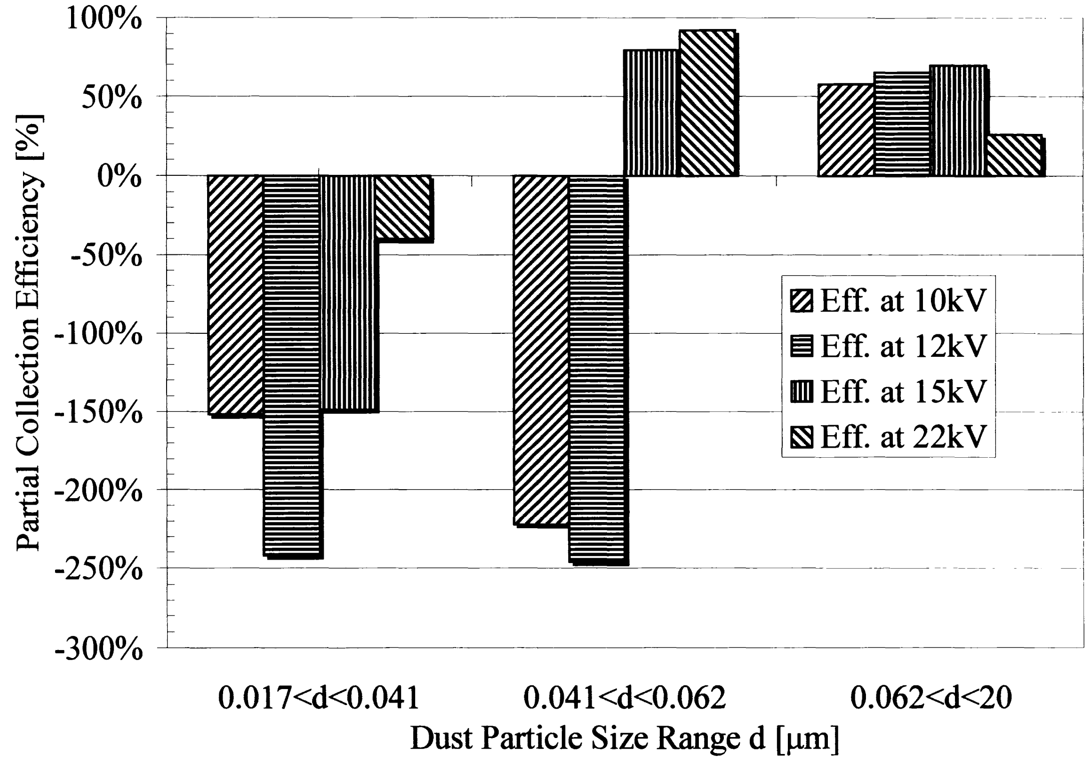

Figure 5.16 Partial collection efficiency of three particle size groups at various applied voltages and main gas flow rate of *16.9* m^3/h.

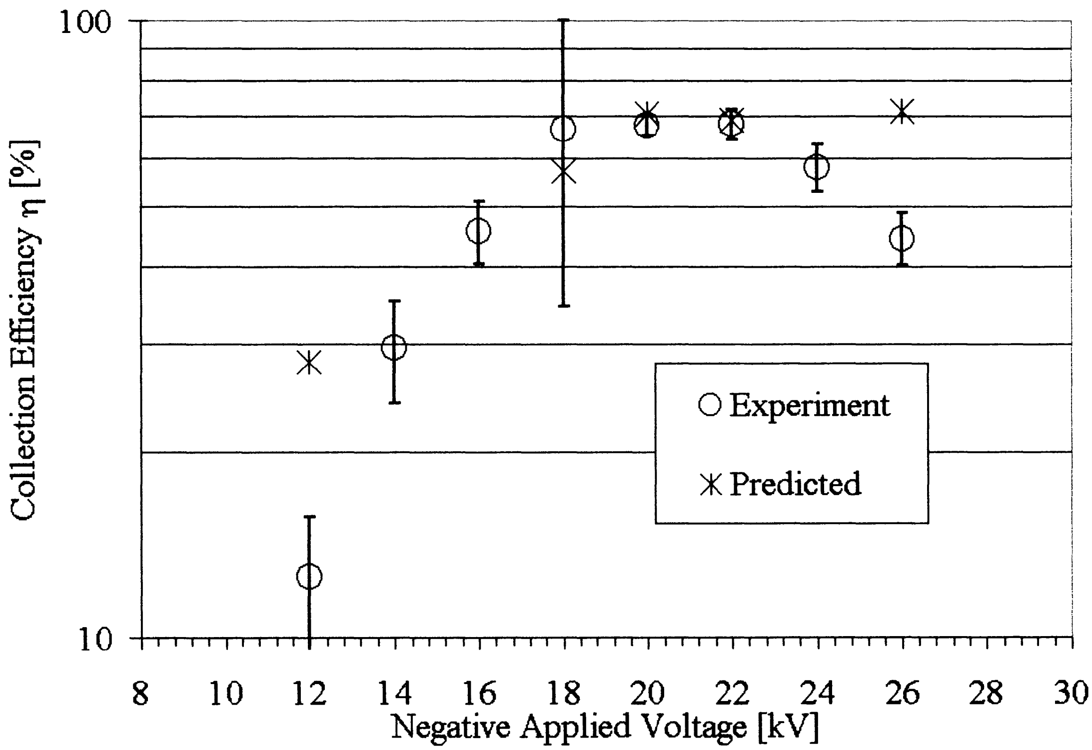

Figure 5.17 Measured and predicted total dust collection efficiency of one-field spike-plate type ESP at main gas flow rate of *16.9 m^3/h*.

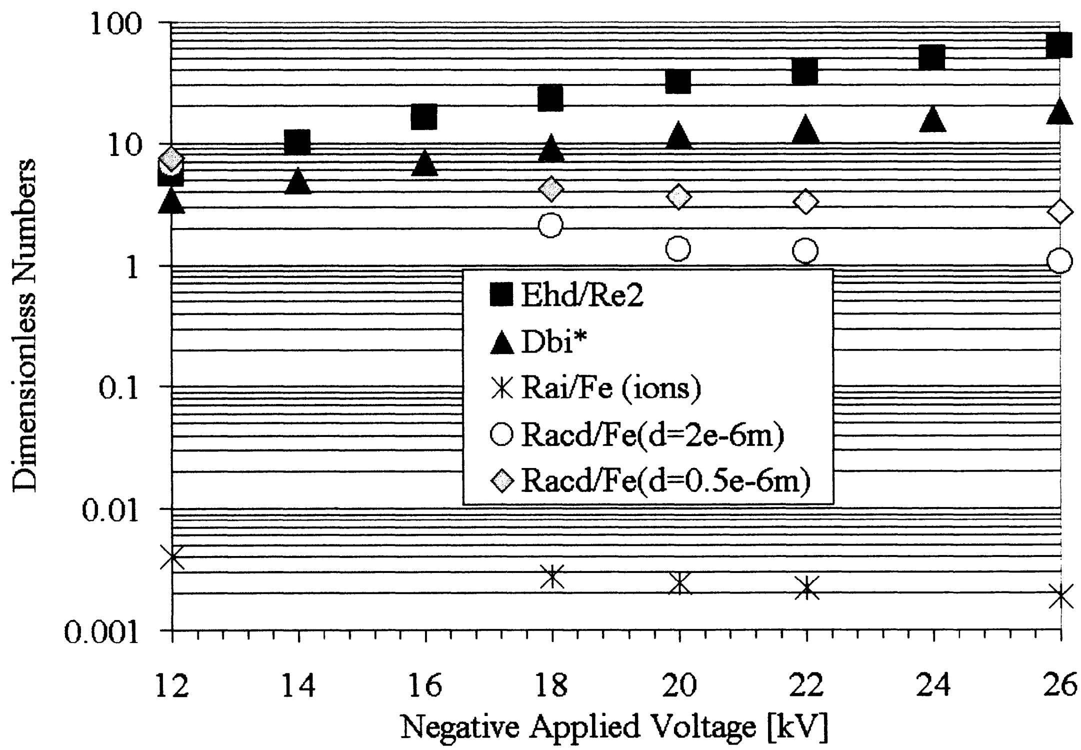

Figure 5.18 Dimensionless EHD Number (E_{EHD}/Re^2), Ion Debye Number (Db_i^*) and diffusion Reynold Number of ions and charged dust (Ra_i, Ra_{cd}) versus Electric Field Numbers (F_E) of single-field spike-plate type ESP

5.4.2 Two-Field ESP with Spike Type DE

Figure 5.19 shows total collection efficiency of dust particles as a function of applied voltage and current-voltage curve at various main gas flow rates. At very low gas flow rate of $3.5\ m^3/h$, the total collection efficiency is held above $80\ \%$ for applied voltages in the range from $8\ kV$ to $27\ kV$. At $28\ kV$ the collection efficiency dropped below $12\ \%$ probably due to the EHD induced secondary flow. At $16.9\ m^3/h$, the collection efficiency tends to increase up to a certain value and then to decrease with increasing applied voltage. At high flow rate of $25.8\ m^3/h$, high collection efficiency is observed at voltages close to corona on-set. After that the total collection efficiency decreases with increased voltage up to $12\ kV$, where it reaches the local minimum. By further increase of applied voltage, the total collection efficiency increases again.

The partial collection efficiency is restricted to analysis of three groups of particle size ranges as shown in Figure 5.20. The first group contains dust particles ranging from *0.01* to $0.062\ \mu m$ in diameter. The second group takes into account dust particles with diameter greater than $0.062\ \mu m$ and smaller than $0.122\ \mu m$. The last group consists of dust particles with diameter greater than $0.122\ \mu m$ and less than $20\ \mu m$. Partial collection efficiency of these three groups at a voltage range from *18* to $24\ kV$ are shown in Figure 5.20. From *18* to $20\ kV$, the collection efficiency of the first group is increasing. However, at *22* and $24\ kV$ the collection efficiency of the first group is negative and tends to decrease with increasing applied voltage, probably due to re-entrainment from collecting plates. At *18* to $20\ kV$ the results do not have a physical meaning since they are a product of mathematical interpretation of measuring error. At voltages higher than *22 kV*, the second particle size group is again present, and collection efficiency is increasing with increasing applied voltage. The collection efficiency of the third group is increasing with increasing voltage.

A numerical simulation of total collection efficiency conducted for $16.9\ m^3/h$ and various applied voltages is shown in Figure 5.21. At *16 kV*, the model underestimates collection efficiency by *10 %*. For a voltage range from *20* to *22kV*, the model agrees in the range from *10* to *5 %*, respectively. After *22 kV* the model overestimates collection efficiency by *39 %*. Further, dimensionless numbers shown in Figure 5.22 show that there is a space charge effect $(Db_i^* > 1)$, EHD induced secondary flow $(E_{HD}/Re^2 > 1)$, and convection of dust particles $(Ra_i/F_E > 1)$. One of the reasons of impaired collection efficiency may be the EHD induced secondary flow since $(E_{HD}/Re^2 > 100)$.

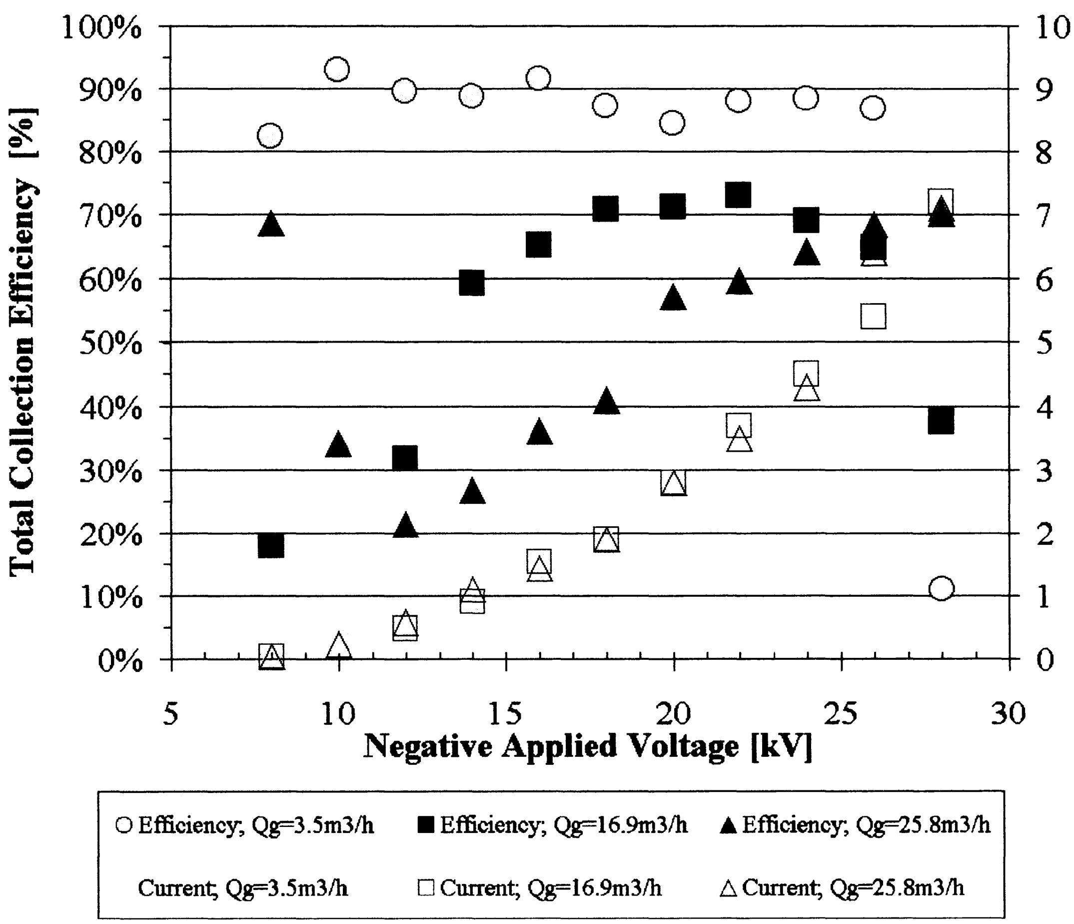

Figure 5.19 Measured collection efficiency of dust particles as a function of applied voltage and current-voltage curve at various main gas flow rates.

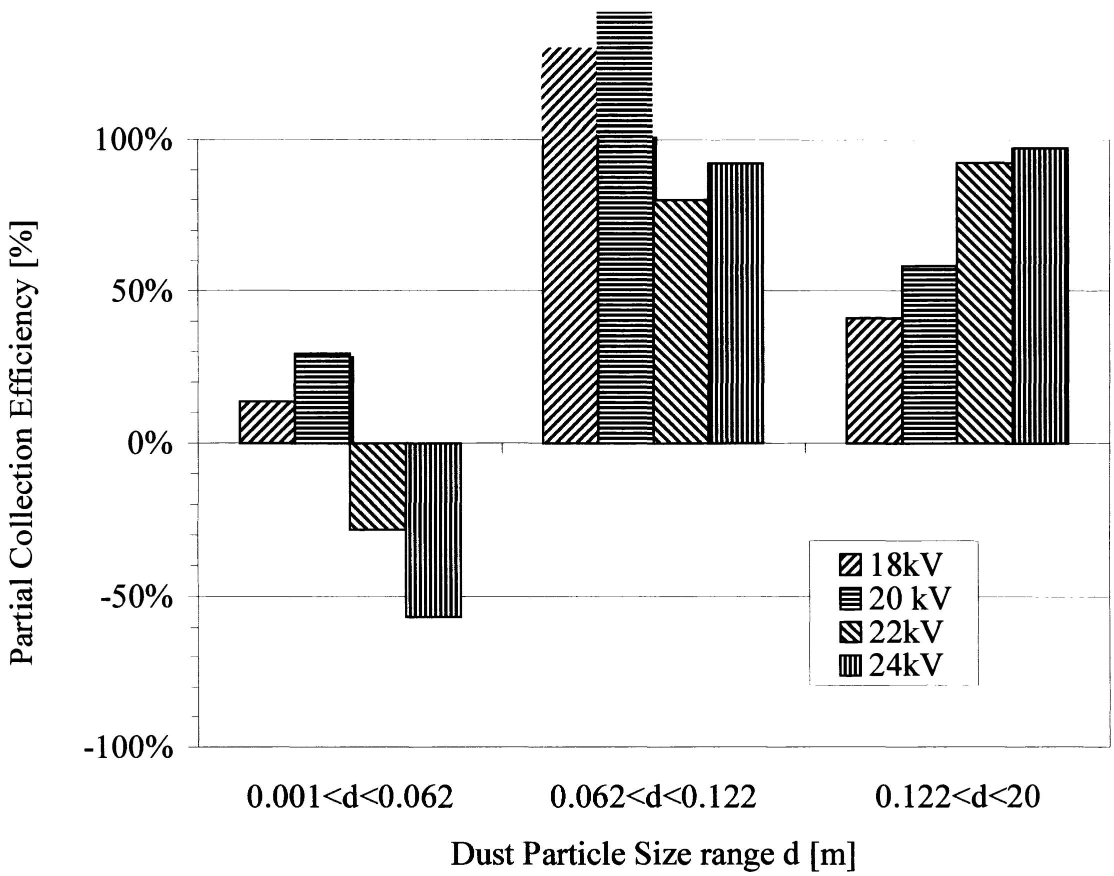

Figure 5.20 Partial dust collection efficiency of three particle size groups at gas flow rate of $21m^3/h$ and voltages in the range from 16 kV to 24 kV .

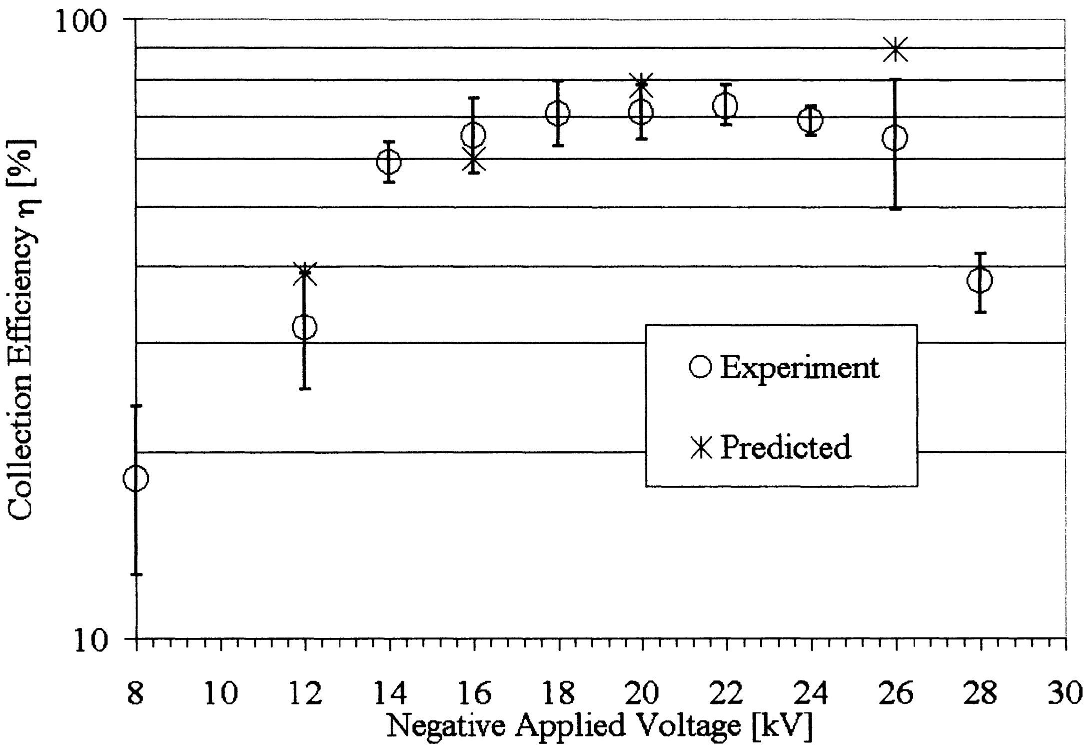

Figure 5.21 Measured and predicted total dust collection efficiency of two-field spike-plate type ESP at main gas flow rate of 16.9 m^3/h

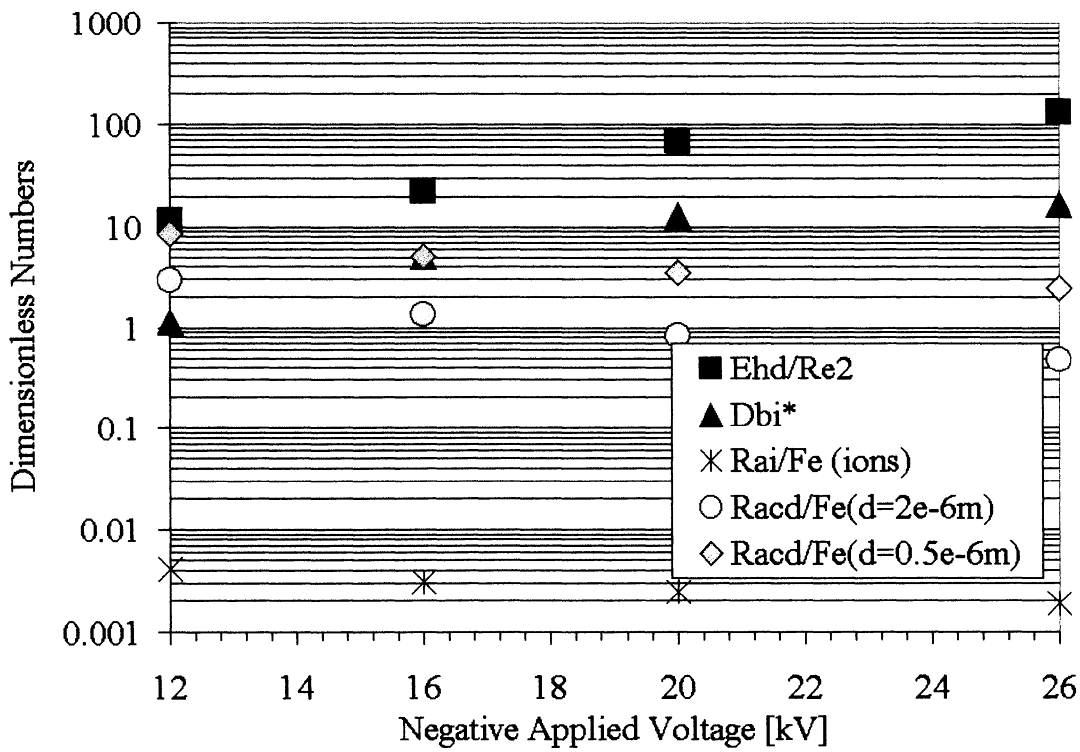

Figure 5.22 Dimensionless EHD Number (E_{EHD}/Re^2), Ion Debye Number (Db_i^*) and Ion Reynold Number (Ra_i) versus Electric Field Numbers (F_E) of two-field spike-plate type ESP

CHAPTER 6

CONCLUSIONS

Numerical simulations were conducted for wire, rod and spike type discharge electrodes placed between I, U and C type collecting electrodes for mean gas flow velocities from *0.5* to *1 m/s*, operating voltages from *-20* to *-30 kV*, and dust particle sizes from *0.01* to *10 μm*. Numerical results are discussed with regard to their effect on the collection efficiency evaluation and also presented in the form of dimensionless numbers.

1) These results show that submicron and ultrafine collection efficiency can be predicted with good accuracy for various geometries of discharge and dust collection electrodes.
2) At the same applied voltage of *-30 kV*, the spike-type discharge electrode (DE) with the I-type collecting electrode (CE) improves collection efficiency when compared to the wire or rod discharge electrode with I-type collecting electrode from *22 to 50 %* depending on the particle size.
3) The spike DE better improves the collection efficiency of ultrafine and submicron than micron size particles. By comparing the predicted collection efficiencies at *-25 kV* for *0.01, 0.5* and *10 μm* dust particles, the spike DE improved collection efficiency by *4.75, 3* and *2.9* times, respectively.

4) The collection efficiency improvement increases up to several times when efficiencies are compared at lower voltages.
5) The volume averaged value of the electric field is higher for the spike-type compared to that of the wire-type discharge electrode. At *-25 kV,* the volume averaged value of the electric field is approx *84 %* higher.
6) The volume averaged ion density for the spike-type discharge electrode is one order of magnitude higher than for the rod electrode geometry due to the higher initial number of ions or discharge current.
7) A decrease in collecting electrode length and collecting electrode spacing affects differently particle charging and collection efficiency of submicron and ultrafine dust particles.
8) A decrease in collecting electrode length (Y) from *20* to *10 cm* decreases the particle surface charge in the range from *-24 %* to *-7 %* and the collection efficiency in the range from *-45 %* to *-23 %* for particles ranging from *0.01* to *10* μm.
9) The major reason for reduced collection efficiency is shorter charging time due to the shorter section.
10) Decrease in plate-to-plate spacing increases the particle charging and the collection efficiency due to the higher volume averaged ion density, and volume averaged electric field.
11) A decrease in plate-to-plate spacing (D) from *10* to *5 cm* increases the particle surface charge in the range from *28 %* to *113 %* and the collection efficiency in

the range from *141 %* to *42 %.* Some of the reasons for improved collection efficiency are *239 %* higher volume averaged ion density, and *138 %* larger volume averaged electric field.

12) In spite of the smaller $<N>/N_{io}$ ratio with U and C–type CEs, the volume averaged value of ion densities are *69.3 %* and *76 %* higher, compared to the I-type CE due to the higher initial number of ions N_{io}.
13) The longer the fins in U and C type CEs, the higher the discharge current or initial number of ions (N_{io}). The initial number of ions are 2.6 and 3 times higher for U and C-type CEs than for the I-type CE. Whereas, the $<N>/N_{io}$ ratios are *8.6 %* and *7.8 %* for U and C-type CEs, and *13.4 %* for I-type CE.
14) The U and C-type CEs increase particle collection efficiency in the range from *7* to *27 %* depending on the particle size. Smaller dust particles experienced higher improvement in the collection efficiency than larger particles due to the higher increase of the ion density compared to the increase of the modulus of electric field $|\xi|$.
15) The U type CE provides better collection efficiency than C-type due to the larger ξ_x component of electric field.
16) The numerical results show that the longer the fin lengths L_{F1}^* and L_{F2}^*, the higher the discharge current or initial number of ions (N_{io}).
17) Fins have an adverse effect on the electric field. They reduce the ξ_x component of electric field near the collecting electrode in the middle section of the ESP field, and increase both components close to the L_{F2} tip.

18) There is an optimum fin length for which the highest collection efficiency can be reached. When cross sectional averaged moduli of the electric field were compared to I type CE, the modulus of electric field of any four combinations was higher in the $-0.84<y^*<0.84$ section than with I-type CE. When particles' surface charges were compared, the highest value was achieved for a $L_{F1}^*{\times}L_{F2}^*=0.57{\times}0.6$ combination. However, the best collection efficiencies were achieved with a $L_{F1}^*{\times}L_{F2}^*=0.57{\times}0.4$ combination, for which the collection efficiency of *10 μm* particles was increased by *12 %,* and of *0.01 μm* particles by *42 %.*
19) The number of spikes does not affect significantly the collection efficiency when spikes spacing is less than *3.2 cm*. When the number of spikes was reduced from *17* to *9* all particle sizes experienced around a *3 %* reduction of collection efficiency.
20) From the point of view of submicron particles, more favourable are discharge and collecting electrode geometries that impose high ion density regions such as C-type CE and spike-type DE with longer spikes since they promote diffusion charging.

Comparison of experimental and predicted results for bench and full scale ESPs shows that:

21) *0.25 mm* smooth wire had the lowest corona on-set and spark-over voltage, than the spike discharge electrode and *1.5 mm* wire.

22) Current distribution near the collecting electrode for spike-plate electrode arrangement shows good qualitative agreement with Ohkubo et al.'s [30] experimental results performed with a rod-needle-type discharge electrode.

23) The total collection efficiency predicted by the present model agrees well with experimental results for the applied voltage range for which the discharge spots are relatively uniform along the discharge wire length.

24) The total collection efficiency of 0.25 mm wire in the voltage range from -8 to -20 kV is impaired due to the problems with non uniform corona discharge in the axial direction.

25) Optical emission analysis suggested that the non-uniformity of corona discharge in the radial direction may be one of the reasons for the very unusual shape of the collection efficiency versus applied voltage curve of 1.5 mm rod as a discharge electrode.

26) The spike-type discharge electrode does not exhibit any significant problems with corona discharge for a voltage range from -14 to -22 kV, for which the model and experimental results agree within 10 %.

27) One of the reasons for the discrepancy between experimental and predicted results for the spike-type electrode at higher applied voltages is believed to be the EHD induced secondary flow.

28) The predicted partial collection efficiency agrees well with measured for submicron and larger ultrafine particles.

29) The multi-field ESP exhibits high collection efficiency over a much larger voltage range than the single-field ESP.

30) Dimensionless numbers indicate that EHD induced secondary flow is stronger in the case of a spike type discharge electrode for the same input power. As the input power increases the difference decreases.

31) The ion space charge effect of a spike type electrode is almost one order of magnitude higher than with a wire-type discharge electrode.

32) The ion convection based on $Ra_i/F_E << 1$, may be neglected. However, numerical studies have shown that even for $Ra_i/F_E = 2.43\times10^{-3}$ in the case of a wire discharge electrode, convection of ions can be observed in the first centimetre of the ESP.

33) The Ra_{cd}/F_E ratio of 0.5 μm and 2 μm dust particles is approximately 50 % higher for spike than for the wire discharge electrode at $E_{HD}/Re^2=30$.

34) Based on the large-scale wire-plate type ESP experiments, conducted for various gas temperatures and dust resistivities, the present simulation results agree quantitatively and qualitatively with the experimental results. The collection efficiency is increased by reducing the gas temperature from *130* to *80* °C. High collection efficiency was maintained even with gas temperatures of *130* or *90* °C for lower resistivity ashes from coal A and B. However, with coal C, at a conventional operating temperature of *130* °C, the dust concentration at the outlet of ESP was increased due to the high resistivity dust problem. The collection efficiency was increased sharply by reducing the gas temperature to *80* °C.

35) The model proved to be useful for prototype design of spike-type discharge electrodes, as well as for prediction of the dust collection efficiency in scaled-up ESPs.

The constitutive relationship developed from the optical spectrometry analysis can be used to simulate ion distribution of corona discharge for various discharge electrodes.

36) The emission of the 2nd positive band of the N_2 molecule that is directly proportional to the electron density and indirectly proportional to the negative ion distribution can be used to set the boundary condition for ion density around the discharge electrode circumference.
37) The emission profile on the surface of very thin wire, 0.25 mm in diameter, has a symmetrical distribution with respect to the centre of wire.
38) The emission profile on the surface of the 1.5 mm wire has a dual distribution, indicating discharge locations from the surface closer to the collecting electrode at applied voltage of - 22 kV.
39) The emission profile on the spike surface has a symmetrical distribution at -22 kV. At -15 kV the profile was also symmetrical however, the maximum of emission intensity is approximately 0.5 mm shifted to the left with respect to the centre of the electrode, indicating that corona discharge may start from the edge of the spike surface at lower voltages.

40) The optical emission profile of the visual spectra at -15 kV and -22 kV have similar profiles as the pixel intensity profile from digital image analysis.

CHAPTER 7

RECOMMENDATIONS FOR FURTHER WORK

Some potential research directions are given based on the improvement of the model after experimental validation of the numerical results.

The first group of improvements should address and expand the assumptions regarding the boundary conditions for ions and neutral dust particles. At present, the ion boundary conditions on the wire surface assume uniform distribution in the axial direction, which in the case of wire type discharge electrodes of large diameters, wire surface contamination, and low applied voltages, is not valid. At present, the non uniformity of corona discharge in the axial direction can be captured by adjusting the number of tuft spots, which are at present knowledge, based on experimental observations. Modifications would have to be made to introduce the empirical equation expressing the number of tufts as a function of wire diameter and applied voltage. The non-uniformity of corona discharge in the radial direction was based on experimental results of optical emission of corona discharge at two voltage levels, *15* and *22 kV*. Modifications would have to be made to adjust the radial boundary conditions with change of applied voltage, which would require some additional experiments. With respect to the boundary conditions of neutral dust at the collecting electrode, the modifications would require introduction of the re-entrainment dependent source factor in the dust transport equation. Some preliminary experiments showed that re-entrainment of dust particles from the dust layer is not negligible at high applied voltages. In the present form the prediction of collection efficiency when back-corona discharge is based on semi-empirical approach. In order to implement the back-corona discharge further modification should address the bi-polar composition of discharge current as well as the bi-polar charging mechanism of dust particles.

A second group of modifications should address the limitations with respect to the modifications of the main gas flow due to the EHD induced secondary flow or aerodynamically generated by the fin structures in the case of U and C-type discharge electrodes.

In future work, the already existing Mode 2, based on the neutral and charged dust profile at the inlet and outlet section of the ESP, should be validated especially for spike-type discharge electrode with U and C-type CEs. Further application of the present model could involve the prediction of threaded and rectangular discharge electrodes as well as the full-scale ESPs performance with spike type discharge electrodes.

REFERENCES

[1] "Air Quality," Environmental Monitoring and Reporting Branch of the Ministry of the Environment, 1998.

[2] "A Compendium Of Current Knowledge on Fine Particulate Matter in Ontario," Prepared by The Ontario Ministry of the Environment for The Ontario Smog Plan Steering Committee, March 1999.

[3] "Clearing Air: Covering Asthma and Other Childhood Diseases," February 1999, Available: www.rtnda.org/prodev/beats/airtext.htm#17

[4] "Coal-Fired Electricity Generation in Ontario," The Ontario Ministry of the Environment, March 2001.

[5] W.I. Li, M. Perzi, G. A. Ferron, R. Batycky, J. Heyder, and D.A. Edwards, "The Macrotransport Properties of Aerosol Particles in the Human Oral-Pharyngeal Region," *Journal of Aerosol Science*, vol. 29, no. 8, pp. 995-1010, 1998.

[6] "Hamilton-Wenthwort Air Quality Initiative," Ministry of the Environment, Summary report, October 1997.

[7] "Strategic Options to Address the Fine Particulate Issue in Ontario," Prepared by The Ontario Ministry of the Environment for The Ontario Smog Plan Steering Committee, March 1999.

[8] "International Standards on Particulate Control," Internal report, *Eight International Conference on Electrostatic Precipitation*, 2001

[9] "1995 Criteria Air Contaminant Emissions for Canada," www.ec.gc.ca/pdb/cac/cacdoc/1995e/canadddda95.htm, 1995

[10] K.R. Parker, "Effective Capture of Respirable-sized Particulates Using Electrostatic Precipitator Technology," *Electrostatic Precipitation, Engineering Science and Educational Journal*, February 2000, pp. 33-40

[11] J.S. Chang, "*Dust Collection System*," Lecture Notes

[12] S. Masuda and S. Hosokawa, "Electrostatic Precipitation," in *Handbook of Electrostatic Processes*, Marcel Dekker, Inc., 1995, Chapter 21,

[13] Hohlfeld, "The Precipitation of Smoke by Electrical Means," *Kastner Archive Naturlehre*, vol. II, pp. 205-206, 1824.

[14] O.J. Lodge, "The Electrical Collection of Dust and Smoke, with Special Reference to the Collection of Metallic Fume, and a Possible Purification of the Atmosphere" , *Journal of Society of Chemical Industry* (London, England), vol. V, no. 11, pp. 572-76, 1886.

[15] L. Zaishi, H. Sanming, and L. Zhe, "A Study of Wide-Spacing ESP," in *The 4th International Conference on Electrostatic Precipitation*, pp. 339-342.

[16] C. Riehle and F. Loffler, "Can the Effective Migration Rate Increase Observed in Electrostatic Precipitators with Wider Plate-Spacings or Faster Gas Streams Really be Regarded as a Non-Deutschian phenomenon?," in *The 4th International Conference on Electrostatic Precipitation*, pp. 104-122.

[17] J.H. Ko and S.H. Ihm, "A Two Dimensional Model for Polydisperse Particles on the Effective Migration Rate of the Electrostatic Precipitator with Wider Plate Spacing," *Aerosol Science and Technology*, vol. 26, no. 5, May 1997.

[18] T. Guoshan and G. Jin , "The Development and Performance Evaluation of Wide Spacing Electrostatic Precipitator," in *The 4th International Conference on Electrostatic Precipitation,* pp. 343-347

[19] D.O. Heinrich, W.J. Frank and L.J. Schon, "Study of Wide-plate Spacing," *Staub-Reinhaltung der Luft* , 1978

[20] S. Masuda et al., "A Pulse Voltage Source for Electrostatic Precipitation," *Conf. Record IEEE/IAS 1983 Ann. Meeting*, Oct., Mexico City, pp. 23-30 I

[21] S. Masuda and S. Hosokawa, "Pulse Energization System of Electrostatic Precipitator for Retrofitting Application," *IEEE Trans. IAS*, vol. 24, no. 4, pp. 708-716, July/August 1988.

[22] G. Dinelli , V. Bogani, and M. Rea, "Enhanced Precipitation Efficiency of Electrostatic Precipitators by Means of Impulse Energization," *IEEE Transactions on Industry Applications*, vol. 27, no. 2, pp. 323-330, March/April 1991.

[23] T. Yamamoto and H. R. Velkoff, "Electrohydrodynamics in an Electrostatic Precipitator," *J. Fluid Mech.*, vol. 108, pp. 1-18, 1981.

[24] K. R. Parker and G. Hughes, " A Visual Investigation of Corona Induced Turbulence in a Laboratory Scale Model Precipitator," in *Proceedings of the Third International Conference on Electrostatic Precipitation*, Padova, Italy,

October 1987, pp. 379-399.

[25] T. Adachi, "Ionic Wind in the Electrostatic Precipitator Experimental treatment by Schlieren Method," *Elec. Eng. In Japan*, vol. 93, no. 4, pp. 47-48, 1973.

[26] G.A. Kallio and D.E. Stock, "Flow Visualization Inside a Wire-Plate Electrostatic Precipitator," *IEEE Transactions on Industry Applications*, vol. 26, no. 3, pp. 503-514, May/June 1990.

[27] D. Blanchard, L. M. Dumitran, and P. Atten, "Electrodynamic Secondary Flow in an Electrostatic Precipitator and its Influence on the Transport of Small Diameter Particles" , in *Proceedings 8th international conference on Electrostatic Precipitation*, May 2001, vol. 1, A1-4.

[28] T. Adachi, T. Ohkubo, T. Murakami and J. S. Chang, "Analysis of Flow Field in ESP," in *Proceeding of the Third International Conference on Electrostatic Precipitation*, Abano-Padova, Italy-October 1987, pp. 363-368.

[29] T. Adachi, T. Ohkubo, Y. Nomoto, J. S. Chang and M. Akazaki, "Similarity Phenomena of Electrohydrodynamic Flow Field Inside ESP," in *Proceedings of International Conference on Modern Electrostatics*, Bejing, China, 1988, pp. 28-31.

[30] T. Watanabe, "Calculation of Flyash Particle Motion and its Migration Velocity in an Electrostatic Precipitator," *1989 IEEE*, pp. 2126-2136.

[31] S.H. Kim and K.W. Lee, "Experimental Study of Electrostatic Precipitators Performance and Comparison with Existing Theoretical Prediction Models," *Journal of Electrostatics*, vol. 48, pp. 3-25, 1999.

[32] Y. Zhuang, Y.J. Kim, T. G. Lee, and P. Biswas, "Experimental and Theoretical Studies of Ultra-Fine Particle Behaviour in Electrostatic Precipitators, " *Journal of Electrostatics*, vol. 48, pp. 245-260, 2000.

[32a] G. Dinelli, F. Mattachini, V. Bogani, A. Baldacci, and R. Tarli " Industrial Demonstration of Impulse Energization on Electrostatic Precipitators ", *Proceedings of the 3nd International Conference on Electrostatic Precipitation*, Abano, Padova, Italy, October 1987, pp. 137-149.

[33] T. Nakane, T. Hirata and K. Seya, "Experiment on Electrostatic Precipitator with Application of Ultrasonic Agglomeration," *Proceedings of International Conference on Modern Electrostatics*, 1988, Bejing, China, pp. 49-52.

[34] T.L. Hoffmann, "Environmental Implications of Acoustic Aerosol Agglomeration," *Ultrasonics*, vol. 38, pp. 353-357, 2000.

Agglomeration," *Ultrasonics*, vol. 38, pp. 353-357, 2000.

[35] H. Aoyoma, J.S. Chang, T. Nakane and K. Seya, "Effect of High Intensity Ultrasonics on the Performance of Electrostatic Precipitators," in *Proc. Japanese Sound Soc. 1993 meeting*, 1993, pp. 1065-1066.

[36] Y. Koizumi, M. Kawamura, F. Tochikubo, and T. Watanabe, "Estimation of the Agglomeration Coefficient of Bipolar-charged Aerosol Particles," *Journal of Electrostatics*, vol. 48, pp. 93-101, 2000.

[37] T. Ohkubo, S. Kanazawa, Y. Nomoto, T. Adachi, and J. F. Hughes, "The Electrostatic Agglomeration of Fine Particles Inside ESP with a Bi-Polar Charging Section," *Proceedings of the Fourth International Conference on Electrostatic Precipitation*, Beijing, China, September, 1990, pp. 590-596.

[38] J.S. Chang, "The Theory of the Low Energy Electron Dust Particle Removing System," *Conference Proceedings of the International Conference on Applied Electrostatics*, 1993 Bejing, pp. 355-358.

[39] L.C. Thanh, W.C. Finney, and R.H. Davis, "Total Separation of Charged Produced by Electron Beam Ionization in a Precipitator Development System," *Conf. Record of IAS-IEEE 1980 Meeting*, pp. 935-940.

[40] A. Maisels, F. Jordan and H. Fissan, "On the effect of charge recombination on the aerosol charge distribution in photo charging systems," *Journal of Aerosol Science*, vol. 34, pp. 117-132, 2003.

[41] M. Shimada, K. Okuyama, Y. Inoue, M. Adachi and T. Fujii, "Removal of Airborn Particles by a Device Using UV/Photoelectron method under reduced Pressure Conditions," *Journal of Aerosol Science*, vol. 30, no. 3, pp. 341-353, 1999.

[42] P. Kulkarni, N. Namiki, Y. Otani and P. Biswas, "Charging of Particles in Unipolar Coronas Irradiated by in-situ Sift X-rays: Enhancement of Capture Efficiency of Ultrafine Particles," *Journal of Aerosol Science*, 33, pp. 1279-1296, 2002.

[43] A. Zukeran., P.C. Looy, A. Chakrabarti, A.A. Berezin S. Jayaram, J. D. Cross, T. Ito, and J.S. Chang, "Collection Efficiency of Ultrafine Particles by an Electrostatic Precipitator Under DC and Pulse Operating Modes," *IEEE Transactions on Industry Applications*, vol. 35, no. 5, pp. 1184-1191, September/October 1999.

[44] F. Loffler, "Electrostatic Enhancement of Particle Collection in Fibre Filters," *Proceedings of International Conference on Modern Electrostatics*, 1988,

Bejing, China, pp. 37-40.

[45] M..J. Matteson and E. Y. H. Keng, "Aerosol Size Determination in the Submicron Range by Thermophoresis," *Journal of Aerosol Science*, vol. 3, pp. 45-53, 1972.

[46] R. Tsai and L.J. Liang, "Correlation for Thermophoretic Deposition of Aerosol Particles onto Cold Plates," *Journal of Aerosol Science*, vol. 32, pp. 473-487, 2001.

[47] F.J. Romay, S.S. Takagaki, D.Y. H. Pui and B.Y.H. Liu, "Thermophoretic Deposition of Aerosol Particles in Turbulent Pipe Flow," *Journal of Aerosol Science*, vol. 29, no. 8, pp. 943-960, 1998.

[48] M. Griem, "Ionizing Wet Scrubbers Removal of Submicron Particulates at a High Level of Energy Efficiency," *Proceedings of the Third International Conference on Electrostatic Precipitation,* Padova, Italy, October, 1987, pp. 903-915

[49] C. Lanzerstorfer, "Solid/Liquid –Gas Separation with Wet Scrubbers and Wet Electrostatic Precipitators: A Review," *Filtration and Separation*, pp. 30-34, June 2000.

[50] M. Jedrusik, A. Swierczok, P. Modzel, "Migration Velocity and Visualization of the Trajectory of Fly Ash Particles inside an Electrostatic Precipitator," *Journal of Electrostatics*, vol. 44, pp. 77-84, 1998.

[51] J.R. Pajak, "Rigid Discharge Electrode and Wide Spacing Electrostatic Precipitators in Poland"

[52] J. Miller, B. Hoferer and A. J. Schwab, "The impact of Corona Electrode Configuration on Electrostatic Precipitator Performance," *Journal of Electrostatics*, vol. 44, pp. 67-75, 1998.

[53] S.A. Self, K.D. Kihm, and M. Mitchner, "Precipitator Performance Improvement Through Turbulence Control," *Proceedings of the Third International Conference on Electrostatic Precipitation*, Padova, Italy, October, 1987, pp. 443-480.

[54] A.F. Howe and J. Houlgreave, "An Experimental Investigation of the Charging of Different Sized Particles in a Precipitator," *Proceedings of the Third International Conference on Electrostatic Precipitation*, Padova, Italy, October, 1987, pp. 329-336.

[55] J.H. Davidson and P.J. McKinney, "EHD Flow Visualization in the Wire-Plate and Barbed Plate Electrostatic Precipitator," *IEEE Trans. On Industry Applications*, vol. 27, no. 1, pp. 154-160, January/February 1991.

[56] C. Haldin, R. Hakansson, L.E. Johansson and K. Porle, "Particle Field in a *Comercial Design ESP during Intermittent Energization*"

[57] K. H. Yoo, J.S. Lee, and M. D. Oh, "Charging and Collection of Submicron Particles in Two-Stage Parallel-Plate Electrostatic Precipitator," *Aerosol Science and Technology*, vol. 27 no. 3, pp. 308-323, 1997.

[58] P. A. Lawless, L. E. Sparks, "A Review of Mathematical Models for ESPs and Comparison of Their Successes," *IEEE Transactions on Industry Applications*, vol. 31, no. 6, pp. 1446-1451, November/December 1995.

[59] L. Canadas, B. Navarrete, l. Salvador, "Theoretical Modelling of Electrostatic Precipitators Performance (PRELEC code) ," *Journal of Electrostatics*, vol. 34, pp. 335-353, 1995.

[60] P. A. Lawless, R. F. Altman, "ESPM: an Advanced Electrostatic Precipitator Model," *IEEE Transactions on Industry Applications*, 0-7803-1993-1/94, pp. 1519-1526, 1994.

[61] T. Ohkubo, Y. Nomoto, and T. Adachi , "Corona Discharge Characteristics for Rod with Discharging Needle to Parallel Plate Electrode-Parameter of Needle-Angle," vol. 8, no. 6, pp. 398-404, 1984.

[62] K. Ohyama, J.S. Chang, and K. Urashima, "Numerical Modelling of Wire-Plate Electrostatic Precipitator for Control of Submicron and Ultra Fine Particles," *J. Aerosol Sci.*, vol. 31, pp. S162-S163, 2000.

[63] P.A. Lawless, " ESPVI 4.0 Electrostatic Precipitator V-I and Performance Model," *Program and Manual, EPA PB92-169614*.

[64] P. A. Lawless, "Modeling Particulate Charging in ESPS II: Analytic Approximations and Refinements," *1989 IEEE*, pp. 2154-2162.

[65] T. Yamamoto, "Effect of Turbulence and Electrohydrodynamics on the Performance of Electrostatic Precipitators," *Journal of Electrostatics*, vol. 22, pp. 11-22, 1989.

[66] I. Gallimberti, "Recent Advancements in the Physical Modelling of Electrostatic Precipitators," *Journal of Electrostatics*, vol. 43, pp. 219-247, 1998.

[67] S. Cristina and M. Feliziani, "Calculation of Ionized Fields in DC Electrostatic Precipitators in the Presence of Dust and Electric Wind," *IEEE Transactions on*

Precipitators in the Presence of Dust and Electric Wind," *IEEE Transactions on Industry Applications*, vol. 31, no. 6, pp. 1446-1451, November/December 1995.

[68] A. Soldati, "On the Effects of Electrohydrodynamic Flows and Turbulence on Aerosol Transport and Collection in Wire-Plate Electrostatic Precipitators," *J. Aerosol Sci.,* vol. 31, no. 3, pp. 293-305, 2000.

[69] P.L. Levin, "Comparison of the Donor Cell Method to Other Computational Techniques for the Duct Electrostatic Precipitator," *Journal of Electrostatics*, vol. 25, pp. 201-220, 1990.

[70] P.L. Levin and J. F. Hoburg, "Donor Cell-Finite Element Descriptions of Wire-Duct Precipitator Fields, Charges and Efficiencies," *IEEE Transactions on Industry Applications*, vol. 26, no. 4, pp. 662-670, July/August 1990.

[71] D.E. Stock and E.J. Eschbach; "Predicting Particle motion and efficiency of Electrostatic Precipitators", *Polyphase Flow and Transport Technology*; TA357.S927, pp. 233-237, 1980.

[72] B.S. Choi, C.A.J. Fletcher, "Turbulent Particle Dispersion in an Electrostatic Precipitator," *Applied Mathematical Modelling*, vol. 22, pp. 1009-1021, 1998.

[73] C. Riehle and F. Loffler, "Grade Efficiency and Eddy Diffusivity Models," *Journal of Electrostatics*, vol. 34, pp. 401-413, 1995.

[74] C. Lu and H. Huang, "A Sectional Model to Predict Performance of a Plate Wire Electrostatic Precipitator for Collecting Polydisperse Particles," *Journal of Aerosol Science,* vol. 29, no. 3, pp. 295-308, 1998.

[75] U. Kogelschatz, W. Egli, and E.A. Gerteisen, "Advanced Computational Tools for Electrostatic Precipitators," *ABB Review*, vol. 4, pp. 33-42, 1999.

[76] W. J. Liang and M.F. Cheng, "Turbulent Model for the Performance of an Electrostatic Precipitator," pp. 533-545

[77] P. Cooperman; "A Theory for Space-Charge-limited Currents with Application to Electrical Precipitation," pp. 47-50, 1960.

[78] R. G. Corbin, "Electrical Performance of Serrated Strip Electrodes in Electrical Precipitators," in *Proceedings of the Third International Conference on Electrostatic Precipitation*, Padova, Italy, October, 1987, pp. 843-855.

[79] L.B. Loeb, *Basic Processes of Gaseous Electronics*, California Press, Barkeley, 1961

[80] J.S. Chang, P.A. Lawless, T. Yamamoto. , "Corona Discharge Processes," *IEEE Transaction on Plasma Science*, vol. 19, no. 6, pp. 1152-1166, December 1991.

[81] J.S. Chang , "Electromagnetic Emissions from Atmospheric Pressure Gas Discharges," *IEICE Trans. Commun.*, vol. E79-B, no. 4, pp. 447-456, April 1996.

[82] T.G. Beuthe and J.S. Chang, *Gas Discharge Phenomena, in Handbook of Electrostatic Processes*, Marcel Dekker Inc, 1995 Chapter 9.

[83] G. B. Nichols, "Interpreting Electrical Data From Electrostatic Precipitators," *Proceedings of the Fourth International Conference on Electrostatic Precipitation*, Beijing, China, September, 1990, pp. 93-103.

[84] J. R. McDonald, W. B. Smith, and H.W. Spencer, and L. E. Spark, "A Mathematical Model for Calculating Electrical Conditions in Wire-Duct Electrostatic Precipitation Devices," *Journal of Applied Physics,* vol. 4, no. 6, pp. 2231-2243, June 1977.

[85] P.A. Lawless, K.J. McLean, L.E. Sparks and G. H. Ramsey, "Negative Corona in Wire-Plate Electrostatic Precipitators. Part I: Characteristics of Individual Tuft-Corona Discharges," *Journal of Electrostatics*, vol. 18, pp. 199-217, 1986.

[86] B.S. Rajanikanth and D.V.S. Sarma, "Modeling of Prebreakdown V-I Characteristics of an Electrostatic Precipitator," *IEEE Transactions on Dielectrics and Electrical Insulation*, vol. 9, no. 1, pp. 130-139, February 2002.

[87] G. Hughes and R.B. Richardson, "Electrostatic agglomeration- A Feasibility Study," in *Proceedings of the Third International Conference on Electrostatic Precipitation*, Padova, Italy, October, 1987, pp. 337-342

[88] C. Buccella, "Computation of V-I Characteristics in Electrostatic Precipitators," *Journal of Electrostatics*, vol. 37, pp. 277-291, 1996.

[89] S. Cristina, G. Dinelli, and M. Feliziani, "Numerical Computation of Corona Space Charge and V-I Characteristic in dc Electrostatic Precipitators," *IEEE Transactions on Industry Applications*, vol. 27, no. 1, pp. 147-153, January/February 1991.

[90] T. Ohkubo, Y. Nomoto, T. Adachi, and K.J. McLean, "Electric Field in a Wire-duct Type Electrostatic Precipitator," *Journal of Electrostatics*, vol. 18, pp. 289-303, 1986.

[91] E. Lami, F. Mattachini, I. Gallimberti, R. Turri and U. Tromboni, "A Numerical Procedure for Computing the Voltage-Current Characteristics in Electrostatic Precipitator Configurations," *Journal of Electrostatics*, vol. 34, pp. 385-399, 1995.

[92] Z. Xiangrong, W. Lianze and Z. Keqin, "An Analysis of a Wire-Plate Electrostatic Precipitator," *Journal of Aerosol Science*, vol. 33, pp. 1595-1600, 2002.

[93] J. Anagnostopoulos and G. Bergeles, "Corona Discharge in Wire-Duct Electrostatic Precipitator," *Journal of Electrostatics*, vol. 54, pp. 1129-147, 2002.

[94] J. Miller, C. Riehle, A. J. Schwab, F. Loffler, "Numerische Feldberechnung in Elektrofiltern im Hinblick auf Elektrisch Ahnliche Betriebszustande," *Journala of Electrostatics*, vol. 33, 1994, pp. 213-228, 1994.

[95] I. Gallimberti, "Physical Models of Corona Discharges," *Proceedings of the Third International Conference on Electrostatic Precipitation*, Abano, Padova, Italy, October 1987, pp. 25-43.

[96] K. J. McLean, "Tuft Corona Method of Calculating Characteristics of Electrostatic Precipitators," *Proceedings of the 3nd International Conference on Electrostatic Precipitation,* Abano, Padova, Italy, October 1987, pp. 107-118

[97] K. Adamiak, "Simulation of Corona in Wire-Duct Electrostatic Precipitator by Means of the Boundary Element Method," *IEEE Transactions On Industry Applications*, vol. 30, no. 2, pp. 381-386, March/April 1994.

[98] K.J. McLean, P.A. Lawless, L.E. Sparks and G. H. Ramsey, "Negative Corona in Wire-Plate Electrostatic Precipitators. Part II: Calculation of Electrical Characteristics of Contaminated Discharge Electrodes," *Journal of Electrostatics*, vol. 18, pp. 219-231, 1986.

[99] Dascalescu, A. Samuila, D. Rafiroiu, A. Luga, and R. Morar, "Multiple-Needle Corona Electrodes for Electrostatic Processes Application," *IEEE Industry Applications Society Annual Meeting New Orleans, Louisiana*, October 5-9, 1997, pp. 1811-1816.

[100] M.T. El-Mohandes, S. Ushiroda, S. Kajita, Y. Kondo and K. Horii, "Current Density Distribution on the Plane Electrode in Multineedle to plan configuration," *IEEE*, pp. 1527-1532.

[101] G. Risheng, Z. Hongdi, and Z. Xizonger, " A Study of Novel Electrode Geometries by Plate- Current Characteristics of Electrostatic Precipitators,"

Proceedings of the Fourth International Conference on Electrostatic Precipitation, Beijing, China, September, 1990, pp. 348-351.

[102] C. Riehle and F. Löffler, " The Significance of the Current-Voltage Characteristics in Geometric- Similar Parallel Plate Precipitators," *Proceedings of the Fourth International Conference on Electrostatic Precipitation*, Beijing, China, September, 1990, pp. 123-135.

[103] J.A. Houlgreave, K.S. Bromley and J.C. Fothergill, "Prediction of Monopolar Corona Charge Injection and Current Distribution in Air for Complex Geometries," *The Seventh International Conference on Dielectric Materials Measurements and Applications*, September 1996, Conference Publication no. 430 IEE, pp. 190-193.

[104] J.H. Davidson , P.J. McKinney and P. Linnebur, "Three-Dimensional (3-D) Model of Electric Field and Space Charge in the Barbed Plate-to-Plate Precipitator," *IEEE Transactions on Industry Applications,* vol. 32, no. 4, pp. 858-866, July/August 1996.

[105] J.H. Davidson and P.J. McKinney, "Current Distribution for Barbed Plate-to-Plane Coronas," *IEEE Transactions on Industry Applications*, vol. 28, no. 6, pp. 1424-1431, November/December 1992.

[106] H. Rohmann, "Method of Size Measurement for Suspended Particles," *Zeitschrift fur Physik*, vol. 17, pp. 253-265, 1923.

[107] P. Arendt and H. Kallmann , *Zeitschrift fur Physik*, vol. 35, pp. 421-441, 1925.

[108] M. M. Pauthenier and M. Moreau-Hanot , "La Charge Des Particules Spheriques Dans un Champ Ionise," *Journal De Physique*, no. 12, pp. 590-613, 1929.

[109] N.A. Fuchs, "The Charges on the Particles of Aerocolloids," *Izv. Akad. Nauk. SSSR, Ser. Geogr. Geofiz.*, 341, 1947.

[110] H. J. White, "Particle Charging in Electrostatic Precipitation," *AIEE Transactions*, vol. 70, pp. 1186-1191, 1951.

[111] J. R. Brock, "Noncontinuum Unipolar Charging of Aerosols: The Role of External Electric Fields," *Journal of Applied Physics*, vol. 41, no. 5, pp. 1940-1944, April 1970.

[112] L.W. Parker, "Field Charging Theory for Electrostatic Precipitation of Ultrafine Particles," in *68th Ann. Meeting of Air Pollution Const. Ass.*, 1975, no. 75-02.2.

[113] J.S. Chang, P. Beckwith and J. D. Miller, "Unipolar Charging of Ultra-Fine Particles Under an Electric Field," *The Eleventh Annual Conference of the*

Particles Under an Electric Field," *The Eleventh Annual Conference of the Association for Aerosol Research*, pp. 270-273.

[114] J.G. Laframboise and J.S. Chang, "Theory of Charge Deposition on Charged Aerosol Particles of Arbitrary Shape," *J. Aerosol Sci.*, vol. 8, pp. 331-338, 1977.

[115] J.S. Chang, "Theory of Diffusion Charging of Arbitrarily Shaped Conductive Aerosol Particles by Unipolar Ions," *J. Aerosol Sci.*, vol. 12, pp. 19-26, 1981.

[116] M. R. Cochet, "Théorie de la Charge des Particules Submicroniques dans les Champs Electriques Ionisés; vitesse de Précipitation de ces Particules," *Academie des Sciences*, pp. 243-246, 16 Juillet 1956.

[117] R.A. Fjeld and A. R. McFarland, "Evaluation of Select Approximations for Calculating Particle Charging Rates in the Continuum Regime," *Aerosol Science and Technology*, vol. 10, pp. 535-549

[118] J.S. Chang, *Electrostatic Charging of Particles, in Handbook of Electrostatic Processes*, Marcel Dekker Inc, 1995 Chapter 3.

[119] S.W. Davison and J.W. Gentry, "Modeling of ion Mass Effect on the Diffusion Charging Process," *The 11th Annual Conference of the Association for Aerosol Research*, pp. 262-270

[120] P. Atten, L.M. Dumitran, D. Blanchard, "Numerical Simulation of Fine Particle Charging and Collection In an Electrostatic Precipitator with Regular Barbed Electrodes," *J. Electrostatics*, 2003 (In Print)

[121] S.H. Kim, H. Park, and K.W. Lee, "Theoretical Model of Electrostatic Precipitator Performance for Collecting Polydisperse Particles," *Journal of Electrostatics*, vol. 50, pp. 177-190, 2001

[122] T. Yamamoto, P.A. Lawless and N.Plaks, "Evaluation of the Cold Precharger," *IEEE 1988*

[123] W. Deutsch, "Bewegung und Ladung der Elektrizitetstrager im Zylinderkondensator," *Ann. Phys*. No. 68, pp. 335-334, 1922.

[124a] G. Cooperman, "A New Theory of Precipitator Efficiency," *Atm. Environ.*, no. 5, pp. 541-551, 1971.

[124b] G.L. Leonard, M. Mitchner, and S. A. Self, "Experimental Study of the Effect of Turbulent Diffusion on Precipitator Efficiency," *J. Aerosol Sci. Technol.*, vol. 13, no. 4, pp. 271-284, 1983.

[125] T.J. Krinke, K. Deppert, M. H. Magnusson, F. Schmidt, H. Fissan, "Microscopic Aspects of the Deposition of Nanoparticles from the Gas Phase," *Journal of Aerosol Science*, vol. 33, 1341-1359, 2002.

[126] Y.Mochizuki, S. Sakakibara, and H. Asano, "Electrical Re-entrainment of Particles Deposited on Collecting Plate in Electrostatic Precipitator," Proceedings," in 8^{th} *International Conference on Electrostatic Precipitation*, May 2001, vol. II, C5-2.

[127] S. Masuda and A. Mizuno, "Initiation Condition and Mode of Back Discharge," *Journal of Electrostatics*, vol. 4, pp. 35-52, 1977.

[128] S. Masuda, I. Doi, M. Aoyama, A. Shibuya, "Bias-Controlled Pulse Charging System for Electrostatic Precipitator," *Staub-Reinhalt Luft*, no. 36, pp. 19-26, 1976.

[129] B. Hoferer and A.J. Schwab, "Local Occurrence of Back Corona at the Dust Layer of Electrostatic Precipitators," *2000 Conference on Electrical Insulation and Dielectric Phenomena*, pp. 93-96

[130] C. L. Chang and H. Bai, "An Experimental Study on the Performance of a Single Discharge Wire-plate Electrostatic Precipitator with Back Corona," *Journal of Aerosol Science*, vol. 30, no. 3, pp. 325-340, 1999.

[131] R.J. Peterson and J.H. Davidson, "Modification of Gas Flow by Charged Particles," *IEEE*, pp. 1513-1518, 1994.

[132] P. Atten, F. M. J. McCluskey, and A.C. Lahjomri, "The Electrohydrodynamic Origin of Turbulence in Electrostatic Precipitators," *J. Fluid Mech.*, vol. 127, pp. 123-140, 1983.

[133] D.Blanchard, L. M. Dumitran and P. Atten, "Effect of Electro-aero-dynamically Induced Secondary Flow on Ttransport of Fine Particles in an Electrostatic Precipitator," *Journal of Electrostatics*, vol. 51-52, pp. 212-217, 2001.

[134] T. Yamamoto, M. Okuda and M. Ohkubo, "Three-dimensional Electrohydrodynamics in Electrostatic Precipitators," *2002 Annual Report Conference on Electrical Insulation and Dielectric Phenomena*, October 2002, Mexico, pp. 228-231.

[135] M. Mitchner, S.A. Self, and K.D. Khim, "The Role of Turbulence in Electrostatic Precipitators," *Proceedings of the Fourth International Conference on Electrostatic Precipitation*, Beijing, China, September, 1988, pp. 539-569

[136] D. Blanchard, P. Atten, and L. M. Dumitran, "Correlation Between Current Density and Layer Structure for Fine Particle Deposition in a Laboratory Electrostatic Precipitator," *IEEE Transactions on Industry Applications*, vol. 38, no. 3, pp. 832-839, May/June 2000.

[137] S.A. Self, D. H. Choi, M. Mitchner, and R. Leach, "Experimental Study of Collector Plate and Re-entrainment in Electrostatic Precipitators," *Proceedings of the Fourth International Conference on Electrostatic Precipitation*, Beijing, China, September, 1990, pp. 514-560

[138] S.L. Soo, *Fluid Dynamics of Multiphase Systems*, Blaisdell Pub. Co., Waltham

[139] W.C. Hinds, *Aerosol Technology, Properties, Behaviour, and Measurement of Airborne Particles*, John-Wiley & Sons, 1982

[140] A. Yabe, *Heat Engineerong, in Handbook of Electrostatic Processes*, Marcel Dekker, Inc., 1995, Chapter 25.

[141] K. J. McLean, "Properties of the Precipitated Dust Layer That Arise Because of its Particulate Structure," *Proceedings of the 2nd International Conference on Electrostatic Precipitation*, November 1984, Kyoto, Japan, pp. 236-240

[142] R.A. Lawless, T. Yamamoto, and Y. Otani, "Modelling of Electrostatic Precipitators and Filters," *in Handbook of Electrostatic Processes*, Marcel Dekker Inc, 1995, Chapter 22.

[143] D. Brocilo, J.S. Chang, and R.D. Findlay, "Modeling of Electrode Geometry Effects On Dust Collection Efficiency of Wire-Plate Electrostatic Precipitators," *Proceedings, 8th international conference on Electrostatic Precipitation,* May 2001, vol. II, A4-3.

[144] T. Misaka, K. Urashima, A. Akasaka, T. Oura, and J.S. Chang, "Development of Short Pulse Energized Electrostatic Precipitator Model for the Collection of High Resistivity Dust Particles," *Journal of Aerosol Science,* vol. 32, Supplement 1, pp. S949-S950, September 2001.

[145] A.D. Moore, *Electrostatics and Its Applications*. New York, Wiley, 1973

[146] F.W. Peek, *Dielectric Phenomena in High Voltage Engineering, McGraw-Hill*. New York, 1929.

[147] F. Lewellyn-Jones, *Ionization and Breakdown in Gases*. London- Methuen-New York, Wiley, 1957.

[148] A. von Engel, *Ionized gases*. Woodbury, NY-AIP Press, 1994.

[149] J.M Meek and J.D. Craggs, *Electrical Breakdown of Gases*. Oxford, Clarendon Press, 1953

[150] E.A. Mason and E.W. McDaniel, *Transport Properties of Ions in Gases*. New York, Wiley, c1988

[151] J. S. Chang and A. Kwan, "Modelling of Dry Air Chemistry In a Coaxial Wire-Pipe Negative Corona Dischargev," *ESA-IEJ Joint Symposium on Electrostatics 1998 Proceedings*, Press Morgan Hill, California, June 1998, pp. 390-407.

[152] T. Yamamoto, P. A. Lawless, L. E. Sparks, "Gas and Electrical Sneakage in Electrostatic Precipitators," *Proceedings of the Third International Conference on Electrostatic Precipitation*, Padova, Italy, October, 1987, pp. 843-855.

[153] L. Salasoo and J.K. Nelson , "Simulation and Measurement of Corona for Electrostatic Pulse Powered Precipitators," *Journal of Appl. Physics*, vol. 58, no. 8, pp. 2494-2960, 1985.

[154] J.S. Chang, M. Kamitsuma and J.G. Laframboise, "Streamline Curvature Up-Wind Difference Method for Modelling of Steady heat, Mass and Plasma Transfer to Cylinder in Cross-Flow," in *Proc. Int. Conf. Comp. Fluid Dynamics*, K. Oshima, Ed. vol. 1, pp. 422-434.

[155] M.S. Kao and C.S. Wang, "Reactive Oxygen Species in Incense Smoke," *Aerosol and Air Quality Research*, vol. 2, no. 1, pp. 61-69, 2002.

[156] J. S. Chang, "Users Sector Workshop on The Control of Toxic Emission From Flue Gases by An Advanced Electrostatic Precipitator," *Workshop Report*, May, 1997.

[157] J. S. Chang, P. C. Looy, C. Webster, A. A. Berezin, A. Zukeran, T. Ito, "The Collection of Fine Particles by an Electrostatic Precipitator with Quadrupole Prechargers," *Proceedings 7th international conference on Electrostatic Precipitaton*, 1998

[158] F.L. Arnot, *Collision Processes in Gases*. 2nd edition, London, Methuen, 1942.

[159] D.G. Samaras, *Theory of Ion Flow Dynamic*. Englewood Cliffs, N.J., Prentice-Hall, 1962.

[160] J. E. Jones, "On the Drift of Gaseous Ions," *Journal of Electrostatics*, vol. 27, pp. 289-318, 1992.

[161] J. H. D. Eland, *Photoelectron Spectroscopy: An Introduction to Ultraviolet Photoelectron Spectroscopy in the Gas Phase*. London, Butterworths, 1974.

[162] W.S. Struve, *Fundamentals of Molecular Spectroscopy*. New York-Wiley, 1989.

[163] G. Herzberg, *Molecular Spectra and Molecular Structure*. New York, Prentice-Hall, 1939.

[164] R. W. B. Pearse and A. G. Gaydon, *The Indentification of Molecular Spectra. Chapman and Hall*, London, 4th edition, 1976.

[165] C.E. Moore ; edited by J.W. Gallagher, *Tables of Spectra of Hydrogen, Carbon, Nitrogen, and Oxygen Atoms and Ions*. Boca Raton, CRC Press, 1993.

[166] Y. Kim, S.H. Hong, M.S. Cha, Y.H. Song, and S.J. Kim, "Measurement of Electron Energy by Emission Spectroscopy in Pulsed Corona and Dielectric Barrier Discharges," *Journal of Adv. Oxid. Technology*, vol. 6, no. 1, 2003.

[167] S.V. Pancheshnyi, S.V. Sobakin, S.M. Starikovskaya, and A.Y. Starikovskii, "Discharge Dynamics and the Production of Active Particles in a Cathode-Directed Streamer," *Plasma Physics Reports*, vol. 26, no. 12, pp. 1054-1065, 2000.

[168] N. Ikuta, K. Kondo, "A spectroscopic Study of Positive and Negative Coronas in N_2 O_2 mixture," *Proceedings of 4th International Conference on Gas Discharges and Their Applications*, Swansea, UK, 1976, pp. 227-230.

BIBLIOGRAPHY

J. Böhm, *Electrostatics Precipitators*, Elsevier, New York, 1982.

T.G. Beuthe and J.S. Chang, "Chemical Kinetic Modelling of Non-Equilibrium Ar-CO2 Thermal Plasmas," *Jpn. J. Appl. Phys.*, vol. 36, Part 1, no. 7B, pp. 4997-5002, July 1997.

T.G. Beuthe and J.S. Chang, "Chemical Kinetic Modelling of Non-Equilibrium Ar-H2 Thermal Plasmas," *Jpn. J. Appl. Phys.*, vol. 38, Part 1, no. 7B, pp. 4576-4580, July 1999.

R. J. Van Brunt, "Physics and Chemistry of Partial Discharge and Corona," *IEEE Transactions on Dielectrics and Electrical Insulation,* vol. 1, no. 5, pp. 761-784, October 1994.

J.S. Chang and A. Watson, "Electromagnetic Hydrodynamics," *IEEE Transaction on Dielectrics and Electrical Insulation,* vol. IA-23, no. 1, pp. 871-895, January/February 1987.

J. S. Chang and T. G. Beuthe, "Modelling of Dry Air Chemistry In a Coaxial Wire-Pipe Negative Corona Discharge," *J. High Temp. Chem. Proc.*, vol. 1, pp. 333-341, 1992.

J.S. Chang, "Numerical Modeling of Charged Ultrafine Particle Deposition on an Electrically Enhanced Cylindrical Wire," *Proceedings 2nd International Aerosol Conference,* September 1986, Berlin, pp. 704-707.

J. S. Chang and R. Godard, "A Revised Model of Particle Charging for Electrostatic Precipitation or Dust Charging," *Proceedings of the SCS'95 Ottawa, Ontario,* Canada, July 24-26, 1995 Tuncer L Oren and Louis G. Birta (eds.) 1995 by the SCS, pp. 751-755.

J.S. Chang and S. Ono, "Diffusion Charging of Nonsperical Particles by Bipolar Ions under External Magnetic Fields," *Journal of Aerosol Science,* vol. 18, no. 6, pp. 765-768, 1987.

C.S. Chen, J.G. Laframboise, and J.S. Chang, "Diffusion and sedimentation of aerosol particles from Laminar Flow in inclined Channels," *10th annual conference of the Association for Aerosol Research,* pp. 283-286.

V. Cooray, "Charge and Voltage Characteristics of Corona Discharges in a Coaxial Geometry," *IEEE Transactions on Dielectrics and Electrical Insulation,* vol. 7, no. 6, pp. 734-743, December 2000.

J.A. Cross, *Electrostatics: Principles, Problems and Applications*, Bristol: Adam Hilger, 1987.

S. Cristina and M. Feliziani, " Calculation of Ionized Fields in DC Electrostatic Precipitators in the Presence of Dust and Electric Wind," *IEEE Transactions on Industry Applications,* vol. 31, no. 6, pp. 1446-1451, November/December 1995.

C. R. Cottingham, "Electrostatic Precipitator Upgrading Meeting the Challenge, " *Power Station Maintenance: Profitability Through Reliability,* 30 March - 1 April 1998. Conference Publication No. 452, IEE, 1998, pp. 90-96.

J.L. Davis and J.F. Hoburg, "Wire-Duct Precipitator Field and Charge Computation Using Finite Element and Charactersitics Methods," *Journal of Electrostatics*, vol. 14, pp. 187-199, 1983.

W. Deutsch, " Bewegung und Ladung der Elektrizitatstrager im Zylinderkondensator, *Annalen der Physik,* iV Folge, Bd. 68, pp. 335-344, 1922.

L. M. Dumitran, D. Blanchard, P. Atten, and P. Notingher, "Estimate of Effective Migration Velocity of Fine Particles From Fractional Efficiency Measurements in an Electrostatic Precipitator," *2000 IEEE,* pp. 559-562.

L. M. Dumitran, P. Atten, D.Blanchard, and P. Notingher, "Drift Velocity of Fine Particles Estimated From Fractional Efficiency Measurements in a Laboratory-Scaled Electrostatic Precipitator," *IEEE Transactions on Industry Applications*, vol. 38, no. 3, pp. 852-857, May/June 2002.

G. S. Dulikravich and S. R. Lynn, "Unified Electro-Magneto-Fluid Dynamics (EMFD): Introductory Concepts," *Int. J. Non-Linear Mechanics*, vol. 32, no. 5, pp. 913-922, 1997.

G. S. Dulikravich and S. R. Lynn, " Unified Electro-Magneto-Fluid Dynamics (EMFD): A Survey of Mathematical Models," *Int. J. Non-Linear Mechanics*, vol. 32, no. 5, pp. 923-932, 1997.

A.A. Elmoursi and G. S. P. Castle, "Modeling of Corona Characteristics in a Wire Precipitator Using the Charge Simulation Technique," *IEEE Transactions on Industry Applications*, vol. IA-23, no. 1, pp. 96-102, January/February 1987.

N.A. Fuchs, " On the stationary Charge Distribution on Aerosol Particles in a Bipolar

Ionic Atmosphere," *Pure and Applied Geophysics*, vol. 56, pp. 185-193, 1963.

J. P. Gooch, E. B. Dismukes, R.E. Bickelhaupt, and R. F. Altman, " Flue gas Conditioning Studies," *Proceedings of the 2nd International Conference on Electrostatic Precipitation, November 1984*, Kyoto, Japan, pp. 200-209.

M. Jadrusik, J. B. Gajewski, and A.J. Swierczok, "Effect of the particle diameter and corona electrode geometry on the particle migration velocity in electrostatic precipitators," *Journal of Electrostatics*, Volumes 51-52, pp. 245-251, 2001.

S. Jayaram, J.S. Chang, A.A. Berezin, P.C. Looy, R. Mangal, and M. S. Mozes, "Semipilot plant Pulse Energized Cold-Precharger Electrostatic Precipitator Tests for Collection of Moderately High Resistivity Flyash Particles," *IEEE Transactions on Industry Applications,* vol. 32, no. 4, pp. 851-857, July/August 1996.

H. Jiming, H. Krbin, and C. Hongxun, "Simulating Electrostatic Enhancement of Particle Collection in Fibre Filters', *Proceedings of International Conference on Modern Electrostatics,* 1988, Bejing, China, pp. 37-40.

K.C. Kao, "Some Electromechanical Effects on Dielectrics," *British Journal of Applied Physics,* vol. 12, pp. 629-632, November 1961.

C. Kanaoka, J Chutmanop, and M. Kitada, "Inertial Separation of Ultrafine Particles by a Laval Nozzle Type Supersonic Impactor," *Powder Technology*, vol. 118, pp. 188-192, 2001.

Y. Kousuka, K. Okuyama, and M. Adachi, " Bipolar and Unipolar Diffusion Charging of Ultrafine Aerosol Particles," *The 11th Annual Conference of the Association for Aerosol Research,* pp. 261-262.

M. Lackowski, "Unipolar charging of aerosol particles in alternating electric field," *Journal of Electrostatics*, vol. 51-52, pp. 225-231, 2001.

E. Lami, F. Mattachini, I. Gallimberti, R. Turri, and U. Tromboni, "A Numerical Procedure for Computing the Voltage-Current Characteristics in Electrostatic Precipitator Configurations," *Journal of Electrostatics*, vol. 34, pp. 385-399, 1995.

A. Laskin and J.P. Cowin, "On deposition efficiency of point-to-plate electrostatic precipitator," *Journal of Aerosol Science*, vol. 33, pp. 405-409, 2002.

L. Linmao, L. Jie, W. Haijun, S. Lianxi, and X. Dezhi, "Electrostatic Precipitator with Transverse Electrodes for Collecting High Resistivity Dust," *IEEE Transactions on Industry Applications*, pp. 2054-2058, 1996.

D. P. Lymberopoulos and D. J. Economou, "Two-Dimensional Self-Consistent Radio

Frequency Plasma Simulations Relevant to the Gaseous Electronics Conference RF Reference Cell," *Journal of Research of the National Institute of Standards and Technology*, vol. 100, no. 4, pp. 473-494, July-August 1995.

Z. M. Al-Hamouz, "A Combined Algorithm Based on Finite Elements and a Modified Method of Characteristics for the Analysis of the Corona in Wire-Duct Electrostatic Precipitators," *IEEE Transactions on Industry Applications*, vol. 38, no. 1, pp. 43-49, January/February 2002.

S. Masuda, " Effect of Temperatue and Humidity on the Apparent Conductivity of High Resistivity Dust," *Electrotech. J. Japan*, vol. 7, 1962, pp. 108-113

M. J. Matteson and E.Y.H. Keng, "Aerosol Size Determination in the submicron range by thermophoresis " *Powder Journal of Aerosol Science*, vol. 3, 1972, pp. 45-53

J. Mizeraczyk, M. Kocik, J. Dekowski, M. Dors, J. Podlinski, T. Ohkubo, S. Kanazawa, and T. Kawasaki, "Measurement of the velocity field of the flue gas flow in an electrostatic precipitator model using PIV method," *Journal of Electrostatics*, vol. 51-52, pp. 272-277, 2001.

J. Miller, C. Riehle, A. J. Schwab, and F. Loffler, "Numerische Feldberechnung in Elektrofiltern im Hinblick auf elektrisch ahnliche Betriebszustande," *Journal of Electrostatics*, vol. 33, pp. 213-228, 1994.

T. Misaka, A. Akasaka, T. Oura, M. Hirano, and H. Asano. " Electrostatic Precipitator combined pulse charging section with moving electrode section for high resistivity soot," Proceedings, *6th International Conference on Electrostatic Precipitation*, 1996, pp. 45-50.

A. Mizuno, "Electrostatic Precipitation," *IEEE Transactions on Dielectrics and Electrical Insulation*, vol. 7, no. 5, pp. 615-624, October 2000.

S. Oglesby and G.B. Nichols, "Electrostatics Precipitators," Marcel Dekker Inc, New York, 1978.

Shih-I Pai, *Magnetogasdynamics and Plasma Dynamics*, Spring-Verlag, Vienna, 1962.

K. R. Parker, "The Precipitation of Difficult Dust," *Journal of Electrostatics*, vol. 8, pp. 355-367, 1980.

G. W. Penney, "Electrostatic Precipitation of High Resistivity Dust," *AIEE transactions*, vol. 70, pp. 1192-1196, 1951.

W. Peukert and C. Wadenpohl, "Industrial Separation of Fine particles with Difficult dust Properties," *Powder Technology*, vol. 118, pp. 136-148, 2001.

K. Porle, "Pulsed Energization of electrostatic Precipitators; A Review of Worldwide Experience," *Proceedings of International Conference on Modern Electrostatics*, 1988, Bejing, China, pp. 9-13.

B. S. Rajanikanth and B. R. Prabhakar, "Modeling of Prebreakdown VI Characteristics of a Wire-Plate Electrostatic Precipitator Operating Under Combined DC-Pulse Energization, *IEEE Transactions on Dielectrics and Electrical Insulation*, vol. 1, no. 6, pp. 1058-1067, December 1994.

M. Rea, " Advanced Electrostatic Applications to Flue Gas Cleaning," *Proceedings of International Conference on Modern Electrostatics*, 1988, Bejing, China, pp. 20-22.

U. Riebel, R. Radtke, and R. Loos, "An experimental Investigation on Corona Quenching," *Journal of Electrostatics*, vol. 54, pp. 159-165, 2002.

C. Riehle and F. Loffler, "Grade Efficiency and Eddy Diffusivity Models," *Journal of Electrostatics,* vol. 34, pp. 401-413, 1995.

C. Riehle and F. Loffler, "Electrical Similarity Concerning Particle Transport in Electrostatic Precipitators," *Journal of Electrostatics*, vol. 29, pp. 147-165, 1992.

R. S. Sigmond, "The Unipolar Corona Space Charge Flow Problem," *Journal of Electrostatics*, vol. 18, pp. 249-272, 1986.

O.M. Stuetzer, "Magnetohydrodynamics and Electrohydrodynamics," *The Physics of Fluids,* vol. 5, no. 5, pp. 534-544, May 1962.

K. M.Sullivan, " Resistivity, Ash Chemistry and Conditioning," *Proceedings of the 2nd International Conference on Electrostatic Precipitation,* November 1984, Kyoto, Japan, pp. 283-293.

T. Tianyou and Z. Lian, Preliminary Study on the Collection of Fine Particles by Charged Drops," *Proceedings of International Conference on Modern Electrostatics, 1988,* Bejing, China, pp. 53-56.

J.Y. Tu, "Computation of Turbulent Two-Phase Flow on Overlapped Grids," *Numerical Heat Transfer*, Part B, vol. 32, pp. 175-195, 1997.

H.J. White, *Industrial Electrostatic Precipitation*, Addison Wesley Pub.Co., 1963.

C. Xuegou, H. Huifen, and M. Jinyuan, "A Research on the Mechanism of Dust Collection in Electrostatic Lentoid Fields', *Proceedings of International Conference on Modern Electrostatics*, 1988, Bejing, China, pp. 41-44.

APPENDICES

EXPERIMENTAL RESULTS FOR CORONA DICHARGE, DUST PARTICLE AND FLUE GAS CHARACTERIZATION

A1 EXPERIMENTAL SET-UP

Figure A.1 shows a schematic diagram of the bench-scale experimental set-up used in this study. It is composed of the electrostatic precipitator, power supply, gas flow control system, dust particle injection and dust particle measurement equipments. Several experiments were performed in order to determine the boundary conditions on the discharge/collecting electrodes, as well as the particulate matter characteristics. These are: a) current–voltage characteristic measurements, b) measurement of the current density profile on the collecting plate, c) measurement of light emission from discharge electrodes by optical spectrometry and digital imaging, d) Neutron Activation Analysis (NAA) of particulate matter, e) Fourier Transform Infrared spectroscopy (FTIR) of a gas phase , and f) the shape and the size distribution of particulate matter entering the ESP, found by: Scanning Electron Microscopy (SEM), Environmental Scanning Electron Microscopy ESEM, Transmission Electron Microscopy (TEM), and a Condensation Nucleation Particle Counter (CNPC).

A1.1 Bench-scale electrostatic precipitator

The bench-scale ESP was of wire-plate type. The ESP housing was made from stainless steel. The housing length by width by height dimensions are *0.9*, *0.1*, and *0.4 m*, respectively. Two stainless steel plates were attached parallel to the walls of the housing and were used as a collecting electrode. The ESP was tested with two collecting electrodes of *0.1015* and *0.2035 m* in length and various type of discharge electrodes. The collecting electrodes were grounded through the analogue multi-meter. The plate-to-plate spacing was *0.0515 m*. Discharge electrodes were installed on the insulation frame half between the plates, and connected to the power supply. Typical operating voltages ranged from *–8* to *–30 kV*. The main gas was obtained from the compressed air intake. The air intake was placed approximately three meters upstream from the ESP. The composition of the main gas flow could be changed from pure air to natural gas combustion composition. The air flow rate was changed from *3* to $21\ m^3/h$. The air temperature from *20* to $150\,^{o}C$ is regulated by an electrical heater and the air humidity from *20* to *80 %* is regulated by a humidifier. The dust particles are introduced to the main gas flow by burning the various numbers of incense sticks for the inlet dust loading range from *20* to $100\ mg/m^3$.

A1.2 Measuring Equipment

The airflow rate was measured upstream of the ESP by the air rota-meter. The gas flow temperature and composition were obtained by the flue gas analyser (Eurotron Greenline Mk2). The time averaged applied voltage and current were measured by analogue meters on the power supply side (Universal Voltronics LABTROL). The instantaneous voltage and current applied to the discharge electrode was displayed on a digital oscilloscope *(Textronix TDS 420A, 200 MHz)* by using a voltage probe *(Textronix P6015A, 20 kV dc,* *100 MΩ)* or a current probe *(IPC CM-10MG, 0.1 V/A),* accordingly. The discharge current on the side of the collecting electrodes was measured by an analogue electrometer *(Keithley Instruments Model 600B).* The dust particle number and concentration were obtained by the condensation particle counter *(TSI 3010)* and *(HUZDUST II).*

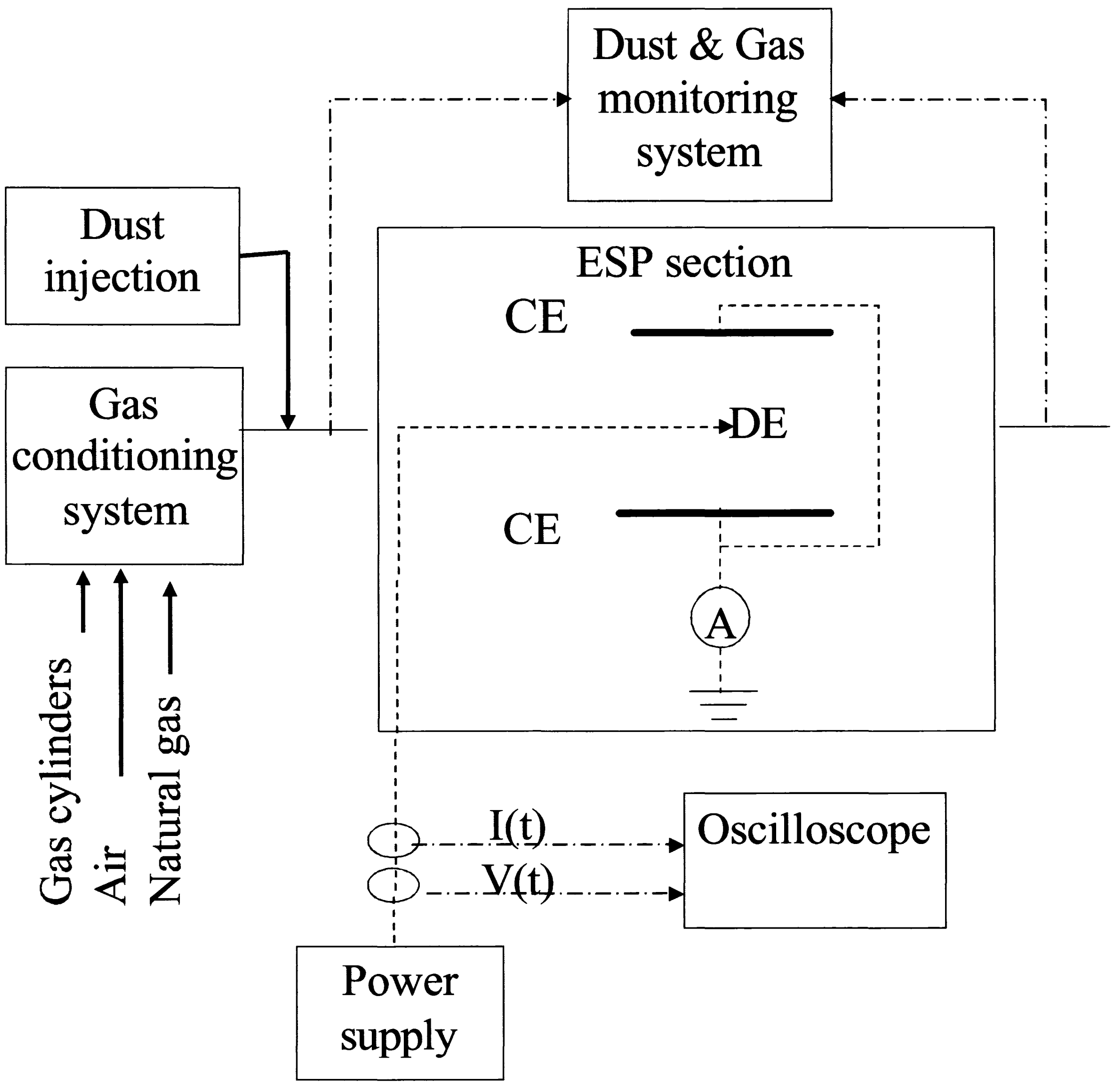

Figure A.1 Schematic diagram of the experimental set-up used for the measurement of current-voltage characteristics and dust collection efficiency (DE...Discharge electrode; CE...Collecting electrode)

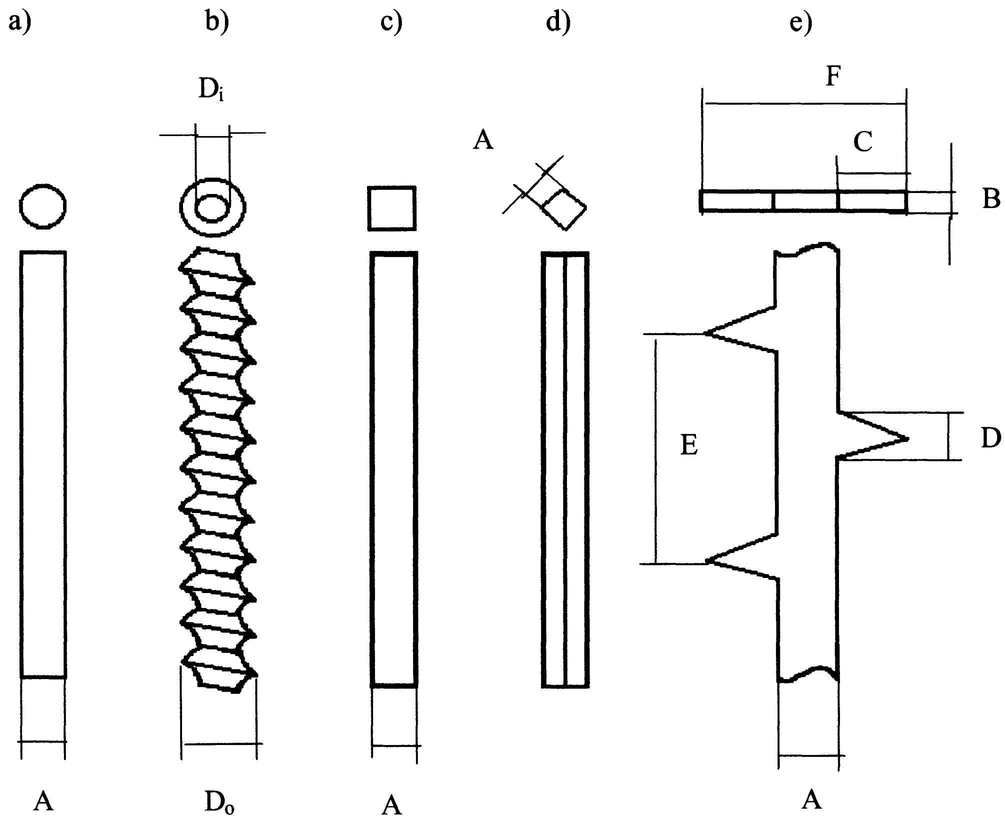

Figure A.2 Dimensions of discharge electrodes: (a) round A={0.25;1.5, 3} mm (b) threaded {Do; Di}={2.5; 2} mm, (c) rectangular A=2.7 mm, (d) romboid A=2.7 mm, (d) spike S_1={ A=10 mm, B=2 mm, C=D=9 mm, E=80 mm, F=28 mm} and S_2={ A=10 mm, B=1.5 mm, C=D=9 mm, E=32 mm, F=28 mm}.

A2 CHARACTERISTICS OF PARTICULATE MATTER GENERATED BY BURNING INCENSE

Inhalable particulate matter (PM) includes both fine and coarse particles. These particles can accumulate in the respiratory system and are associated with numerous health effects. Exposure to coarse particles is primarily associated with the aggravation of respiratory conditions, such as asthma. Fine particles are closely associated with increased hospital admissions and emergency room visits for increased respiratory symptoms and diseases, decreased lung function, and even premature death of the sensitive groups that include the elderly, individuals with asthma, and children. Combustion of incense sticks generates particulate matter of different chemical compositions, sizes and shapes. There are several paths by which the toxic elements can reach the environment. Volatile trace elements are usually emitted with the flue gas. Non-volatile components reach the environment via disposal of the bottom ash or via emission of particulate matter.

The trace element composition of incense and bottom ash was analysed by Neutron Activation Analysis (NAA). The gas phase was analysed by Fourier Transform Infrared spectroscopy (FTIR). The shape and the size distribution of the incense stick, bottom ash, and particulate matter entering ESP were analysed by: Scanning Electron Microscopy (SEM), Environmental Scanning Electron Microscopy ESEM, Transmission Electron Microscopy (TEM), and a Condensation Nucleation Particle Counter (CNPC). These techniques are used due to the different properties of a particulate matter at different locations in the ESP loop. The incense stick and bottom ash, composed from solid particles, are analysed by SEM. Since, particulate matter, sampled from collecting electrodes, contains both solid and liquid components ESEM is used to obtain information about the solid component. The CNPC was used to measure dust size distribution of liquid as well as solid components of particulate matter less than $20\ \mu m$ from the entrance and exit of the bench-scale ESP.

The composition of particulate matter usually reflects the source of the burning material and particle formation process. Besides a wooden core and additive substances, the most important components of incense stick are its resins. In particulate, myrrh and frankincense are the most commonly used ingredients. The gas and particulate matter phase of burning incense contains various compounds, which include organic compounds, polycyclic aromatic hydrocarbons (PAHs), elemental carbon, carbon monoxide, sulphates, nitrates, reactive oxygen compounds ROC [155], and metals. PAHs and ROCs are produced whenever wood, paper, coal, candle, cigarette, incense, gasoline, or diesel is burned. PAHs are a group of toxic chemicals, some of which are known to be either mutagenic or even carcinogenic. ROCs can cause respiratory inflammation, lung cancer, and other adverse health effects. Regarding formation processes of particulate matter, condensation of vapour phase elements and agglomeration of droplets lead to a different composition of trace elements. Table A.1 classifies some trace elements based on their volatility.

A2.1 Composition of Flue Gas by FTIR

Detection of the basic structure of compounds by Fourier Transform Infrared spectroscopy (FTIR) is based on the spectral locations of their infrared absorptions. The

Table A.1. Trace element classification [156]

Elements	Volatility Characteristic; Formation Process	Source of Trace Elements
N, S	Volatile; N forms nitrates; S forms sulfates	Flue gas and/or burning material
B, Br, Cl, F, Hg, I, Se	Volatile; Cl forms salts	
As, Cd, Pb, Sb, Ti, Zn	Volatile; Vaporize during combustion and than condense on the fine particulates	Burning material
Be, Co, Cu, Ge, Mo, Ni, P, U, V, W		
Ba, Mn, Rb, Sr		
Al, Ca, Ce, Cr, Cs, Eu, Fe, K, La, Mg, Na, Rb, Sc, Sm, Sr, Si, Tn, Ti	Non Volatile; Contained as nuclei in liquid droplets that are formed during the combustion. Later, they form particulates by agglomeration of droplets and evaporation of liquid phase.	

FTIR instrument consists of a source, interferometer, sample and a detector. The source energy is send through an interferometer onto the sample. In the interferometer the light passes through a beam-splitter, which sends the light in two directions at right angles. One beam goes to a stationary mirror then back to the beam-splitter. The other goes to a moving mirror. The motion of the mirror makes the total path length variable versus that taken by the stationary-mirror beam. When the two meet up again at the beam-splitter, they recombine. The recombined beam passes through the sample. The sample absorbs all the wavelengths characteristic of its spectrum, and this subtracts specific wavelengths from the interferogram. The detector now reports the variation in energy versus time for all wavelengths simultaneously. A Fourier transform was used to convert an intensity as a function of a time into an intensity as a function of a frequency spectrum.

At first, the functional group regions, between *4000* and *1500* cm^{-1}, were examined followed by a matching in a fingerprint region, between *1500* and *400* cm^{-1}.

The infrared spectrum of incense smoke is shown in Figure A.3. This shows a strong absorption at just over $1710\ cm^{-1}$ and a medium absorption from 2500 to $3000\ cm^{-1}$. These bonds correspond to the $C{=}O$ and $O\text{-}H$ group found in carboxylic acid $(C_xH_yO_z)$. The peak in the functional group region may also indicate the presence of N_xH_y, which evidence is also found in the fingerprint region. The strong evidence of sulphuric and chlorine bonds in ESP gas phase has not been found. With respect to the sulphur contained, only a small percentage may be contained in the gas phase due to the low combustion heat around $350\ °C$. The sulphur concentration ratio between the bottom ash and incense stick, around ten, indicates that the bottom ash will have a higher sulphur content than the particulate matter entering the ESP. In the case of chlorine, a very small enrichment factor, less than 0.2, indicates that the chlorine compound should be evident either in a gas phase or as particulate matter. Since there are some uncertainties related to a $C_xH_yCl_z$ bond by FTIR, it is believed that the chlorine is mainly represented in a particulate matter in the form of various salts.

A2.2 Trace Element Composition of Incense Stick, Bottom Ash and Collected Particulate Matter

The trace element composition of incense stick, bottom ash and collected particulate matter was analysed by Neutron Activation Analysis (NAA). NAA is based upon the process of neutron activation and decay. During the activation-time, the irradiated target nucleus will capture a neutron, transfer in a highly excited state, and then convert to a radioactive nucleus by emitting a prompt gamma ray. During the decay-time the radioactive nucleus will transform into a stable nucleus by emitting the decay-gamma-rays and beta particles. The decay of gamma rays depends on the disintegration rate,

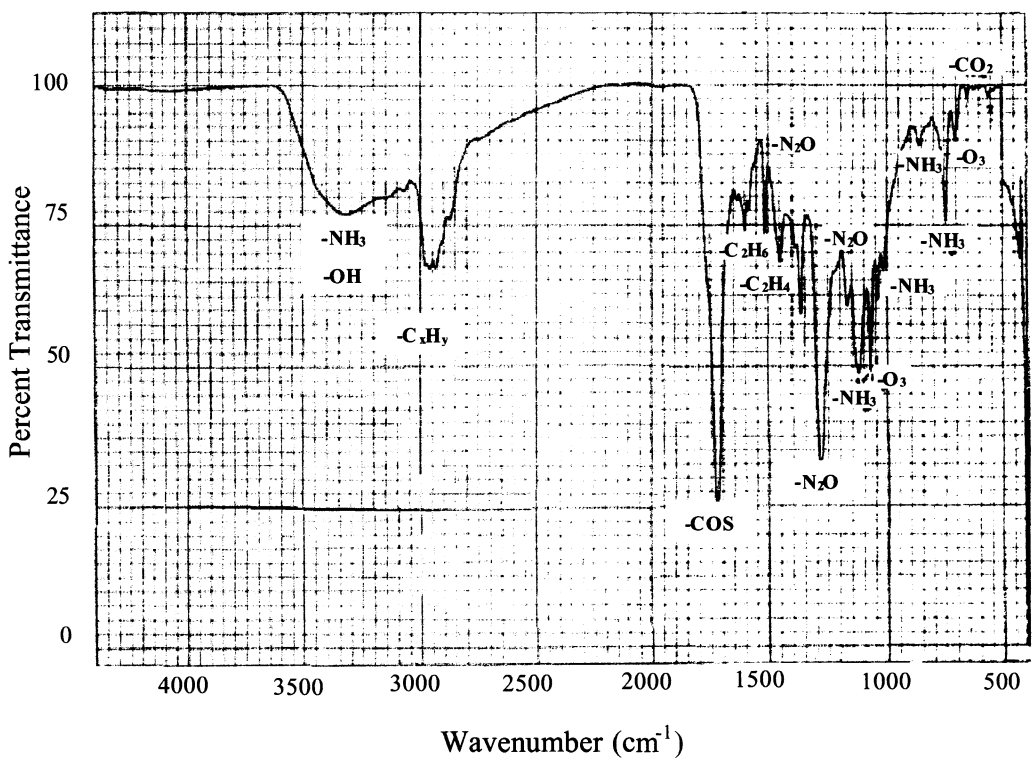

Figure A.3 NaCl IR window after 30 minutes exposure to incense smoke which is directly proportional to the total concentration of the target nucleus or parent element. Figures A.4 and A.5 show major and trace elements of an incense stick and a bottom ash. The incense stick contains twelve major elements with concentrations greater than *100 ppm* and sixteen trace elements with concentration less than *100 ppm*. Besides *C, H, O* and *N* the major elements are *Ca 2.1 %, Cl 0.9 %, K 0.3%,* and *Fe 0.2%.* The other major elements have a concentration less then *0.1%.* By burning the incense stick the concentration of most elements in the bottom ash increases. The concentration of *Al, Ba, Ca, Dg, K, Mg, S, Sm, Rb, Th* and *V* has increased more than ten times. The concentration of *Cr, Fe, La, Mn, Na, Sr,* and *Ti* has increased from three to seven times. The concentration of *As, Br, Co, Mo, Nd, Sb,* and *Zn* is approximately at the same level. Only *Cl* has reduced concentration. By analysing the trace elements of the PM collected by ESP, the *Na, Mn, Al* and *Cl* concentrations were above the present NAA detection limits. The enrichment factor of *Na* and *Mn* is around seven, therefore the trace elements with enrichment factor less than seven could be also found in fly ashes. Elements such as *Mn* can cause lung irritations, *Sr* can be mistaken by a body instead of *Ca, Cr* compounds could be highly toxic, *Sb* can cause liver damaging, *Nd* can cause skin and eye irritations, *Br* may causes depression and weight loss, *Zn* may cause lung diseases, and *Cl* has strong oxidizing nature. Those trace elements may also form various compounds such as oxides, sulfites and chlorides. Since there are some uncertainties related to chloride compounds in a flue gas phase, it is believed that the chlorine is mainly represented in a small fly ash particles consisting of inorganic chloride such as $NaCl$, KCl, $AsCl_3$, $MnCl_2$, $ZnCl_2$, etc.

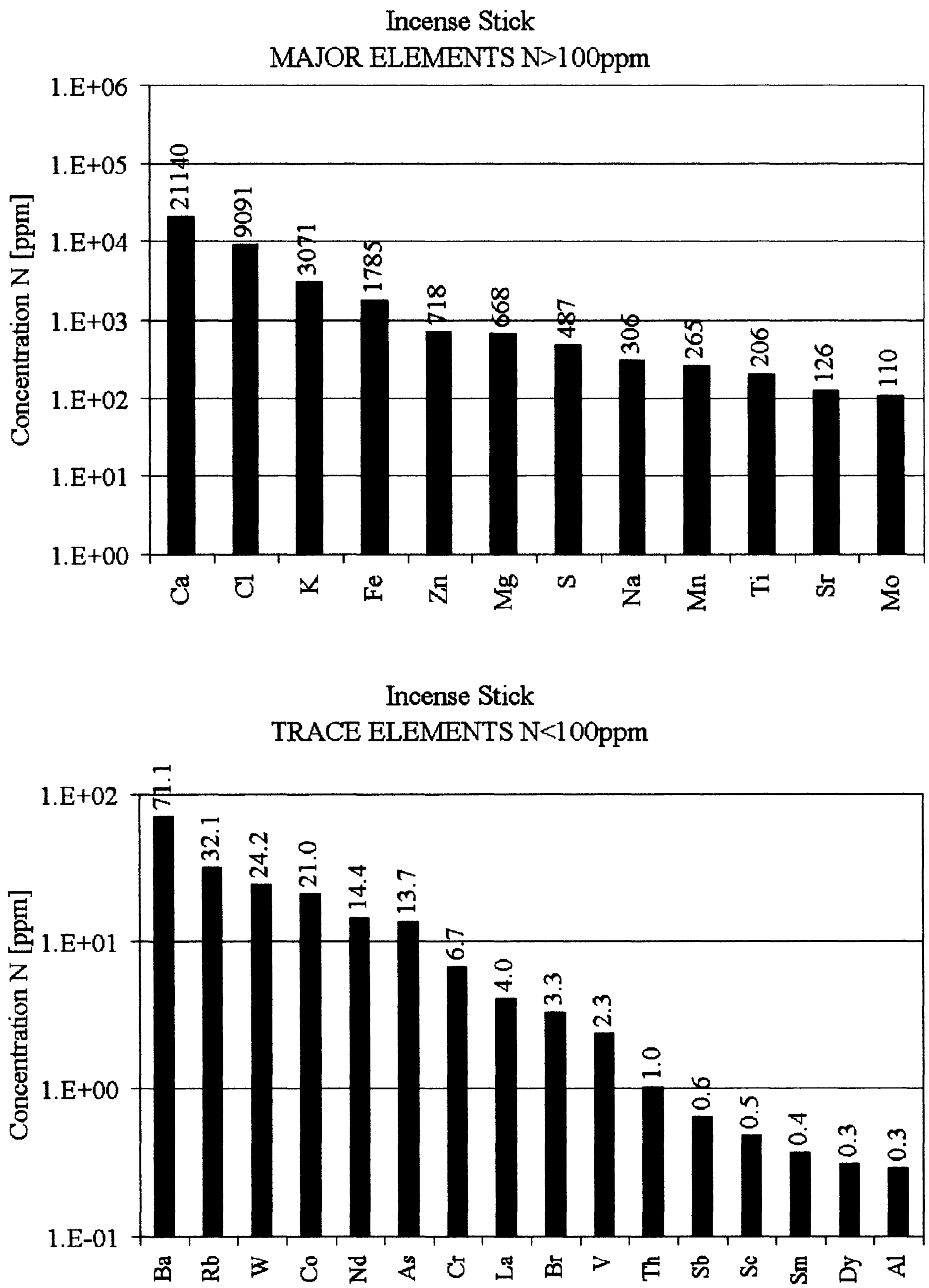

Figure A.4 Major and trace elements in incense stick.

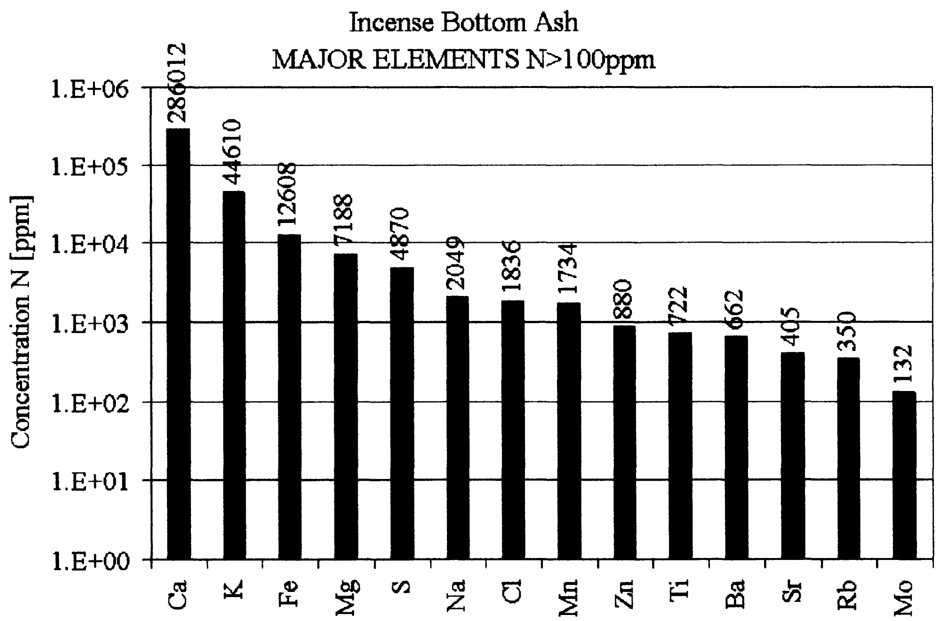

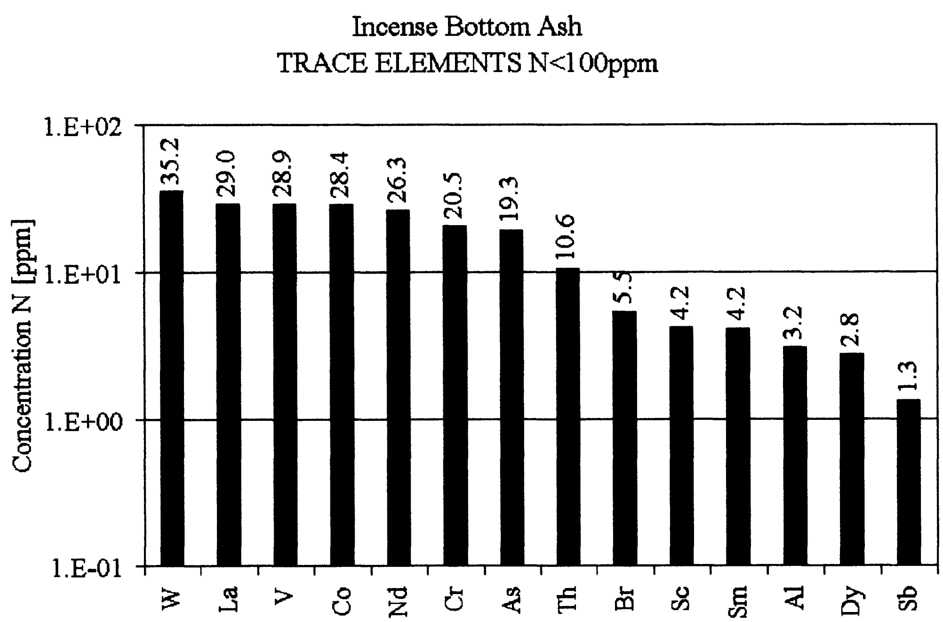

Figure A.5 Major and trace elements in bottom ash

A2.3 Particle Shape and Size Distribution

During the combustion of the incense stick, fine and coarse particulate matter are generated. The two populations have generally distinctly different physical characteristics and chemical composition.

As shown on Figures A.6 and A.7, the incense stick and the bottom ash consist of a solid particles of various shapes and dimensions. Coarse particulate matter in the form of chain aggregates of solid spherical particles is usually formed by combustion of volatile substances.

Fine particulate matter of spherical shape consists of a solid nucleus or liquid droplets that are the water solution of sulphuric or other acid. Zukeran et al. [157] observed that the fine particulate matter entering an ESP consists of solid spherical particles of dual distribution with peaks around *0.5* and *1.5* μm, as shown in Figure A.8. Unfortunately, liquid particles smaller than 0.1 μm lose their identity when analysed by SEM, therefore CNPC and ESEM was used. The CNPC study of ultrafine particles agrees with Zukeran et al's study [157] showing a peak around *0.05-0.08* μm. The evidence of liquid particles can be found in the form of sticky residue on collecting plates, together with solid particles as shown in figures A9 and A12. Digital images of a dust layer at collecting electrodes show that the collected spherical particles form a chain like structure as long as *2 mm*, as shown on figures A11 and A12. The chain growth direction is normal to the surface of the electrode.

However, SEM pictures of particles collected from the bottom support rack indicates that coarse particles bigger than 2 μm of a non-spherical shape are created by surface reaction as shown on the Figure A.13.

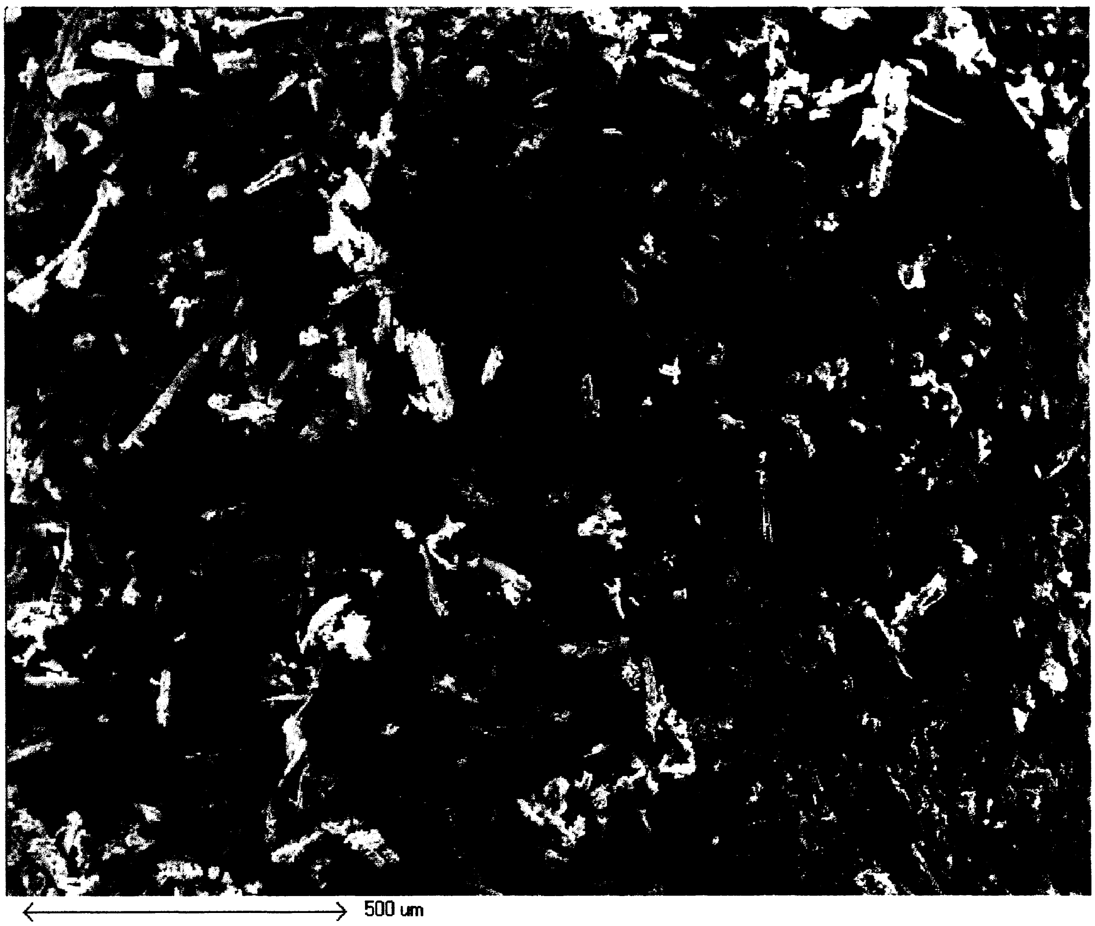

Figure A.6 SEM pictures of surface of an incense stick.

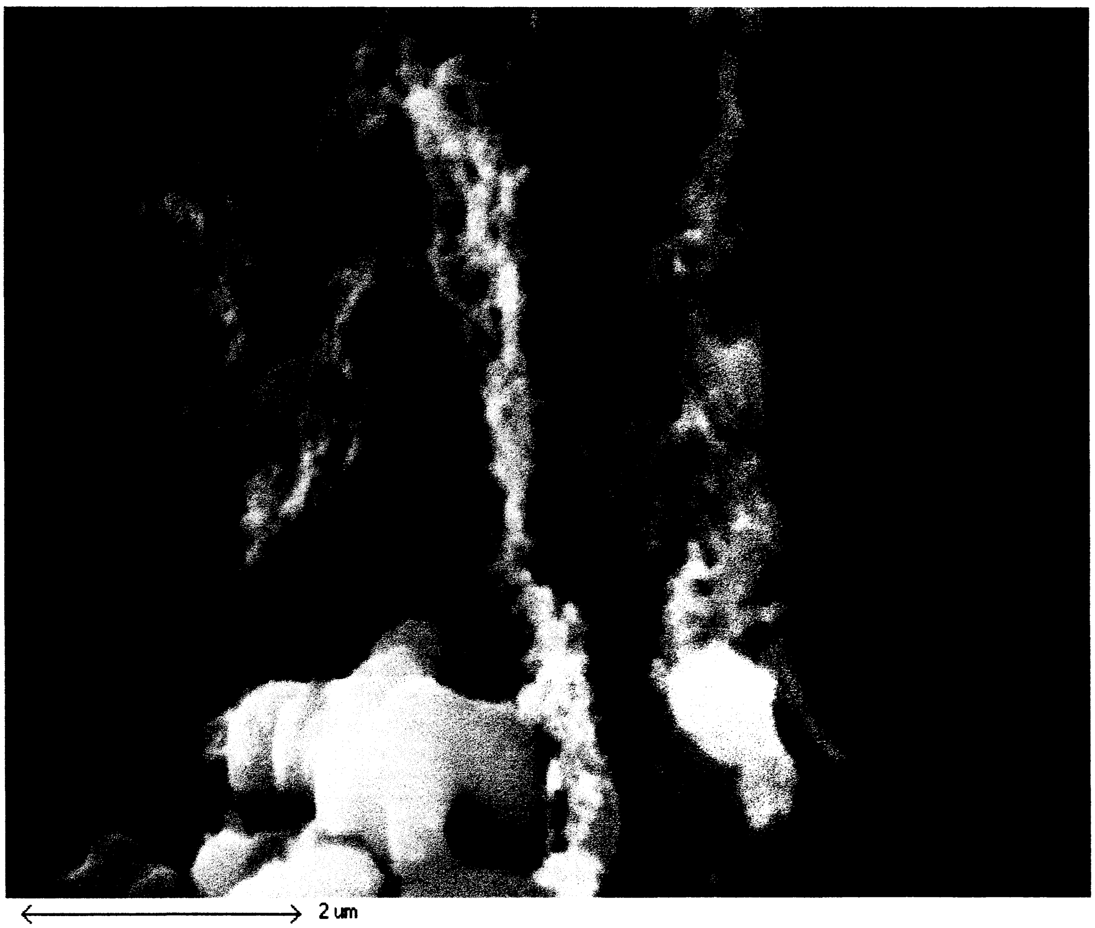

Figure A.7 SEM pictures of a bottom ash .

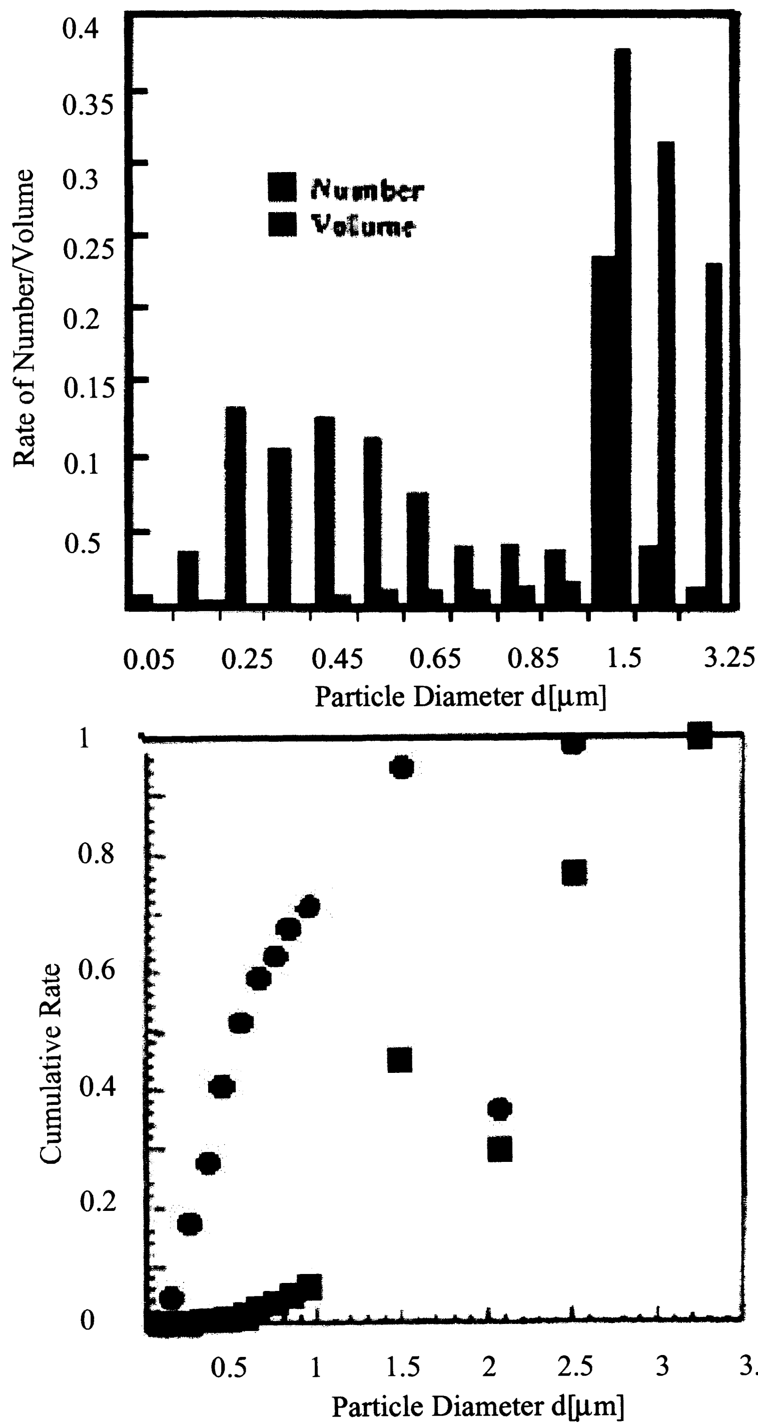

Figure A.8 Characteristics of Aerosol particles entering ESP by SEM: (a) size Distributions, and (b) cumulative rate Zukeran et al. [157]

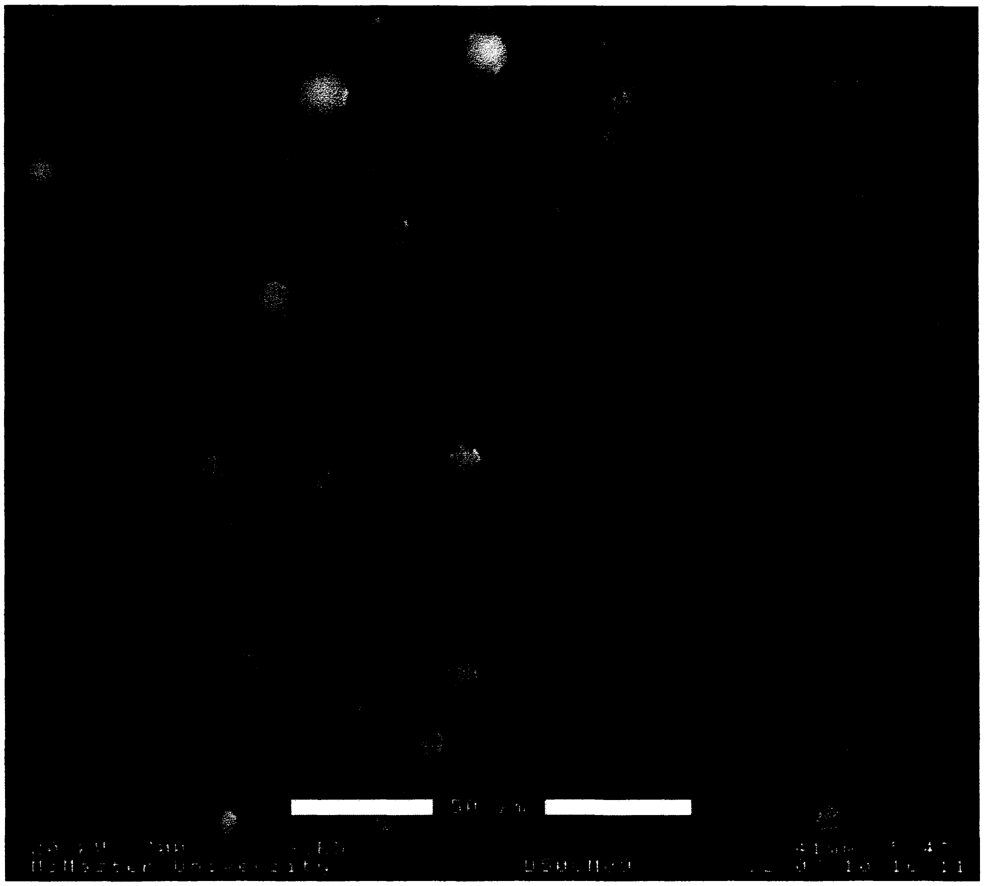

Figure A.9 ESEM pictures of collected dust particles for a spike-plate electrode arrangement in the area of spike projection

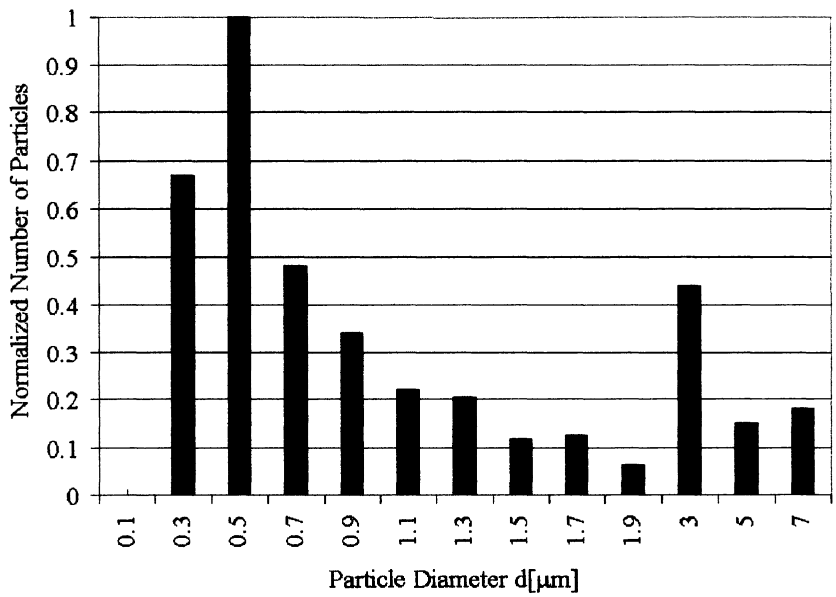

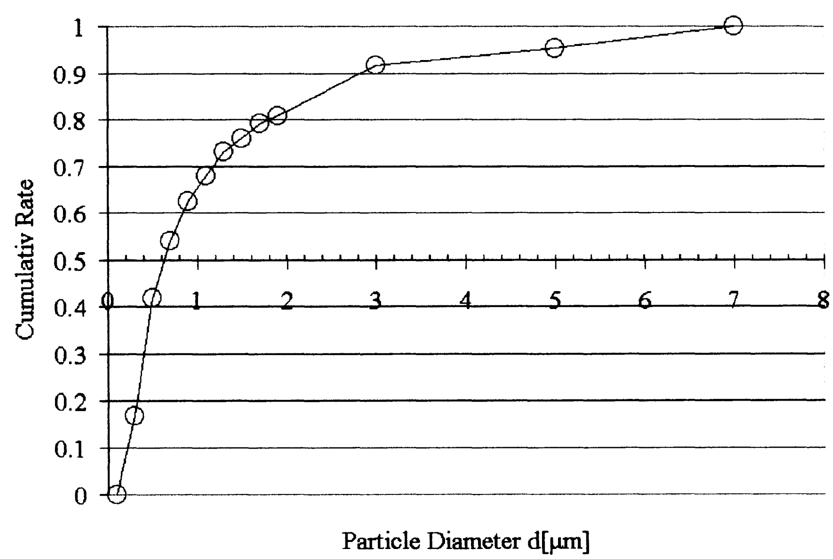

Figure A.10 Dust Size Distribution of ESEM image: (a) Particle size histogram, and (b) Cumulative rate of dust particles.

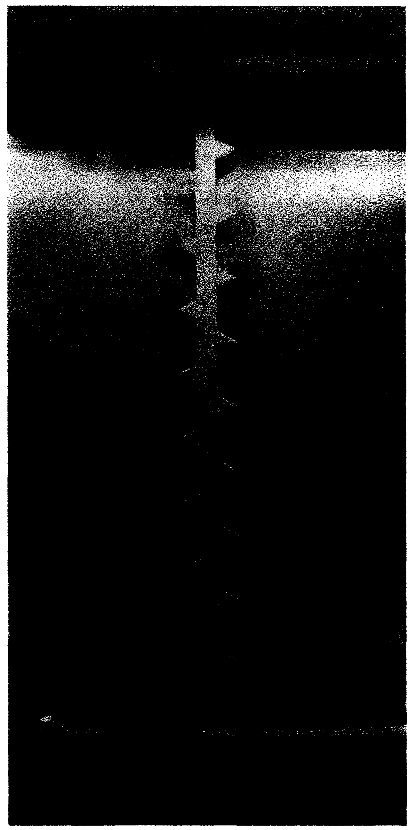

Figure A.11 Digital image of a collected plate after 6h of operation with spiked discharge electgrode.

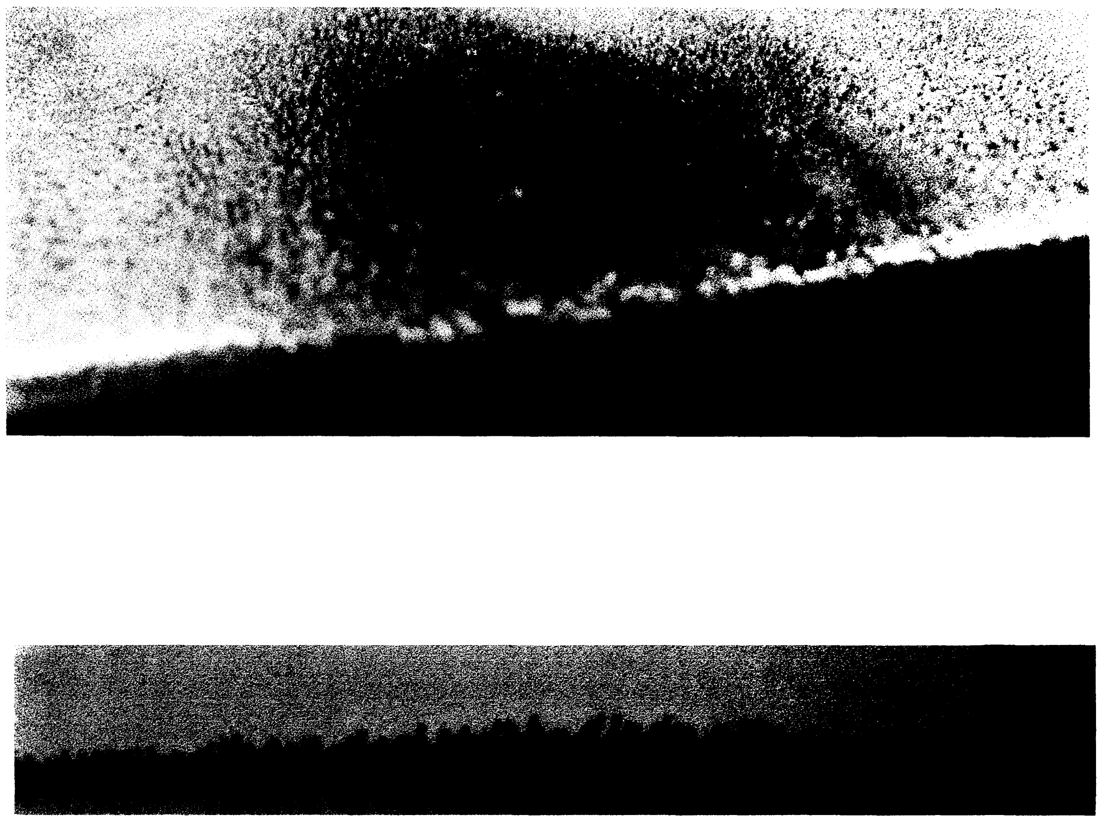

Figure A.12 Digital images of collected particulate matter. Shown are: (a) the bottom section of the collecting electrode in a wire-plate electrode arrangement, and (b) side view of above section, showing agglomerated chain structures.

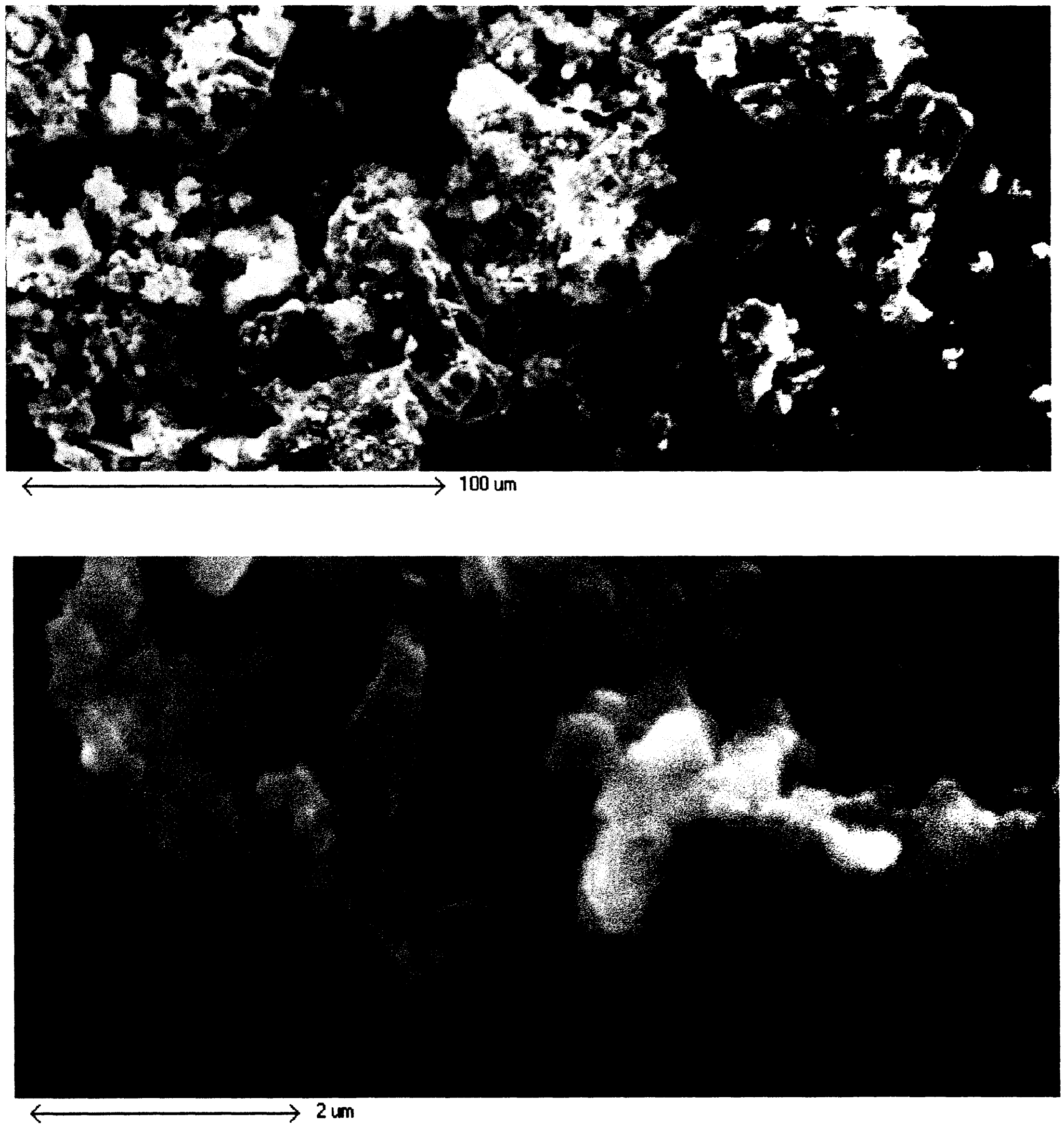

Figure A.13 SEM pictures of non-spherical particles from the bottom support rack. (a) bar indicates 100 micro metre, (b)) bar indicates 2 micro metre.

A3 MEASUREMENTS OF CURRENT –VOLTAGE CHARACTERISTICS

Corona discharge current and voltage were measured by analogue meters on the power supply side. Various discharge electrodes were tested, placed between collecting electrodes. Collecting electrodes were of *0.1015 m* and *0.2035 m* in length. The main gas flow was varied from still air conditions to the flow rate condition of $21\ m^3/h$.

A3.1 Current–Voltage Characteristics of Various Discharge Electrodes

Experimentally obtained results for various discharge electrode geometries are plotted in Figure A.14. The surface condition and dimensions of discharge electrode determine the form of the corona discharge. The corona discharge on very thin wire starts in the form of "corona tufts" and then develops into an unsteady corona as the voltage level increases. Negative glow corona along the whole length of the wire was observed only on new wires with clean surface. When displaying in square root of current per unit length versus applied voltage, the current-voltage characteristic of very thin wires can be approximated by a straight line. The corona discharge on rod-type discharge electrodes started as a local tuft corona. As the voltage level was increased, the corona discharge developed into a rapidly moving corona along short sections interrupted by localised tufts caused by electrode surface imperfections. The current-voltage characteristic, displayed in a square root of current per unit length versus applied voltage, has discontinuity. Therefore, it can not be approximated by one straight line, but with a series

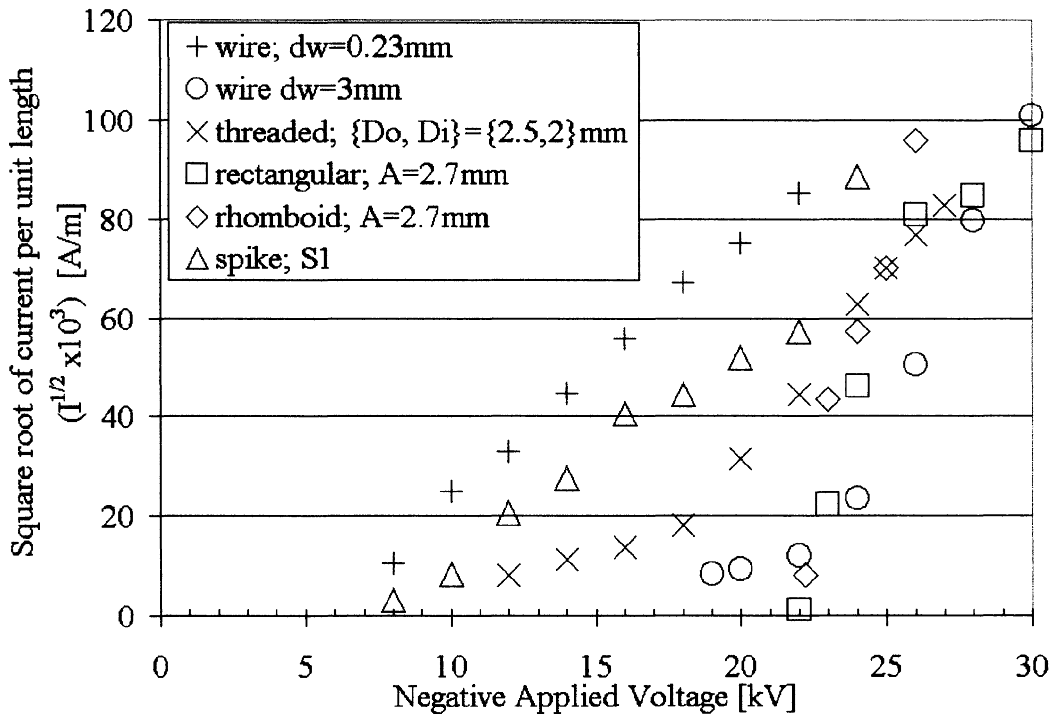

Figure A.14 Measured I-V curves for various discharge electrodes placed in the centre of 0.1015 m ESP field.

of two lines. The spike-type discharge electrode combined the electrical advantages of thin wire, low corona-onset voltage and high spark-over voltage, and the mechanical advantage of the rod type, rigid construction. Discharge spots were localized at the spike surface for a wide range of voltages. When spike-to-spike distance was high, rapidly moving corona was observed between the spike at higher voltages. The current-voltage characteristic of spike-type electrode has two discontinuities. The first discontinuity was around *-16 kV* and second one was around *-24 kV*. The first discontinuity occurred at a voltage level for which two visual discharge spots on the surface of the spike were registered. The second discontinuity occurred at a voltage level for which additional corona discharges between spikes were initiated. The effect of collecting electrode length on the current-voltage characteristic is shown in Figure A.15. Compared to the short collecting electrode characteristic, the current voltage characteristic of a spike electrode with long collecting electrode has a higher discharge current and sparking voltage. The experimental results show also different degrees of discharge current response to gas flow for spike-type electrodes, as shown in Figure A.16. Compared to the stationary conditions, discharge current and sparking voltage increase with the increasing gas flow velocity due to ion transport and effective electrode cooling by the gas flow. The sparking voltage may increase, due to the loss of charge from the current channel by convective charge transport [149-150,158-159].

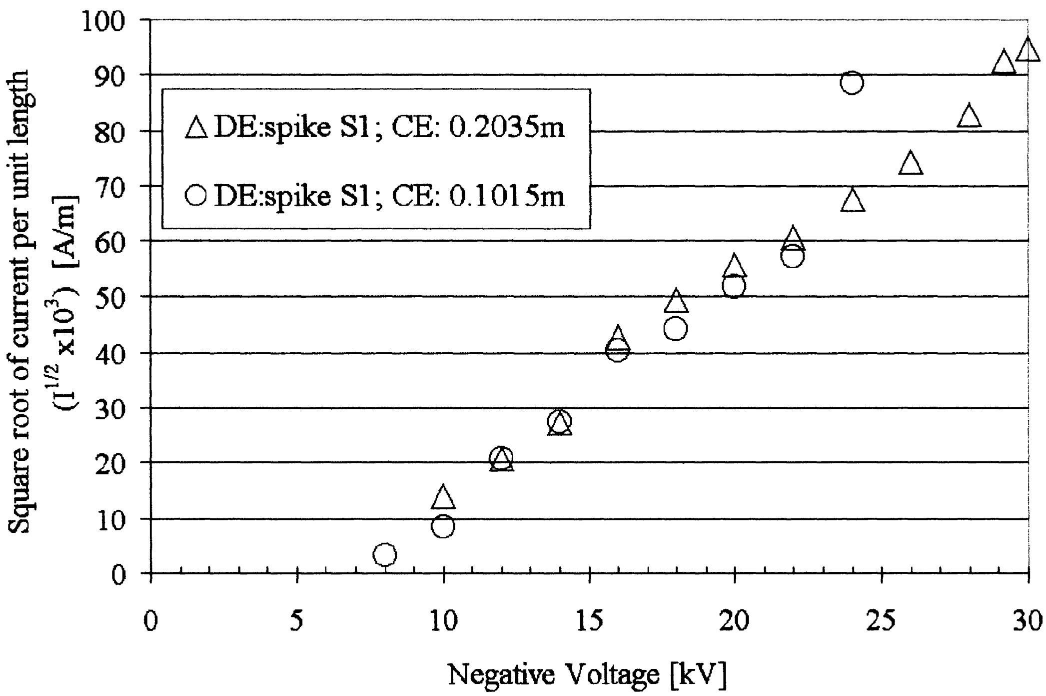

Figure A.15 Measured I-V curves for spike-type discharge electrode placed in ESP field of *0.1015 m* (short) and *0.2035 m* (long) in length.

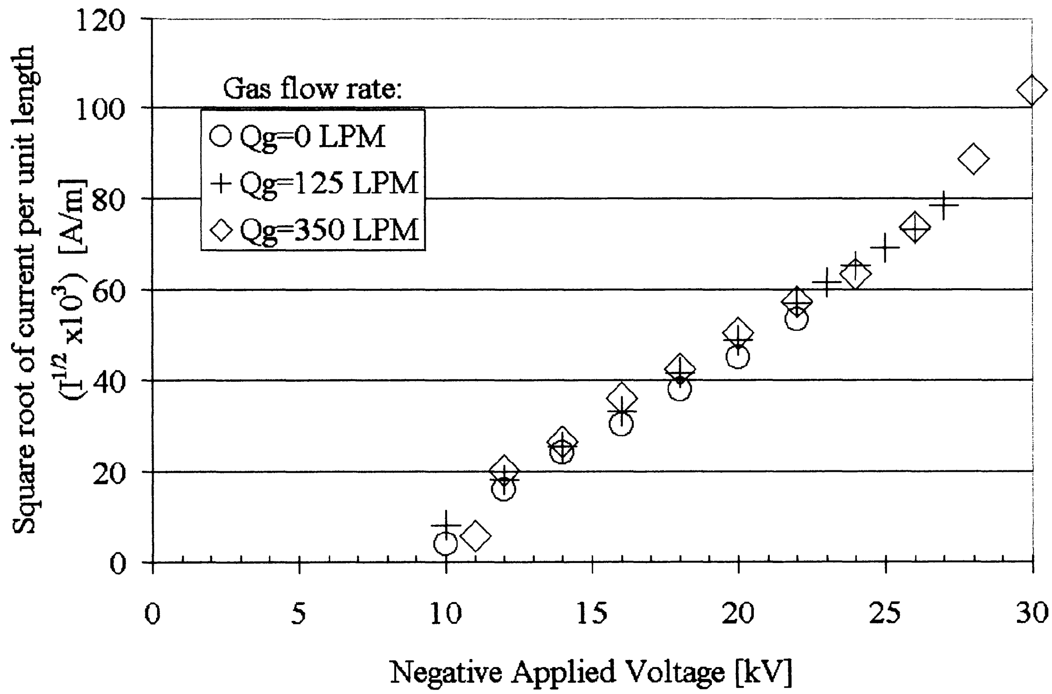

Figure A.16 Effect of gas flow on I-V characteristic for spike-plate ESP geometry

A.3.2 Discussion and Numerical Validation

Figure A.17 shows the comparison between experimental and predicted I-V curves for round and spike type discharge electrode geometries. From the experimental validation of current-voltage characteristics the following was concluded: The surface condition factor m_G for thin and thick wires is *0.9*. For larger wire diameters with rough surface condition, the factor may reduce to *0.85*. The threaded wire geometry can be modelled by the mean thread diameter and a surface condition factor of *0.55*. The rectangular discharge electrode and its orientation were successfully modelled by side length. The geometry correction coefficients k_G' of aligned and rotated rectangular electrodes are $k_G'=7$ and $k_G'=9$, respectively. The surface condition of spikes and their spacing are very important. Namely, the slope change of current-voltage characteristics coincides with appearance of dual discharge points on the surface of the spike at approximately *-17 kV* and initiation of corona discharge between spikes at *-24 kV* for the spike S1 electrode placed in a short *(0.1045 m)* ESP field.

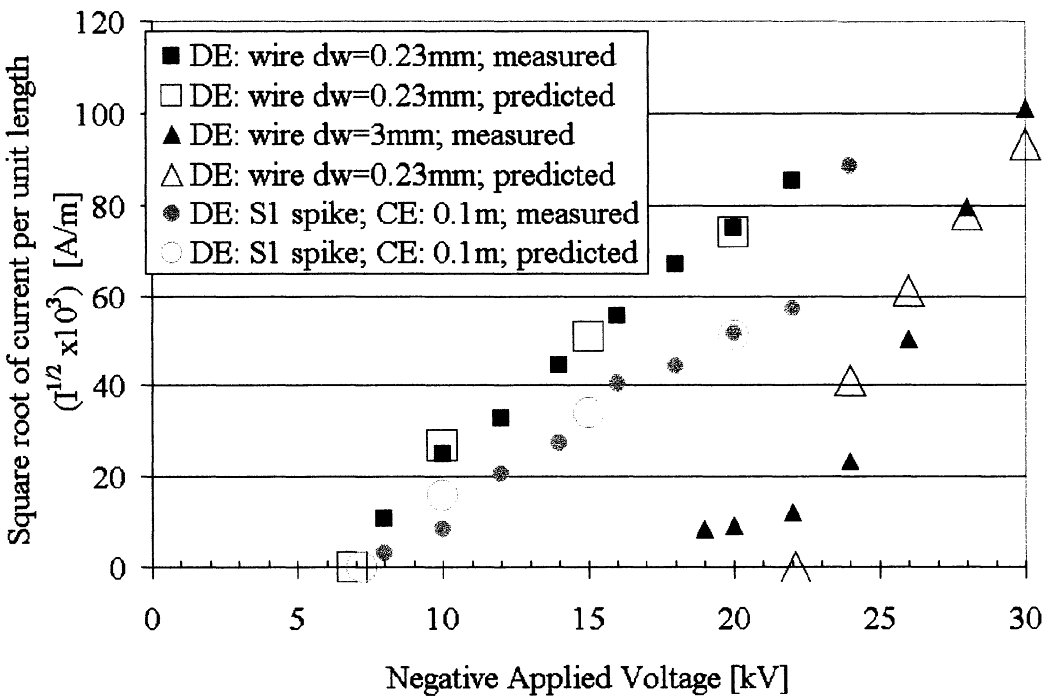

Figure A.17 Comparison between measured and predicted I-V curves for wire and spike type discharge electrodes. Collecting electrode length is *0.1015 m*.

A.4 MEASUREMENT OF CURRENT DISTRIBUTION ON THE COLLECTING PLATE FOR VARIOUS DISCHARGE ELECTRODES

The goal of this experiment was to determine indirectly the boundary condition of negative ions on the collecting electrode by measuring the current density distribution near the collecting electrode surface.

A.4.1 Experimental Set-up

The experimental set-up is shown in Figure A.18. It is composed of the laboratory-scale electrostatic precipitator, disk-type current probe, and electro-metre. Various discharge electrode types were placed between collecting electrodes. The experiment was performed in still air under negative corona. The current probe was placed on the movable rack parallel with the surface of the collecting electrode. The movable rack allowed for the fine position steps in horizontal and vertical direction.

A.4.2 Current Distribution on the Collecting Electrode for Various Discharge Electrodes

Figures A.19 and A.20 show current distributions near the collecting electrode surface for the spike-type discharge electrode. High current densities were observed near the projection of the spike tip. The current distribution is symmetrical with respect to the horizontal line passing through the spike tip, as shown in Figure A.19. Low current densities were observed in the regions between spikes and parallel with the

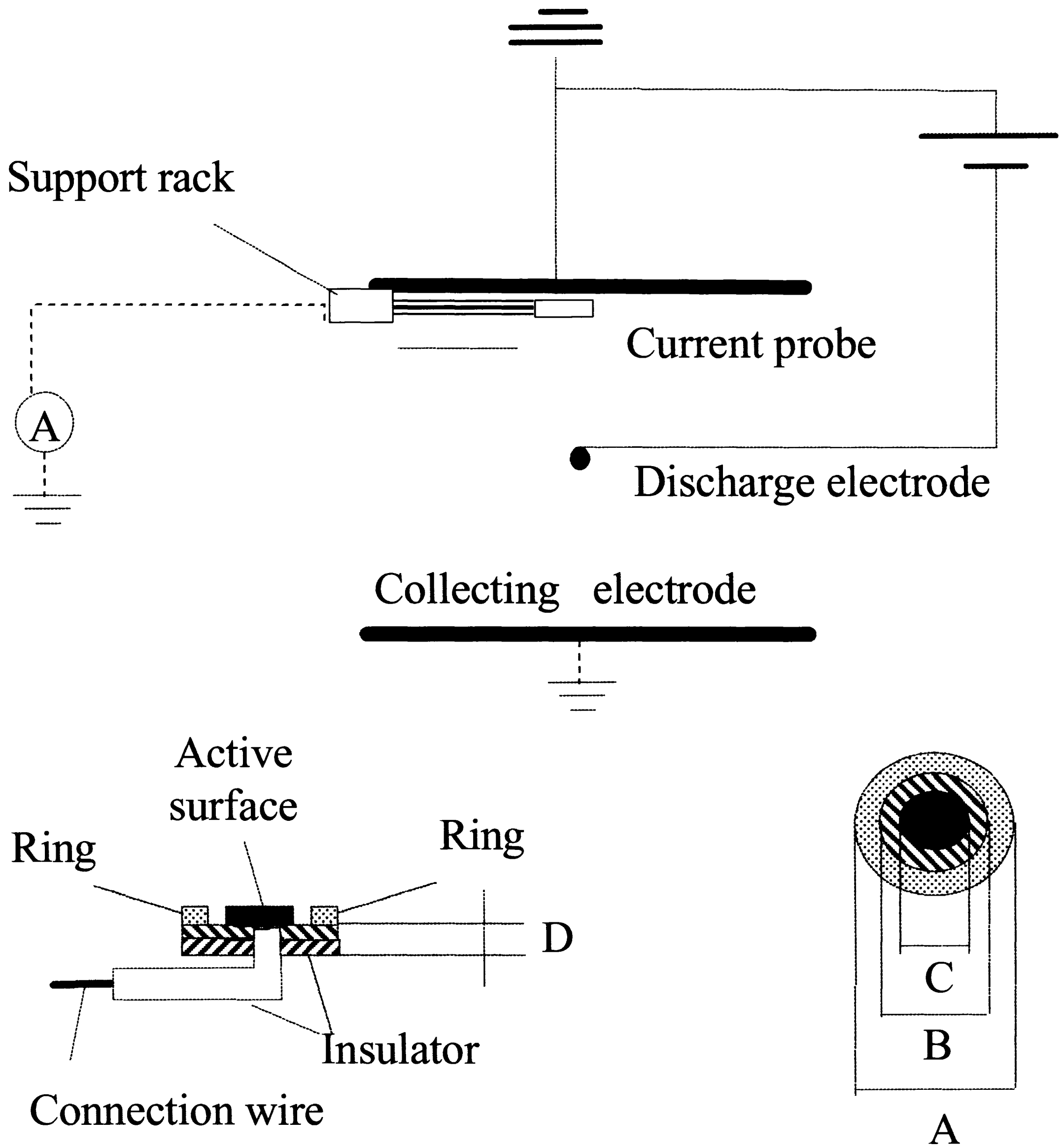

Figure A.18 Schematic diagram of: a) the experimental set-up, and b) disk-type current probe (*A=6.86 mm; B=4.59 mm; C=3.33 mm; D=1 mm*)

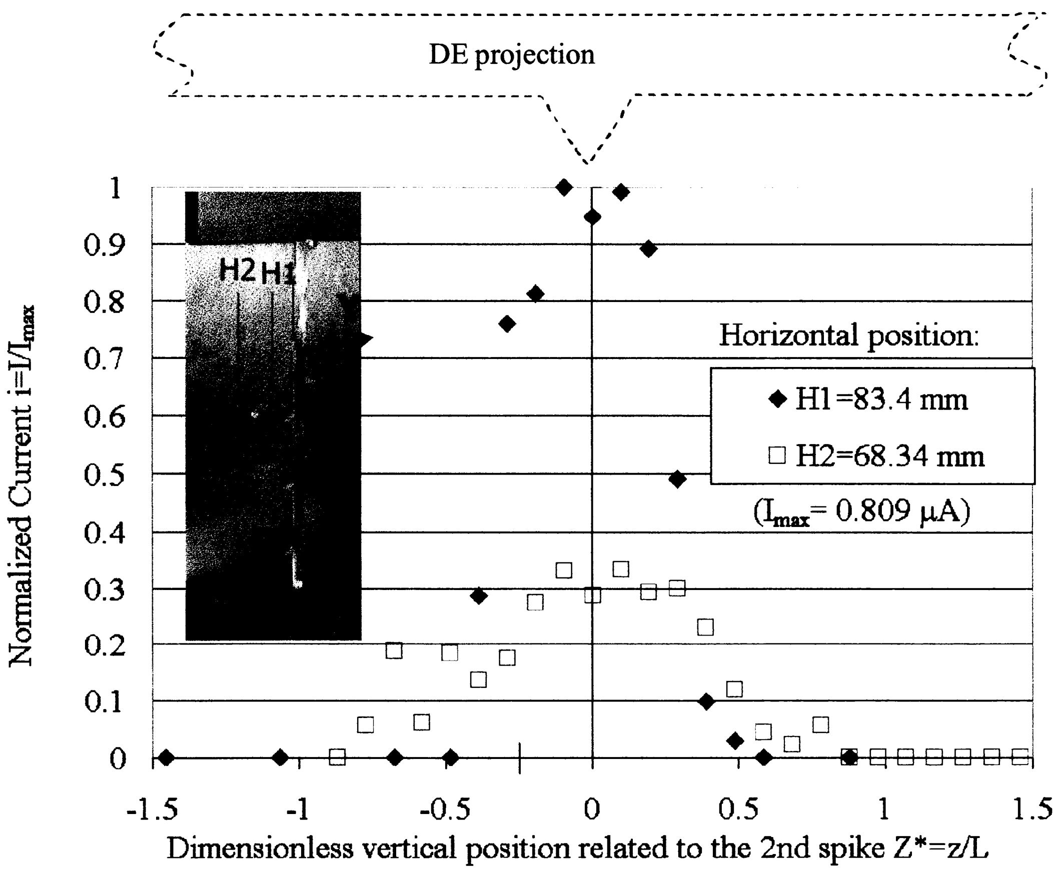

Figure A19 Normalized current along two vertical lines near the collecting electrode surface

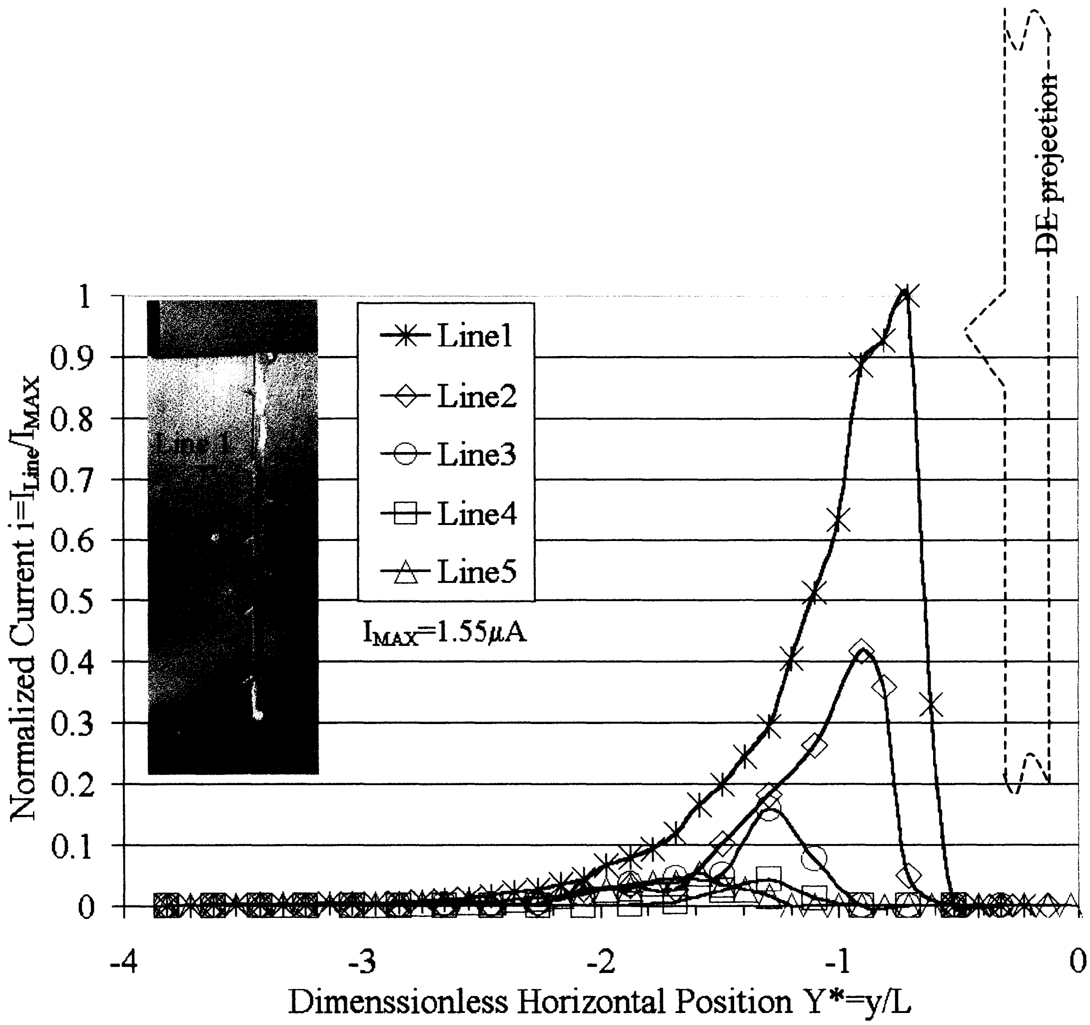

Figure A.20 Normalized current along five horizontal lines near the collecting electrode surface

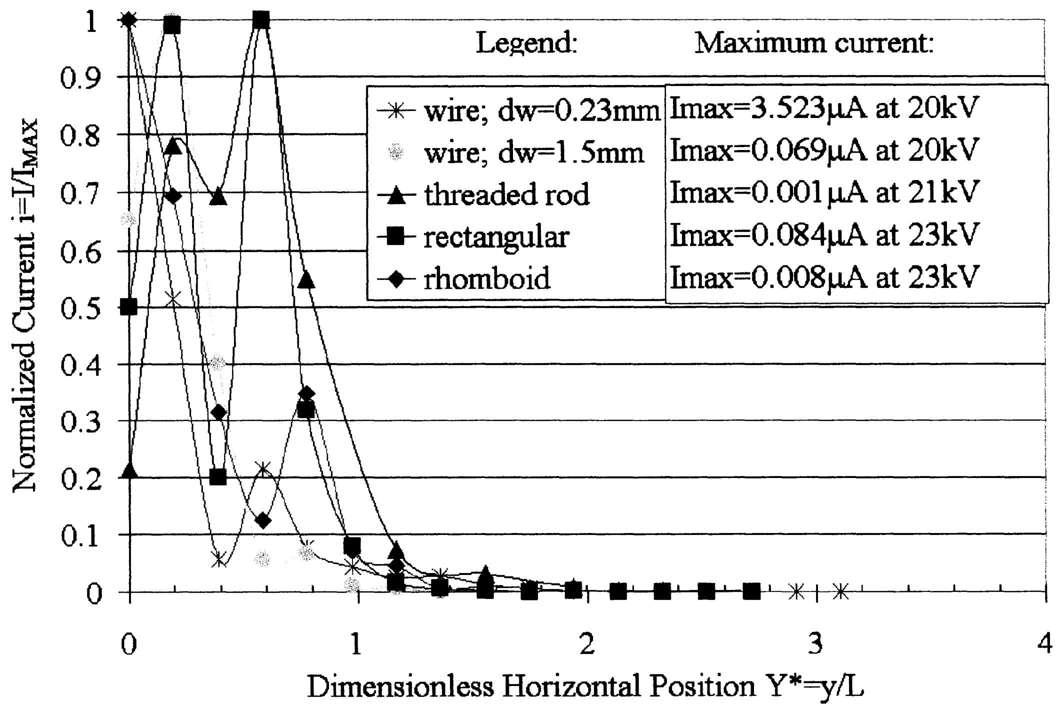

Figure A.21 Normalized current for various discharge electrode types near the collecting electrode surface discharge electrode, as shown in Figure A.20. Due to the staggered arrangements of the spikes, the current distribution is not symmetrical with respect to the vertical line that is passing through the centre of the electrode. Current distributions near the collecting electrode surface for other discharge electrode geometries are shown in Figure A.21. Thin wire, rod and spike electrodes were tested at *-20 kV*. Rectangular electrodes and threaded wire could not be tested at higher voltages due to the sparking.

A.4.3 Discussion and Numerical Validation

Comparisons between current density experiments and approximated functions for thin-wire, rod and spike type discharge electrodes are shown on the Figure A.22. The current distribution curve of the spike electrode shows very good agreement with the experimental results from Ohkubo et al. for a rod-needle–type discharge electrode [61]. However, the results of the thin wire experiments deviate from Warburg's current distribution [90, 160], probably due to the probe interference. The maximum of the current distribution of the rod type discharge electrode is shifted with respect to the projection of the centre of the electrode, due to the position of the local discharge that is not constant along the circumference of the electrode. Therefore, Warburg's and Ohkubo's current distribution law [90] are used for the thin-wire and rod-type discharge electrodes.

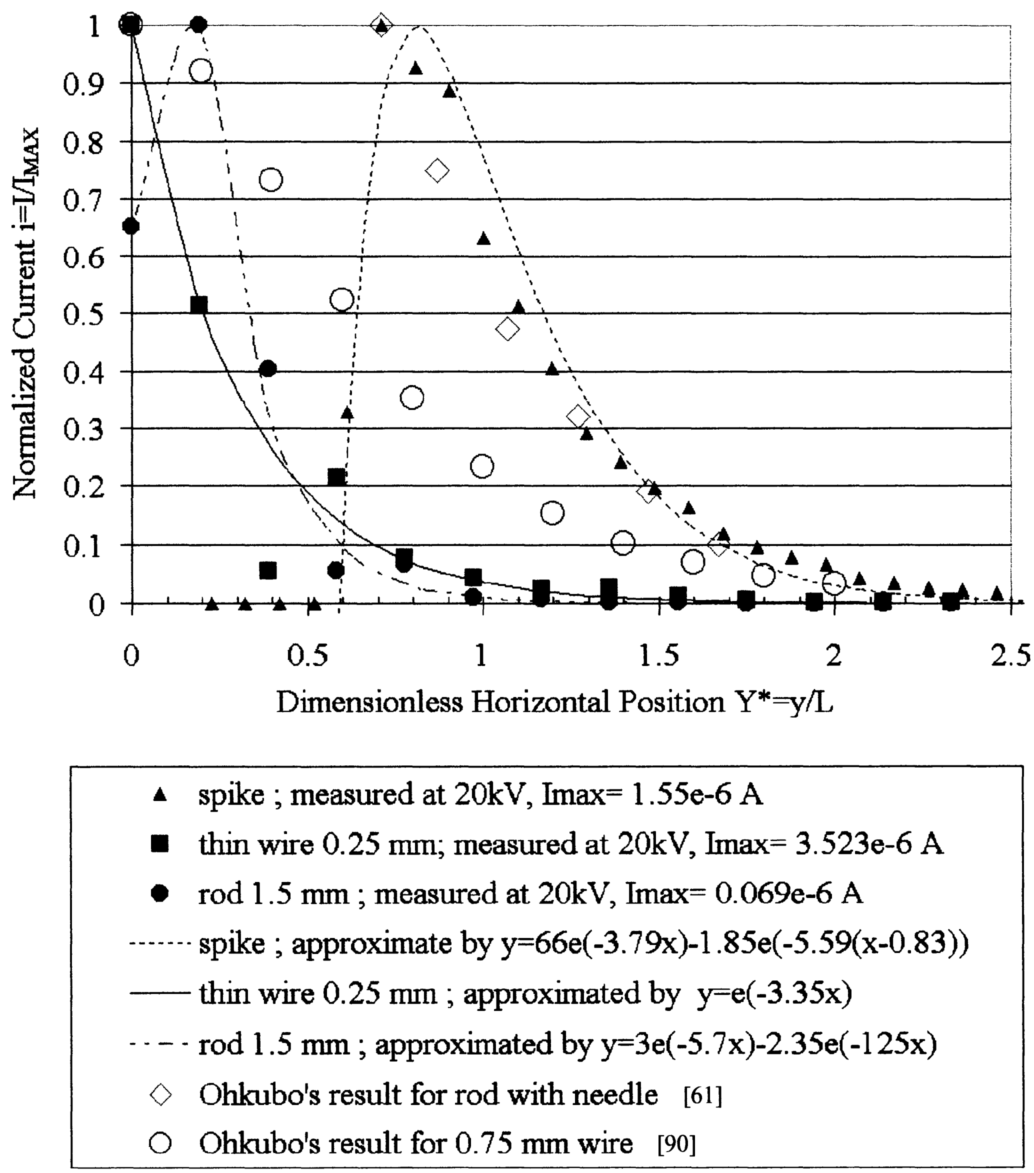

Figure A.22 Approximate current distribution near the collecting electrode surface for various discharge electrode types

A.5 MEASUREMENT OF LIGHT EMISSION FROM DISCHARGE ELECTRODES BY OPTICAL SPECTROMETRY AND DIGITAL IMAGE ANALAYSIS

The goal of this experiment was to link the optical emission at certain wavelengths to the concentration of ions and electrons, in order to determine boundary conditions on the discharge electrode surface. Namely, it was visually observed that the light emission pattern from the surface of the spike-type discharge electrode varies with applied voltage from one to two-discharge spots. Additionally, some preliminary numerical simulation of ion density distribution showed that the boundary conditions on the discharge electrode have a significant effect on the current density distribution on the collecting plate. Since a digital camera or an eye can register only visual spectra (ranging from *400 nm* blue to *700 nm* red), optical spectroscopy was used to determine the optical emission of lower wavelengths. Additionally, the digital image of the corona discharge was compared to visible wavelength spectra from the optical spectrometry system to indicate any possible errors due to the optical probe dimension.

A.5.1 Experimental Set-up

Figure A.23 shows a schematic diagram of the experimental set-up. It is composed of the bench-scale electrostatic precipitator, optical spectrometry system and digital camera. The experiment was performed under negative corona, where the light emitted from the discharge electrode was sent via single strand optical fibre to the

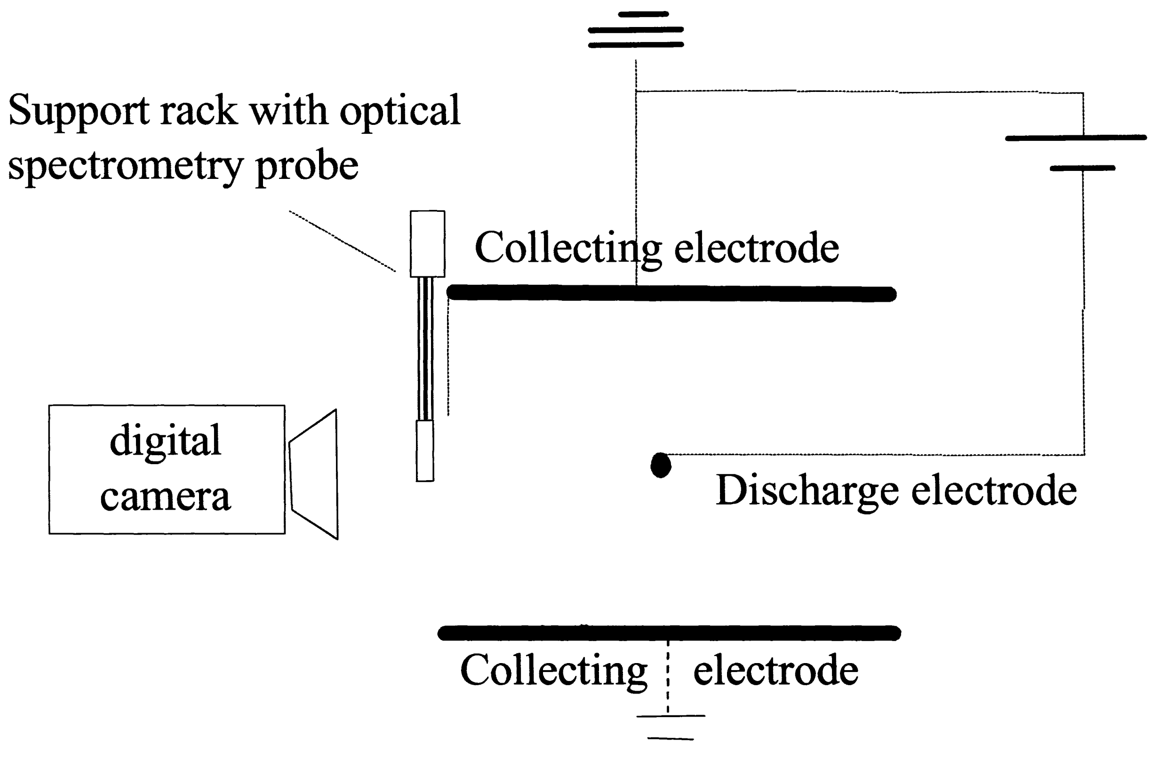

Figure A.23 Schematic diagram of the experimental set-up for measurement of light emission during corona discharge spectrometer card that was connected to the personal computer. The sampling rate was set to *1 kHz* with an integration time of approximately *4s*. Optical fibre with SMA termination, *5 mm* in diameter, was used as a probe. The probe was mounted on the movable rack with fine position steps of half a millimetre in horizontal and vertical direction. For each position, three data sets were recorded. Then, the light intensity of the averaged data set was analysed. The wavelength and corresponding state of gas molecules or gas ions were determined. After that, the normalized intensity profile was used to set the negative ion density profile on the surface of various type of discharge electrodes. Additionally, the digital image of the corona discharge was compared to visible wavelength spectra from the optical spectrometry system. A digital image was used to determine the number of corona discharge spots. The camera was placed approximately one and a half metres in front of the discharge electrode.

During the corona discharge, the nitrogen molecules are transferred from the ground state into an excitation or ionic state in collision with the energetic electrons. After that the excited and ionized molecules transit into their ground state by emitting radiations of specific wave length. The emitted spectral line contains the information of the electron energy and density. Spectral emission lines in air mainly originate from nitrogen molecules. For example, the nitrogen molecule can be transferred from the ground state $N_2(X^1\Sigma_g^+)$ into $N_2(C^3\Pi_u)$ excited state by the impact of electrons with energy greater than $11\ eV$. In the process of radiative emission the $N_2(C^3\Pi_u)$ will transfer into $(B^3\Pi_g)$ state by emitting a photon of the $337.1\ nm$ wavelength. If electrons have an energy greater than $18.7\ eV$, nitrogen ions will be produced $N_2^+(B^2\Sigma_u^+)$, that will release a photons of *391.4 nm* wavelength by transferring into the $N_2^+(X^2\Sigma_g^+)$ state. Typical emission spectra measured near the discharge electrode with indicated emission spectral line of N_2 second positive band and N_2^+ first negative band are shown in Figure A.24. Other emission spectra are sometimes ambiguous due to the overlapping with other bands. Some candidates for other emission bands are shown in Table A2.

Table A2. Candidates for vibration transitions [161-168]

Experiment		**Candidates**				
Wave Length	**Intensity**	**Wave Length**	**Molecule**	**Type**	**System**	**Appearance**
318.57	**120.2**	316.19	N_2		Goldstein-K.	Degraded to red
		315.93	N_2	9(1,0)	2nd Positive	Degraded to red; Close tripleheader
		321.08	O_2^+	8(2,6i)	2nd Negative	Degraded to red Double headed
		321.1	O_2		Herzberg I	Degraded to red
		323.2			Schummann-R	
		318.88	O_3	Other peaks 320.6;320.1;319.48; 318.15;317.16;316.26		
340.37	**379.4**	***337.13***	$\boldsymbol{N_2}$	***10(0,0)***	***2nd Positive***	***Degraded to red***
		339.78	O_2^+	8(0,6i)	2nd Negative	Degraded to red
		342.12		8(0,6ii)		
		341.62		2(2,7ii)		
		339.31		4(2,7i)		
		337	O_2	10(3,5)	Herzberg I	
		340.26	O_3	Other peaks:343.22;342,14;337.77		
356.45	**82.8**	***353.67***	$\boldsymbol{N_2}$	***8(1,2)***	***2nd Positive***	
		358.21	N_2^+	*9(1,0)*	*1st Negative*	
		356.39		*9(2,1)*		
		354.89		7(3,2)		
		354.2	O_2	8(3,6)	Herzberg I	
		359.45	O_2^+		2nd Negative	
		351.77				
360.87	**271.4**	***357.69***	$\boldsymbol{N_2}$	***10(0,1)***	***2nd Positive***	
		358.21	N_2^+	9(1,0)	1st Negative	
		359.45	O_2^+		2nd Negative	
		362.98		8(0,7ii)		
		360.37		7(0,7i)		
		363.3	O_2	8(3,6)	Herzberg I	

Table A2. (continued)

Experiment		Candidates				
Wave Length	**Intensity**	**Wave Length**	**Molecule**	**Type**	**System**	**Appearance**
378.46	**73.2**	***375.54***	***N_2***	***10(1,3)***	***2^{nd} Positive***	
		380.49		10(0,2)		
		378.28	N_2^+	8(18,15)	1^{st} Negative	
		376.16		10(20,16)		
		375.61		5(22,17)		
		379.2	O_2	(6,3ii)	Chamberlains	Tripleheader
		377.1		(6,3iii)		
383.38	**114.8**	***380.49***	***N_2***	***10(0,2)***	***2^{nd} Positive***	
		383.05	O_2^+	8(0,8i)	2^{nd} Negative	Double headed
		382.9	O_2	8(2.7)	Herzberg I	
		384		5(0,6)		
		385.79	N_2^+	4(2,2)	1^{st} Negative	
394.3	**14.2**	***391.44***	***N_2^+***	***10(0,0)***	***1^{st} Negative***	
		394.3	N_2	8(2.5)	2^{nd} Positive	
		398.5	O_2	6.4ii	Chamberlains	Triple headed
397	**24**	***399.84***	***N_2***	***9(1,4)***	***2^{nd} Positive***	
		398.5	O_2	6.4ii	Chamberlains	Triple headed
		393.8	O_2	7(1,7)	Herzberg I	
402.97	**37.6**	***405.94***	***N_2***	***8(0,3)***	***2^{nd} Positive***	
		403.1	O_2	6.4i	Chamberlains	Triple headed
		400.9		6.4ii		
		398.5		6.4iii		
		406.4		5(0,7)	Herzberg I	
408.93	**39**	***409.48***	***N_2***	***8(0,3)***	***2^{nd} Positive***	
		406.4	O_2	5(0,7)	Herzberg I	
		408.24	O_2^+	8(0,9i)	2^{nd} Negative	
		411.58		8(0,9i)		
430.45	**6**	***427.81***	***N_2^+***	***9(0,1)***	***1^{st} Negative***	
		430.9	O_2	7(0,8)	Herzberg I	
		432.6	O_2	(5,5ii)	Chamberlains	Triple headed
		431.7		(3.4iii)		
634.65	**9.2**	632	N_2		1^{st} Positive	Degraded to violet Triple headed
		630	O_2			Dimol emission
677.35	**17**	***670.48***	***N_2***		***1^{st} Positive***	

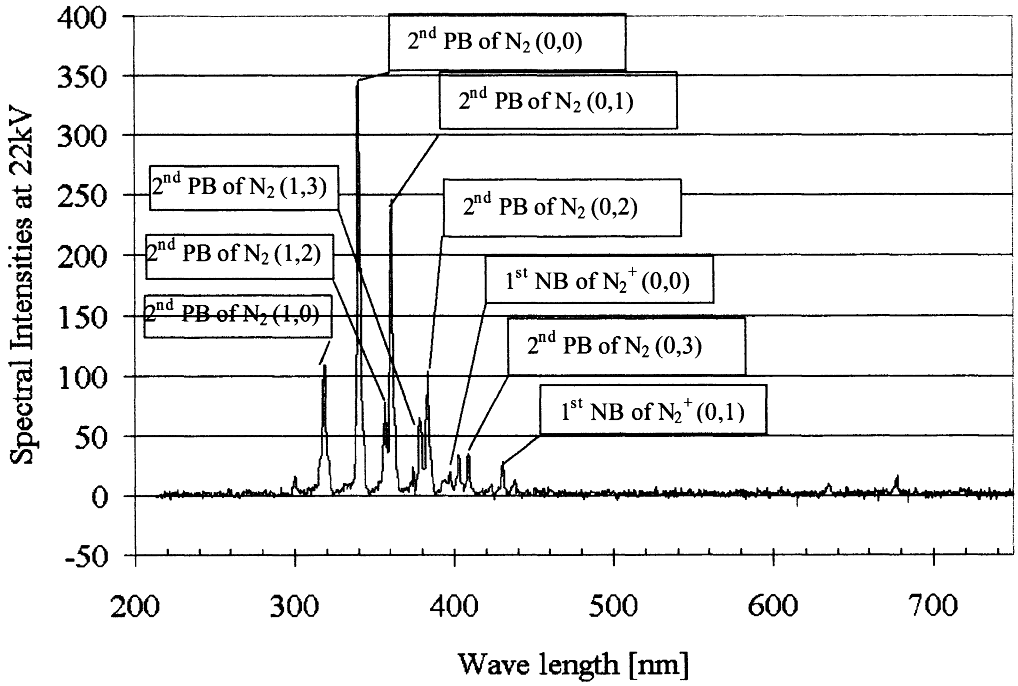

Figure A.24 Spectral Intensity at 22kV

A.5.2 Experimental Results for Spike-type Discharge Electrode

At first, the light intensity of various wavelengths at various voltages was determined. For this test, the position of the optical spectrometry probe was fixed with respect to the upper left edge of the second spike. There is almost a linear increase in light intensity with applied voltage up to *-24 kV*, after which the intensity is decreasing, as shown on the Figure A.25. The optical emission of *340 nm* wavelength (2nd positive band of nitrogen N_2 molecule) was used to determine the boundary conditions on the surface of discharge electrode. After that, the area around the second spike was mapped approximately *3 mm* in the horizontal and *1.5 mm* in the vertical directions from the centre of the spike.

Figures A.26 and A.27 show the horizontal profile of the normalized wavelength intensities of 2^{nd} positive band of nitrogen molecule at various vertical positions for *-15* and *-22 kV*. Both figures show a symmetrical profile around the maximum value. However, the actual location of the maximum of emission intensity at *-15 kV* is approximately *0.5 mm* shifted to the left of the centre of the electrode. The optical emission profile of the visual spectra at *-15* and *-22 kV* has different distributions than the 2^{nd} positive band of N_2 molecule, as shown on Figure A.27 and Figure A.29. The visual spectra by optical spectrometry and digital image analysis show similar profiles as shown on the Figure A.30.

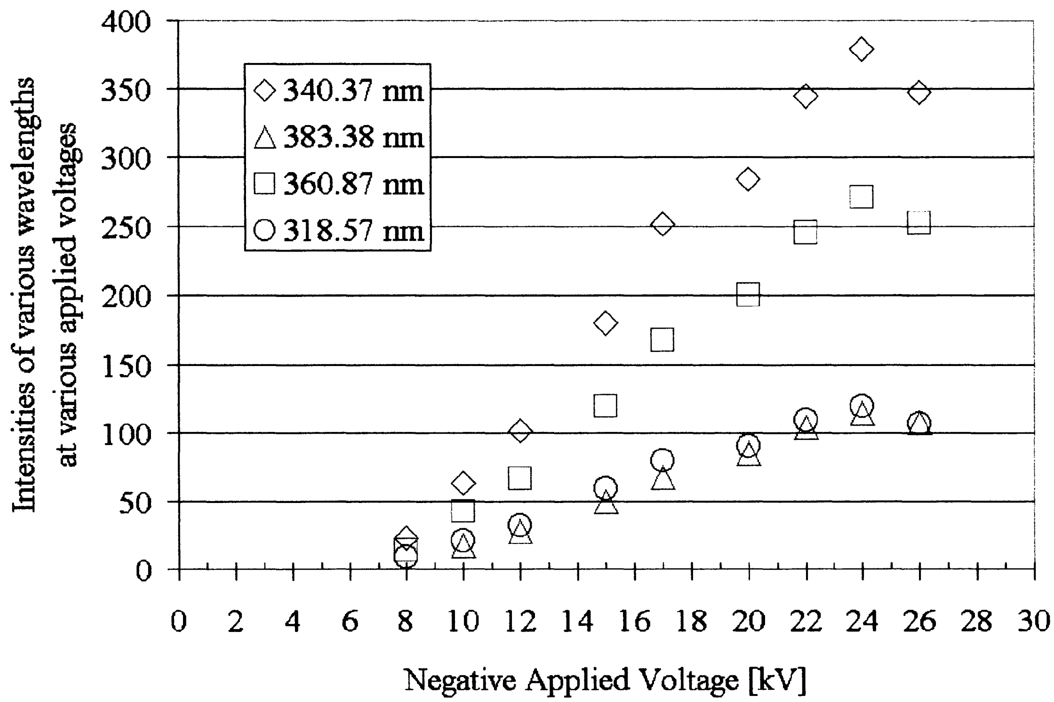

Figure A.25 Intensities of various wave length spectra. (Probe position was not at the point of maximum intensity)

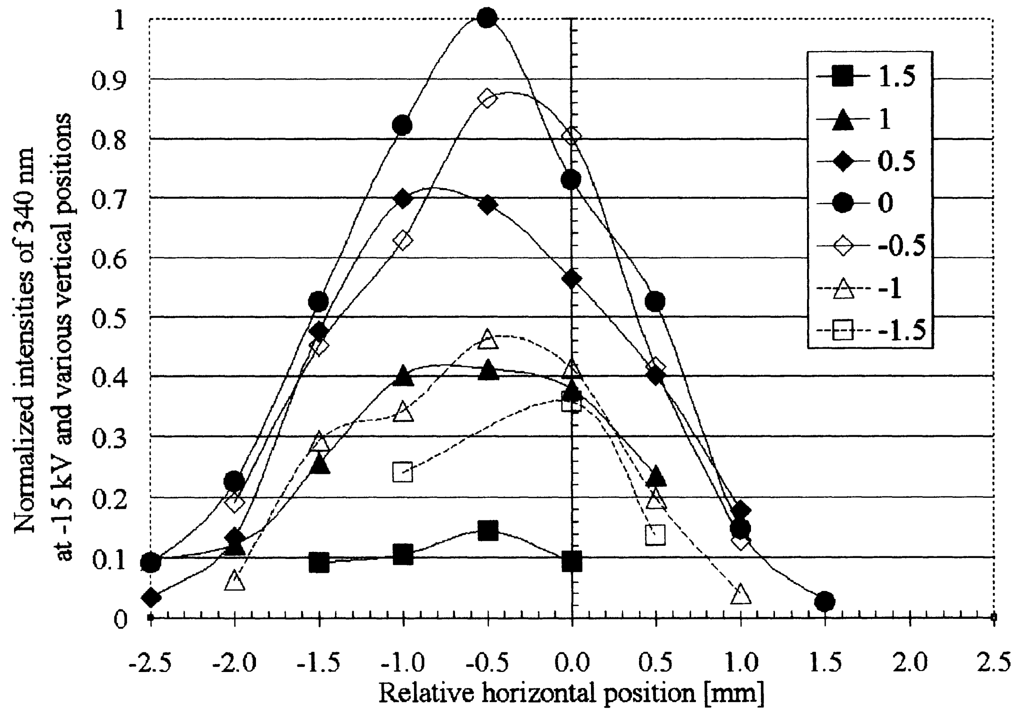

Figure A.26 Normalised intensities of the 2nd positive band of N_2 molecule at *15 kV*.

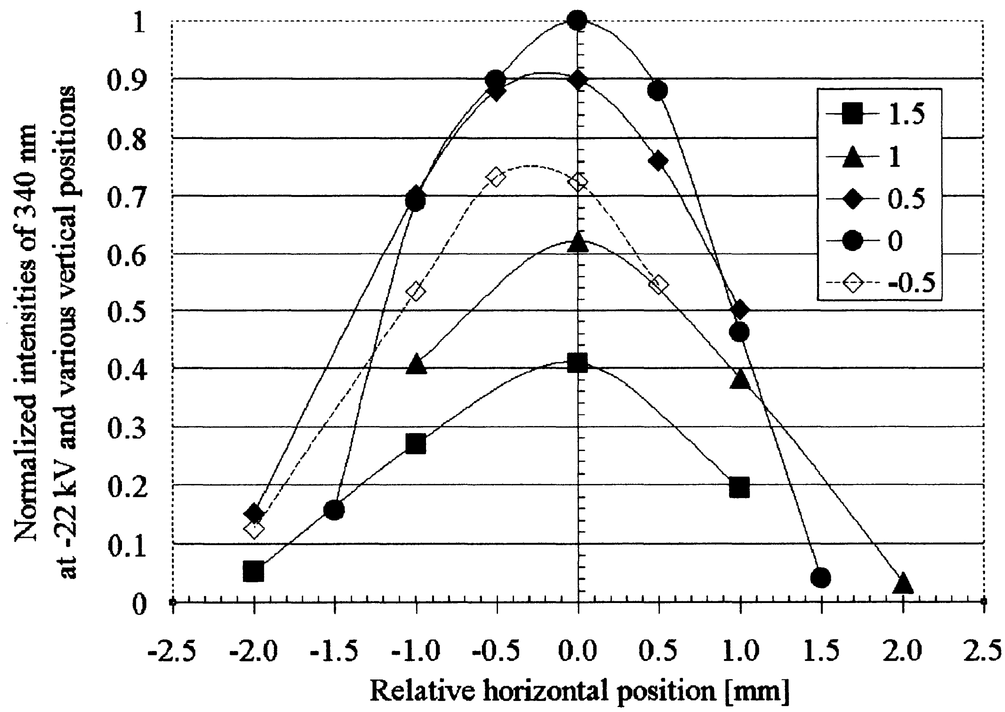

Figure A.27 Normalised intensities of the 2[nd] positive band of N_2 molecule at *22 kV*.

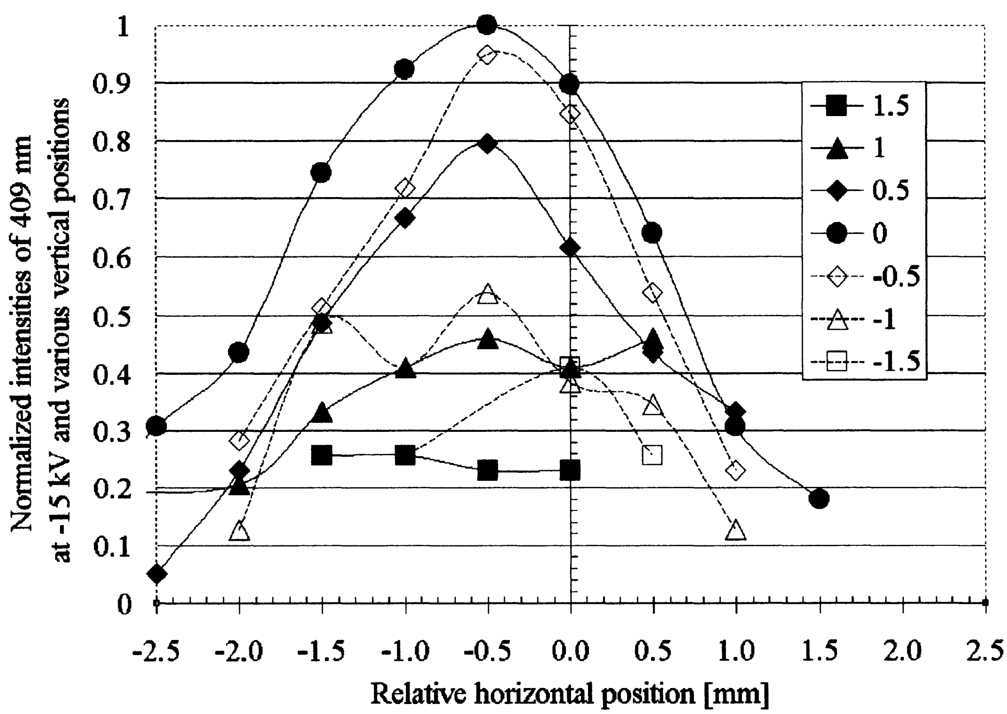

Figure A.28 Normalised intensities of visual wave length at *15 kV*.

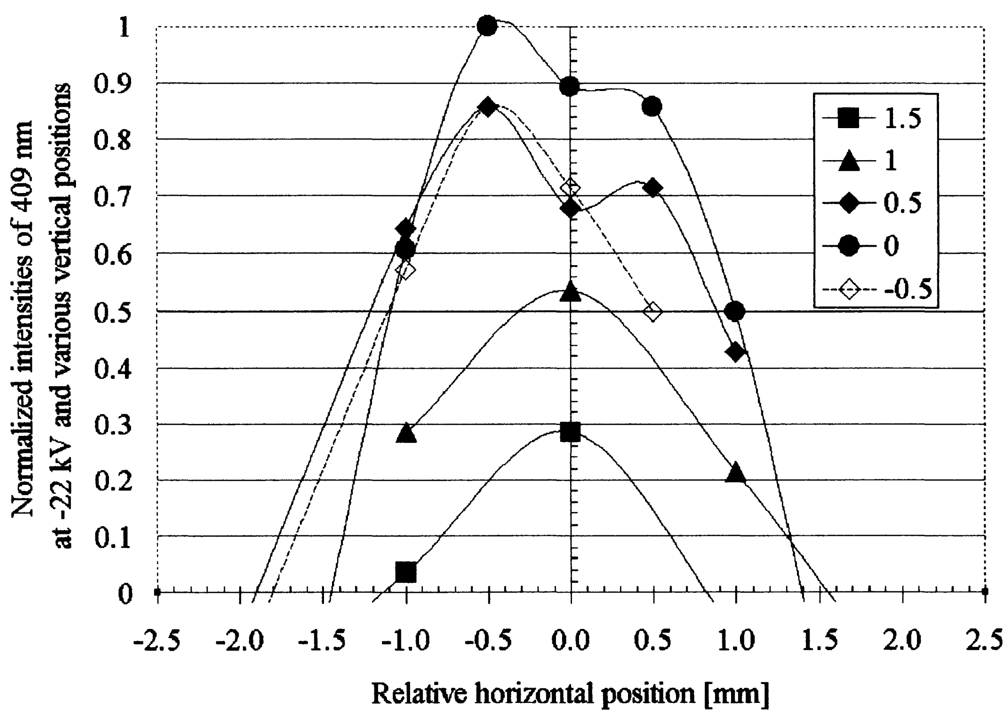

Figure A.29 Normalised intensities of visual wave length at *22 kV*.

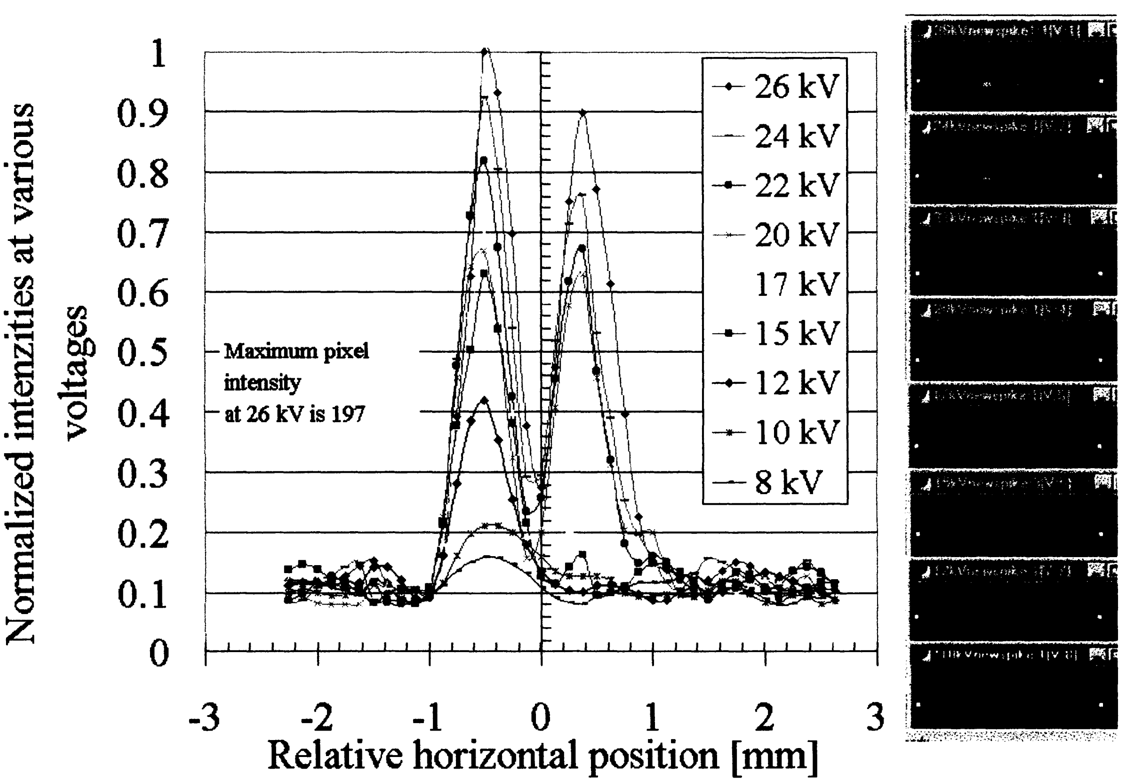

Figure A.30 Pixel intensity profile during corona discharge from spike-type discharge electrode at various voltages
(The above graph shows the change of the pixel intensity profile with applied voltage along the horizontal line passing through the centre of the spike.)

A.5.3 Experimental Results for Rod-type Discharge Electrode

In this experiment the rod-type discharge wire of one and a half millimetres in diameter was placed in the centre between two grounded electrodes. Figure A.31 shows the profile of the normalized wavelength intensity at 22 kV with respect to the centre of electrode. For this particular vertical position discharge points are on the surface of the electrode that is closer to the collecting electrode. Therefore, the wavelength intensity of the second positive band of nitrogen molecule has a dual distribution.

The number of discharge spots in the axial direction is determined from the digital image analysis. Figure A.32 shows the pixel intensity values along three vertical lines at 30 kV. The central line is placed on the surface of the electrode. Pixel intensity values at various voltages along the right, central, and left lines, placed approximately one millimetre from the centre of the electrode, are shown in Figures A.33 to A.35. In general, the fraction of discharge positions from the left and right side of electrode is much higher than from the centre of the electrode.

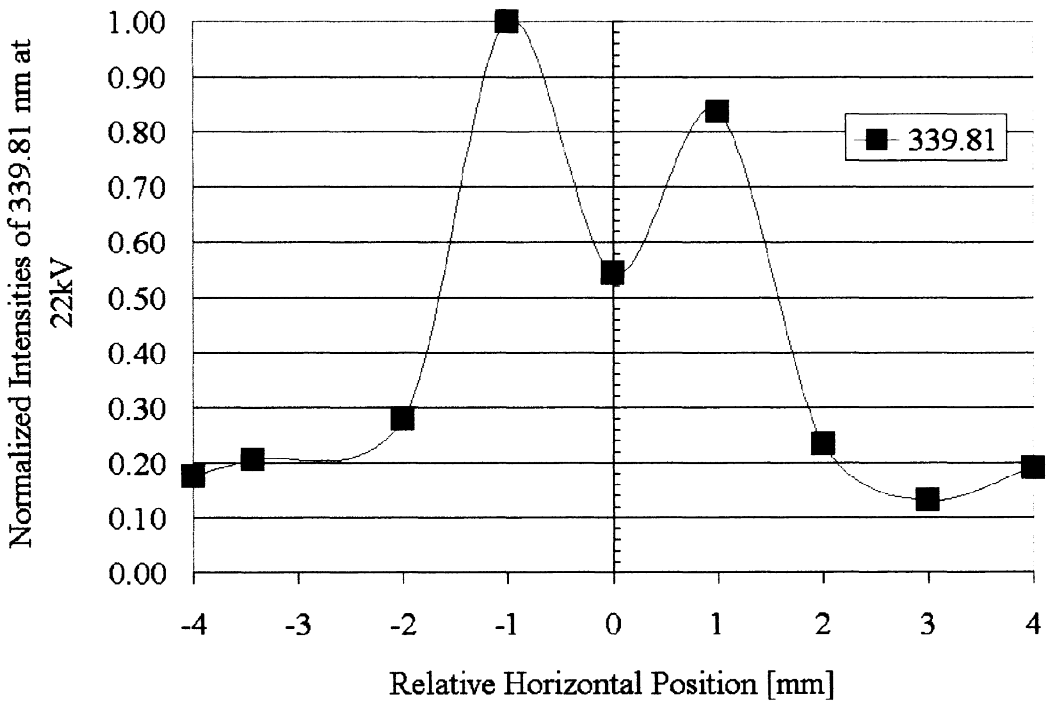

Figure A.31 Normalized wavelength intensity of 339.81 nm wave-length emission.

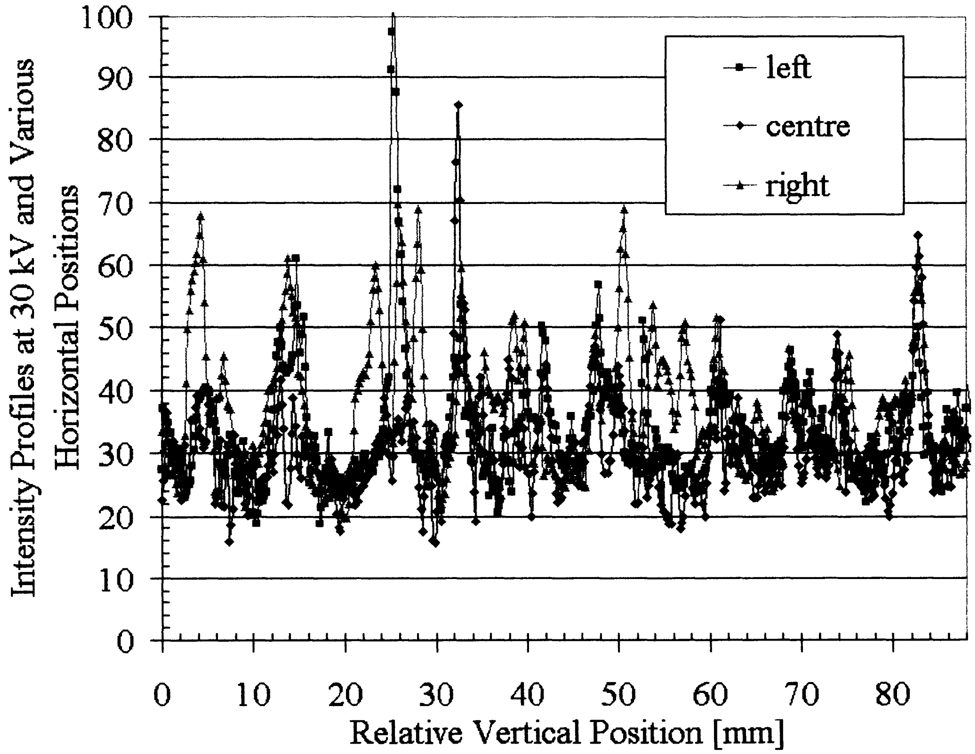

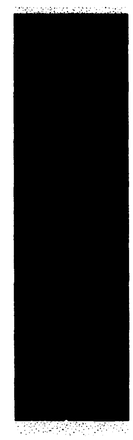

Figure A.32 Pixel intensities along three vertical lines at 30kV

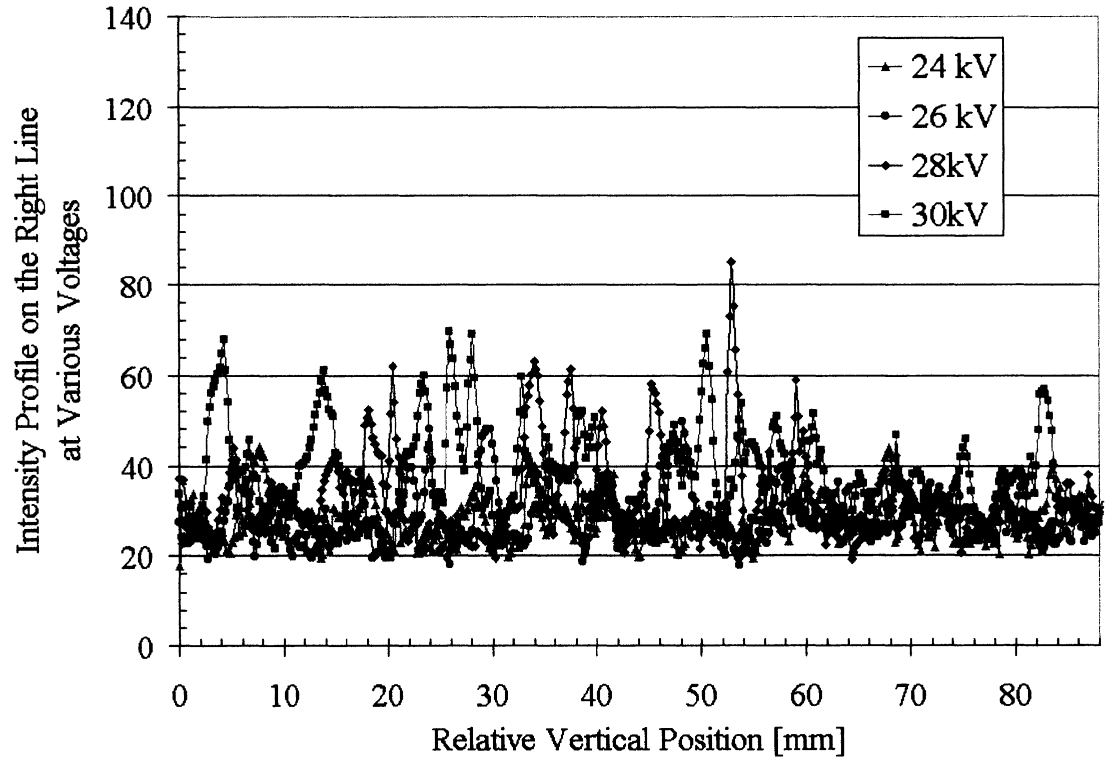

Figure A33 Pixel intensities along the right vertical line placed 1mm from the centre of the electrode.

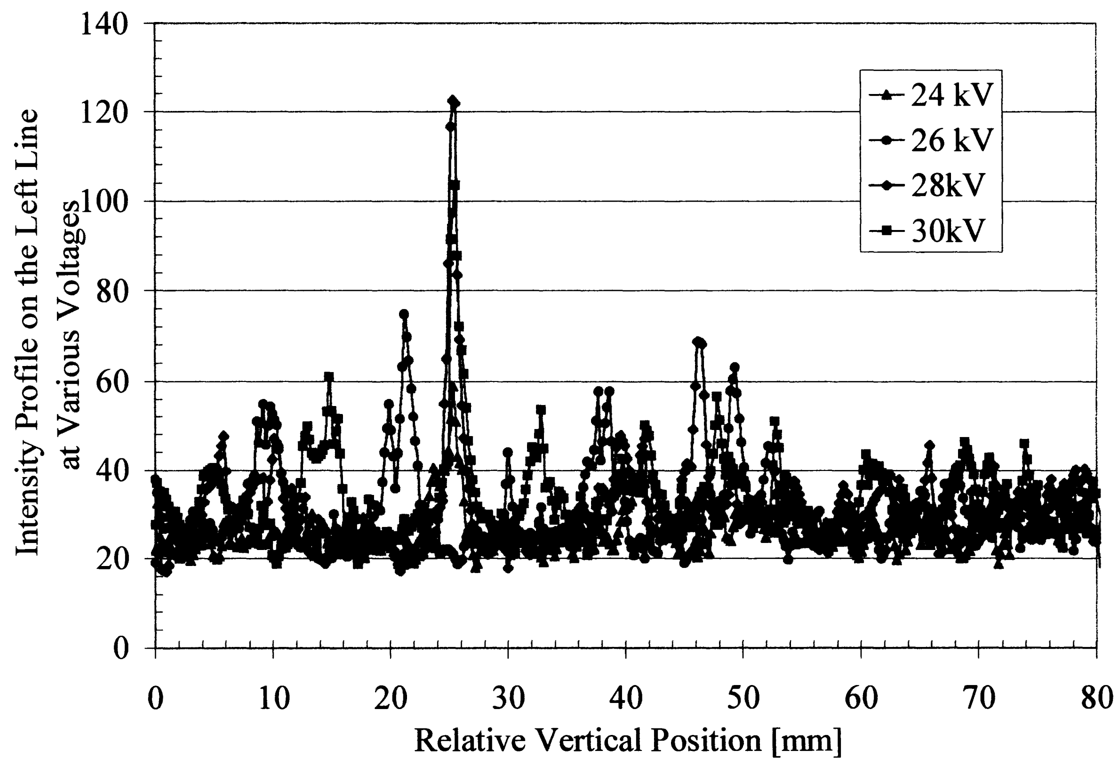

Figure A.34 Pixel intensities along the left vertical line placed 1mm from the centre of the electrode.

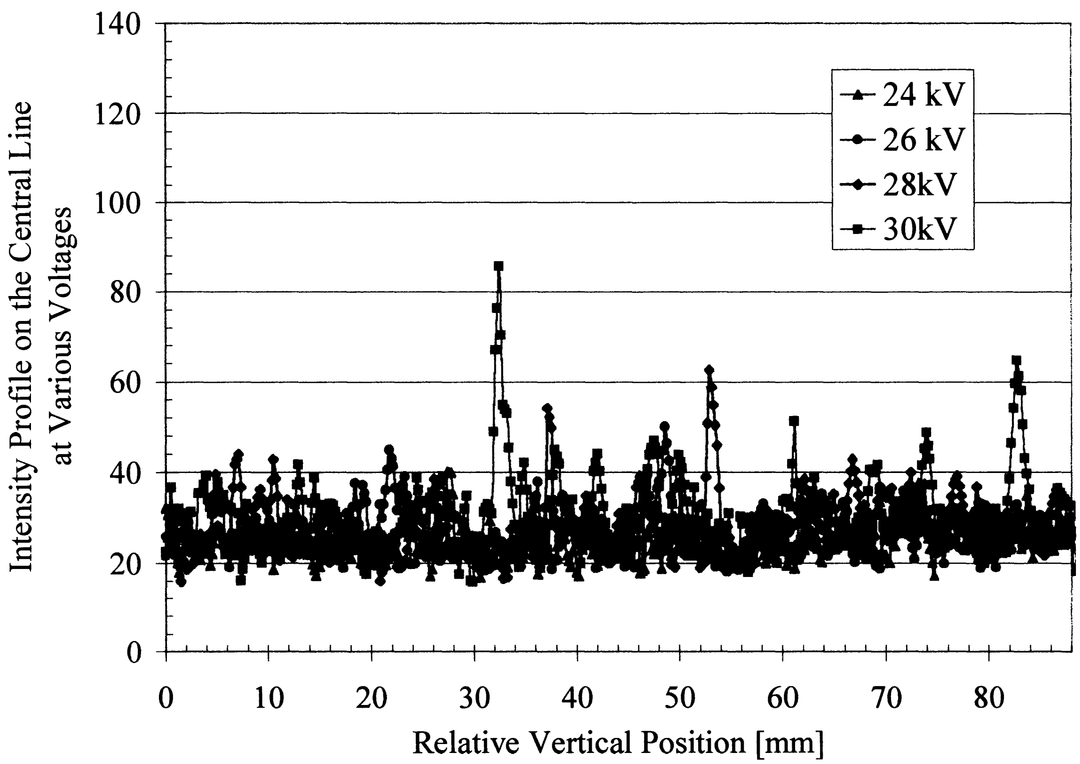

Figure A.35 Pixel intensities along the central line.

A.5.4 Discussion and Numerical Validation

The emission of the 2nd positive band of N_2 molecules that is directly proportional to the electron density and indirectly proportional to the negative ion distribution was used to set the boundary condition for ion density on the discharge electrode surface. In the case of a rod-type electrode, the *340 nm* emission is higher on the left side of the electrode. The possible reason for that might be: (a) the micro-roughness on the left side of the wire or (b) the wire was not aligned with the centre of ESP, having as a consequence stronger electric field on the left side. The approximation functions $A_f(x')$ and $B_f(x')$ of the *340 nm* wavelength emission profile at spike and rode DEs implemented in Chapter 3 are developed under the assumption of a good alignment between discharge and collecting electrodes.

Digital image analysis used to determine the boundary conditions in the axial direction for a rod type discharge electrode indicates a non-linear relationship between number of discharges and applied voltage, as shown in Figure A36. It appears, as if there is some interaction between discharge points [85, 98]. At first, by increasing the voltage, the light intensity increases up to the point when new spots are formed, as shown in Figures A.33-35. After that, the relocation of discharge spots occurs, whereby the light intensity of discharge spots may decrease compared to the intensity of discharge spots at previous voltage. The average intensity of discharge spots slightly increases with increasing voltage except at *-22 kV.* At voltages closer to spark-over value fusion of discharge spots may occur.

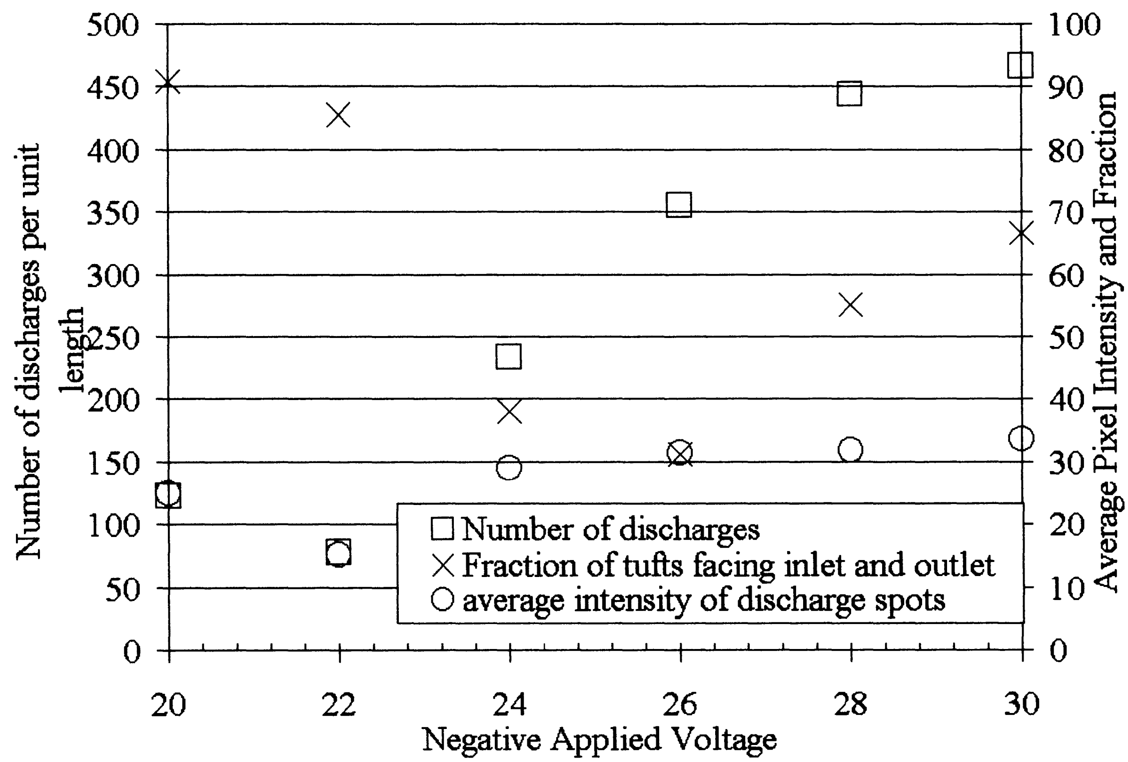

Figure A.36 Number of discharge spots (tufts), fraction of discharge spots located on the discharge electrode surface facing inlet and outlet plane of ESP (expressed in percentage), and average light intensity for wire type discharge electrode

A.6 APPROXIMATION FUNCTIONS FOR THE PARTICLE CHARGING MODE 2

Table A.3a
Dimensionless surface potential due to the field (F_{dc}) and diffusion charging (F_{fc})

	Free Molecule Kn=10	**Transition** 0.1=Kn=10	**Continuum** Kn=0.1
Diffusion	White (1951) Equation 2.2b $\Phi_{dc} = \ln(1+\frac{e^2 r_p \bar{v}_i N_i}{4\varepsilon_o kT} t)$	Chang (1891) Approximation functions for numerical solutio n of Equation 2.1b for Kn=1 $for\ \tau_{dc} \geq 20$ $\Phi_{dc} = 1.05\ln\tau_{dc} + 0.2495$ $for\ 1 \leq \tau_{dc} < 20$ $\Phi_{dc} = 0.8935\ln\tau_{dc} + 0.6056$ $for\ 0.1 \leq \tau_{dc} < 1$ $\Phi_{dc} = 0.7644\tau_{dc}^{0.8826}$ $for\ \tau_{dc} < 0.1$ $\Phi_{dc} = \tau_{dc}$	Chang (1891) Approximation functions for numerical solution of Equation 2.1b for Kn=0.01 $for\ \tau_{dc} \geq 20$ $\Phi_{dc} = 1.2022\ln\tau_{dc} + 0.3493$ $for\ 1 \leq \tau_{dc} < 20$ $\Phi_{dc} = 1.0651\ln\tau_{dc} + 0.6198$ $for\ 0.1 \leq \tau_{dc} < 1$ $\Phi_{dc} = 0.8127\tau_{dc}^{0.907}$ $for\ \tau_{dc} < 0.1$ $\Phi_{dc} = \tau_{dc}$
Field	Ohyama et al. (2000) $\Phi_{fc} = S_i \Phi_{dc}$	Ohyama et al. (2000) $\Phi_{fc} = S_i \Phi_{dc} \frac{1+Kn}{Kn}$	Pauthenier & Moreau-Hanot (1932) Equations 2.5 $\Phi_{fc} = \Phi_s \frac{\tau_{fc}}{\tau_{fc}+4}$

Table A.3b
Dimensionless charging rate equations due to
the field (?F_{dc}/?t) and diffusion charging (?F_{fc}/?t)

	Free Molecule Kn=10	**Transition** 0.1=Kn=10	**Continuum** Kn=0.1
Diffusion	White (1951) Equation 2.2a $\frac{d\Phi_p}{d\tau_{dc}'}=\frac{er_p\bar{v}_i}{4\mu_i kT}e^{-\Phi_p}$	Chang (1891) Approximation functions for numerical solution of Equation 2.1b for Kn=1 $for\ \tau_{dc}\geq 20$ $\frac{\partial\Phi_{dc}}{\partial\tau_{dc}}=1.05\frac{1}{\tau_{dc}}$ $for\ 1\leq\tau_{dc}<20$ $\frac{\partial\Phi_{dc}}{\partial\tau_{dc}}=0.8935\frac{1}{\tau_{dc}}$ $for\ 0.1\leq\tau_{dc}<1$ $\frac{\partial\Phi_{dc}}{\partial\tau_{dc}}=0.6747\tau_{dc}^{0.8826-1}$ $for\ \tau_{dc}<0.1$ $\frac{\partial\Phi_{dc}}{\partial\tau_{dc}}=1$ or for known F $_{dc}$ $\frac{d\Phi_{dc}}{d\tau_{dc}}=\frac{(1+\kappa)\Phi_{dc}}{(1+\kappa\Phi_{dc})e^{\Phi_{dc}}-1}$	Chang (1891) Approximation functions for numerical solution of Equation 2.1b for Kn=0.01 $for\ \tau_{dc}\geq 20$ $\frac{\partial\Phi_{dc}}{\partial\tau_{dc}}=1.2022\frac{1}{\tau_{dc}}$ $for\ 1\leq\tau_{dc}<20$ $\frac{\partial\Phi_{dc}}{\partial\tau_{dc}}=1.0651\frac{1}{\tau_{dc}}$ $for\ 0.1\leq\tau_{dc}<1$ $\frac{\partial\Phi_{dc}}{\partial\tau_{dc}}=0.7371\tau_{dc}^{0.907-1}$ $for\ \tau_{dc}<0.1$ $\frac{\partial\Phi_{dc}}{\partial\tau_{dc}}=1$ or for known F $_{dc}$ $\frac{d\Phi_{dc}}{d\tau_{dc}''}=\frac{\Phi_{dc}}{e^{\Phi_{dc}}-1};$
Field	Ohyama et al. (2000) $\frac{\partial\Phi_{fc}}{\partial\tau}=S_i\frac{\partial\Phi_{dc}}{\partial\tau_{dc}}$	Ohyama et al. (2000) $\frac{\partial\Phi_{fc}}{\partial\tau}=S_i\frac{1+Kn}{Kn}\frac{\partial\Phi_{dc}}{\partial\tau_{dc}}$	Pauthenier & Moreau-Hanot (1932) Equations 2.5 $\frac{\partial\Phi_{fc}}{\partial\tau_{fc}}=\frac{\Phi_S}{4}(1-\frac{\Phi_{fc}}{\Phi_S})^2$

A.7 CONTRIBUTIONS TO KNOWLEDGE

This work has several contributions to knowledge including:

1. Development of the model for the prediction of the dust particle collection efficiency for complex discharge and collecting electrode geometries.
2. Determination of the parameters influencing submicron and ultrafine dust particle charging and collection efficiency.
3. Development of constitutive relationship between the profile of the 2nd positive band of N2 molecule and boundary conditions on the surface of various discharge electrodes for simulation of ion distribution during negative corona discharge.

Several papers and conference presentations which have been published or accepted based on this work are listed as follows:

4. D. Brocilo, J.S. Chang and R.D. Findlay, "Numerical Prediction of High Resistivity Fly Ash Collection Efficiency for Large Scale Wire-Plate type ESPs," *Accepted for oral presentation for the European Aerosol Conference*, August, 2003, Madrid, Spain
5. D. Brocilo, J.S. Chang and R.D. Findlay, "Numerical and Experimental Studies of the Spike Plate and Wire-Plate Electrostatic Precipitators for Collection of Sub-micron Particles," *Accepted for poster presentation for the European Aerosol Conference*, August, 2003, Madrid, Spain
6. D. Brocilo, J.S. Chang and R.D. Findlay, "Characteristics of Bottom Ash and Aerosol Particle Compositions Generated by Burning Incense," *Accepted for poster presentation for the European Aerosol Conference*, August, 2003, Madrid, Spain

7. D. Brocilo, J.S. Chang and R.D. Findlay, "The Numerical Simulation of Multi-Field Wire-Plate Electrostatic Precipitators," *Proceedings for Electrostatics 2003*, April, 2003, Edinburgh, Scotland.

8. D. Brocilo, J.S. Chang and R.D. Findlay, "Light Emission from the Surface of Spike-type Discharge Electrode at Negative Corona Discharge in a Non-Thermal Plasma Reactor," *Accepted for oral presentation for the 30th IEEE International Conference on Plasma Science, June 2-5, 2003, Jeju, Korea*, (Selected for publication in IEEE Transaction on Plasma Science for April 2004. Submitted for reviewers comments).

9. T. Misaka, T. Oura, D. Brocilo, K. Urashima, R.D. Findlay and Jen-Shih Chang, "Precipitation of high resistivity dust particles of steel sintering plant by hybrid electroststic precipitators with pulsed corona and moving electrode," *Conference Proceedings for the 6th International Aerosol Conference 2002*, Tapei, Taiwan, Vol. 2, pp. 699-700

10. T. Misaka, A. Akasaka and T. Oura, K. Urashima, D. Brocilo, R.D. Findlay and Jen-Shih Chang ,"Validation of MESP Code for Moving Electrode Electrostatic Precipitators With and Without First Field Pulse Energization," *Conference Proceedings ICAES 2001*, Dalian, China, pp. 282-287.

11. D. Brocilo, J.S. Chang , R.D. Findlay, Y. Kawada, and T. Ito, "Modeling of the Effect of Electrode Geometries on the corona Discharge Current-Voltage characteristic for Wire-plate Electrostatic Precipitators," *Annual Report Conference on Electrical Insulation and Dielectric Phenomena*, October 2001, Kitchener, Canada, pp. 681-684.

12. D. Brocilo, J.S. Chang and R.D. Findlay, "Modeling of Two-stage Electrostatic Precipitators for Fine Particle Removal," *Journal of Aerosol Science*, Vol. 32, September 2001, pp. 893-894.

13. D. Brocilo, J.S. Chang and R.D. Findlay, "Modeling of Electrode Geometry Effects on Dust Collection Efficiency of Wire Plate Electrostatic Precipitators," *Proceedings of 8th International Conference on Electrostatic Precipitation, May 2001*, Birmingham, Alabama, Vol. 1, A4-3, pp. 1-18.

14. D. Brocilo, "Current density distribution in wire-plate electrostatic precipitators with rigid discharge electrode," *CAGE Club Student Conference 2001*, Toronto. (First price in graduate students category)

15. D.Brocilo, "Optimization of Two Stage Wire-plate Type Electrostatic Precipitator for Submicron Particle Collections," *CAGE Club Student Conference 2000*, Hamilton. (Shared first price in graduate students category).

Regarding McMaster University's policy on the ownership of intellectual property and graduate student work, it is understood that both of my supervisors, Dr. J.S. Chang and Dr. R.D. Findlay, and myself co-own the intellectual property rights and copyright for the work presented in this thesis and completed during graduate work.